Imperial College London

Low-cost, Non-contact Sensor Networks for River Stage Monitoring and Dynamic Discharge Estimation

by Neeraj Sah

Department of Civil and Environmental Engineering
Imperial College London

Low-cost, Non-contact Sensor Networks for River Stage Monitoring and Dynamic Discharge Estimation

by

Neeraj Sah

A thesis submitted in fulfilment of the requirements for the degree of
Doctor of Philosophy and Diploma of Imperial College London

October 2022

Declaration of Originality

The contents of this dissertation are all my own work, and any quotation from, or description of, the work of others is fully acknowledged by reference to the sources, whether published or unpublished.

The sensors used in this study were built by the main supervisor, Prof. Wouter Buytaert, and members of his group.

Copyright Declaration

Abstract

River monitoring and discharge estimation are crucial to developing mitigation measures for weather and climate extremes. This study demonstrates the potential of non-contact, low-cost, bespoke lidar sensors for monitoring river levels and proposes a methodology for estimating discharge using river stage data from such sensor networks. Firstly, using different laboratory and field experiments, this study evaluates the sensor performance as a function of measurement distance, surface roughness, air temperature, water turbidity, and measurement angle to monitor river levels. To enable the computational experiments that underpin my scientific enquiry and part of discharge estimation methodology development, I developed a Python application to calibrate hydraulic models under homogenous and heterogenous Manning's n assumptions, perform uncertainty and sensitivity analysis of unsteady flow parameters, and perform probabilistic flood inundation analysis in HEC-RAS. Then, using synchronous measurements of stage data from a network of sensors, a novel method for estimating the dynamic river discharge has been developed. This methodology has been tested on idealised rivers with varying channels and flow conditions, as well as on the Wandle River in the UK. After testing the developed discharge estimation method, two approaches for optimising a sensor network, that is the sensor position, number, and spacing, have been developed and assessed for various case studies. The laboratory experiments demonstrate that the sensors can take measurements under all tested conditions, up to an incidence angle of ~ 40° and within a relative error of 0.1%. The test results show that the developed discharge estimation method can be successfully applied to both prismatic and natural channels with or without lateral flow. Moreover, unlike previous studies, this method does not require an initial discharge value. The optimisation results show that, compared to three sensors, using four sensors placed closer to the downstream boundary improves parameter calibration and discharge estimation.

Acknowledgements

The completion of this thesis was only possible with the support of many people. I would especially like to thank my lead supervisor, Prof. Wouter Buytaert, for his guidance, inspiration, and ongoing support in shaping this work into what it is today. My co-supervisor, Dr Athanasios Paschalis, provided insightful comments and feedback that helped me refine this research, and I am grateful for that. Additionally, I would like to thank Dr Ana Mijic for her valuable feedback during internal evaluations.

I am grateful to the Imperial College London and NERC SHEAR Studentship Cohort (SSC) for providing financial support. I would like to express my gratitude to the UK's Environmental Agency for providing data on observed discharge and rating curves to support the various case studies discussed in this work. I am thankful for the help, technical discussions, and support received from the post-docs in my research group, especially Dr Jonathan Paul, Dr Boris Ochoa Tocachi, Dr Simon De Stercke, Dr Simon Moulds, and Dr Charles Zogheib. Additionally, I want to express my gratitude to my PhD colleagues, Anna, Will, Clara, Deema, Yuting, Khanh, Manjari, and many others, for being there during this journey.

A very special thanks to Will, Jonathan Rowe, and Dr Jonathan Paul for helping out with the river Wandle fieldwork. I am grateful to Practical Action, Nepal, Tribhuvan University, Department of Hydrology and Meteorology Nepal team for providing much-needed help to plan and carry out fieldwork in Nepal.

I also want to thank the research team and the support staff at Imperial College London, especially Sarah Willis, Hannah Rigby, Dion Kordopati, Sharon Russell-Verma, and Greta Antonini, for their unwavering assistance and support.

Without the support of my wife, this research could not have been finished. I am grateful for her support, feedback, and remarks. Last but not least, I want to express my gratitude to all the people who have helped me along the way, especially my loving parents Pawan Devi and Om Prakash Sah.

Publication arising from this thesis

Paul, J.D., Buytaert, W. & **Sah, N.** (2020) A Technical Evaluation of Lidar-Based Measurement of River Water Levels. *Water Resources Research*. 56 (4). doi:10.1029/2019WR026810.

My contribution: Design and implementation of laboratory and field experiments, experimental data analysis and co-writing the results, and addressing reviewers' comments.

Paul, J.D., Cieslik, K., **Sah, N.**, Shakya, P., Parajuli, B.P., Paudel, S., Dewulf, A. & Buytaert, W. (2020) Applying Citizen Science for Sustainable Development: Rainfall Monitoring in Western Nepal. *Frontiers in Water*. 2. doi:10.3389/frwa.2020.581375.

My contribution: Citizen science material preparation, translation of materials into Nepali language, citizen science activity implementation and delivery, feedback and editing of the paper

My PhD was part of the Landslide-EVO project and was supported by the NERC SHEAR (Science for Humanitarian Emergencies and Resilience) Studentship Cohort (SSC). The Landslide-EVO project aimed to develop an early warning system for precipitation-induced landslides in western Nepal. Therefore, to collect and analyse the rainfall in the study area, we installed several tipping bucket rain gauges. To disseminate information about the Landslide-EVO project and engage the local community in project activities, we created "Rainfall Watch" groups in several schools. As we had already installed rain gauges, we intended to set up a hydrological model and a hydraulic model in the western Nepal study area, particularly the Karnali sub-catchment, to test the value of the high-resolution discharge data obtained through the developed methodology when calibrating and updating the hydrological model. However, we could not proceed with this plan due to COVID-19 pandemic-related travel restrictions.

Abbreviations

AARE	Average Absolute Relative Error
ADCP	Acoustic Doppler Current Profiler
ADV	Acoustic Doppler Velocimeters
AMHG	At Many Stations Hydraulic Geometry
API	Application Programming Interface
BAM	Bayesian-AMHG-Manning
COM	Component Object Model
Cov	Covariance
CSA	Continuous Slope Area
CV	Coefficient of Variation
DAPT	Dense Arrays of Pressure Transducers
DLL	Dynamic Link Library
DSS	Data Storage System
EA	Environment Agency
EC	Electrical Conductivity
HEC-RAS	Hydrologic Engineering Centre-River Analysis System

ICT	Information and Communication Technology
IoT	Internet of Things
KGE	Kling-Gupta Efficiency
LIDAR	Light Detection and Ranging
LoRa	Long Range
mAOD	Meters Above Ordnance Datum
mASD	Meters Above Stage Datum
MC	Monte Carlo
NIR	Near Infrared
PIV	Particle Image Velocimetry
RMSE	Root Mean Square Error
SWE	Shallow Water Equations
SWOT	Surface Water Ocean Topography
UK	United Kingdom
USACE	U.S. Army Corps of Engineers
VBA	Visual Basic for Applications
WPM	Wandle Park Main channel

Contents

List of figures

List of tables

1 Introduction

A long series of river discharge data is essential to develop improved river and water management strategies and to cope with water-related hazards such as floods and droughts. However, continuous measurement of river discharge using direct methods, e.g., salt dilution, is practically infeasible. Therefore, in practice, indirect methods that measure proxy variables, especially river geometry, river stage, and flow velocity, that can be used to calculate discharge are usually used (Costa et al., 2006). The indirect methods can be divided into two groups 1) contact methods, and 2) non-contact methods. In contact methods, the device which measures the variables for discharge estimation is in direct contact with water. As the measurement device must be in the water, contact methods are not suitable to measure high flows due to safety concerns for the operators and the instruments. Furthermore, this method is labour-intensive, and the devices used in contact methods are difficult to maintain and are prone to damage (Yang et al., 2014; Spada et al., 2017b). Therefore, at many gauging sites around the world, non-contact methods of discharge estimation are used.

The most common indirect, non-contact method for estimating river discharge is the use of an empirical stage-discharge relationship or rating curve. In this method, the river stage is measured as a proxy for river discharge. The underlying assumption behind the usage of a rating curve is that there is a one-to-one relationship between a stage and a discharge value; therefore, a pre-established rating curve at a gauging site can be used to measure a discharge for any stage in the river. However, this assumption is only valid when the river flow has a distinct kinematic behaviour, i.e., when river flow is governed by gravitational force (riverbed slope > 10^{-3}). Therefore, the use of a rating curve is fraught with uncertainties, including (a) the hysteresis effect during unsteady flow; (b) extrapolation error during high flows; and (c) the need for regular updating due to changes in hydraulic resistance and changes in channel geometry (Perumal et al., 2007a; Aricò, Nasello & Tucciarelli, 2009; Dottori, Martina & Todini, 2009; Lee, Firoozfar & Muste, 2017; Harlan et al., 2021).

To partially overcome the limitations of steady flow rating curves and to estimate the unsteady flow discharge, recent studies, for example (Perumal et al., 2007a, 2007b; Aricò, Nasello & Tucciarelli, 2009; Dottori, Martina & Todini, 2009; Sahoo et al., 2014; Spada et al., 2017b; Muste, Bacotiu & Thomas, 2019; Harlan et al., 2021), have developed dynamic discharge estimation methods. These methods are based on the measurement of stage data from two to three water level sensors located at the ends of a selected river reach and the application of unsteady flow hydraulic modelling (solves governing equations or shallow water equations (SWE) of river flow). However, these methods (a) solve SWE in conservative form (i.e., one or more terms, such as acceleration and or pressure force terms, are removed from the momentum equation when solving the SWE), (b) are most suitable for prismatic channels with no lateral flow, thus reducing the possibilities for operational applications, (c) require one flow value, and (d) assume channel roughness or calibrate it by using observed stage data from two or three gauging locations. Although stage data from two or three gauging locations is theoretically adequate to calibrate channel roughness, error margins are still high in practice due to the suboptimal positioning of gauging stations and the coarse temporal resolution of existing measurement networks.

Therefore, this study hypothesises that a larger network of high-frequency, non-contact water level sensors along a river reach, as shown in Figure 1.1, allows for 1) better river stage monitoring; 2) better calibration of Manning's roughness coefficient and initial flow of a hydraulic model of a river; and 3) dynamic and more accurate estimation of unsteady flow discharge.

This research focuses on the development of a non-contact, robust, and cost-effective approach for dynamic river discharge estimation. Here, I demonstrate the use of bespoke lidar sensors (Paul, Buytaert & Sah, 2020) to monitor the river stage at high resolutions (1-minute). Further, I propose a methodology to calibrate the channel roughness and initial flow of a river reach, which is required to get a unique solution to SWE, by using only stage data from a network of such sensors (refer to Figure 1.1) and estimate unsteady flow river discharge dynamically. Additionally, I propose and demonstrate methods to optimise the configuration, especially location, number, and spacing, of such sensor networks to improve the accuracy of the river discharge estimates. Lastly, I extend the methods developed in this research to develop a Python application that can 1) calibrate hydraulic models under homogenous and heterogenous

Manning's n assumptions, 2) perform uncertainty and sensitivity analysis of unsteady flow parameters, and 3) perform probabilistic flood inundation analysis in HEC-RAS.

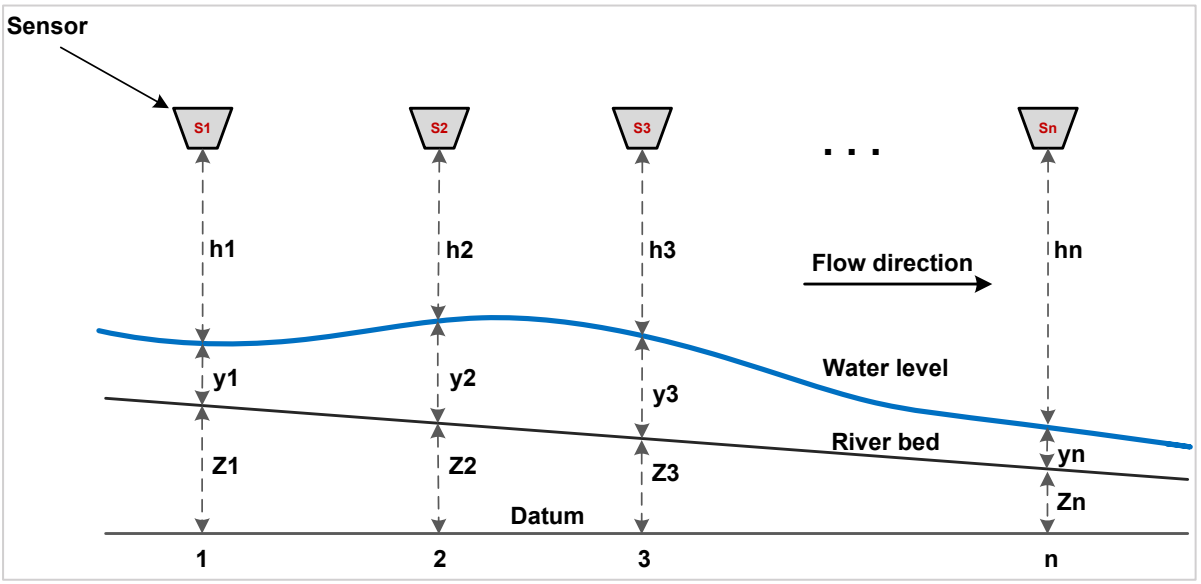

Figure 1.1: Schematic of a sensor network along a river reach

1.1 Research aim and objectives

The overall aim of this research is to test the potential of low-cost sensors and sensors network in river monitoring and indirect river discharge estimation. The objectives of this study are therefore to:

1) test the potential of lidar sensors for river monitoring
2) develop and test a methodology for dynamic river discharge estimation using only stage data from a network of sensors
3) design a method for optimising sensor network configuration (location, number, and spacing) for river discharge estimation
4) outline the additional uses (with examples) of the developed discharge estimating methodology, such as calibration and sensitivity analysis of unsteady flow parameters

1.2 Thesis structure

In the second chapter, I provide a review of the existing literature on various river monitoring sensors and existing discharge estimation methods. In the third chapter, I provide a summary of the characteristics of the lidar sensor used in this study and discuss the laboratory and field experiments carried out to test the potential of this sensor in monitoring the river stage. Then, with examples, I present Python scripts developed for the calibration of unsteady flow parameters, sensitivity analysis, and probabilistic flood inundation in HEC-RAS as a precursor to methodology development for next chapter. In chapter 5, I describe the methodology developed for dynamic discharge estimation and discuss the results from the test application of the methodology on idealised and natural rivers in the fourth chapter. Lastly, I propose and test approaches to optimising the configuration of the sensor network and analyse and discuss the results from various case studies.

2 Literature review

This chapter presents a literature review on the subjects relevant to the scope of this study. This review includes the importance of river monitoring, sensors for monitoring rivers, existing river discharge estimation methods, unsteady river flow simulation in HEC-RAS, and the Monte Carlo method. A more specific literature review is included in the introduction of each chapter.

2.1 River monitoring

The river level, or stage, is the selected reference height for the water's surface. River level monitoring is an important component of hydrometry because it can indirectly reflect important but relatively difficult to measure parameters such as discharge. The river level is traditionally measured using reference gauges, such as staff gauges, inclined gauges, and float-tape gauges (Herschy, 2008). Frequent measurements of river stages and corresponding discharges at a gauge station are used to develop a rating curve (Herschy, 2008). A continuous and long series of river stage data aids in water resource management, resulting in economic and societal benefits. Additionally, the understanding of discharge leads to more direct progress in many areas compared to the stage, including flood forecasting and mitigation, water supply management, agriculture, hydropower generation, drought response, and other hydrological applications (Villarini & Strong, 2014; Pan, Wang & Xi, 2016). Yet, despite improvements in technology, both the quality and quantity of water level data are in decline globally (Shiklomanov, Lammers & Vörösmarty, 2002; Hannah et al., 2011). From 1987 to 2007, there has been a decrease in the number of hydrometric gauging stations in Canada because of their environmental impacts and high demands for maintenance. Other countries, such as North America and developing nations, have shown similar trends (Hannah et al., 2011). Increased public concern about environmental issues and reduced funding are the two main reasons for decreasing stage data (Fekete & Vörösmarty, 2007). The closure of the various gauging stations

has led to a decrease in the spatial and temporal resolution of data. Additionally, where data is available, restricted access to data as a result of data owner policies and transboundary and national policies has a negative impact on data collection (Gerlak, Lautze & Giordano, 2011).

Faced with such difficulties in collecting stage data, the introduction of new technology and the development of low-cost sensors is a way to prevent the continuation of such tendencies. In recent years, the use of new types of in-situ sensors has been growing in environmental monitoring and hydrological decision-making processes. Applications include flood warning (Cheng et al., 2018; Tang et al., 2018), agriculture systems (for example Gutierrez et al. (2014), Montesano et al. (2018), Soulis & Elmaloglou (2018)), sanitation distribution systems (Nasirudin, Za'bah & Sidek, 2011), and soil moisture sensing for drip irrigation scheduling (Soulis & Elmaloglou (2018)).

These emerging technologies have the potential to create a more effective water level monitoring system. From a technical standpoint, new technologies have the potential to improve sensing parameters such as spatial and temporal resolution than conventional methods (i.e., reference gauges), robustness, and accuracy. In addition, the development of wireless sensor networks enables real-time data transmission and more flexible and intelligent sampling procedures.

The second type of advantage relates to economic concerns. These low-cost, simple-to-use sensors can aid in enhancing access to sensing equipment and lower the threshold for data collection. This has the potential to increase the inclusiveness of water resource management, particularly in developing nations. Typically, these sensors are easier to operate, so there is no need to hire experienced technicians. In addition, an emerging method known as "citizen science" enables non-scientists to provide immediate and accurate data. In conjunction with technologies for inexpensive sensors, they have the potential to enhance the data collection, interpretation, and analysis processes (Bhusal et al., 2017; Assumpção et al., 2018). There are already excellent examples of citizen science applications in precipitation, river water, and soil moisture measurement (Buytaert et al., 2014; Paul et al., 2020). These various methods can result in greater spatial coverage of hydrometric networks.

2.1.1 River monitoring sensors

Table 2.1 provides a summary of various sensors commonly used to monitor river levels.

Table 2.1: A summary of water level monitoring sensing technologies

Technique	***Description***	***Merits***	***Demerits***
Ultrasonic Level Sensor	Ultrasonic level instruments operate according to the time-of-flight principle, which states that sending a sound wave from a piezoelectric transducer to the contents of the vessel, which may contain liquid, solid, or slurries, will determine the level of the contents. The sensor consists of two components: an electronic transceiver and a relatively efficient transducer. In the case of a liquid level controller, the fluid level can be determined by measuring the trip time difference between an ultrasonic pulse that has been transmitted and an echo that has been reflected.	Good accuracy, no moving parts, compact, reliable, not affected by media properties	Expensive, performance can be affected by various elements in the environment, limited range (6-10m)
Radar Level Sensor	The radar level measurement system is based on the measurement of the time required for the microwave pulse and its reflected echo to make a full return trip between the non-contacting transducer and the liquid level being measured. The transceiver then converts this electrical signal into distance/level information and outputs it as an analogue and/or digital signal.	Very accurate, no calibration required, multiple output options	Expensive, can be affected by the environment, limited detection range, very sensitive to the build-up on the sensor surface.
Optical Level Sensors	An infrared LED and a light receiver constitute the optical sensor. The LED emits light that is directed towards a prism that forms the level sensor's tip. If there is no liquid in the tank, the LED light is reflected by the prism and receiver. When the liquid level rises and submerges the sensing prism, the light is refracted into the liquid, leaving the receiver with minimal or no light.	Compact, no moving parts, high pressure, and temperature capability, can detect tiny amounts of liquids	High cost of installation, invasive as the sensor requires contact with the liquid, requires power, certain thick substances

Technique	*Description*	*Merits*	*Demerits*
	The receiver activates electronic switching within the level unit to operate an external alarm or control circuit upon detecting this change.		can cause coating on the prism.
Pressure Transducers	The river depth is determined by converting the pressure exerted on the sensor by the head of water above the sensor. A pressure sensor measures the combined atmospheric and water pressure exerted on it. A vented pressure sensor, on the other hand, automatically adjusts for changes in barometric pressure and therefore does not require a barometer. For each of these types, the sensor is mounted below the anticipated minimum water level, and a cable carrying the sensor signals is connected to a data logger.	Relatively cost-effective to install and maintain	Vulnerable to debris during high water flows and water pollution.
Bubblers Sensors	Bubblers sensors measure the water level by detecting the pressure required to force an air bubble through a submerged tube. The pressure is proportional to the water level. A bubble tube connects a shore-mounted air compressor or air tank to an opening in the stream's surface water. The orifice is positioned below the anticipated minimum water level and diffuses the air bubble into the water.	Damage from debris and floods is minimal as the bubble tubing and orifice are inexpensive; offer high accuracy and do not drift over time.	Not ideal for sites with migrating or shallow channel; system requires more power to operate compressor.

Source: summarised from various literature (Herschy, 2008; Simon, Tormos & Danis, 2015; Moore et al., 2016; Stevens water monitoring systems Inc., 2017; YSI Incorporated, 2017; Process Sensing Technologies, 2017; Wai-Lok Lai, Dérobert & Annan, 2018; OTT HydroMet, 2018)

2.1.2 Why low-cost sensor networks?

Traditional hydrometric methods rely strongly on in-stream infrastructure such as weirs and flumes, which are intrusive and costly to install and maintain. Additionally, these in situ monitoring stations have limited spatial coverage and temporal resolution. Although alternative methods for automated river monitoring have been developed (e.g., ultrasonic time-of-flight and electromagnetic gauging), these remain niche applications because of practical and theoretical limitations (Herschy, 2008; Environment Agency (UK), 2018). Hence, there is an urgent need to develop novel approaches to river gauging, distributed in space-time, as cost-effective as possible, and with minimal impact on the river's eco-hydrology, in order to support directly urgent societal challenges such as global water resources management, flood and prediction and mitigation, and climate impact assessment.

Advances in sensing technology and ICT (Information and Communication Technology) for data processing, storage, and transmission are yielding a new generation of distributed sensor network technologies (Hart & Martinez, 2006). This is part of a larger evolution towards pervasive interconnectedness of appliances, commonly referred to as the Internet of Things (Gubbi et al., 2013), which holds great promise to improve data collection, transmission, and curation in a water resources context. Recent studies (Zhang et al., 2017; Mao et al., 2018) have identified large potential for robust, cost-effective, and pervasive monitoring networks to complement current hydrometrical monitoring networks. The low-cost sensor networks have the following specific advantages:

- Reduction in component costs makes it possible to employ sensors in much larger quantities than was previously possible, which increases the flexibility in design of sensor networks. It allows for optimising the balance between spatial coverage, the cost/quality ratio of individual sensors, and network redundancy
- Improved data storage and transmission capacities make it possible to monitor at much higher temporal resolution than is current practice. Measuring at time steps of minutes or even seconds within a sensor network would make it possible to measure hydraulic characteristics such as the energy gradient or the flood wave celerity
- Monitoring unobtrusively in environmentally fragile, remote, or hazardous environments, where the implementation of hard and/or expensive infrastructure is not recommended, such as developing regions and regions of conflict.

- Monitoring under extreme conditions (low flows and flooding) when most methods are typically more prone to errors and practical difficulties.

2.2 River discharge estimation methods

The discharge of a river is the total volume of water flowing through a river channel cross section per unit time at any given point. There are numerous methods for calculating river discharge, and new methods are constantly being developed to improve the accuracy of discharge estimation. The existing methods of discharge estimation are categorised into direct and indirect methods and are shown in Figure 2.1 (Morlock, 1996; Fenton & Keller, 2001; Mueller, 2003; Costa et al., 2006; Perumal et al., 2007a; Herschy, 2008; Nihei & Kimizu, 2008; Smith & Pavelsky, 2008; Dottori, Martina & Todini, 2009; Aricò, Nasello & Tucciarelli, 2009; Pan, 2013; Wolfs & Willems, 2014; Chacon-Hurtado, Alfonso & Solomatine, 2017; Dobriyal et al., 2017; Prudhomme et al., 2017; Tauro, Piscopia & Grimaldi, 2017; Bjerklie et al., 2018; Eltner, Sardemann & Grundmann, 2019; Muste, Bacotiu & Thomas, 2019; Harlan et al., 2021).

Direct methods of river discharge estimation do not require river geometry or velocity information, for example, dilution gauging. However, direct methods are not suitable for continuous river discharge estimation. Therefore, in the field, indirect methods are used. In the indirect methods river stage, river geometry, roughness, and average velocity of a river in a cross-section are utilized to estimate river discharge.

Depending on whether the instrument used to measure river stage or velocity is in direct contact with the water surface or not, the discharge estimation method can be classified into contact and non-contact methods, respectively.

However, several of the parameters required for the indirect methods, such as flow velocity, are not suitable for continuous river discharge estimation either. As a potential alternative, dynamic discharge estimation techniques can be used. The dynamic discharge estimation methods are based on flood or channel routing concepts and estimate the unsteady flow river discharge. In flood routing, river stage data from two or more sensors are used to solve a diffusion or dynamic wave model of unsteady flow and estimate river discharge. The need for dynamic discharge estimation techniques, their concept, and a critical literature review of past studies are discussed in detail in chapter 5.

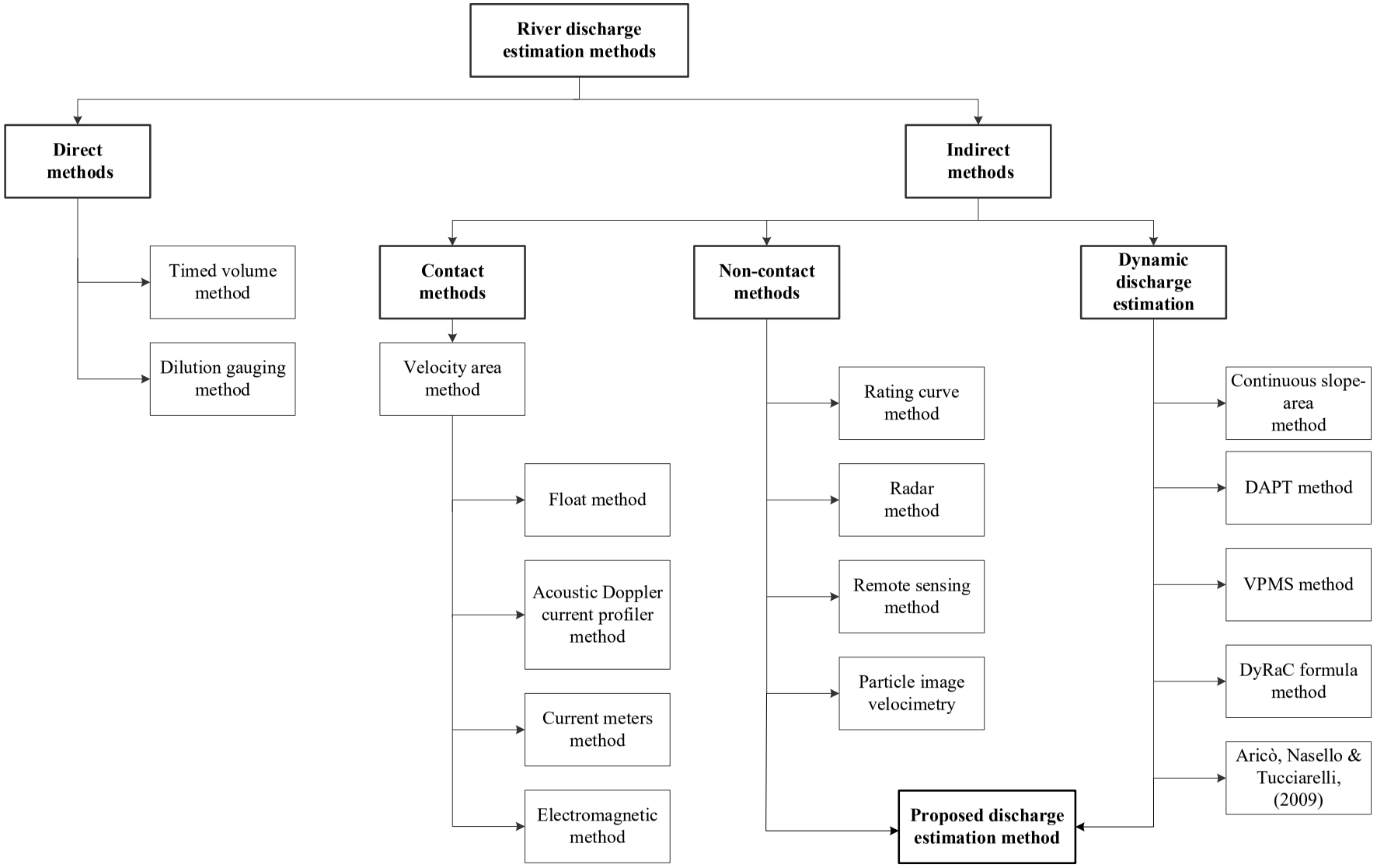

Figure 2.1: Summary of river discharge estimation methods with overlap of the methodology developed in this thesis

2.2.1 Timed volume method

This technique is used for streams in which the entire flow converges into a single descent. The time required to fill a container with a known volume is recorded and later utilised to determine the average flow rate (Lawson, 1995). For reliable and accurate results, the container must be large, the flow rate must be measured at least five times, and the stream width and depth must be recorded in more than three replicates (Pfeffer & Wagenet, 2012).

2.2.2 Dilution gauging method

Dilution gauging measures streamflow based on the rate of diffusion of a tracer, which can be a chemical or radio isotope (Comina et al., 2014). The rate of diffusion of a tracer such as table salt is measured using an electrical conductivity (EC) metre and analysed to estimate average flow velocity. This method is economical. It is an absolute method because only volume and time are used to calculate the discharge (Herschy, 2008). It is most useful during turbulent flow conditions, as conventional methods are difficult to apply (Gordon et al., 2004). However, the method can produce erroneous results due to tracer loss and incomplete mixing caused by the velocity difference between the upper and lower stream surfaces. Furthermore, trained officials are required to implement this method in the field.

2.2.3 Velocity area method

The discharge is estimated by multiplying the flow area of water in a river cross-section by the average velocity of water in that cross-section (Herschy, 2008). In this method, current meters are employed to determine the average velocity of water in a cross-section. This is one of the most accurate indirect methods, and most of the river discharge estimation methods are based on the velocity–area principle.

2.2.4 Acoustic doppler current profiler (ADCP)

The acoustic doppler current profiler method (ADCP) emits sound waves into the water and receives echoes from particles suspended in the river. The difference in frequency between the transmitted sound and the echoes is used to calculate the velocities of the suspended particles and water (Doppler effect) (Costa et al., 2000, 2006). The ADCP is mounted on a motorised

boat that traverses the river against the flow. It measures boat speed and direction by following the riverbed and the internal software compensates for the boat's movement and calculates the water velocities (Oberg & Mueller, 2007). The ADCP can therefore be viewed as a velocity–area method providing a single discharge value. ADCPs measure a significantly larger portion of the water column, allowing for faster and more accurate river discharge measurements (Mueller & Wagner, 2009). The ADCP method is non-invasive, but expensive and requires trained personnel to measure the river discharge.

2.2.5 Radar method

The radar method is also based on the velocity-area principle. Here, radar sensors are used to estimate average water velocity (Costa et al., 2006; Alimenti et al., 2020). Radar sensors emit radio waves that are reflected by floating debris and received by the sensor. This information is used to measure the surface velocity.

2.2.6 Particle image velocimetry method

The particle image velocimetry (PIV) method is based on the velocity-area principle. In this method, tracer particles are introduced into the river, and, for sufficiently small particles, it is assumed that the flow dynamics are valid. The water with suspended particles is illuminated in the images. The movement of the illuminated particles, using either an Eulerian or Lagrangian approach, in the subsequent images is used to estimate the surface velocity of the water (Tauro, Piscopia & Grimaldi, 2017). With additional processing and assumptions, the surface velocity is used to estimate the average velocity. Then, the river discharge is obtained using the velocity-area principle. Using the right tracers, lighting conditions, and image-processing procedures is important for image-based methods to give accurate quantitative information (Fujita, Muste & Kruger, 1998; Jodeau et al., 2008). These constraints limit the application of the above approaches to niche users.

2.2.7 Remote sensing method

Remotely sensed hydraulic information such as water surface elevation and channel widths are coupled with channel slope and roughness data to estimate river discharge. The remote sensing

method mostly utilises Manning's equation or kinematic wave model for river discharge estimation (Durand et al., 2016; Bjerklie et al., 2018).

2.2.8 Continuous slope-area method

The conventional slope area method is used to estimate peak discharges based on high watermarks after large flood events, as such events are typically uncommon and present a measurement challenge for obtaining reliable sample data. The obtained data is then used to extend the upper limit of the stage-discharge rating curve, which provides a crucial foundation for timely flood management decisions. The method estimates peak discharge (single value) by measuring water level drops between upstream and downstream flood marks (e.g., typically high watermarks on bridge piers and flood embankments). The drop in water surface elevations for a uniform channel reach represents energy losses caused by bed roughness. The peak discharge is indirectly estimated using Manning's equation, measured cross sections, estimated channel roughness coefficients, and friction slopes, that is, channel bed slopes for a uniform reach (Herschy, 2008).

The continuous slope area (CSA) method works on the same physical principle as the conventional slope area method, but it uses at least two upstream and downstream water level sensors to continuously measure drops in water surface elevations rather than high watermarks. This allows us to estimate stream/river discharges continuously during a hydrologic event (Lee, Firoozfar & Muste, 2017; Muste, Bacotiu & Thomas, 2019).

2.2.9 Dense arrays of pressure transducers (DAPT) method

To estimate river discharge, DAPT employs a Bayesian-AMHG-Manning (BAM) algorithm developed for the forthcoming Surface Water Ocean Topography satellite (SWOT) (Hagemann, Gleason & Durand, 2017). BAM is one of several SWOT-related discharge algorithms that estimate discharge based on anticipated river width, height, and slope measurements (Durand et al., 2014; Garambois & Monnier, 2015; Oubanas et al., 2018; Andreadis, Brinkerhoff & Gleason, 2020). BAM is an algorithm for mass-conserving flow-law inversion (Gleason, Garambois & Durand, 2018). BAM employs two different flow laws to estimate discharge: AMHG (at-many-stations hydraulic geometry), which uses width alone, and Manning's equation, which uses river width, slope, and cross-sectional area. The array of

pressure transducers is used to calculate the dynamic river water surface slope (or slope), which is then utilised in Manning's equation to estimate the river discharge.

2.3 Shallow water equations (SWE)

The shallow water equations (SWE) or Saint Venant equations are governing equations of gradually varied unsteady river flows (Venant, 1871).

$$\frac{\partial Q}{\partial x} + \frac{\partial A}{\partial t} = 0 \tag{2.1}$$

$$\frac{\partial Q}{\partial t} + \frac{\partial}{\partial x}\left(\frac{Q^2}{A}\right) + gA\frac{\partial y}{\partial x} + gA\left(S_f - S_0\right) = 0 \tag{2.2}$$

Where Q [L^3T^{-1}] is discharge, A [L^2] is area of cross-section, x is flow direction, t [T] is time, S_f is the friction slope, S_0 is bed slope and y [L] is flow depth.

Equation 2.1 is known as the "continuity equation" and equation 2.2 represents the "conservation of momentum". Equation 2.2 contains the following components:

- $gA\left(S_f - S_0\right)$ is the force due to gravity and friction.
- $gA\frac{\partial y}{\partial x}$ is pressure force.
- $\frac{\partial Q}{\partial t}$ is local acceleration and $\frac{\partial}{\partial x}\left(\frac{Q^2}{A}\right)$ is convective acceleration.

The SWE have the following assumptions (Strelkoff, 1969; Yen, 1973):

- Flow is one-dimensional and the distribution of velocity along a channel section is uniform
- The pressure distribution is hydrostatic
- The bed slope, θ, is small enough to satisfy $\tan\theta \approx \sin\theta$. Therefore, the flow depth measured vertically is regarded as equal to that measured perpendicular to the channel bottom
- The water density is constant

Unsteady-flow equations are typically not amenable to analytical, closed-form solutions due to their complexity. To solve these equations, numerical methods are required. Since the early 1960s, researchers have developed various efficient solution methods for unsteady-flow equations, and excellent reviews of these methods can be found in the scientific literature (for example, Lai, 1986). The various numerical methods can be classified broadly as finite difference or finite element methods.

2.3.1 Kinematic, diffusion and dynamic wave model

If only the gravity and friction force of the momentum equation is considered to simulate the unsteady river flow, the resulting flow model is called as kinematic wave model (Equation 2.4):

$$\text{i.e., } gA\left(S_f - S_0\right) = 0 \tag{2.3}$$

$$S_0 = S_f \tag{2.4}$$

The kinematic wave model is most suitable for gradually varied flow in channels with steeper slopes. This model assumes that the wave moves only in the downstream direction and thus it neglects backwater effects. Further, the kinematic wave cannot disperse because the wavelength of a flood hydrograph does not change with time. Additionally, the flood peak cannot reduce or increase except due to changes in slope, cross-section shape or due to lateral inflow or outflow (Lai, 1986; Akan, 2006).

If both forces due to gravity and friction and the pressure of the momentum equation are considered, then the resulting unsteady flow model is called as diffusion wave model (Equation 2.5):

$$gA\frac{\partial y}{\partial x} + gA\left(S_f - S_0\right) = 0 \tag{2.5}$$

The diffusion wave equation causes a diffusion of the modelled flood wave so that the flood peak generally becomes smaller as it moves downstream. The diffusion wave is most suitable for gradually varied flow in channels with milder slopes. Because the pressure force term is included, backwater effects can be represented.

When all the terms of equation 2.2 are considered, the resulting unsteady model is known as the dynamic wave model. The dynamic wave model provides a good representation of the backwater flows and is usually needed where wave fronts are steep.

2.4 HEC-RAS

HEC-RAS (Hydrologic Engineering Centre-River Analysis System), developed and maintained by the Hydrologic Engineering Centre (HEC) of the U.S. Army Corps of Engineers (USACE), is one of the most widely used hydraulic engineering analysis software (Goodell, 2014). It has been extensively used for the hydraulic modelling of open channel systems to simulate water surface profiles for flood studies (di Baldassarre & Montanari, 2009; Timbadiya, Patel & Porey, 2011; Sönmez & Doğan, 2016; Husain, 2017; Vojtek et al., 2019), dam break analysis (Xiong, 2011; Balaji & Kumar, 2018; Shahrim & Ros, 2020; Bharath et al., 2021), sediment transport (Crawford, 1991; Joshi et al., 2019; Sisinggih et al., 2020), and hydraulic structures including culverts, bridges, and weirs, as well as flood protection dikes (Lee, Ho & Chyan, 2006; Brunner et al., 2016). Furthermore, it has also been widely used to calibrate channel roughness and develop rating curves (Parhi, Sankhua & Roy, 2012; Lacasta et al., 2017; Wara et al., 2019; Timbadiya, Patel & Porey, 2011). The model can be used for both 1D and 2D modelling (Brunner et al., 2016; Brunner, 2016a, 2016b).

In this study, HEC-RAS is utilised because:

i. the model solves the full SWE of mass and momentum conservation; the model can therefore account for backwater flow
ii. the numerical scheme used to solve the SWE is non-dissipative and stable in a semi-implicit form (weighting factor of 0.6) under unsteady flow conditions
iii. the model can handle transitions between subcritical and supercritical flow conditions
iv. the model is configurable for various hydraulic structures, including culverts, bridges, gated spillways, overflow weirs, weirs (sluice or radial, broad, ogee or acute crested), and drop structures
v. most importantly, the model is freely available, and its API (Application Program Interface) is openly accessible, thereby providing opportunities to couple HEC-RAS with other software and automating river flow simulations

vi. it is continually upgraded to improve the accuracy of the solutions and adds new features for river flow simulations

The purpose of this work is to develop open-access tools and scripts for automated river reach calibration and discharge estimation. Therefore, other models that can be used to implement the methodology developed in this study, such as MIKE 11, which was not freely available, were not considered for this study.

2.4.1 Numerical solution of SWE

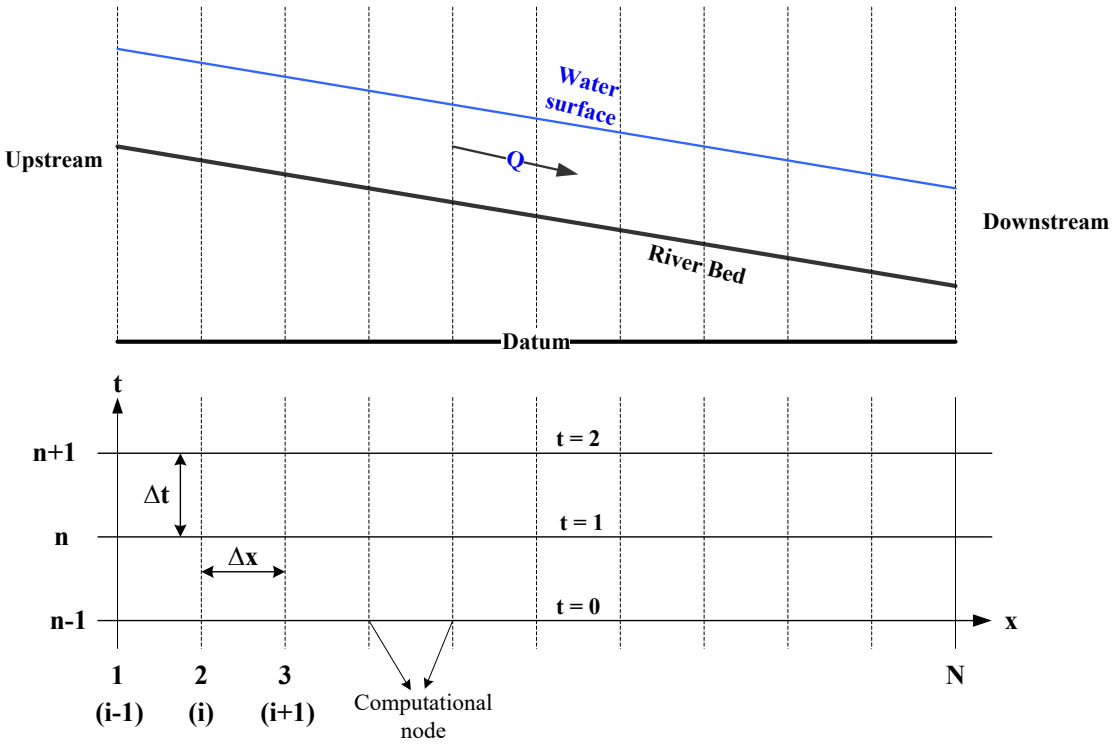

Figure 2.2: Computational grid [adapted from (Akan, 2006; Brunner et al., 2016)]

The vertical lines of the computational grid shown in Figure 2.2 represent different cross-sections or locations (x) along the channel, and the horizontal lines correspond to the discrete times (t) at which we seek a numerical solution. Δx and Δt are increments in space and time. The horizontal line marked 't=0' represents the initial time, and the initial flow conditions. The vertical line labelled as 1 represents the upstream end of the channel, and that labelled N represents the downstream end. The boundary conditions apply to the nodes on these lines.

HEC-RAS uses the four-point implicit finite difference scheme (also called as Preissman method) to compute unknown Q and y at each node (Brunner, 2016a). In the implicit finite difference scheme, the values at time stage n+1 as well as stage n are used to approximate the spatial and time derivates and the dependent variables of the Saint-Venant equations. This formulation leads to a set of algebraic, non-linear equations. These equations are solved simultaneously to obtain the results at stage n+1.

Continuity equation in finite difference form is written as (Akan, 2006):

$$\frac{(A_{i+1}^{n+1} + A_i^{n+1}) - (A_{i+1}^{n} + A_i^{n})}{2\Delta t} + \frac{\theta(Q_{i+1}^{n+1} - Q_i^{n+1}) + (1-\theta)(Q_{i+1}^{n} + Q_i^{n})}{\Delta x} = 0 \tag{2.6}$$

Similarly, the momentum equation in finite difference form is written as (Akan, 2006):

$$\begin{aligned}
&\frac{(Q_{i+1}^{n+1} + Q_i^{n+1}) - (Q_{i+1}^{n} + Q_i^{n})}{2\Delta t} + \theta \frac{\left\{\left[\frac{(Q_{i+1}^{n+1})^2}{A_{i+1}^{n+1}}\right] - \left[\frac{(Q_i^{n+1})^2}{A_i^{n+1}}\right]\right\}}{\Delta x} \\
&\quad + (1-\theta) \frac{\left\{\left[\frac{(Q_{i+1}^{n})^2}{A_{i+1}^{n}}\right] - \left[\frac{(Q_i^{n})^2}{A_i^{n}}\right]\right\}}{\Delta x} + g\theta \frac{(A_{i+1}^{n+1} + A_i^{n+1})}{2} \frac{(h_{i+1}^{n+1} - h_i^{n+1})}{\Delta x} \\
&\quad + g(1-\theta) \frac{(A_{i+1}^{n} + A_i^{n})}{2} \frac{(h_{i+1}^{n} - h_i^{n})}{\Delta x} \\
&\quad + g\theta \frac{(A_{i+1}^{n+1} + A_i^{n+1})}{2} \frac{(S_f)_{i+1}^{n+1} + (S_f)_i^{n+1}}{2} \\
&\quad + g(1-\theta) \frac{(A_{i+1}^{n} + A_i^{n})}{2} \frac{(S_f)_{i+1}^{n} + (S_f)_i^{n}}{2} = 0
\end{aligned} \tag{2.7}$$

Where, h = elevation of water surface; θ = weighting factor, which lies between 0 and 1. A weighting factor of $\theta = 1$ yields a fully implicit scheme. This four-point implicit scheme is unconditionally stable for $0.5 \leq \theta \leq 1$, conditionally s for $\theta = 0.5$ and unstable for $\theta \leq 0.5$. The accuracy of a numerical solution increases if θ approaches to 0.5 (Fread, 1974; Liggett & Cunge, 1975).

2.4.2 Model accuracy

Model accuracy is defined as the degree of closeness of the numerical solution to the true solution or the analytical solution of the SWE. It mainly depends on the assumption of the model structure (for example, a 1D model), the accuracy of the river geometry data, the accuracy of the flow/stage/rating curve data, and boundary conditions, and the numerical accuracy of the solution scheme (because finite difference solutions are approximate).

2.4.3 Model stability

When a particular numerical error increases, the solution begins to oscillate. If the error is very large, the computation may stop. This results in the instability of the model. When modelling unsteady flows in HEC-RAS, the following factors typically influence the model's stability and accuracy.

2.4.3.1 Cross-section spacing

- Should be placed at representative locations which describe changes in geometry
- Steeper slopes require more cross-sections
- Streams flowing at high velocity require cross-sections on the order of 30 meters or less
- Too far apart cross-sections; will cause additional numerical diffusion, due to the derivates w.r.t distance being averaged over too long of a distance. It might also cause the Courant number to go below 1.0, which will cause instability in the model.

2.4.3.2 Computational time step

The computation time step, Δt, should be selected such that it satisfies the Courant condition (Courant, Friedrichs & Lewy, 1928):

$$C_r = V_w \frac{\Delta t}{\Delta x} \leq 1.0 \tag{2.8}$$

For C_r = 1; (2.9)

$$\Delta t \leq \frac{\Delta x}{V_w}$$

where V_w = flood wave speed, which is normally greater than the average velocity; C_r = Courant number. A value of 1.0 is optimal; Δx = distance between the cross-sections

For most rivers the flood wave speed can be calculated as:

$$V_w = \frac{dQ}{dA} \tag{2.10}$$

However, an approximate way of calculating flood wave speed is to multiply the average velocity by a factor (summarised in Table 2.2).

Table 2.2: Factors for computing wave speed from average velocity (Brunner, 2016a)

Channel Shape	**Ratio (V_w/V)**
Wide rectangular	1.67
Wide parabolic	1.44
Triangular	1.33
Natural Channel	1.5

In the numerical solution of SWE, discharge, and flow depth derivatives with respect to distance and time are calculated. When the hydraulic properties of a flood wave at a given cross-section change rapidly with respect to time, the program may become unstable if a larger than necessary computation time step is selected. If a smaller time step is selected, then the leading edge of the flood wave may become steeper and cause model instability. Therefore, the computation time must be equal to or less than the time required for a flood wave to travel from one cross-section to the next.

2.4.3.3 Theta weighting factor

Theta is a weighting that is applied to the finite difference approximation when solving the equations for unsteady flow. Theta can theoretically range from 0.5 to 1.0. However, an acceptable range is between 0.6 and 1.0. A value of Theta of 1.0 offers the most stability, but less numerical accuracy. A value of 0.6 for Theta provides the greatest accuracy, but less numerical stability.

When selecting theta, one must find a balance between accuracy and computational robustness. Greater values of theta produce more robust solutions. Although smaller values of theta are more accurate, they tend to cause oscillations in the solution, which are amplified when a large number of internal boundary conditions are present (Brunner, 2016a).

2.4.3.4 Bad downstream boundary condition

If the downstream boundary condition causes abrupt jumps in the water surface or water surface elevations that are too low (approaching or falling below the critical depth), this can cause oscillations in the solution, which may result in the solution becoming unstable and stopping. For example, rating curves with insufficient points or too few stages, and normal depth boundary conditions with excessive friction slope or bed slope (Brunner, 2016b).

Other factors, such as hydraulic structures and the slope of riverbed profiles, can contribute to model instability; however, they are beyond the scope of this study.

2.5 HECRAS Controller

HECRAS Controller is an application programming interface (API) component of the HEC-RAS. It is a collection of programming tools, including classes, sub-routines, and functions. This API allows access to the HEC-RAS elements as a Component Object Module (COM). HEC-RAS computations may be controlled by any program able to interact with the COM DLL (Dynamic-Link Library). As HEC-RAS is developed using VBA, the most convenient method is to use Visual Basic in any form, i.e., as a separate suite for developers or linked to another application, such as Microsoft Excel.

This API's primary capabilities include running HEC-RAS and specific HEC-RAS editors, executing computation plans, reading flow simulation results, etc. The ability to manipulate roughness coefficients is a very interesting feature provided by this API. Numerous researchers have studied the impact of the roughness coefficient on river flow simulation (Yang et al., 2014; Lacasta et al., 2017; Li, Geng & Mao, 2020).

However, HECRAS Controller is still limited in its capabilities. Even the primary author advocating for the use of this programming tool, Goodell (2014), recommends manipulating HEC-RAS data files in ASCII format. The use of Visual Basic/VBA also presents a problem

because of its reduced use. Python and its extension ArcPy have replaced VBA in ArcGIS, for instance. Consequently, HECRAS Controller is being implemented with other languages, such as MATLAB (Leon & Goodell, 2016a) and Python (Dysarz, 2018).

A detailed description of the above-mentioned collection of programming tools is presented in Goodell (2014).

2.6 Why the Monte Carlo method?

In this study, the Manning's roughness coefficient and initial flow of a hydraulic model of a river reach are calibrated to estimate unsteady flow river discharge. To calibrate the hydraulic model, the governing equations of the river flow (or SWE) are used as the optimisation function. During the calibration process, optimal values of parameters, such as Manning's roughness coefficient and initial flow, that minimise the difference between the simulated and observed stages at the downstream of the hydraulic model are searched (Lacasta et al., 2017).

This search can be done using different techniques. They are usually classified into two main groups: gradient-based and gradient-free (Chaparro et al., 2008). Gradient-based methods, such as adjoint formulation, necessitate evaluating the gradient as a guide when searching for the optimum. This is very efficient when dealing with convex problems. Gradient-free methods, such as Monte Carlo (MC), perform the operation over the whole domain, and they are very convenient when multi-modal and noisy functions need to be minimised. These methods offer a suitable technique to cover the domain where the variable to be calibrated can be found (Cervantes, 1972).

Both the gradient-based method (Sanders & Katopodes, 2000; Piasecki & Sanders, 2002; Ding & Wang, 2006) and the gradient-free method (Fread & Smith, 1978; Wasantha Lal, 1995; Pappenberger et al., 2005a) have been applied in the calibration of the hydraulic model, especially Manning's roughness coefficient. However, compared to gradient-free methods, gradient-based methods require more computational capacity. In addition, gradient-free methods are used to solve global optimisation problems using heuristic and stochastic algorithms. Adaptive stochastic methods such as Monte Carlo inspired approaches are among these methods. They search for the answer by random sampling. Instead of locating the optimal value using the information in the gradient, it is possible to search for the minimum and recursively shrink the domain to find the minimum. This reduction occurs once the best

solutions among all those assessed have been determined (Lacasta et al., 2017). Atanassov & Dimov (2008) provide an engaging discussion of MC techniques. Typically, these stochastic methods are referred to as nondeterministic, and the MC method is among the most prominent. Moreover, the Monte Carlo method enables for the observed variability in important inputs to be accounted for and seeks to simulate reality by randomly selecting from a range of potential inputs. When more than two variables must be accounted for in a modelling analysis, Monte Carlo modelling is typically the only feasible method (Babister et al., 2016a).

There has been a significant growth in the application of Monte Carlo techniques for flood estimation and hydraulic model calibration (Hoang et al., 1999; Rahman et al., 2002; Weinmann et al., 2002; Li, Geng & Mao, 2020; Timbadiya, Patel & Porey, 2011). Therefore, in this study, the Monte Carlo method has been used for the calibration of the hydraulic model. Furthermore, the developers of HEC-RAS have been planning to implement the Monte Carlo method within the HEC-RAS GUI for performing uncertainty and sensitivity analysis of unsteady flow parameters (Goodell, 2014). However, it has not yet been done. Therefore, this study also aimed to develop a Python application to implement the Monte Carlo framework for carrying out calibration and uncertainty and sensitivity analysis for river flow simulations in HEC-RAS.

2.6.1 Monte Carlo (MC) method

The MC method is a class of probabilistic computing algorithms that compute their results by repeatedly sampling random variables of interest from a pool of random variables (von Neumann, 1951; O'Connor & Kleyner, 2011). The underlying concept is to employ randomness to solve problems that are in principle deterministic (Anon, 2016). It is best suited for simulating phenomena in which the inputs are subject to high uncertainty. The MC method is frequently used in physical and mathematical problems and is particularly useful when alternative approaches are difficult or unattainable (Signoret & Leroy, 2021). MC methods are primarily used to solve three types of problems: optimization, numerical integration, and drawing random numbers from a probability distribution. For example, reliability analysis, risk propagation, random process simulation, probabilistic design, and so on.

2.6.1.1 Advantages of the MC method

- In the MC simulation, the most probable events occur first, thus it is self-approximating
- It is advantageous for modelling phenomena with considerable uncertainty in the inputs, and it always works regardless of the model's complexity
- In contrast to other numerical methods, MC is simple and easy to implement
- It does not require specific knowledge of the form of the solution or its analytic properties
- It does not constrain what form the distributions take, and the distributions need not necessarily even have a mathematical representation
- It is widely used to answer 'What-if' scenarios, the sensitivity of the outputs to input and uncertainty analysis (Beven & Binley, 1992)

2.6.1.2 Disadvantages of the MC method

- MC method is computation intensive, especially with complex models requiring a large number of simulations runs. However, with increasing computational efficiency and capabilities it is less of a problem nowadays
- MC implicitly assumes that all the parameters are independent, which may not be the case, especially with complex models
- It is difficult to estimate an error as there are no hard bounds on the error in the computed results.

2.6.1.3 Monte Carlo method implementation

The basic steps for performing MC simulations are summarized below (von Neumann, 1951; O'Connor & Kleyner, 2011; Lacasta et al., 2017) :

i. Define the problem and the objective of the study. Evaluate the existing data and the anticipated conclusion
ii. Define the system and develop a parametric model e.g., $y = f(x_1, x_2, x_3, \dots, x_n)$
iii. Design simulation: define the number of parameters/inputs to be simulated, determine the probability distributions for each of the inputs and the number of simulations runs. It should be noted that the number of simulations runs (say m) is affected by the complexity of the model and the desired accuracy of the results
iv. Generate a set of random inputs from the chosen probability distribution function
v. Run the deterministic system model with the set of random inputs

vi. Evaluate the model and store the results as y_i
vii. Repeat steps iv, v and vi for $i = 1\ to\ m$
viii. Analyse the results

2.7 River types and flow conditions

There are various types of rivers and river systems around the world. Based on permanence of flow, rivers are categorized as perennial, intermittent and ephemeral rivers. Perennial rivers have continuous flow of water (e.g., Amazon, Nile, Koshi) throughout the year, it gets water from range of sources, including snow melt and rainfall. Unlike, perennial rivers, intermittent rivers flow seasonally due to seasonal weather patterns. These rivers are found mainly in dry and semi-dry areas (e.g., Ugab river in Namibia). These rivers are fed by a mixture of runoff from rainfall and groundwater. Ephemeral rivers are characterised by a temporary rapid flow resulting from abnormally strong rainfall or rapid snowmelt. The bed of these rivers is dry for most of the year because the water table lies well below the surface and there is no base flow (Gordon et al., 2004; Chow, 2006).

These rivers have different flow regimes or conditions which may remain constant or vary throughout the year. River flow dynamics is influenced by friction, channel topography and channel shape. Based on different criteria, rivers flow is categorized into different types. For example, depending on effect of viscosity of water relative to inertia of flow, river flow is categorized as laminar, turbulent, and transitional flow. Similarly, depending on whether depth of flow of river is changing with time or not, river flow is distinguished as steady or unsteady flow respectively. (Chow, 2006) provides detailed discussion on types of river flows. River flow conditions is also influence by geological properties of different catchments, particularly their permeability, have a significant impact on river flow patterns. For instance, under identical climatic conditions, the flow regime sustained by discharges from the underlying Chalk is significantly more stable than that of impermeable clay catchment, allowing for a quicker response to precipitation events (e.g., Lambourn and Ock catchments in the UK) .

The low-cost water level sensors used in this study were tested in rivers of Nepal and the UK. Table 2.3 provides a summary of rivers of Nepal and the UK.

Table 2.3: Summary of rivers in the UK and Nepal (Water and Energy Commission Secretariat (WECS), 2011; NRFA, 2022)

Rivers in the UK	*Rivers in the Nepal*
▪ UK has around 1500 discrete river systems, comprising over 200,000 km of watercourses. However, in comparison to rivers in the world they are considered as streams because the rivers are short, shallow, and subject to considerable man-made structures. ▪ Rivers range from mountain torrents draining headwaters receiving up to five metres of rain per year, to much more placid groundwater-fed streams in parts of the southern and eastern England where rainfall per year is less. River flows can typically range through several orders of magnitude and low flows tend to be very modest in most river basins. For this reason, rivers are sensitive to regime changes – e.g., heavy abstraction rates and major land use change. ▪ Relative to most parts of the world, UK river flow patterns are less dominatingly influenced by seasonal contrasts in rainfall or melt-water contributions. UK rainfall is, on average, fairly evenly distributed throughout the year with a modest tendency	▪ There are about 6000 rivers in Nepal with a total drainage area of 194,471 sq. km. Out of this, 74 % lies within the country, 33 of these rivers have a drainage area that exceeds 1000 sq. km. ▪ Based on the origin or source of the river and discharge, Nepal has four main river systems. They are Mahakali, Karnali, Gandaki and the Koshi river systems. They originate in the Himalaya and carry snowfed flows with significant discharge even in the dry season. These rivers are perennial and have tremendous potential as a source of irrigation and hydropower development. The Babai, West Rapti, Bagmati, Kamala, Kankai and the Mechi are medium rivers. These rivers originate in the Midlands or the Mahabharat Range and are fed by precipitation as well as groundwater regeneration (including springs). These rivers too are perennial but are commonly characterized by a wide seasonal fluctuation in discharge. In addition to these large and medium river systems, there are a large number of small rivers in the Terai which mostly originate in the Siwalik Range. ▪ The rivers in Nepal are characterized by wide, seasonal fluctuation of flow. The monthly flows generally reach their maximum in July-August and decline to their minimum in February-March. About 80% of the total flow occurs during five months (June - October) and the rest during the remaining months. It can be

Rivers in the UK	*Rivers in the Nepal*
towards an autumn/winter maximum, particularly in western catchments.	generalized that the smaller the size of the river catchment area, the wider is the range of flow fluctuation.
▪ Seasonal variations in temperature and sunshine amounts ensure that evaporation losses are heavily concentrated in the summer half-year (April-September). In turn, this imposes a marked seasonality on river flows with maximum flows normally in the winter and minimum flows normally occurring in the summer or autumn. In winter, the UK is affected by cyclones, resulting in more than usual rainfall.	▪ The temporal and spatial variations of river flows are mainly due to the physiographic and climatic characteristics of the country resulting in time and space distribution of rainfall. Although Nepal lies near the northern limit of the tropics, there is a very wide range of climate from the summer tropical heat and humidity of the Terai to the colder, dry continental and alpine winter climate through the middle and the northern mountainous sections. The amount of precipitation and the range of temperature vary considerably because of the exceptionally rugged terrain. Nepal has two rainy seasons. The more prominent of the two lasts from June to September when the south-west monsoon brings about 80% of the total rainfall. The other, which accounts for 20% of the total annual rainfall, occurs during the winter. The eastern part of the country experiences more rain than the western part. The downpour is maximum in the hilly regions of the central part of the country. This is mainly due to the highly spatially varying topography resulting in varying orographic effects in the country. In both spring and autumn, Nepal can be affected by the tail of cyclones generated over the Indian Ocean and which reach the country through the Bay of Bengal. These can give several days of heavy rain. The other pre- and post-monsoon rains occur during unsettled climatic conditions just before and after the monsoon.

3 A technical evaluation of lidar-based measurement of river water levels

For many applications, including discharge estimation and flood prediction, measuring river water level (stage) is essential. There are many in situ and non-contact methods available, but there is a pressing need for new, more practical ones. The development of time-of-flight distance sensors and the use of non-contact techniques have accelerated due to rapid technological advancement. Because of its low-cost, high-energy efficiency, and small measurement footprint, the use of lidar for distance measurement is among the techniques that show promise. However, measuring water levels with lidar hasn't been done very often. In this chapter, a near-infrared lidar sensor (905 nm) is evaluated to determine if it can accurately measure stages in a variety of environmental conditions. Using various laboratory and field experiments, the lidar sensor performance is evaluated as a function of measurement distance, surface roughness, air temperature, water turbidity, and measurement angle.

3.1 Introduction

3.1.1 Non-contact methods to measure river stage

Accurate monitoring of water levels is an integral part of hydrological practise, informing, for example, flood-risk management systems, groundwater resource planning, and irrigation control systems. Nevertheless, despite the vast array of available methods, the global density of river gauging stations is still well below the operational optimum, even in densely gauged nations. Numerous existing records are fragmented, and inconsistencies in format and a lack of metadata are pervasive issues in numerous locations (Hannah et al., 2011). Although there are numerous obstacles to river gauging, technological advancements may help to reduce the number of resources required to obtain accurate measurements, thereby increasing the density

of the river gauging network. This is especially important in locations with limited data (Alabyan et al., 2016; Hund, Johnson & Keddie, 2016; Paul et al., 2018). There, enhancements to the cost, accessibility, and automation of monitoring technology could result in a significant increase in data collection.

Increasingly, non-contact methods for monitoring river levels (stages) are being implemented. In contrast to the susceptibility of in situ methods, such as pressure transducers, to fouling and damage from extreme events, noncontact methods offer greater installation flexibility in safer and more convenient locations. Diverse technologies are employed for such ground-based water level sensing, but most operational systems today are based on measuring the time of flight of ultrasonic and radar wave pulses reflected on the water surface. Ultrasonic systems emit acoustic waves (typically 20–200 kHz) from a transducer that also measures reflections, whereas radar sensors emit a stream of microwave spectrum pulses (1–100 GHz). In both cases, the recorded transmission time is converted to a distance within a few millimetres of accuracy (e.g., Boon & Brubaker, 2008). Approximately 5% of the U.K. Environment Agency's National River Flow Archive stations measure river levels at 15-minute intervals using ultrasonic or, more recently, radar sensors (Environment Agency (UK), 2018).

3.1.2 Lidar distance sensing (ranging)

Lidar-based distance sensing is a frequently used technique, for example in digital terrain mapping (Liu, Peterson & Zhang, 2005; Höfle et al., 2009; Ozcan & Unsalan, 2017). The principle of lidar distance measurement depends on the roughness of the reflective surface to generate non-specular reflection (i.e., scattering) of the incoming laser beam. Similar to radar, lidar range measurement utilises higher frequency waves with greater pulse intensities to calculate flight time. Near-infrared (NIR) light is typically used for this purpose, typically over wavelengths of 900–1,100 nm (270–330 THz) due to the low cost of lasers operating in this wavelength range and lower energy density compared to the visible spectrum (Smart, Bind & Duncan, 2009; Fernandez-Diaz et al., 2014).

Two technical characteristics determine the accuracy of lidar distance sensing: pulse width and the accuracy of the method used to measure the time of flight. Reducing the pulse width improves accuracy but necessitates a higher pulse power and, consequently, a more powerful laser. Currently available systems employ 0.5 μs pulse widths with a 50% duty cycle (i.e., when the system is active 50% of the time: Garmin, 2016). Similarly, measurement precision can be

improved by increasing the pulse power, narrowing the pulse width, and expanding the receiver's bandwidth, which allows the receiver channel to respond to the laser pulse with full amplitude and reduced noise.

The precision of the time-of-flight measurement is determined by the internal timer, which measures the interval between laser pulse emission and reception (Kilpelä, Pennala & Kostamovaara, 2001). With advances in the sophistication of micro-oscillators and time-to-digital converters, the precision of timers has increased from 10 nanoseconds in 2001 to picoseconds more recently (i.e., an improvement of up to 10^4: Kilpelä, Pennala & Kostamovaara, 2001; Coddington et al., 2009). In modern time-of-flight ranging systems, atomic clocks of well-defined radiofrequency standards, such as rubidium, with femtosecond precision are frequently employed (e.g., Lee et al., 2010).

However, lidar's use as a static, in-situ method for observing water level is relatively little explored. Tamari & Guerrero-Meza (2016) report a proof-of-concept but provide few technical details. The major difference between marine and terrestrial lidar applications is the lower infrared reflectivity of water surfaces compared to solid objects. A surface of still water may behave as a pure specular surface, which produces reflections rather than dispersing incoming energy. This implies that the reflected beams frequently miss the receiver, particularly in longer-distance airborne surveys, unless observed from normal incidence (Liu, Peterson & Zhang, 2005; Allouis, Bailly & Feurer, 2012; Fernandez-Diaz et al., 2014). In practise, a flat, mirror-like river surface still reflects ~2–3% of an incident beam of infrared radiation, with the remainder passing through the water (Figure 3.1a; Guenther, 1986; Milan et al., 2010). Additionally, under most conditions, the roughness of a water's surface will increase its reflectivity. This may allow lidar to be used as a method for measuring water levels and their variations.

According to Allouis, Bailly & Feurer (2012) and Pfeifer et al. (2008), the laser power received from the water surface as a function of time t, $P_r(t)$, is as follows:

$$P_r(t) = \frac{\rho . P_T(t) . T_{atm}^2 . \eta_r . \eta_t . A_r . \cos^2(\theta_0)}{\pi L^2} \tag{3.1}$$

where ρ is the reflectance at the air/water interface; $P_T(t)$ is the power of the transmitted laser pulse; T_{atm}^2 is the transmission coefficient of the atmosphere; η_t and η_r are the optical transmission and reception efficiencies, respectively; A_r is the area of the receptor; θ_0 is the incidence angle of the sensor; L is the distance of the sensor from the water surface.

The water surface reflectance can be calculated using equation 3.1 (Pfeifer et al., 2008). This method was used by Milan et al. (2010) to generate reflectance curves as a function of laser light wavelength for various concentrations of suspended sediment (Figure 3.1b). Reflectance is less than 10% at 905 nm, the wavelength of many rangefinders that are sold commercially, but it rises as a function of the amount of suspended sediment present.

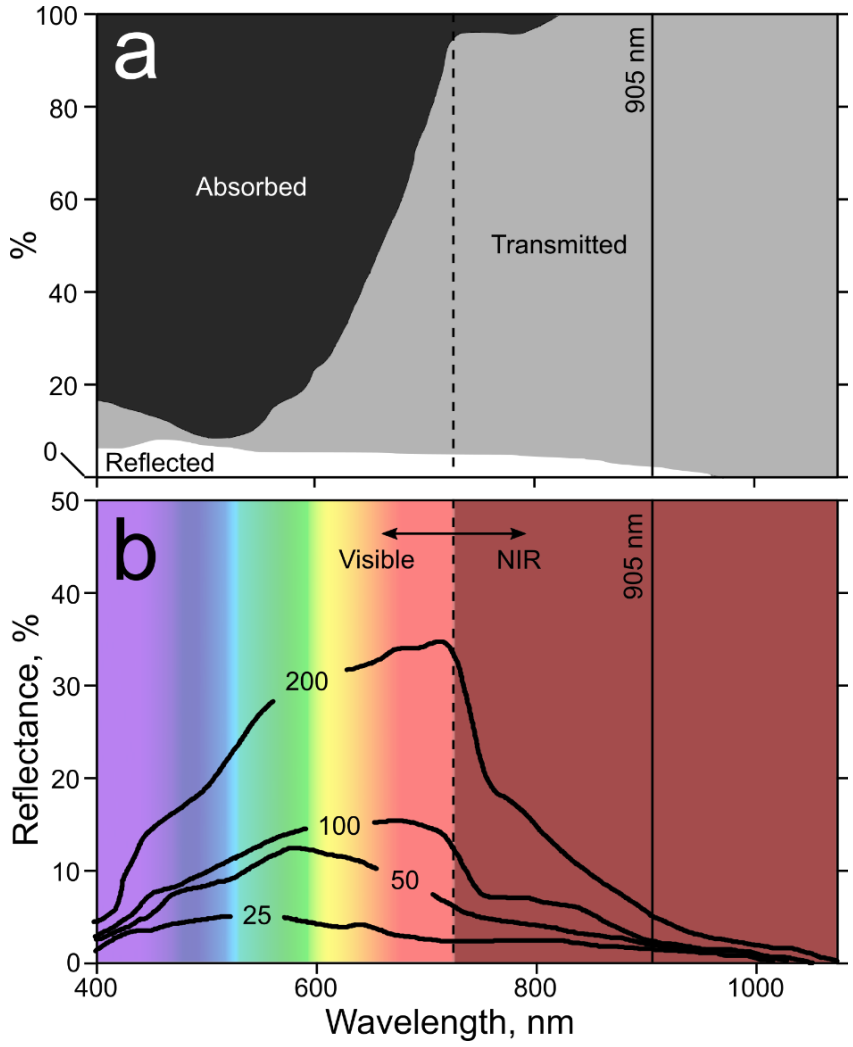

Figure 3.1: (a) Spectral character of clear still water as a function of laser wavelength (Milan et al., 2010; Lednev et al., 2013). (b) Influence of suspended sediment concentration (curves: units of mg L−1) in river upon reflectance (after Milan et al., 2010)

In this chapter, laboratory and field tests are used to evaluate the performance of lidar and its potential as a hydrometric technique under various environmental conditions. For the tests, a commercially available system operating in the NIR spectrum (905 nm), which is representative of the systems in use today, was utilised (section 3.2). In section 3.3, the results of laboratory testing as well as field experiments on the river Thames and other rivers in and around London, UK, are presented.

3.2 Methodology

The laboratory and field tests in this study were conducted with a Garmin Lidar Lite rangefinder sensor (Garmin, 2016), operating at 905 nm, which was connected to a self-built data logger. The rangefinder has an internal measurement frequency of 10–20 kHz; peak laser power is 1.3 W, and the energy per measurement pulse is <280 nJ. Full specifications are given in Table 3.1. The rangefinder sensor is available for ~ £120 (US $130). The sensor uses the time-of-flight principle described above: it sends out pulses with a coded signature and searches for a matching signature in the returned pulses. The time measurement is carried out using an integrated time-to-digital converter with a resolution of 50 ps. The sensor then performs internal averaging over all signature-matching acquisitions until the signal peak in the correlation record reaches a maximum value. If this does not happen or if the signal peak is below a threshold (calculated from the level of ambient noise), then the sensor does not return a measurement (Garmin, 2016). These measurements can be repeated with a typical frequency of 50 Hz and up to 500 Hz. The sensor was connected to an Arduino-based datalogger (for further details see supporting information of Paul, Buytaert & Sah (2020).

The logger was programmed to record 10 successive readings over a time interval of 5 ms. These were averaged to create time series that could be repeated every second to assess the effects of various environmental factors. The measurements were saved to an SD card. In all the test cases, the data obtained from the sensor was compared to observed values to obtain the bias between the measured and observed data. In some tests, e.g., the inclination test, the turbidity test, and the effect of distance from water, the sensor was measuring a known distance; therefore, the known distance was the observed value. The observed water level of the river Thames was obtained from the Environment Agency (Environment Agency, 2021a), and the data of the tidal wave at Battersea was obtained from the British Oceanographic Data Centre (British Oceanographic Data Centre (BODC), n.d.), for the rugosity test. The observed distance

to the water surface for River Lea and Serpentine Lake was measured using a measuring staff. It should be noted that the water level in Serpentine Lake and River Lea did not change during the experiment. A waterproof box with a transparent polycarbonate lid contained the lidar and logger. The setup impeded us from measuring NIR light absorption because polycarbonate is largely transparent to NIR (transmission coefficient of 905 nm light ~ 0.90: Wydeven, 1977). A typical outdoor experimental setup is depicted in Figure 3.2.

Table 3.1: Specifications of Garmin Lidar Lite laser (Garmin, 2016)

Specification	**Measurement**
Wavelength	905 nm
Total laser power (peak)	1.3 W
Energy per pulse	< 280 nJ
Mode of operation	Pulsed (256 pulses per train)
Pulse width	0.5 µs (50 % duty cycle)
Pulse train repetition frequency	10 – 20 kHZ
Beam divergence	8 mRad (~ 0.46°)

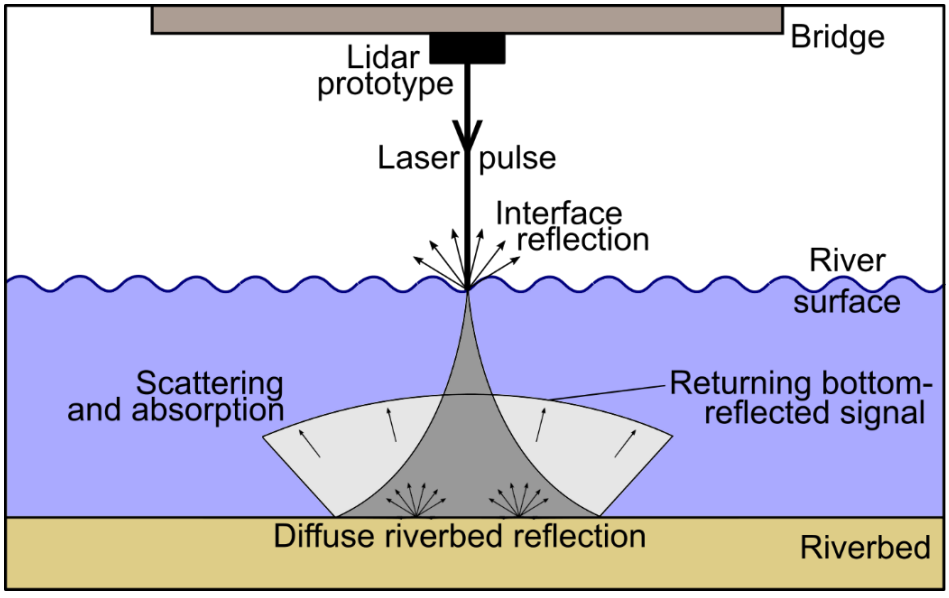

Figure 3.2: Schematic of lidar prototype experiment, where it is clamped to the underside of a bridge to measure river stage

The following tests were carried out:

1. Effect of sample size

To eliminate the potential impact of measurement autocorrelation, the first test was carried out to identify the minimum number of measurements needed to take an average with the least amount of bias. For this test, we measured a known distance of 2 m. The sensor was operated at a frequency of 250 Hz.

2. Effect of distance from water

The purpose of this test (Figure 3.3) was to determine the maximum and minimum distances that the custom-built lidar sensor could measure from the water's surface. To conduct this test, we elevated the sensor vertically along a metal pole above a tank with relatively smooth water (eye-estimated rugosity of < 1 cm) and took measurements at 1-m intervals for the range of 0–10 and 5-m intervals for the range of 10–40 m.

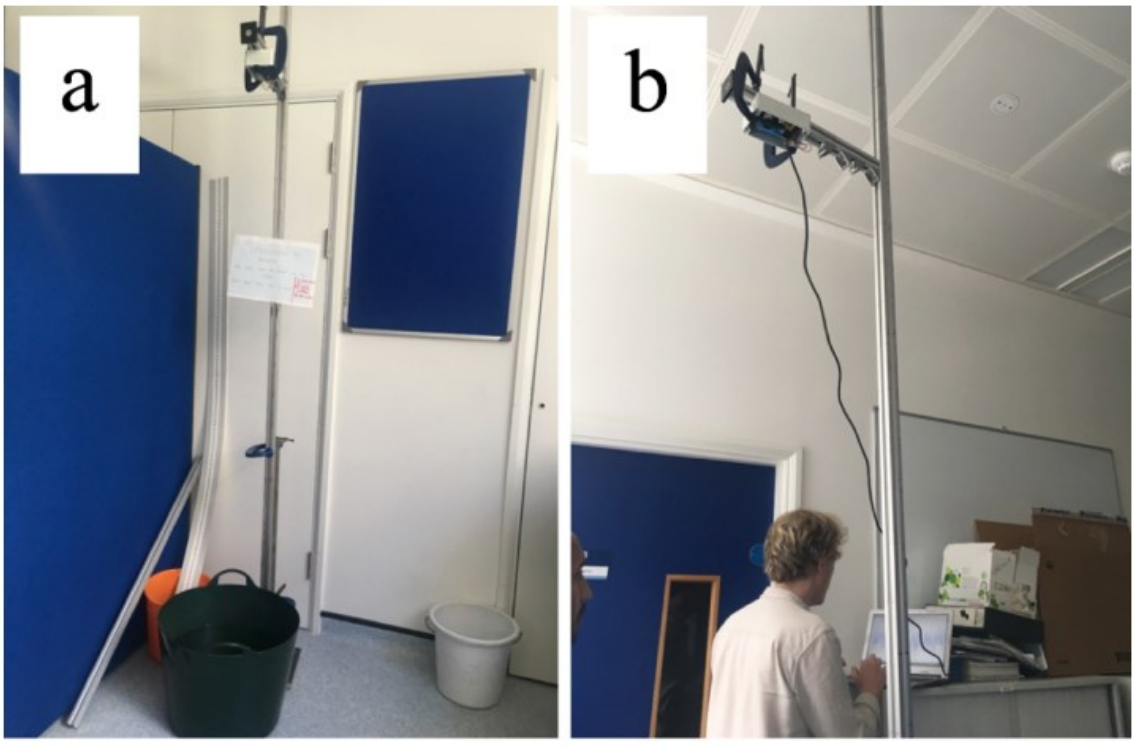

Figure 3.3: a) Laboratory setup for range test. Distance from the sensor to water surface is changed by adjusting the metal pole, **b)** Connection of computer, through which the settings (e.g., measurement frequency) of the sensor system was changed.

3. Effect of water turbidity

According to the specifications of the lidar sensor (Garmin, 2016) employed in this study, turbidity should be considered when measuring distances to water surface. Because of the suspended particles, turbidity can either help or hinder measurement efforts. According to Bhargava & Mariam (1991), small, suspended solids that are afloat on the water's surface can affect laser reflection and reduce the sensor's accuracy. Rivers usually have high turbidity, and since previous experiments were completed using clear water, which does not accurately reflect practical conditions. This test was carried out to analyse the impact of turbidity on water level measurement.

a b)

Figure 3.4: Turbidity test carried out in Imperial College London laboratory: a) Sensor measuring a known distance of 2m, and b) Clay used for the test

We infused the water with various concentrations of kaolin and montmorillonite clay (Bhargava & Mariam, 1990) and measured the turbidity of the solution with the self-built Secchi disk shown in Figure 3.4. Then, for different turbidity level, a known water level ranging from 2-10 meters were measured. Table 3.2 provides a summary of the clay's physical characteristics. We calculated the standard deviation and measurement bias (e.g., Bhargava & Mariam, 1991) between the actual and measured distances.

Table 3.2: Physical characteristics of the clay

Clay	Specific gravity	pH	Organic content (%)
Montmorillonite	2.72	7.91	5.59
Kaolin	2.56	9.05	3.63

4. Effect of inclination

To assess the effect of the inclination of the sensor on measurement, we measured the known distance between the sensor and the water surface in the laboratory and field. From zero degrees (i.e., normal incidence) to a maximum of 60 degrees, the angle at which the sensor was measuring the water surface was changed in steps of 10 degrees (Figure 3.5a). The measurement was carried out for an hour for each inclination angle. In the laboratory, the vertical distance to the water surface was 2 m (Figure 3.5b). In the field test, the distance between the sensor and the water surface was held constant at 6.3 m as the sensor inclination was varied. For each angle of inclination, the bias and data variance were calculated to find the maximum inclination of the sensor and to determine the effect of inclination on the measured distances.

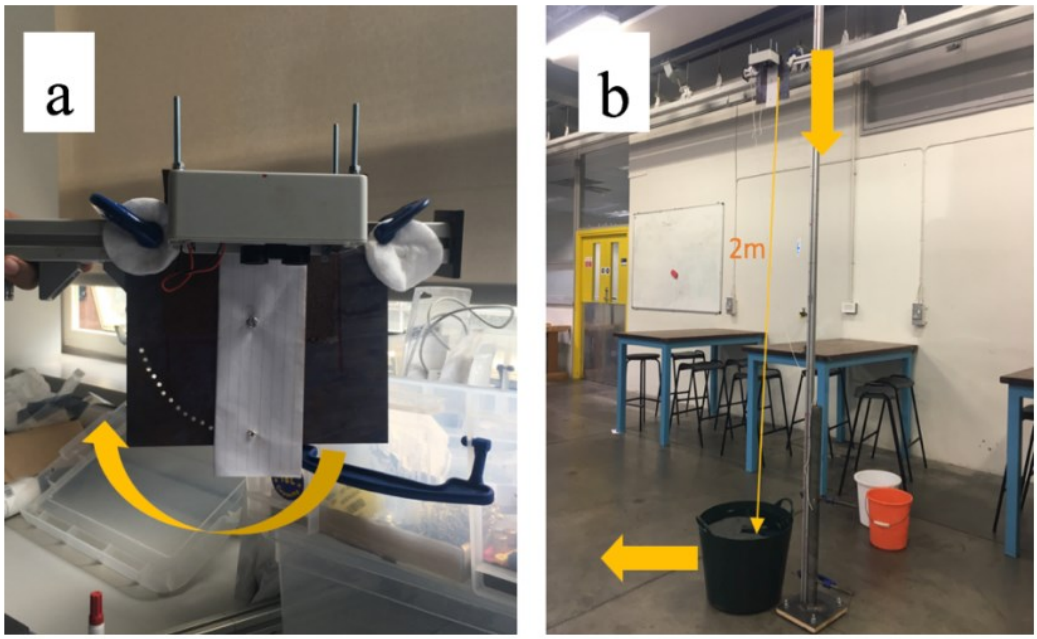

Figure 3.5: a) Laboratory setup for changing incidence angle of sensor – each hole in the metal plate represents 5°. b) Schematic of inclination tests. Distance to the surface was maintained at 2m (for this case); the position of the sensor and bucket was changed, as indicated by the arrows.

5. Effect of ambient temperature

The impact of temperature on measured distances was determined through a series of laboratory experiments. During this test, the sensor was alternately heated by hot air from an industrial welding unit and cooled in a refrigerator or freezer and allowed to return to room temperature. We heated the sensor with hot air to temperatures of ~ 90 °C (greater than the maximum operating temperature of most electronic components, which is 85 °C) and cooled it down to −20 °C in a freezer. We recorded both the measured distance and temperature while the data logger readjusted to room temperature so that we could gain a comprehensive understanding of the temperature range.

6. Effect of water surface rugosity

The water surface roughness or rugosity is also a consideration when measuring water level because it may influence the NIR energy reflected from the water surface. The sensor was tested at four outdoor locations in Greater London (i.e., the River Lea at Tottenham, the Serpentine Lake in Hyde Park, and the River Thames at Battersea and Teddington Lock) (Figure 3.6). In all the cases, the sensor was attached to a bridge wall to measure the water level. In each location, rugosity (i.e., surface wave amplitude) was estimated by eye (wave heights were measured by measuring the height of wave splashing on the boundary wall using a measuring scale). Wave height measurement and influence of tidal wave on river Thames at Battersea is shown in Figure 3.7.

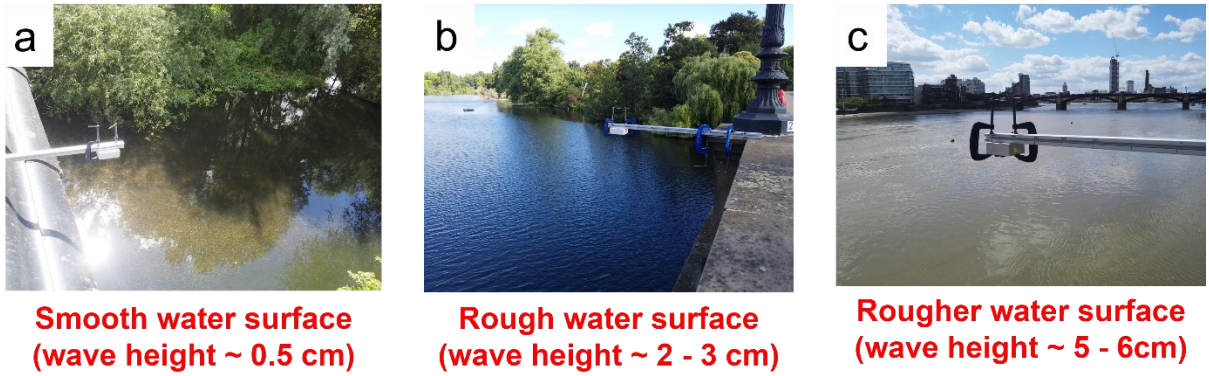

Figure 3.6: Roughness test in field: a) River lea, b) Serpentine Lake and c) River Thames at Battersea.

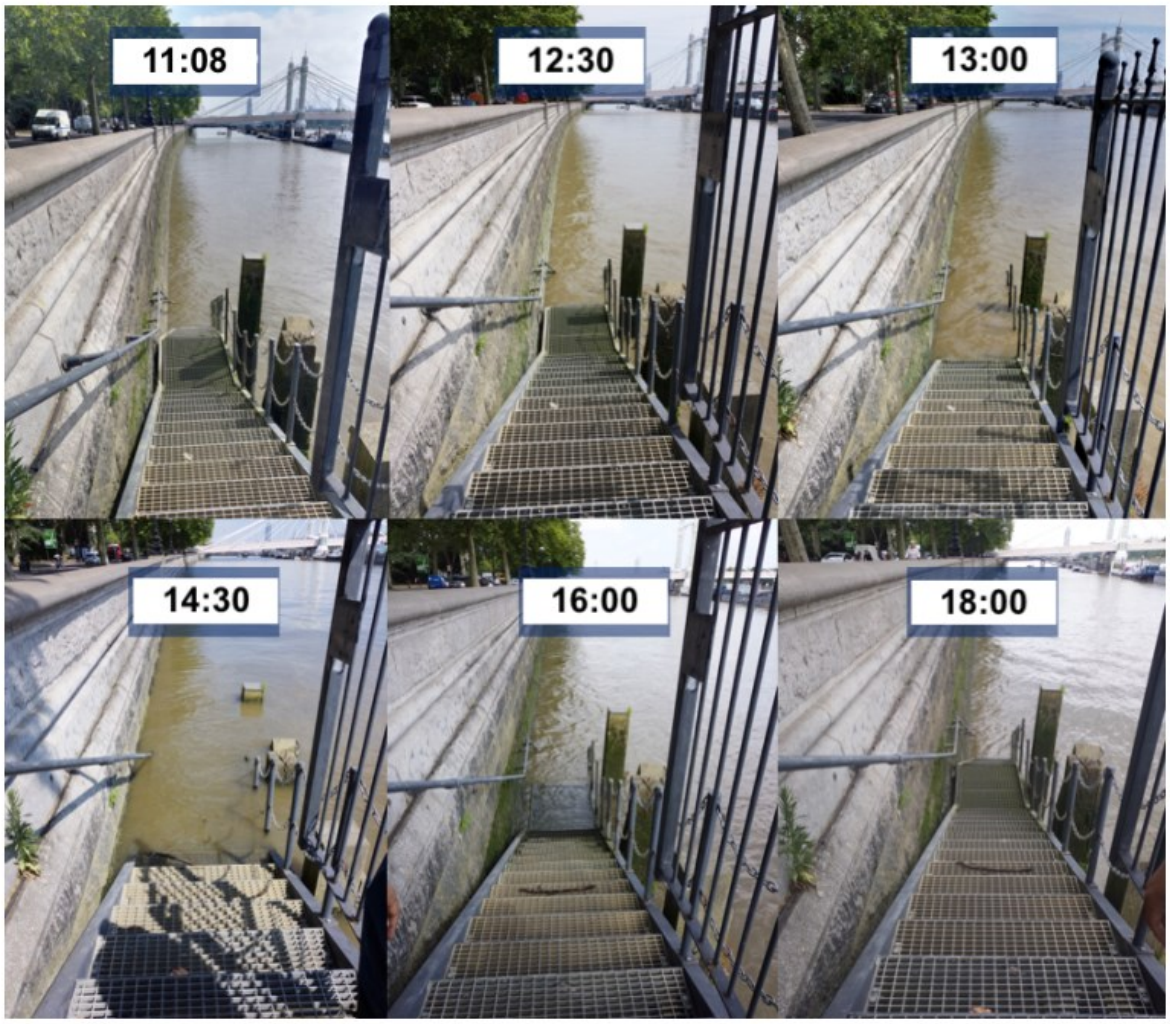

Figure 3.7: Series of photos taken at different times, indicating the water level change of River Thames on 12/07/18. The maximum water level (i.e., high tide) was reached at around 14:30. Wave height was measured by measuring the height of splashing wave on the side wall of the stairs.

3.3 Results and discussion

3.3.1 Sample size and auto-correlation

To reduce the impact of autocorrelation on measurement bias, we first calculated the necessary sample size. The deployed sensor is equipped with an inbuilt receiver bias correction mode. Enabling the bias correction mode results in slower measurements. However, when the receiver bias correction mode is enabled, the bias quickly converges to a value within the sensor's specification (1%; Figure 3.8). With bias correction mode disabled, convergence is slower but within specifications for all but the smallest number of measurements. These findings imply that there was no instrumental drift during the test. Additionally, they imply that a sample size

of much less than 100 measurements, with a relative measurement error of 0.3%, is acceptable for operational practise.

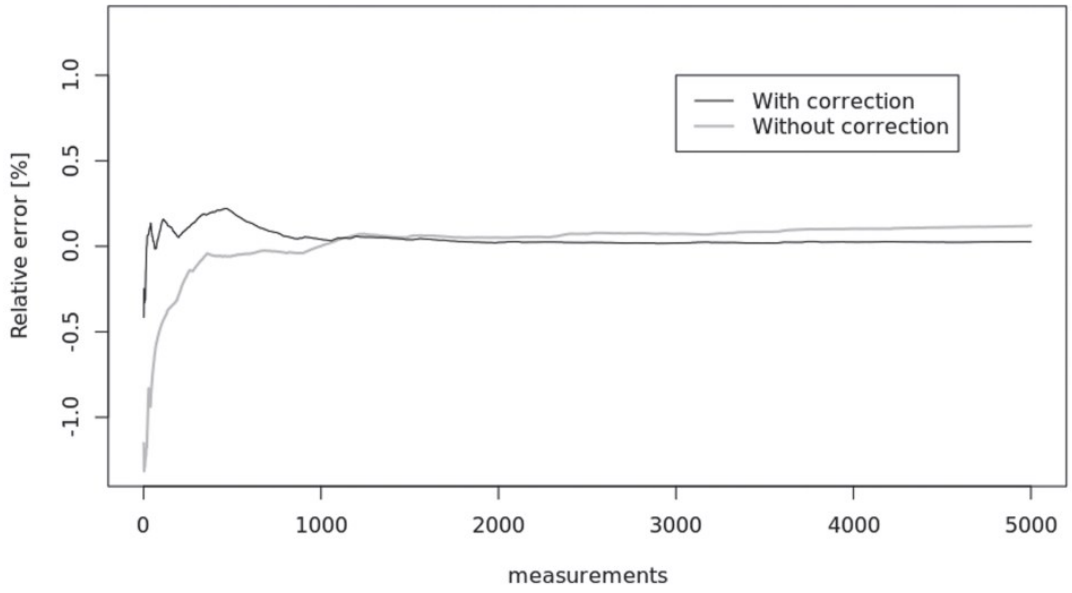

Figure 3.8: Variation of relative measurement error with number of measurements in sample. The distance from the sensor to target was 2.0 m: measurement frequency ~ 250 Hz.

3.3.2 Measured distance

Figure 3.9 suggests that the absolute measurement bias of the evaluated sensor increases with distance (especially beyond 15–20 m). However, the percentage error remains roughly constant, indicating a 0.1% proportional error (i.e., between the mean measurement and the real distance). This implies that the device has a negligible amount of inherent systematic bias.

The specifications for the sensor state that the accuracy is ± 2.5 cm for measurements of less than 5 m and ± 10 cm for measurements of greater than 5 m. The results from our experiments show that they are within these specifications (Garmin, 2016). At 40 m and beyond, no measurements were returned (i.e., no reflections were received). The accuracy is approximately 1 cm for measurement distances of up to 10 m and within 3 cm for measurement distances of up to 30 m (i.e., relative error of <0.1 percent).

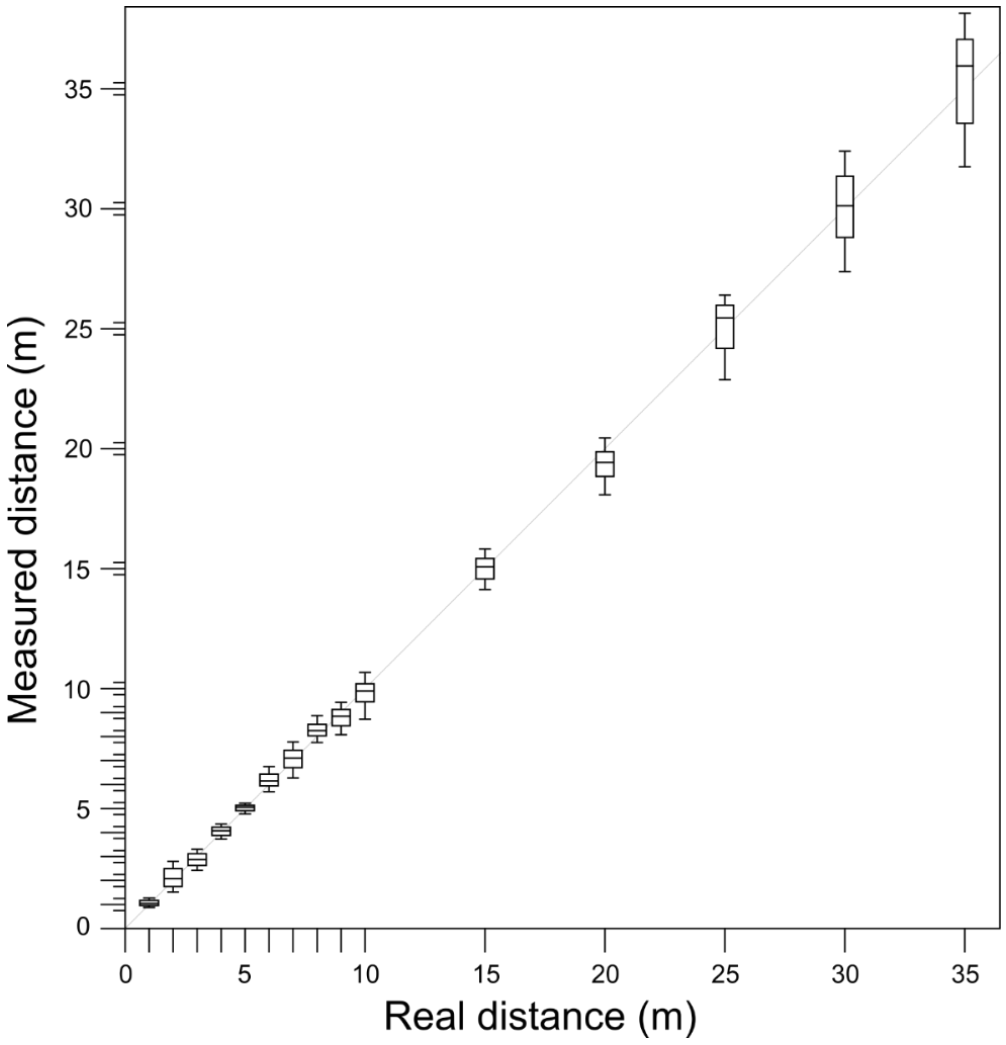

Figure 3.9: Measured versus actual distance. Minor ticks either side of each y-axis, major tick = ±1 cm measured distance, corresponding to vertical scale of box plots. Whiskers span entire range of dataset. Each box plot represents 500 readings.

3.3.3 Turbidity

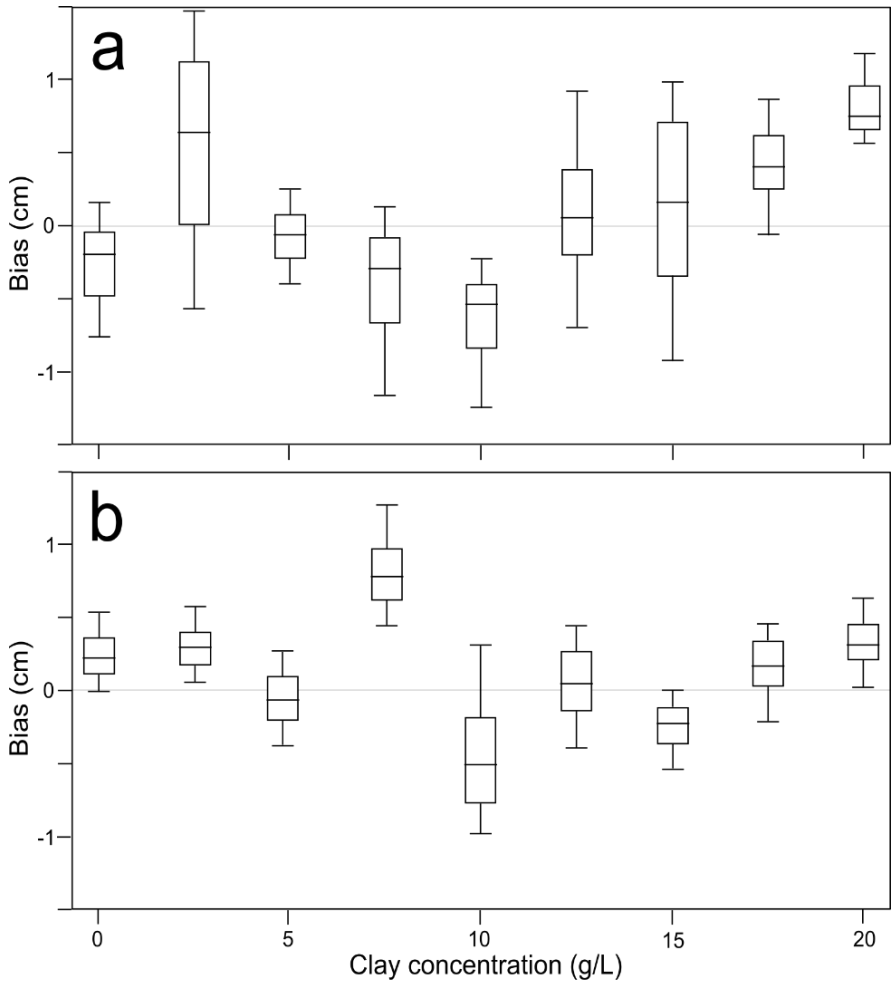

Figure 3.10: Results of turbidity tests using (a) montmorillonite and (b) kaolin. Box plots show measurement bias (from a vertical distance of 2 m) as a function of clay concentration. Whiskers span entire range of dataset.

Bhargava and Mariam (1990) and (1991) investigated the relationship between reflectance and water turbidity using kaolin and montmorillonite clay, finding that reflectance increases linearly with turbidity for both materials within a range of incident light wavelengths of 500 to 1,000 nm. However, we found no effect of water turbidity on the measurement bias and variance (refer to Figure 3.10). This indicates that the receptor is sensitive enough to take accurate measurements under conditions of low reflectance and that a higher reflectance does not improve the reading.

3.3.4 Rugosity

The roughness (rugosity) of the water surface has a theoretical effect on the intensity and number of light waves (or lidar) returned from the air-water interface (e.g., Allouis et al., 2007; Bhargava & Mariam, 1990). To test the effect of surface rugosity under field conditions, we selected four sites with varying rugosities, which were estimated visually. Our installations were temporary (<12-hour measurements). Therefore, problems that could come up with permanent or long-term installations, such as interference from dust, plants, insects, or weather conditions like fog or strong winds, are not considered here.

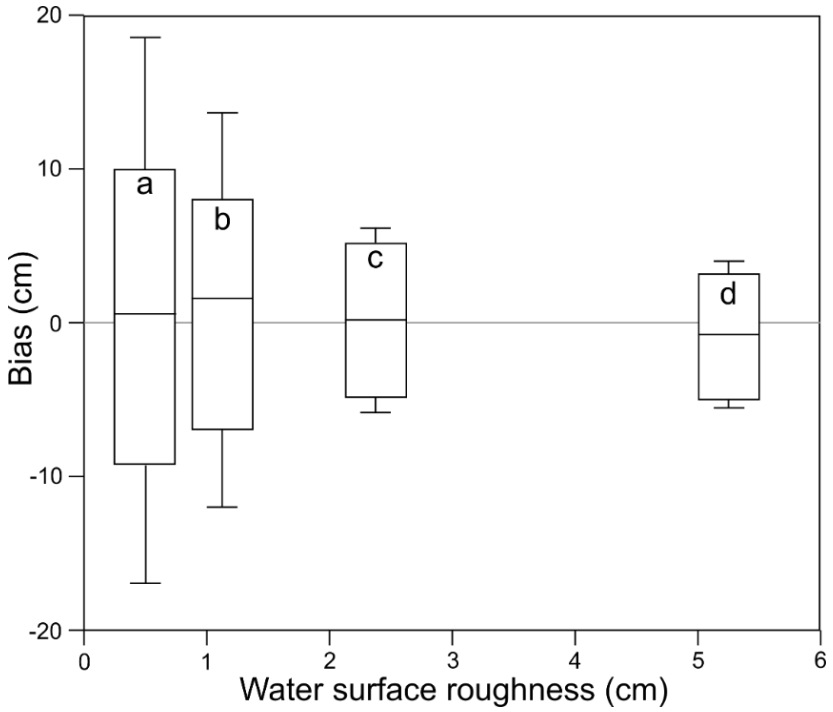

Figure 3.11: Effect of water surface rugosity on measurement bias at four locations in Greater London, UK: (a) River Lea, Tottenham (distance from sensor to water surface = 3.6 m; rugosity = ~0.5 cm); (b) Teddington Lock, River Thames (distance = 4.2–8.3 m; rugosity = ~1–1.5 cm); (c) Serpentine Lake, Hyde Park (distance = 6.2 m; rugosity = ~2.5 cm); (d) River Thames, Battersea (distance = 5.4–10.2 m; rugosity = ~5–5.5 cm). Note clear relationship between data variance and rugosity and low measurement bias in all tests. Whiskers of box plots span entire range of dataset.

The test results indicate that a rougher water surface reduces the measurement variance (Figure 3.11). The variance at the less turbulent River Lea (rugosity of <1 cm) is 8.2 cm (Figure 3.11a), whereas it is only 1.7 cm at the more turbulent River Thames (rugosity of ~5 cm; Figure 3.11d). When the sensor is inclined, a diffuse surface will cause incipient laser energy to disperse uniformly, whereas a smooth, specular surface will mainly reflect energy. In this instance, however, the laser beam is perpendicular to the water surface. Because of this, it is more likely

that more of the radiation that hits more specular water surfaces will be absorbed by (and transmitted through) the water instead of being reflected back to the sensor (see Figure 3.2). Therefore, the sensor receives more dispersed radiation when the water surface is rougher. In each of the four field deployments, the median value of measurement bias, averaged over the duration of the recording, is <1.5 cm (Figure 3.11).

3.3.5 Inclination

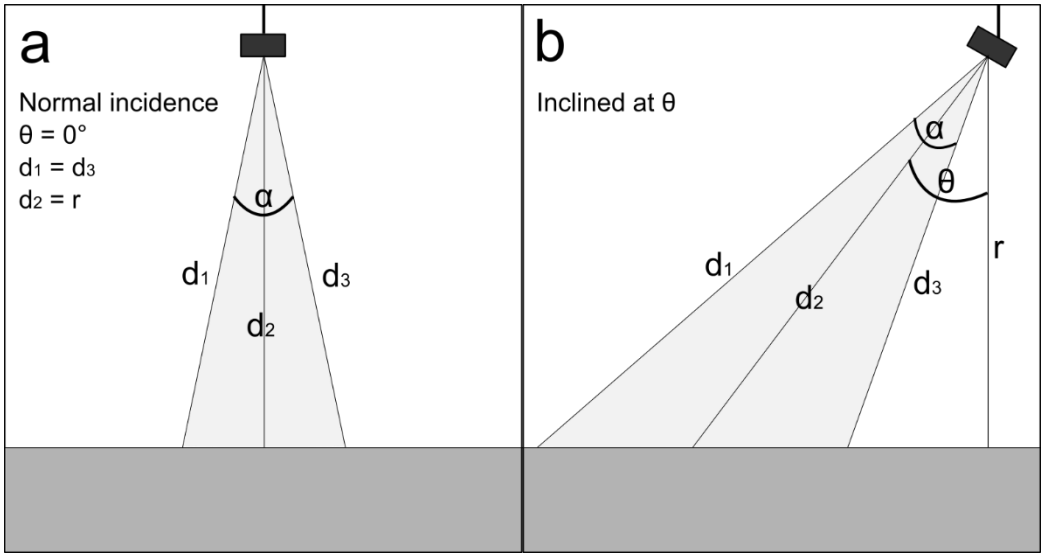

Figure 3.12: Illustrations of lidar tests (a) at normal incidence ($\theta = 0°$) and (b) when inclined ($\theta > 0°$). For this lidar sensor, beam dispersion α = 8 mRad (~ 0.46°: Table 1; Garmin, 2016). r = normal distance from sensor to water surface.

A proxy for beam divergence is the path difference between the laser cone's outer edges, ($d_1 - d_3$), which depends on the inclination angle (θ) as shown in Figure 3.12:

$$d_1 - d_3 = \frac{r}{\cos\left(\theta + \frac{\alpha}{2}\right)} - \frac{r}{\cos\left(\theta - \frac{\alpha}{2}\right)} \tag{3.2}$$

where r is the normal distance from sensor to water surface and d_1 , d_3, and d_2 are the distances travelled by the outer edges and midpoint of the laser cone, respectively. Because of the beam divergence (i.e., $d_1 - d_3$), the theoretical measurement bias and variance increase with increasing incidence angle. These theoretical and calculated relationships are depicted in Figure 3.13, which demonstrates a high degree of congruence. As expected, the increase is greater under conditions of greater surface roughness, as divergence and wave motion reinforce

one another (variations in path length due to water surface waves are not considered here). However, the increase is limited to a few centimetres in all conditions, which may be acceptable in a variety of operational conditions.

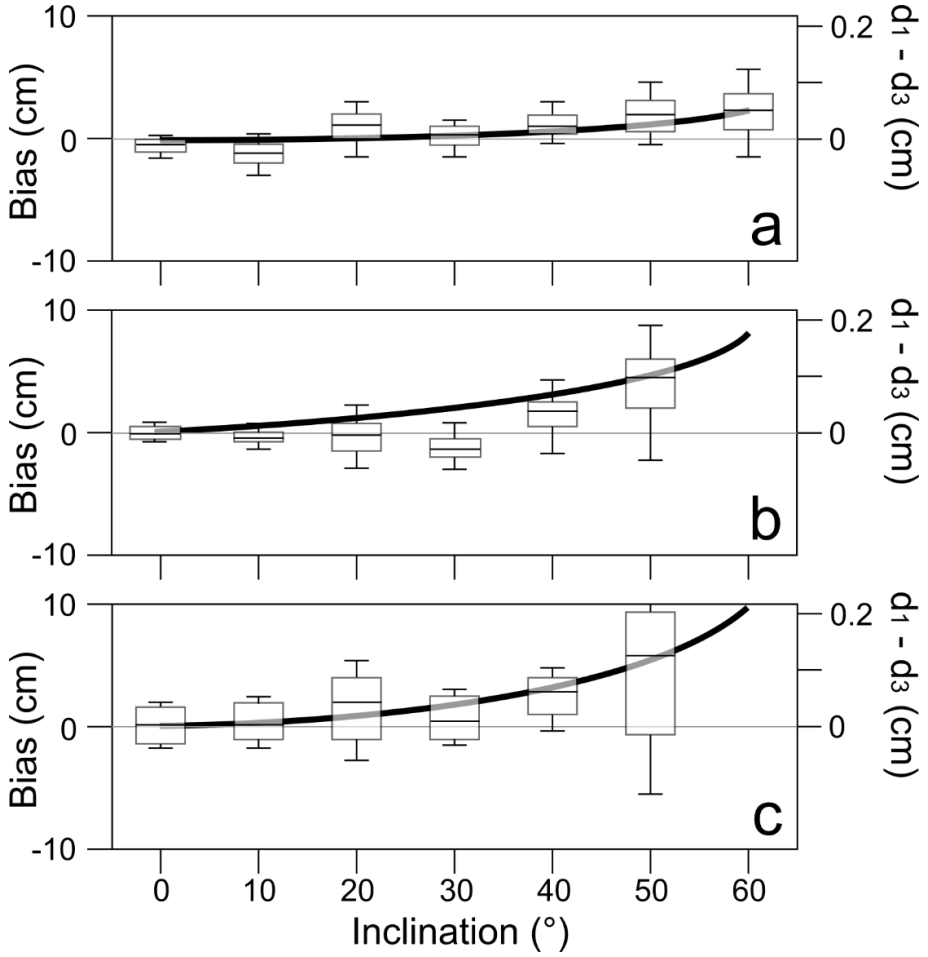

Figure 3.13: Effect of incidence angle on measurement bias and variance (0° = vertical). Box plots = lidar data (left-hand axis); thick black line = predicted beam divergence (i.e., d_1–d_3 on Figure 3.12: right-hand axis). (a) Laboratory test: initial vertical distance from sensor to water surface = 2.0 m. (b) Outdoor test: distance = 6.3 m. (c) Test on River Thames at Battersea: initial distance = 8.0 m. Whiskers of box plots span entire range of dataset.

This opens up new opportunities for the use of lidar in situations where vertical measurement is not possible, such as for rivers whose width varies seasonally or whose banks are too unstable to allow sensor installation above the water.

Guenther (1986) emphasises the significance of water surface roughness to dispersion when imaging at non-normal incidence ("off-nadir geometry"). This roughness manifests as small wavelets or capillary waves with tiny facets perpendicular to the inclined laser beam, allowing energy to be reflected and an interface return to reach the transceiver. However, increasing the

incidence angle has the opposite effect of increasing surface rugosity as laser beam dispersion must be considered.

3.3.6 Temperature

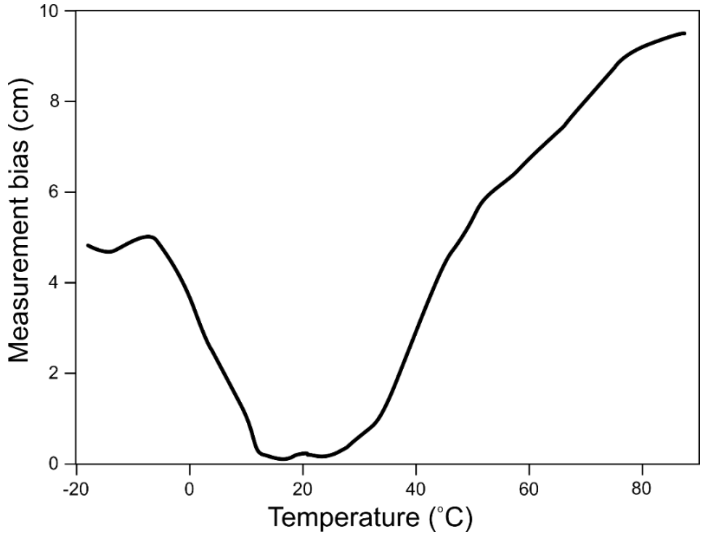

Figure 3.14: Effect of temperature on measurement bias. Actual distance = 2.5 m; graph shows the average bias for 100 tests.

The effect of air temperature on the laser's flight time is insignificant. Nonetheless, a number of electronic components, including the clock and the laser emitter, may be affected by changes in ambient temperature. The resultant slight increase in injection current to the laser diode causes the light intensity and wavelength of any lidar sensor to increase with temperature. However, slow temperature changes do not significantly impact the measured distance value (Jensen et al., 2009). Typical rates of increase have been reported as ~0.04 and ~0.09 nm/°C for lasers with nominal operating wavelengths of 1,062.3 (NIR) and 531 nm (green), respectively (Kikuta, Iwata & Nagata, 1986; Jensen et al., 2009). For different lasers, these values vary slightly.

Figure 3.14 indicates that both heating and cooling produced a positive measurement bias of up to ~9 cm in maximum magnitude. This high sensitivity to ambient temperature may be the result of insufficient temperature compensation within the electronics. Alhashimi, Varagnolo & Gustafsson (2015) note that temperature fluctuations increase the degree of oscillation between laser light's different wavelength modes. This has a significant effect on the accuracy of time-of-flight ranging systems: at extreme temperatures, the laser pulse's actual wavelength is much different from its nominal value (Alhashimi, Varagnolo & Gustafsson, 2015). These

results suggest that, in the field, the sensor should be installed in a location that is shielded from high temperature fluctuations, such as direct sunlight.

Table 3.3 provides a comparison of lidar sensor with other sensors available in the market.

Table 3.3: Comparison of lidar sensor with other sensors available in the market

	Lidar (Garmin Lidarlite 3HP)	**Ultrasound (Maxbotix MB7389)**	**Pressure transducer (Onset HOBO)**	**Radar (Campbell CS475a)**
Range (m)	2-40	0.3 - 5m	Up to 30 m (water depth)	0.05 - 30m
Resolution (mm)	± 10	± 1	± 1	±1
Accuracy (mm)	± 20	± 5	± 10 (0.1%)	± 2
Cost (£)	250 - 300	200 - 250	800	~2000-3000
Installation	Non-contact	Non-contact	Contact	Non-contact
Can be inclined or not	Yes	No	No	No

3.4 Conclusions

The findings indicate that time-of-flight lidar can be utilised to measure water levels with a high temporal resolution. Devices employing this method could be advantageous in regions where establishing a monitoring network is prohibitively costly or inaccessible. The experiments indicate that to improve current hydrometric practise, lidar could be particularly effective when applied to stage measurement, for instance as part of an early-warning system for flooding. Sensors could be mounted under bridges or attached to the bank at an angle. During our tests, we didn't find any evidence that the instruments were drifting. With the right correction algorithm, as few as ~10 measurements may be enough to get a good average distance.

The results demonstrate that, despite the low reflectivity of the air-water interface to NIR radiation, a lidar prototype can take measurements under a variety of environmental conditions and at an angle of no more than ~40°. The accuracy of the sensor is ~1 cm at measurement distances less than ~10 m, while the maximum detectable range is 30–35 m, which is significantly greater than that of existing ultrasonic water-level sensors. The sensor's precision decreases with increasing measured distance and improves with increasing surface roughness. There is no discernible effect of water turbidity on our measurements. Temperature changes

outside of normal operational conditions (i.e., 10–30 °C) result in a systematic increase in measurement bias.

The findings imply that lidar may be a viable method for water level sensing, which has significant and far-reaching implications for hydrometry. Lidar has the potential to be utilised in data-scarce regions where precise measurements of water level (e.g., river stage and groundwater) are essential for flood risk management. It would be useful to determine whether our findings could be generalised to sensors other than the one we used (e.g., lasers of different wavelengths, power, and pulse width). The technique is cost-effective, energy-efficient, and has a small measurement footprint (relative to ultrasound systems; Figure 3.12); it could be utilised to increase the global density of river gauging stations, which is currently suboptimal.

4 A Python application to implement Monte Carlo simulations in HEC-RAS

The Hydrologic Engineering Center's River Analysis System (HEC-RAS) is a widely utilised software application for 1D and 2D steady and unsteady flow river analysis, sediment transport modelling, and water quality analysis. However, the graphical user interface of HEC-RAS only offers a one-click-one-run option, so it does not always provide users with the required capabilities for advanced analyses. For example, users often require automating river flow simulations to conduct probabilistic flood inundation analysis, uncertainty and sensitivity analysis, hydraulic structure optimisation, and so on. In this chapter, I present Python scripts for controlling and automating river flow simulations in HEC-RAS and demonstrate their usage with three examples. Here, the developed scripts are tested on both an idealised river case and a real river, the River Brent in London. The examples illustrate the use of Python applications for 1) calibrating hydraulic models under homogenous and heterogenous Manning's roughness coefficient assumptions, 2) performing uncertainty and sensitivity analyses of unsteady flow parameters, and 3) conducting probabilistic flood inundation analyses in HEC-RAS. The purpose of this chapter is to provide the technical basis to implement the discharge estimation methodology in Chapter 5.

4.1 Introduction

HEC-RAS (Hydrologic Engineering Centre-River Analysis System), developed and maintained by the Hydrologic Engineering Centre (HEC) of the U.S. Army Corps of Engineers (USACE), is one of the most widely used hydraulic engineering analysis software (Goodell, 2014). It is used for a variety of purposes, including one- and two-dimensional steady and

unsteady river flow hydraulic analyses, sediment transport analyses, water quality modelling, and flood control channel hydraulic design (Brunner et al., 2016; Brunner, 2016a, 2016b). While HEC-RAS is one of the best tools available for hydraulic engineering analysis, the software does not always provide users with the capabilities that are needed for more advanced analyses. For example, users of HEC-RAS often require performing Monte Carlo (MC) simulations (Goodell, 2014), a commonly used method for approximating solution outcomes when the inputs have a high degree of uncertainty (O'Connor & Kleyner, 2011; von Neumann, 1951), for modelling the uncertainty associated with river processes. Modelling the uncertainties of river processes is crucial for model calibration (Pappenberger et al., 2005b; Vansteenkiste et al., 2014), flood inundation mapping (Vansteenkiste et al., 2014), and sediment transportation (Shrestha et al., 2016).

In many instances, MC simulations, in which a model is run for many iterations have been used to address the uncertainties in river flow modelling, e.g., (Aronica, Hankin & Beven, 1998; Beven & Binley, 1992; Bozzi et al., 2015; Huang & Qin, 2014; Jung & Merwade, 2012; Liu, 2009; Pappenberger et al., 2004, 2005b; Vrugt & ter Braak, 2011). However, the HEC-RAS graphical user interface (GUI) only provides a one-click-one-run option. Therefore, to use MC simulations, for instance running 5000 realisations of a model for uncertainty analysis, one needs to control and automate HEC-RAS simulations with other tools or programming languages.

HEC has developed an open API (application programming interface) that enables users to develop custom applications that leverage HEC-RAS to solve unique hydraulic engineering problems. This API is referred to as the HEC-RAS Controller (or HECRASController). The API is already available to anyone who has downloaded and installed HEC-RAS version 3.1 or later (Goodell, 2014). The HEC-RAS Controller includes a plethora of procedures that enable external manipulation of HEC-RAS by setting input data, retrieving input or output data, and performing common functions such as opening and closing HEC-RAS, changing plans, running HEC-RAS, and plotting output. Goodell (2014) provides a detailed description of all the functions, classes, and sub-routines available in the HEC-RAS Controller with example applications. The HEC-RAS Controller can also be used to integrate HEC-RAS into third-party software to perform system analysis such as flood risk analysis, optimization of flooding structures under uncertainty, and multi-objective reservoir operation under uncertainty. The HEC-RAS API is available as a component object model (COM) dynamic link library (DLL).

Therefore, the HEC-RAS Controller can be used in conjunction with any programming language that can call a COM DLL. This chapter demonstrates how to use Python to control HEC-RAS simulations and describes scripts with examples for performing MC simulations for a variety of purposes, including calibrating unsteady river flow models, and conducting sensitivity and uncertainty analysis.

The ability to control river flow simulations via external programming languages opens several new possibilities in the fields of flood hazard assessment, water management, and river hydraulics (Dysarz, 2018). However, until now, there have been very limited studies in this area. For example, Leon & Goodell (2016) have demonstrated manipulating input files such as geometry files (.g##, .hdf), unsteady flow files (.u##), extracting output variables, performing parallel computation and visualisation in MATLAB, and Dysarz (2018) has demonstrated controlling and automating HEC-RAS for steady flow simulation, steady flow calibration, and sediment simulation using Python. It should be noted that these studies have focused mainly on steady flows, and the availability of existing codes and software packages for carrying out MC simulations is limited (Vojtek et al., 2019). To my knowledge, there is no freely available software or script that can be used to implement MC simulations in HEC-RAS.

In this chapter, I present and discuss Python scripts to perform unsteady flow simulations, work with different types of input and output file types (e.g., dss, ASCII) to manipulate boundary conditions, and perform MC simulations to calibrate an unsteady flow model for different scenarios. Additionally, I demonstrate other applications of the scripts, such as probabilistic flood inundation analysis and sensitivity analysis (Babister et al., 2016b; Vojtek et al., 2019). This chapter also lists the technical and common errors encountered during the study period and the solutions adopted to rectify them.

4.2 Monte Carlo simulations implementation

First, an unsteady flow hydraulic model was set up in HEC-RAS. Then a Python script is developed to control and automate the HEC-RAS run and perform Monte Carlo (MC) simulations of different unsteady flow parameters. A typical analysis workflow is presented in Figure 4.1.

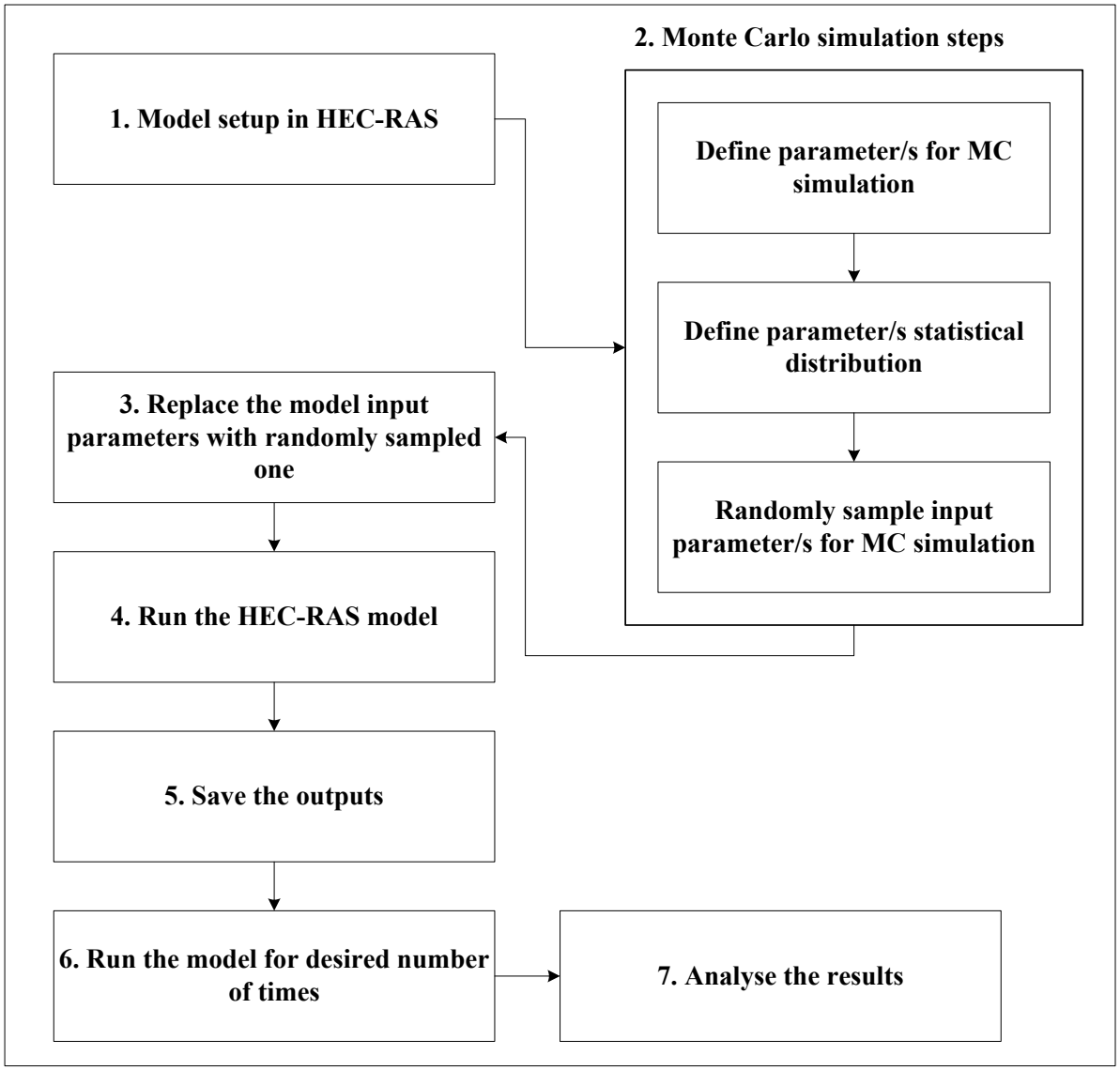

Figure 4.1: Flow chart for performing Monte Carlo simulations

To evaluate the MC simulations, a set of performance evaluation metrics calculation routines is implemented:

$$Modified\ Kling - Gupta\ Efficiency\ (KGE) = 1 - \sqrt{(r-1)^2 + (\beta-1)^2 + (\gamma-1)^2} \tag{4.1}$$

$$r\ (correlation\ coefficient) = \frac{cov\ (Z_i^s,\ Z_i^o)}{\sigma\ (Z_i^s) *\ \sigma\ (Z_i^o)}$$

$$\beta\ (Bias\ ratio) = \frac{\mu\ (Z_i^s)}{\mu\ (Z_i^o)}$$

$$\gamma\ (Variability\ ratio) = \frac{CV\ (Z_i^s)}{CV\ (Z_i^o)} = \left(\frac{\sigma\ (Z_i^s)}{\mu\ (Z_i^s)}\right) \Big/ \left(\frac{\sigma\ (Z_i^o)}{\mu\ (Z_i^o)}\right)$$

$$Error\ in\ Z_p\ [\%] = \frac{Z_{max}^s - Z_{max}^o}{Z_{max}^o} * 100 \tag{4.2}$$

$$Error\ in\ T_p\ [min] = t_{max}^s - t_{max}^o \tag{4.3}$$

$$Root\ mean\ square\ error: RMSE = \sqrt{\frac{\sum_{i=1}^{N}(Z_i^s - Z_i^o)^2}{N}} \tag{4.4}$$

where, Z_p is error in peak stage or depth, Z^s is simulated stage, Z^o is observed stage, Z_{max} is peak stage, t_{max}^s and t_{max}^o is time (in minutes) at which the simulated and observed peak reaches the gauging station, μ, σ is mean and standard deviation, cov is covariance, and CV is coefficient of variation.

The modified KGE is used as a performance measure for parameters calibration as it provides an optimal solution which is simultaneously good for bias, variability, and correlation (Knoben, Freer & Woods, 2019).

4.3 Example applications

4.3.1 Case overview

Two unsteady flow models, called Model-1 and Model-2, were used to test the applications of the MC method/simulations in different contexts.

In recent years, significant advancements have been made in low-cost sensing technology and the Internet of Things (IoT) to collect river stage data (Paul, Buytaert & Sah, 2020). Additionally, there are studies that demonstrate the utility of stage data for a variety of purposes, including estimating river discharge (Harlan et al., 2021; Durand et al., 2014). Therefore, the examples discussed here illustrate the use of stage data, to calibrate river channel parameters and estimate river discharge at an ungauged location (example 1).

Model-1:

Model-1 is a simple prismatic model of an idealised river channel of length 10 km and width 50 m. The depth of the river is assumed to be 10 m. This river reach is assumed to have a constant bed slope (S_o) of 1 in 10000. A stage, or discharge hydrograph, was used as an upstream boundary in different examples. The discharge hydrograph was obtained by using equation 4.5 (Dottori, Martina & Todini, 2009).

$$Q\ (t) = \ Q_b + (Q_p - \ Q_b)\left[\frac{t}{T_p} exp\left(1 - \frac{t}{T_p}\right)\right]^{\gamma} \tag{4.5}$$

where, Q_b = base flow, Q_p = peak flow, T_p = Time to peak, t = time instances and γ = coefficient =16.

For all examples involving the Model-1, Q_b was set to 100 m^3/s, Q_p to 900 m^3/s, and T_p to 24 hours.

Model-1 was first run with a "true or observed" discharge hydrograph and other known input parameters to generate the stage hydrograph for use as an upstream boundary condition. Rather than using an equation, for example, Perumal et al. (2007), HEC-RAS was used to generate a stage hydrograph because the equation can be used only in the case of a prismatic channel, whereas a model can be used for both natural and prismatic channels. Furthermore, it can help us detect systematic model bias.

Normal depth, a Manning's equation approximation which needs an initial guess of the friction slope (average riverbed slope applied), was used as the downstream boundary condition in all the Model-1 examples. The simulation time was set at 60 seconds in accordance with Courant's condition to satisfy the stability and accuracy of the model (Brunner, 2016b).

Model-2:

Model-2 represents a short reach of the river Brent in London, UK. The river reach between Costons Lane (upstream) and Hanwell (downstream) is selected because both the boundaries of the reach have Environment Agency gauging stations (refer to Figure 4.2). The gauging station descriptions are provided in Table 4.1 and the gauged parameters, discharge, and stage, are shown in Figure 4.3 and Figure 4.4 (Environment Agency, 2021a) respectively.

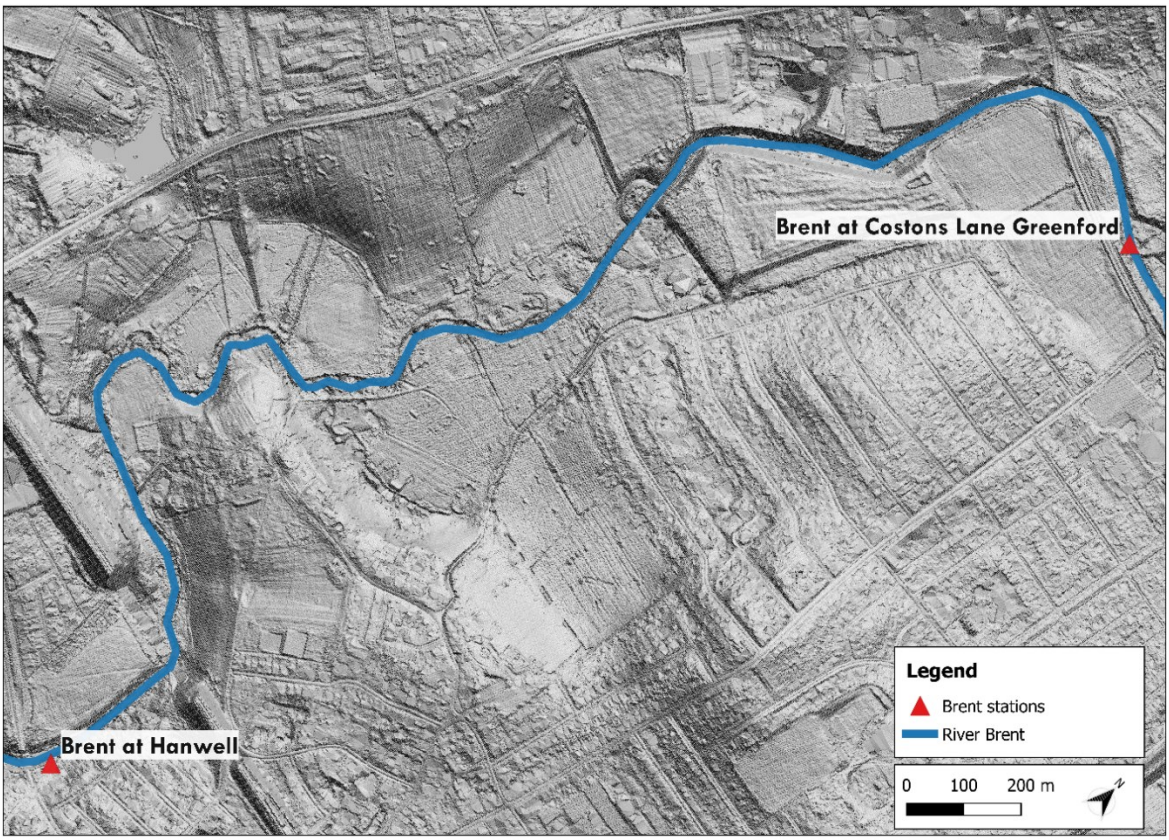

Figure 4.2: River Brent represented in 1m lidar DEM

Stage and discharge data from 30/09/2019 to 08/10/2019 were used for the examples because this selection of data captures the full profile of the stage and flow in the river. Both stage and discharge data are at a 15-minute time interval. The geometry data for the river Brent model was extracted from a 1m resolution LIDAR digital elevation model (DEM) (Environment Agency, 2021b) using RiverGIS (Pasiok & Dębek, 2015) and QGIS (Anon, 2021).

Table 4.1: Gauging stations description

Station name (ID)	**mASD (mAOD)**	**Coordinates**	
		Latitude (°)	**Longitude (°)**
Brent at Costons Lane Greenford* (ID: 3870TH)	12.895	51.527366	-0.344873
Brent at Hanwell** (ID: 3880TH)	7.75	51.508638	-0.342569

* https://environment.data.gov.uk/flood-monitoring/id/stations/3870TH.html
**https://environment.data.gov.uk/flood-monitoring/id/stations/3880TH.html

A total of forty cross-sections were extracted between the two stations, and twenty-eight cross-sections were linearly interpolated using the functions available in the HEC-RAS. The upstream and downstream cross-sections are shown in Figure 4.5. Normal depth, calculated by taking the average slope of the riverbed at its downstream, was used as the downstream boundary condition in all the Model-2 examples. Also here, the simulation time was set at 60 seconds following Courant's condition to satisfy the stability and accuracy of the model (Brunner, 2016b). Other model details are presented in Table 4.2.

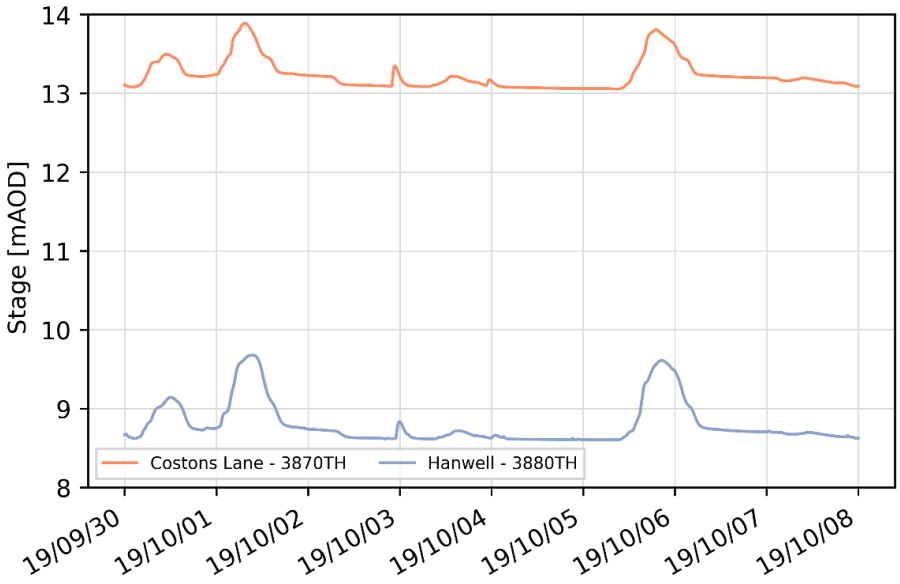

Figure 4.3: Observed stage at Costons Lane and Hanwell station

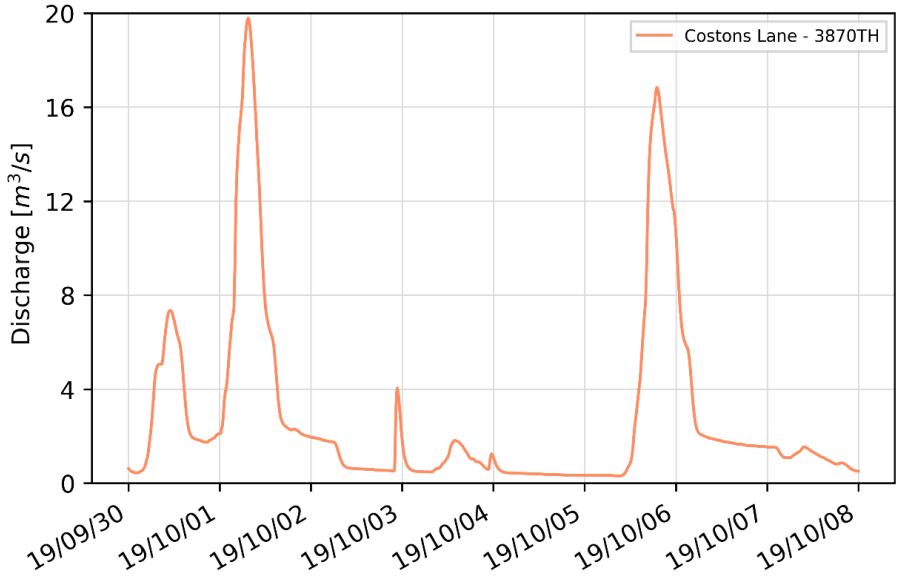

Figure 4.4: Observed discharge at Costons Lane

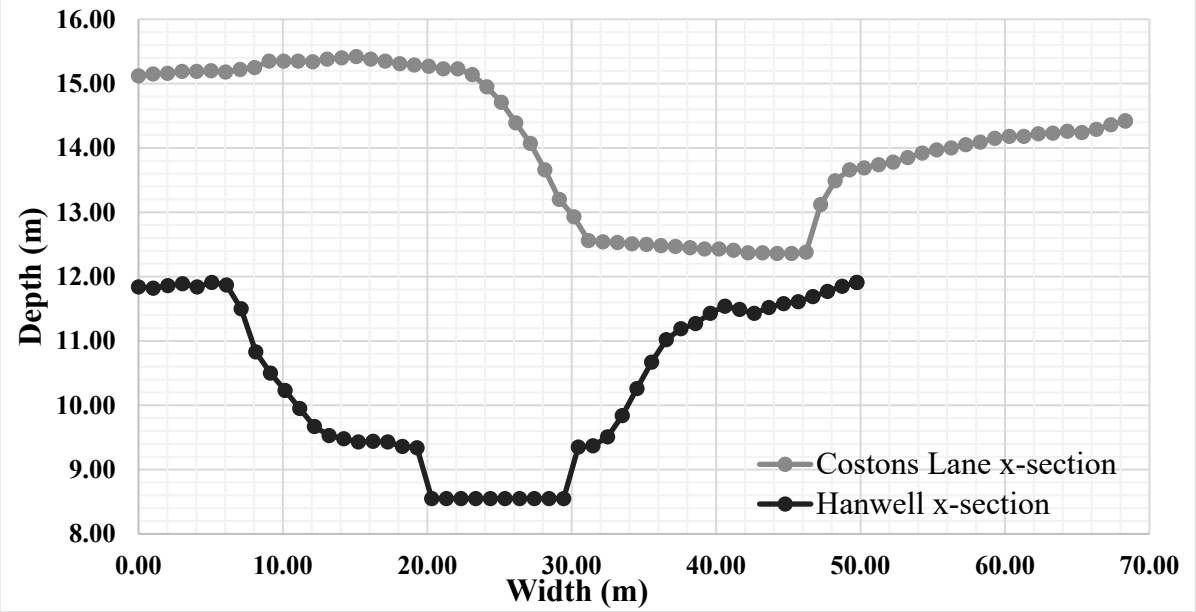

Figure 4.5: Upstream and downstream cross-sections of river Brent hydraulic model

Table 4.2: Details of the 2 model setups

Model Inputs	**Model-1 (prismatic channel)**	**Model-2 (natural channel)**
Channel Geometry	Rectangular (width = 50 m, depth = 10 m)	River Brent (average width = 24.32 m, average depth = 2.5 m)
River reach length	10.0 km	3.342 km
Riverbed slope (S_0)	0.0001	0.0012
Manning's n [$s/m^{(1/3)}$]	0.035 (assumed as True value)	Assumed as 0.052 as the river reach has stones and weeds with deep pools (Chow, 2006)
Number of cross-sections (Xs)	67 at a uniform spacing of 150 m	68 (40 Xs were extracted from 1m LIDAR DEM, the rest were linearly interpolated in the HEC-RAS)
Upstream boundary	Discharge/stage hydrograph	Discharge/stage hydrograph
Downstream boundary	Normal depth (S_0)	Normal depth
Initial flow (Q_i) [m^3/s]	100	2 (assumed)
Simulation time [s]	60 (based on Courant's criteria)	30 (based on Courant's criteria)

4.3.2 Example 1 – Unsteady flow model calibration

Example 1 demonstrates the use of a Python script to calibrate Manning's n and the initial flow of an unsteady flow model. HEC-RAS has an inbuilt unsteady flow calibration functionality. However, it works only when flow data for upstream boundary conditions are available (Brunner, 2016b). Therefore, HEC-RAS inbuilt functionality cannot be used for calibrating ungauged river sections. This example demonstrates a Python script which can be used to calibrate an unsteady flow model with both stage and flow data. This example also includes the calibration of the initial flow, which was usually assumed in previous studies (Aricò, Nasello & Tucciarelli, 2009; Barbetta, Moramarco & Perumal, 2017; Perumal et al., 2007b). Two instances of Manning's n variability along the channel reach are illustrated in this example. In one case, Manning's n of the channel reach is assumed to be homogeneous, that is, constant across all cross-sections; in the other, it is assumed to be heterogeneous. The two cases are illustrated in Scripts 1 and 2 respectively.

To calibrate the initial flow and Manning's n of the channel, it is presumed that at least for one flood event, a simultaneous record of stage hydrograph is available at the downstream and upstream sites of the river. The upstream stage is routed with a set of different initial flows and Manning's n several times (number of MC simulations). Then the resulting routed stages at downstream are compared with the observed stage using performance measures (refer to equation 4.1-4.4). The initial flow and Manning's n for which the modified KGE is the highest, are chosen as the calibrated values.

However, before proceeding to the calibration process, it is prudent to run a simplified version of the unsteady flow model to save variables for use in the calibration process. Therefore, the first part of this example shows a script to run an unsteady flow model.

Two different versions of Model-2, namely Brent_base and Brent_mc, are used in this example. The Brent_base model is used to show a simple case of running an unsteady flow model, saving the outputs, and plotting water surface profiles and hydrographs, and the Brent_mc model is used to demonstrate Manning's n calibration and initial flow calibration.

The difference between the Brent_base and Brent_mc unsteady flow hydraulic models is that the Brent_base has the discharge hydrograph as the upstream boundary condition, whereas the Brent_mc has a stage hydrograph. Because Brent_base has discharge data as the upstream

boundary, it does not require an initial condition. The model uses the first value of the discharge time series as the initial condition. A flow value is assumed as the initial condition for the Brent_mc model.

The code for running an unsteady flow model and calibrating Manning's n and initial flow is presented in Script 1.

Script 1: Calibrating Manning's n and initial flow of an unsteady hydraulic model

```
"""
author: Neeraj Sah (n.sah18@imperial.ac.uk)

"""

import win32com.client
import os
import numpy as np
import math
import pandas as pd
import scipy as sc
from scipy.stats import pearsonr
from datetime import datetime

start = datetime.now ()


# ============================================================
# Section 1: Initialization
# ============================================================

# Initiate the RAS Controller class
# TODO: Change the version of RAS as appropriate (e.g., if you're using v5.0.6,
# Change the prefix of HECRASController to RAS506)

hec = win32com.client.Dispatch ("RAS507.HECRASController") # Dispatch imports all the sub-routines and functions of HEC-RAS to python
hec.ShowRas ()       # show HEC-RAS window (comment this line if you don't want to see the hec-ras GUI)

# ============================================================
# Section 2: Running an unsteady flow model and saving required
# variables/parameters for Monte Carlo simulations
# ============================================================

"""
A pre-setup unsteady flow hydraulic model of river Brent (let's call it - Brent_base) is run to extract parameters/variables required for Monte Carlo simulations.
This model has an assumed Manning's coefficient (from literature, geology of the area, aerial photographs of the reach (Chow, 2006) for the banks and channels, unsteady boundary condition (stage hydrograph), a downstream boundary condition
(Normal depth) and an assumed initial condition (basically a flow value)

"""
# TODO: Change this to match the path on your PC

RASProject = os.path.join (os.getcwd (), r'Brent_base\brent_base_EA_data_pris.prj')

hec.Project_Open (RASProject)  # Opens the pre-setup hydraulic model

# ID numbers of the river and the reach (user defined)

```

```
RivID, RchID = 1, 1

# To get the name of River in the model

NRiver, TabRiver = None, None

NRiver, TabRiver = hec.Geometry_GetRivers (NRiver,TabRiver)

# To get the name of Reach for the user defined river ID

NReach, TabReach = None, None

[_, NReach, TabReach] = hec.Geometry_GetReaches(RivID, NReach, TabReach)

# To get the number of nodes, list of River stations (RS) and node types (e.g., simple cross-sections, bridge, storage area etc.)

NNod, TabRS, TabNTyp = None, None, None

[_, _, NNod, TabRS, TabNTyp] = hec.Geometry_GetNodes (RivID, RchID, NNod, TabRS, TabNTyp)

# To get all the water surface profiles

NProfile, TabProfile = None, None

NProfile, TabProfile= hec.Output_GetProfiles (NProfile, TabProfile)

"""
It has been observed that when we interpolate cross-sections (Xs) between 2Xs, the Manning's n values for banks and the channel get interchanged for interpolated cross-sections.
Therefore, it is prudent to check Manning's n value after interpolating the Xs.
An easier way to avoid this problem is to set the Manning's n using the below function from the HECRAS Controller.
"""

nLOB = 0.05             # TODO: User-defined nLOB/nROB fixed (for now)
nROB = 0.05             # TODO: User-defined
nCh = 0.0348            # TODO: User-defined. This will change in MC run

for j in range (NNod):  # Apply new Manning's n values to all cross-sections
    ErrMsg = None
    [_, _, _, _, _, _, ErrMsg] = hec.Geometry_SetMann_LChR (TabRiver [0],TabReach [0], TabRS [j], nLOB, nCh, nROB, ErrMsg)

hec.Project_Save ()     # Saving the project after applying Manning’s n

# Run the desired plan

NMsg, TabMsg, block = None, None, True

[_, NMsg, TabMsg, _] = hec.Compute_CurrentPlan (NMsg, TabMsg, block)

# Saving water level (W.S. Elev) and discharge (Q Total) data of all cross-sections for all time steps

# IDs of output variables are taken from the Appendix E of Goodell (2014): WSE, Total flow in a cross-section

  WSE_id, Flow_id = 2, 9

  OutBase_WSE = np.zeros ([NProfile-1, NNod], dtype=float)    # NumPy array for WSE

  OutBase_Flow = np.zeros ([NProfile-1, NNod], dtype=float)    # NumPy array for Total Flow

  for i in range (0, NNod):        # reading over nodes
     if TabNTyp [i] == "":       # An empty string "" denotes a cross-section
```

```
        for j in range (0, NProfile-1): # Reading over profiles # Not saving the max WS profile
            #Reading WSE
            [OutBase_WSE[j,i], _, _, _, _, _, _] = hec.Output_NodeOutput (
                RivID, RchID, i+1, 0, j+2, WSE_id
                )

            # Reading Total flow
            [OutBase_Flow [j,i], _, _, _, _, _, _] = hec.Output_NodeOutput (
                RivID, RchID, i+1, 0, j+2, Flow_id
                )
hec.Project_Close ()
hec.QuitRas ()

# Profile plot and stage and flow hydrographs at downstream cross-section

hec = win32com.client.Dispatch ("RAS507.HECRASController")

RASProject = os.path.join (os.getcwd (), r'Brent_base\brent_base_EA_data_pris.prj')

hec.Project_Open (RASProject)

hec.PlotPF(TabRiver,TabReach)

hec.PlotStageFlow (TabRiver,TabReach,TabRS[-1])  # TODO: Change TabRS to plot at other
cross-section

# ==========================================================
# Section 3: Read observed data (stage/discharge)
# ==========================================================

Observed_WSE_US = pd.read_csv (os.path.join(os.getcwd (),
r'brent_costons_lane_hecras.csv'), usecols= ['Stage (ftAOD)']).to_numpy ()

Observed_WSE_DS = pd.read_csv (os.path.join(os.getcwd (),
r'brent_hanwell_hecras.csv'),usecols= ['Stage (ftAOD)']).to_numpy ()

Observed_flow_US = pd.read_csv (os.path.join(os.getcwd (),
r'discharge_cl_EA_rating_curve.csv'),usecols= ['Discharge (ft3/s)']).to_numpy ()

# ==========================================================
# Section 4: Monte Carlo (MC) simulations initialization
# ==========================================================

#  # Step-4.1: Defining parameters/variables for MC simulation

Sim_Q_i = np.array ([], dtype=float)   # Numpy array for simulated initial flow for MC runs.
Sim_nCh = np.array ([], dtype=float)  # Numpy array for Simulated Manning's n for MC runs.

OutMC_WSE_stable = []                 # Empty list to store WSE during each MC run
OutMC_Flow_stable = []                # Empty list to store discharge during each MC run

Stable_Run = np.array([], dtype=int) # Numpy array to store stable runs

NMCRuns = 0
StableRuns = 0

# ==========================================================
# Section 5: Monte Carlo Simulations
# ==========================================================

while StableRuns < 1000:      # TODO: Define desired number of stable MC simulations

    # ====================
    # # Step-5.1: Generate random sample for initial flow and Manning's n
    # ====================

    # It is assumed that the initial flow has a uniform distribution
```

```
171.
172.      Run_Sim_Q_i = np.random.uniform (70.63, 176.57,1)  # TODO: Initial flow ranges from
    [2.0, 5.0] m3/s. Change accordingly
173.
174.      # It is assumed that the Manning's n has a uniform distribution
175.
176.      Run_Sim_nCh = np.random.uniform (0.008, 0.045,1) # TODO: Manning's n ranges from
    [0.012, 0.067] s.m^(-1/3). Change range of n as per (Chow, 2006)
177.
178.      # Save the base flow and Manning's n for future reference
179.
180.      Sim_Q_i = np.append (Sim_Q_i,Run_Sim_Q_i)
181.
182.      Sim_nCh = np.append (Sim_nCh,Run_Sim_nCh)
183.
184.      # ====================
185.      # Step 5.2: Initial condition manipulation at U/S Boundary in each MC simulation
186.      # ====================
187.
188.      # access and replace initial condition in the flow file (text file: has .u## extension)
189.
190.      with open (r'Brent_mc\brent_mc_EA_data_pr.u01', 'r') as f:    # TODO: Change the folder
    and name of unsteady flow file
191.          filedata = f.readlines()
192.
193.      filedata[3] = 'Initial Flow Loc=Brent          ,CL-Han          ,10964.57,' + str(Run_Sim_Q_i
    [0]) +'\n'  # TODO: Change RS when there is change in reach
194.
195.      with open (r'Brent_mc\brent_mc_EA_data_pr.u01', 'w') as f:   # TODO: change the folder
    and name of unsteady flow file
196.          for line in filedata:
197.              f.write (line)
198.
199.      # ====================
200.      # Step 5.3: Changing the Manning's n in the HEC-RAS project (here it's named as
    Brent_mc)
201.      # ====================
202.
203.      hec = win32com.client.Dispatch ("RAS507.HECRASController")
204.
205.      # TODO: Change the path of the model as on your PC
206.
207.      RASProject_MC = os.path.join (os.getcwd (), r'Brent_mc\brent_mc_EA_data_pr.prj')
208.
209.      hec.ShowRas ()
210.
211.      # Open HEC-RAS
212.
213.      hec.Project_Open (RASProject_MC)
214.
215.      nLOB = 0.05     # TODO: User-defined nLOB/nROB fixed (for now)
216.      nROB = 0.05     # TODO: User-defined
217.
218.      # Change Manning's n values of channel at all cross-sections
219.
220.      for j in range (NNod): # apply new Manning's n values to all cross-sections
221.          ErrMsg = None
222.          [_, _, _, _, _, _, _, ErrMsg] = hec.Geometry_SetMann_LChR (TabRiver [0], TabReach
    [0], TabRS [j], nLOB, Run_Sim_nCh [0], nROB, ErrMsg)
223.
224.      # Save the project with the new Manning's n values
225.
226.      hec.Project_Save ()
227.
228.      # ====================
229.      # Step 5.4: Running the HEC-RAS MC model
230.      # ====================
```

```
231.
232.      hec.Compute_HideComputationWindow () # TODO:
    hec.Compute_ShowComputationWindow() to see computation window. Note that hiding
    computation window reduces run time
233.
234.      [NMsg_MC, TabMsg_MC, block] = None, None, True
235.
236.      [_, NMsg_MC, TabMsg_MC, _] = hec.Compute_CurrentPlan (NMsg_MC, TabMsg_MC, block)
237.
238.      # ====================
239.      # Step 5.5: Saving the water level and discharge data for all cross-sections for all time
    steps for stable runs
240.      # ====================
241.
242.      ## IDs of output variables: WSE, Total flow in a cross-section
243.
244.      WSE_id, Flow_id = 2, 9
245.
246.      TabWSE_MC = np.zeros([NProfile-1, NNod], dtype=float)    # NumPy array for WSE
247.
248.      TabFlow_MC = np.zeros([NProfile-1, NNod], dtype=float)    # NumPy array for Total Flow
249.
250.      for i in range (0, NNod):         # reading over nodes
251.         if TabNTyp [i] == "":        # An empty string "" denotes a cross-section
252.            for j in range (0, NProfile-1): # reading over profiles # we are not taking the max WS
    profile
253.               #Reading WSE
254.               [TabWSE_MC [j,i], _, _, _, _, _, _] = hec.Output_NodeOutput (
255.                     RivID, RchID, i+1, 0, j+2, WSE_id
256.                     )
257.
258.               # Reading Total flow
259.               [TabFlow_MC [j,i], _, _, _, _, _, _] = hec.Output_NodeOutput (
260.                     RivID, RchID, i+1, 0, j+2, Flow_id
261.                     )
262.
263.
264.      # Checking whether the model is stable or not. If modified KGE is >=0, then the model is
    considered to be stable else unstable.
265.      # Calculating modified KGE by using computed stage/discharge hydrograph and observed
    stage/discharge hydrograph at the downstream boundary
266.
267.      mod_kge = 1- (math.sqrt ((pearsonr (TabWSE_MC[:,-1], Observed_WSE_DS [:,0])[0]-
    1)**2 + (np.divide (sc.stats.variation (TabWSE_MC[:,-1]),sc.stats.variation
    (Observed_WSE_DS [:,0]))-1)**2 +\
268.                     (np.divide (np.mean (TabWSE_MC [:,-1]),np.mean (Observed_WSE_DS
    [:,0]))-1)**2))
269.
270.      if mod_kge>= 0:  # Stable run
271.
272.         StableRuns = StableRuns+1
273.
274.         OutMC_WSE_stable.append (TabWSE_MC)
275.
276.         OutMC_Flow_stable.append (TabFlow_MC)
277.
278.         Stable_Run = np.append (Stable_Run, NMCRuns)  # Saving the index of stable runs
279.
280.      hec.Project_Close ()
281.      hec.QuitRas ()
282.
283.      del hec
284.      del TabWSE_MC
285.      del TabFlow_MC
286.
287.      print ("number of stable runs=", StableRuns)
288.
```

```
289.      NMCRuns = NMCRuns + 1
290.
291.  Run_time = datetime.now () - start
292.  print ("number of MC runs=", NMCRuns)
293.  print ('Run time (hh:mm:ss) =', Run_time)
294.
295.  # ************************************************************************
296.  # End of Monte-Carlo Simulations
297.  # ************************************************************************
```

The program presented in Script 1 is divided into five sections. Each section has comments and explanations to guide the reader and describe the program in an orderly manner. Additionally, the program has "TODO" comments to inform the reader that they can/should edit the commented or following line of code. Due to space limitations, the program presented in Script 1 is not discussed line-by-line. Dysarz (2018) has provided a good description of the Python scripting technique, highlighting the differences between VBA (HEC-RAS is VBA-based) and Python scripting, the advantages of Python scripting over other languages to control and automate HEC-RAS, and has shown three examples of controlling and automating HEC-RAS using Python. Therefore, readers are referred to Dysarz (2018) for an in-depth discussion of Python scripting. The subroutines and functions of HEC-RAS used in this chapter are well documented in Goodell (2014).

The first section of the script (lines 6-13) imports all the sub-routines and functions of the HEC-RAS into Python using the Dispatch function of win32com.client module. The second section of the script runs a pre-setup unsteady flow hydraulic model (i.e., Brent_base), saves the output stage (lines 110–112) and flow (lines 115–117) at all the cross-sections, and plots the water surface profiles (line 129) and stage and flow hydrographs (line 131) at the downstream cross-sections (i.e., River Brent at Hanwell). The plots from the HEC-RAS model run are shown in Figures 4.6 and 4.7, respectively. In this example, only the stage and flow outputs have been saved. However, the HEC-RAS controller provides access to various other outputs, such as average flow velocity, maximum channel depth, and so on. Any of these outputs from the model run can be saved similarly by using the RAS ID number from Appendix E of Goodell (2014).

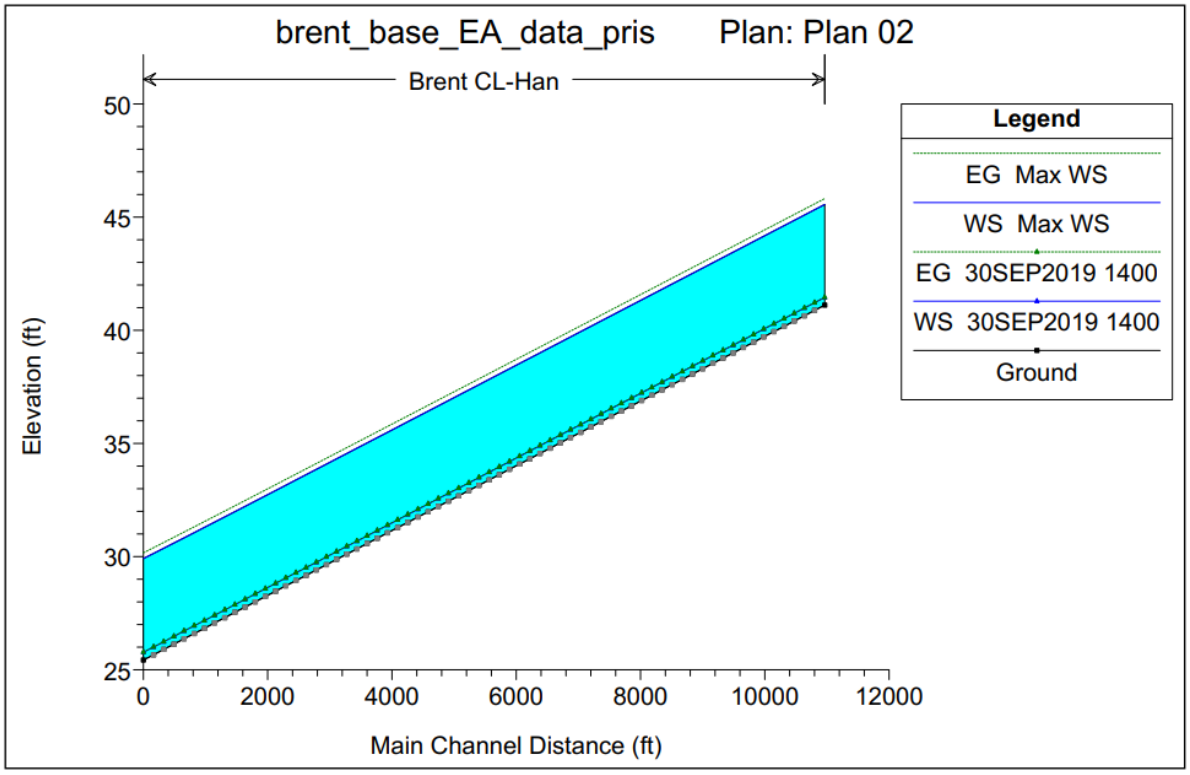

Figure 4.6: Water surface profiles (initial and maximum water surfaces)

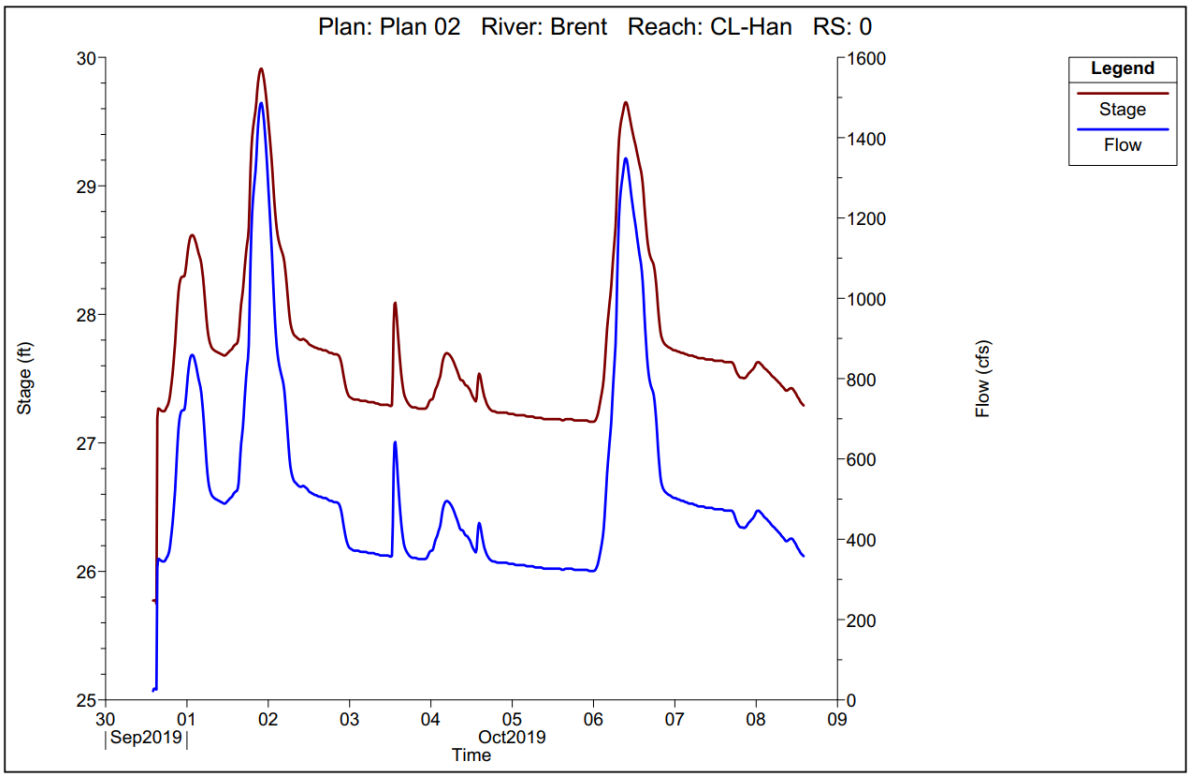

Figure 4.7: Modelled stage and flow hydrographs at the downstream cross-section

The observed stage and flow data of the Brent River are loaded as described in section three of the script (lines 137 - 141). The observed data is used to evaluate the performance of Brent_base and Brent_mc unsteady flow models. For example, the output or (modelled) stage of the Brent_base unsteady flow model is shown in Figure 4.8, along with the observed stage at Hanwell. As can be seen, the modelled stage is significantly underestimated. This could be due to i) assuming a large value of Manning's n for the reach and ii) assuming a constant value of Manning's n for the entire reach.

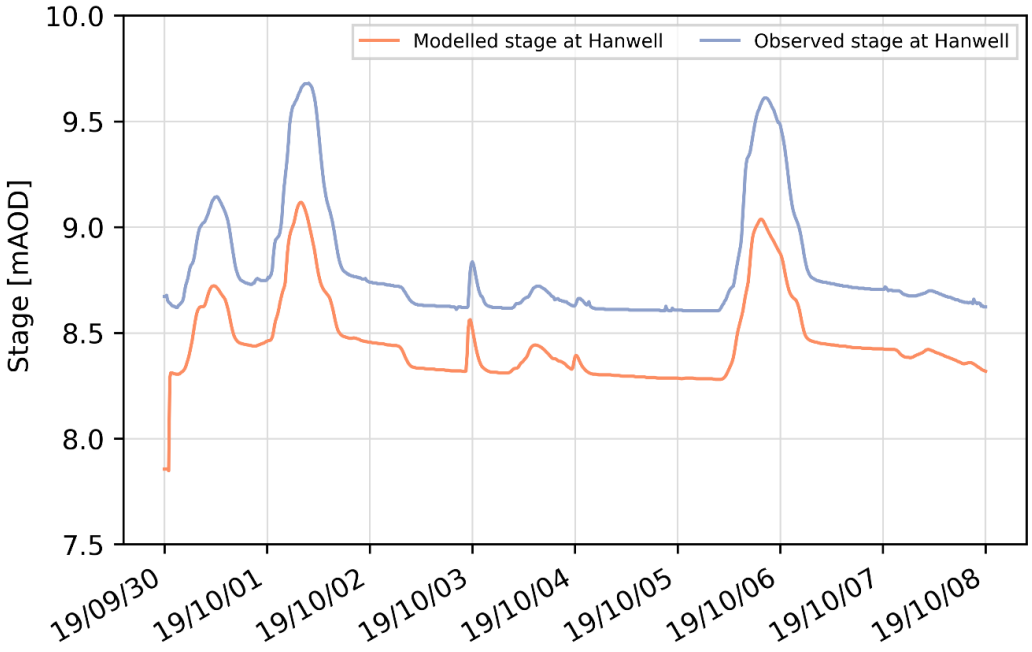

Figure 4.8: Observed and modelled stages at Hanwell from the Brent_base unsteady flow model

In Section 4 of Script 1, the MC simulation is initialized. Here, parameters for MC simulations, in this example, initial flow and Manning's n, are defined. Additionally, variables for the total number of MC simulations and the total number of stable runs are also defined.

In Section 5, the statistical distribution of the MC parameters is defined (refer to Step 2 of Figure 4.1). For this example, it is assumed that both initial flow and Manning's n have a uniform distribution. A uniform distribution is selected because it does not make any assumptions about prior parameter distribution other than specifying a feasible range and scale (Freer, Beven & Ambroise, 1996). However, users can assume any other distribution as per their requirements. Then, in each MC simulation, an initial flow and Manning's n value are randomly sampled (refer to Step 5.1). Then the randomly sampled parameters are updated in subsequent steps. The unsteady flow file of Brent_mc is edited to update the initial flow (refer

to Step 5.2). The unsteady flow file of the HEC-RAS is a text file (ASCII). The code presented in Step 5.2 is a simple way of reading and writing text files in Python and can be used to change the boundary condition of the unsteady flow model as well. After the initial flow has been updated in the unsteady flow file, the HEC-RAS project (or Brent_mc model) is opened and the randomly sampled Manning's n is applied to all the cross-sections using the Geometry_SetMann_LChR function (refer to Step 5.3). It should be noted that, in this example, it is assumed that Manning's n is spatially constant. Once the randomly sampled initial flow and Manning's n are updated in the Brent_mc model, the model is saved and then run (refer to Step 5.4). Here, the computation window of the HEC-RAS is hidden (line 232) because it was observed that hiding the computational window reduced the run time by half. This is very important because more than a thousand runs were implemented during MC simulations. The output stage and flow of each MC simulation are saved for model performance analysis (as discussed in heading 2). It was observed that model runs having a negative value of KGE were generally the results of unstable runs. Therefore, a criterion of stability was applied to save only those outputs where modified KGE at the downstream end is greater than equal to zero. The stability criterion saves computational space and time. Once all the MC simulation runs are completed, the outputs are saved, and the MC simulation is terminated. It should be noted that due to an internal bug in HEC-RAS version 5.0.7 and older, certain functionality of HEC-RAS, e.g., working with DSS files, did not work when the project was in the SI system of units (Kleinschmidt, 2019). Therefore, all the HEC-RAS simulations were carried out in US customary units and later converted to SI units.

In this example, the model is run until 1000 stable runs are obtained (as defined in line 164), i.e., runs having a KGE greater than or equal to zero. It is important to note that, if the parameters are randomly sampled from a uniform distribution, there are no clear guidelines for the minimum number of necessary runs or a stopping criterion (Pappenberger et al., 2005a). The minimum number of runs is dependent on the number of parameters varied and the parameter ranges chosen. In addition, the minimum number of runs required should be able to adequately sample the parameter space, which is difficult to determine a priori. However, when the parameters are normally distributed, a stopping criterion defined by the mean of the sampled parameter space can be used to terminate the MC simulation (for example, Dottori, Martina & Todini, 2009; Goodell, 2014).

After the MC simulation was completed, the results were analysed using the performance criterion. The set of Manning's n and initial flow for which the KGE was highest was chosen as the calibrated values. All the sampled Manning's n and initial flow were plotted against the modified KGE, shown in Figures 4.9 and 4.10. The calibrated values of Manning's n and initial flow are shown by the red line in Figures 4.9 and 4.10. Figure 4.11 shows all the simulated stage hydrographs from MC simulations (grey line), the observed stage hydrograph (blue line) and the stage hydrograph corresponding to the calibrated values or maximum KGE at the downstream of the river Brent (i.e., at Hanwell station).

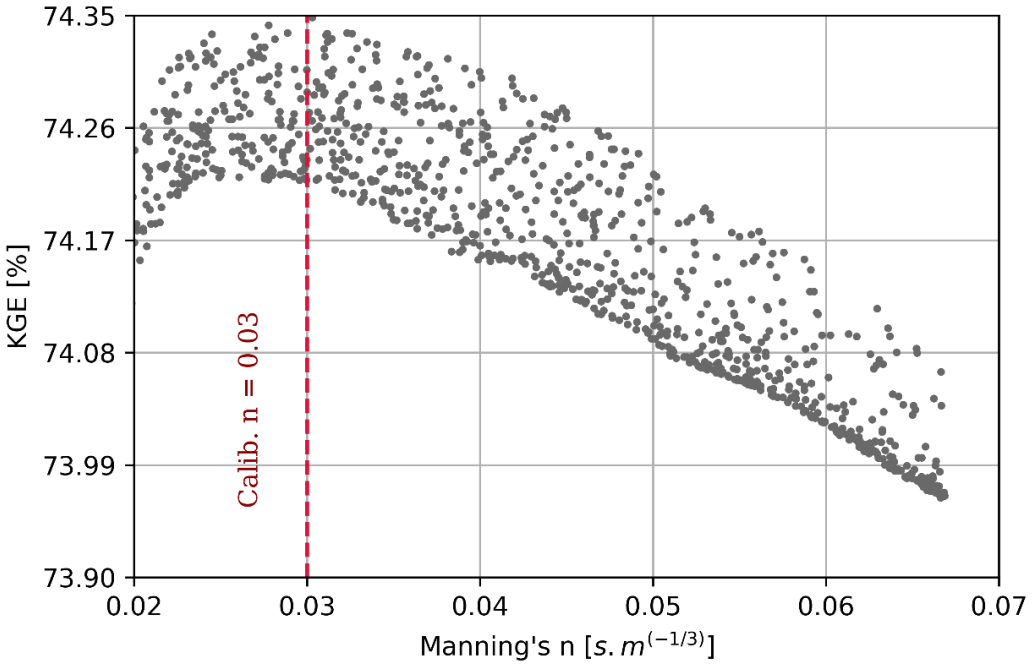

Figure 4.9: Modified KGE for different Manning's n (assumed constant throughout the channel reach length) for the river Brent.

From Figure 4.11, it can be inferred that the calibrated values of Manning's n and initial flow are not able to simulate the peaks of the observed stage hydrograph, as there is a significant difference in the peaks of the observed and simulated stage hydrographs (see red and blue lines). Another thing to note is that most of the simulated stage hydrographs are far below the observed stage hydrograph (i.e., underestimating the observed stage). This can be due to different initial flow conditions in different MC runs, misrepresentation of channel geometry, or because of constant Manning's n assumption since the channel reach is greater than 3 kilometres. Upon investigation, it was found that the separation was caused by Manning's n

assumption that it was constant throughout the channel reach. This is discussed in detail in Script 2, where the spatial variation of Manning's n along the channel reach is considered.

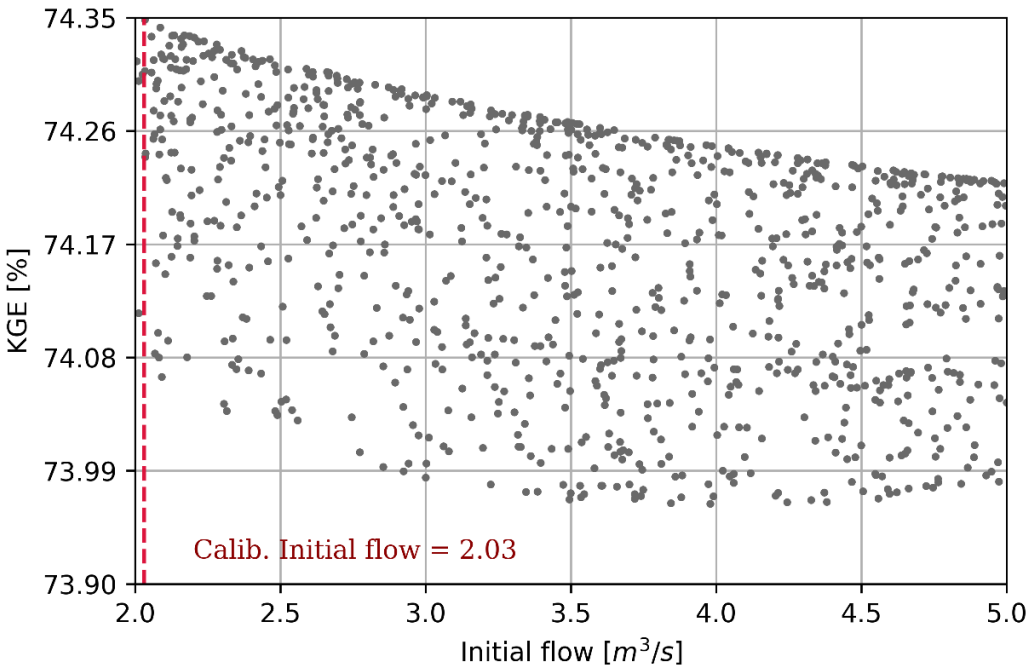

Figure 4.10: Modified KGE for different Initial flow for the river Brent

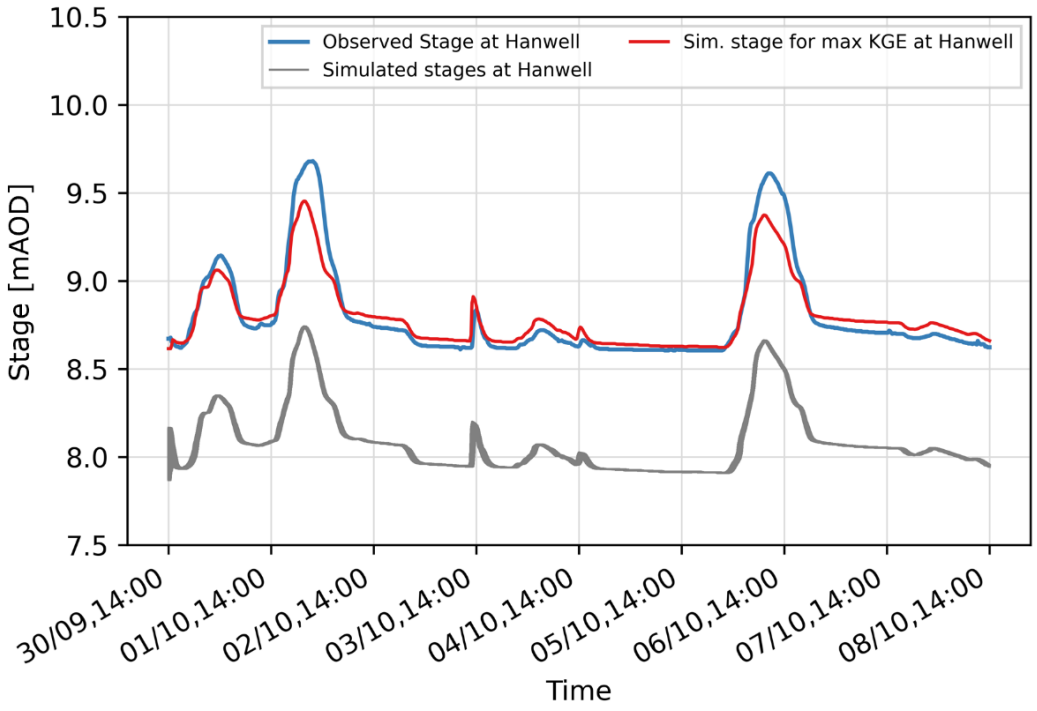

Figure 4.11: Observed (blue), all simulated stages (grey) and simulated stage for maximum KGE value

Script 2: Calibrating Manning's n (heterogenous) and initial flow of an unsteady hydraulic model

```
# ============================================================
# Section 4: Monte Carlo (MC) simulations initialization
# ============================================================

#  # Step-4.1: Defining variables

Sim_Q_b = np.array ([],dtype=float) # Numpy array for Simulated Baseflow/Initial flow for MC Runs.
Sim_nCh = np.array ([],dtype=float) # Numpy array for Simulated Manning's n for MC Runs.
Sim_nCh1 = np.array([],dtype=float) # Numpy array for Simulated Manning's n for MC Runs.

OutMC_WSE_stable = []            # Empty list to store WSE during each MC run
OutMC_Flow_stable = []           # Empty list to store Flow during each MC run

Stable_Run = np.array ([],dtype=int)         # Numpy array to store stable runs


NMCRuns=0
StableRuns = 0

# ============================================================
# Section 5: Monte Carlo Simulations
# ============================================================

while StableRuns < 1000:      # TODO: Define number of stable runs required

    # ====================
    # # Step-5.1: Generate sample for Initialflow and Manning's n
    # ====================

    Run_Sim_Q_b = np.random.uniform(17.657,105.94,1)  # TODO: [0.5, 3.0]: m3/s in CFS


    Run_Sim_nCh = np.random.uniform(0.008,0.045,1) # TODO: Change range of n if needed , Creating Simulated Manning's n for MC Runs.
    Run_Sim_nCh1 = np.random.uniform(0.008,0.045,1) # TODO: Change range of n if needed , Creating Simulated Manning's n for MC Runs.

    ''' Uniformly distributed Manning's n with lower limit = 0.02 and upper limit = 0.035 (user defined)'''


    # Save the base flow and Manning's n for future reference

    Sim_Q_b = np.append(Sim_Q_b,Run_Sim_Q_b)
    Sim_nCh = np.append(Sim_nCh,Run_Sim_nCh)
    Sim_nCh1 = np.append(Sim_nCh1,Run_Sim_nCh1)

   # ====================
    # Step 5.2: Initial condition manipulation at U/S Boundary in each MC run
    # ====================

    # Same as Script 1


    # ====================
    # Step 5.3: Changing the Manning's n in the HEC-RAS project: MC model - 1
    # ====================

hec = win32com.client.Dispatch ("RAS507.HECRASController") # Dispatch imports all the sub-routines and functions of hec-ras to python

    # TODO: Change the path of the MC_model_1 as on your PC
```

```
59.
60.     RASProject_MC = os.path.join(os.getcwd(),r'Brent_mc\brent_mc_EA_data_pr.prj')
61.
62.     hec.ShowRas()
63.
64.     # Open HEC-RAS
65.
66.     hec.Project_Open(RASProject_MC)
67.
68.
69.     nLOB = 0.05 # TODO: User-defined nLOB/nROB fixed (for now)
70.     nROB = 0.05 # TODO: User-defined
71.
72.  # Apply new Manning's n values to all cross-sections in first half of the reach
73.
74.     for j in range(int(NNod/2+1)):
75.         ErrMsg = None
76.         [_, _, _, _, _, _, _, ErrMsg] = hec.Geometry_SetMann_LChR(TabRiver[0],TabReach[0],
    TabRS[j], nLOB, Run_Sim_nCh[0], nROB, ErrMsg)
77.
78.  # Apply new Manning's n values to all cross-sections in second half of the reach
79.
80.     for j in range (int (NNod/2),NNod):
81.         ErrMsg = None
82.         [_, _, _, _, _, _, _, ErrMsg] = hec.Geometry_SetMann_LChR(TabRiver[0],TabReach[0],
    TabRS[j], nLOB, Run_Sim_nCh1[0], nROB, ErrMsg)
83.
84.
85.     # Save the project with the new Manning's n values
86.
87.     hec.Project_Save ()
88.
```

Script 2 is the same as script 1, except it allows Manning's n to vary across the channel. In this example, it is assumed that the first half of the channel (i.e., from upstream to mid-stream) has one value of Manning's n (the river reach passes through a park and an undeveloped area) and that the second half of the channel (i.e., from mid-stream to downstream) has another value of Manning's n (the river reach is in an urban area). It should be noted that the method presented in this script can be used to apply different Manning's n values to different cross-sections as well. However, such high variability in Manning's n rarely occurs in nature. Furthermore, it is impractical to vary Manning's n with adjacent cross-sections. Therefore, it is not presented here.

There are only a few new lines of code in section 4 (line 9) and section 5 (lines 34, 43, 72–83), which are used to vary Manning's n values along two halves of the channel reach. Once the MC simulations were completed, the results were analysed using the performance criterion and a similar analysis was carried out to find the calibrated values of Manning's n and initial flow.

Figure 4.12 shows, that the first half of the river Brent reach (i.e., upstream to mid-stream) has a higher value of Manning's n than that of the second half of the reach. The calibrated values

of Manning's n for the sub-reaches are 0.0368 and 0.0621 $s.m^{(-1/3)}$ for the first and second halves respectively and the calibrated value of initial flow is 2.64 m^3/s (refer to Figure 4.13).

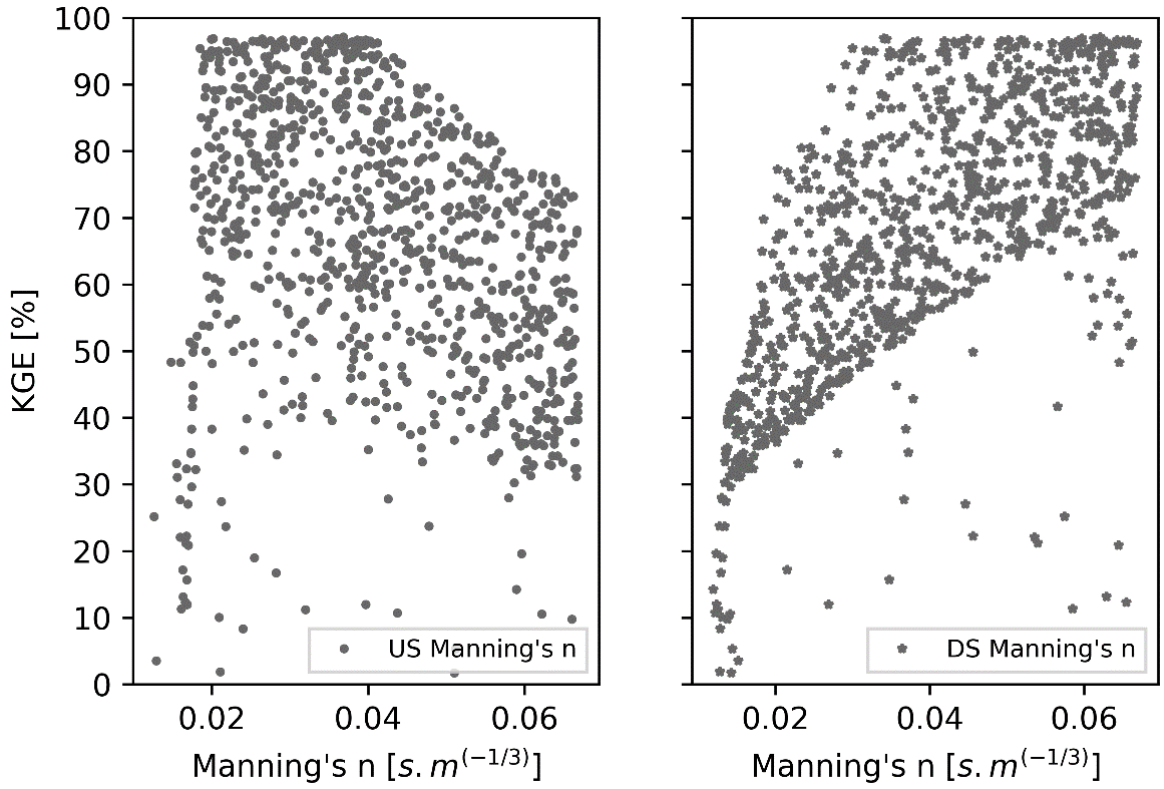

Figure 4.12: Modified KGE for different Manning's n for the river Brent; LHS) upstream to mid-stream and RHS) mid-stream to downstream.

Figure 4.14 depicts all the simulated stage hydrographs from MC simulations (grey line), the observed stage hydrograph (blue line), and the stage hydrograph corresponding to the calibrated values (or maximum KGE) at the river Brent's downstream (i.e., at Hanwell station). Notably, when two distinct sets of Manning's are assumed for the channel reach, the simulated stage hydrograph (red line in Figure 4.14) corresponding to calibrated Manning's n and initial flow closely matches the observed stage hydrograph downstream station of the river Brent (i.e., at Hanwell station).

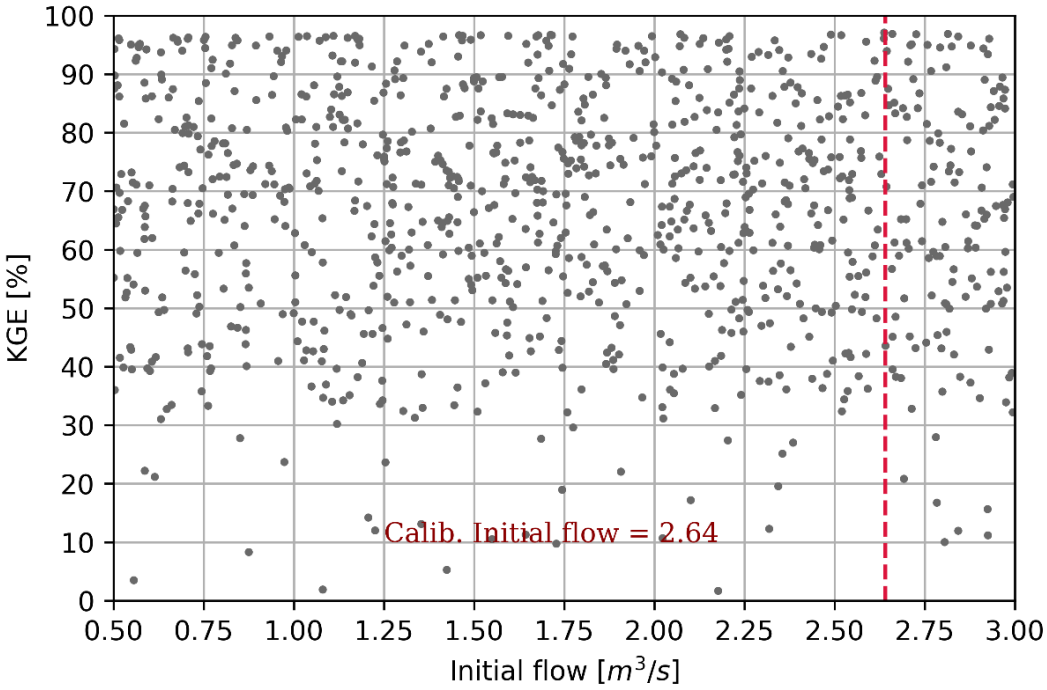

Figure 4.13: Modified KGE for different Initial flow for the river Brent

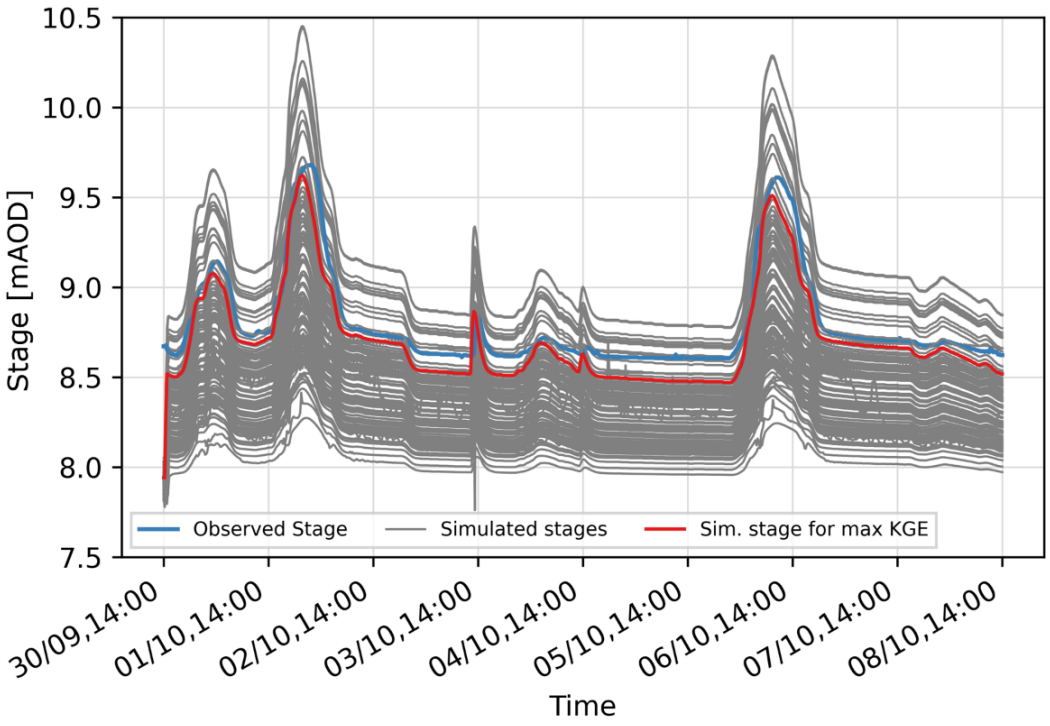

Figure 4.14: Observed (blue), all simulated stages (grey) and simulated stage for maximum KGE value

4.3.3 Example 2 – Scenario analysis

By randomly sampling from a set of possible inputs, the MC simulations account for the observed variability in critical inputs and attempts to replicate reality. This example illustrates how to use MC simulations to generate multiple flood depth scenarios by creating an ensemble of upstream stage or flow inputs. This is advantageous for flood mitigation studies because it enables the identification of all possible flood inundation scenarios through the generation of thousands of plausible synthetic events (or inputs) (Babister et al., 2016a).

Model-1 is used in this example. A flow hydrograph, generated using equation 4.5, is used as the upstream boundary condition. An ensemble of upstream boundary flow hydrographs is then created by perturbing these upstream boundary conditions, to generate all plausible flood depths at the downstream boundary. The ensemble of upstream flow hydrographs is created by changing the values of peak flow (Q_p) and base flow (Q_b) in equation 4.5. Here, as in Example 1, it is assumed that peak flow and base flow have a uniform distribution. It should be noted that the time to peak, in equation 4.5, can also be varied to increase upstream flow hydrograph samples. However, to save computational time and space, the time to peak is kept constant for this example. After an upstream flow hydrograph is generated, it is then updated in the hydraulic model flow file (.u##) during each MC simulation (lines 39-57).

HEC-RAS provides two file types to store hydraulic model flow files. One is an ASCII file type, as shown in Example 1 to calibrate the initial flow, and the other one is a DSS (Data Storage System) file type. DSS (or HEC-DSS) is a database system that is typically used to store and retrieve sequential scientific data, such as time series data, curve data, spatially oriented gridded data, and so on (USACE, 2009). The system was designed to make data retrieval and storage simple for users and application programs. In this example, the DSS file type is used to input the upstream boundary as this file type can handle large volumes of data and can be manipulated using Python. Manipulation of the DSS file type using Python has not been discussed in any of the previous studies (Dysarz, 2018; Leon & Goodell, 2016b). Here, I have used Pydsstools (Basyal et al., 2019) and HEC-DSSvue (USACE, 2009) to manipulate the DSS file type. It should be noted that due to an internal bug in HEC-RAS version 5.0.7 and older, working with DSS files, did not work when the project was in the SI system of units. Therefore, US customary units were used while setting up the unsteady flow model.

Script 3: Flood depths scenario analysis

```
# ============================================================
# Section 1: Generating multiple upstream flow boundary Conditions to be used in MC simulations
# ============================================================

NMCRuns = 4000    # TODO: User defined

# # Step-1.1: Generate MC samples for Base Flow and Peak flow

Sim_Q_b = np.random.uniform(1765.75,8828.75, NMCRuns)  # TODO: [50, 250] m3/s in CFS  # True base flow = 100 m3/s
Sim_Q_p = np.random.uniform(26486.25,35315.0, NMCRuns)  # TODO: [750, 1000] m3/s in CFS  # True peak flow = 900 m3/s

''' Uniformly distributed Base flow with lower limit = 1765.75 and upper limit = 8828.75 (user defined)'''
''' Uniformly distributed Peak flow with lower limit = 26486.25 and upper limit = 35315.0 (user defined)'''
'''
Q (t) = Qb + (Qp - Qb) * [(t/Tp)* exp {1-(t/Tp)}]**16

'''

# Time step for flow hydrograph. To be consistent with the one used in Base model run

T_p = 24   # TODO: Time to peak (hour); change this as per required
t_int = 5 # TODO: time interval of hydrograph (min); change as required according to Base model
t_min = np.arange (0,T_p *3*60 + t_int, t_int) # time in minute
t_hr = np.divide (t_min, 60)

Sim_Q = np.zeros((len(t_hr),NMCRuns), dtype=float)
Sim_WSE_US = np.zeros((len(t_hr),NMCRuns), dtype=float)    # NumPy array for U/S WSE
Sim_WSE_DS = np.zeros((len(t_hr),NMCRuns), dtype=float)    # NumPy array for D/S WSE



for mc in range (NMCRuns):

# # Step-1.2: Generate U/S flow hydrograph for MC runs

    for i in range(len(t_hr)):
        Sim_Q[i,mc] = Sim_Q_b[mc] + (Sim_Q_p[mc] - Sim_Q_b[mc]) * ((np.divide(t_hr[i], T_p)) * math.exp (1-(np.divide(t_hr[i],T_p))))**16

# # Step-1.3: DSS Manipulation for changing U/S boundary flow hydrograph

    dss_file = "US_flow_hyd_fps_model_1.dss"


    pathname = "/RIVER-1/REACH-1/FLOW HYDROGRAPH/" + TabProfile[1][:-5] + "/5MIN/" + TabRS[0] + "/" # TODO: change time interval
    tsc = TimeSeriesContainer()
    tsc.pathname = pathname
    tsc.startDateTime = TabProfile[1]
    tsc.numberValues = NProfile-1
    tsc.units = "CFS"
    tsc.type = "INST"
    tsc.interval = 5                # TODO: 1 = 1 hour interval hydrograph, change to 5 for 5 min and so on
    tsc.values = Sim_Q[:,mc]
    fid = HecDss.Open(dss_file)
    fid.deletePathname(tsc.pathname)
    fid.put_ts(tsc)
```

```
    ts = fid.read_ts(pathname)
    fid.close()

 # # Step-1.4: Run HEC-RAS model and save outputs. Here, U/S and D/S stage hydrographs are saved

    RASProject_BCK = os.path.join (os.getcwd (),r'Model-1\model_1_fps.prj')

    hec.ShowRas ()

    hec.Project_Open (RASProject_BCK)

    hec.Compute_HideComputationWindow ()

    [NMsg, TabMsg, block] = None, None, True

    [_, NMsg, TabMsg, _] = hec.Compute_CurrentPlan (NMsg, TabMsg, block)


    for j in range (0, NProfile-1): # reading over profiles # we are not taking the max WS profile

        #Reading D/S WSE
        [Sim_WSE_DS[j,mc], _, _, _, _, _, _] = hec.Output_NodeOutput (RivID, RchID, NNod, 0, j+2, WSE_id)


    hec.Project_Close ()
    print (mc)
hec.QuitRas ()

```

Flood depths or stage hydrographs corresponding to all the upstream flow hydrograph is saved in each MC simulation. Figure 4.15 shows all the possible flood depths at downstream of Model-1. These flood depths can be used to prepare probabilistic flood inundation maps.

It is important to note that using the DSS file type has additional benefits, for example, including, and updating internal boundary conditions, which is difficult with the ASCII file type. In HEC-RAS, a known stage hydrograph and/or a flow hydrograph can be used as an internal boundary condition to force a known stage and/or flow for part or all of the simulation. Furthermore, the DSS file type will be easy to handle if any user seeks to explore the impact of error in upstream and/or internal boundary conditions on downstream flow depths or overall model performance following the approach illustrated in Example 2.

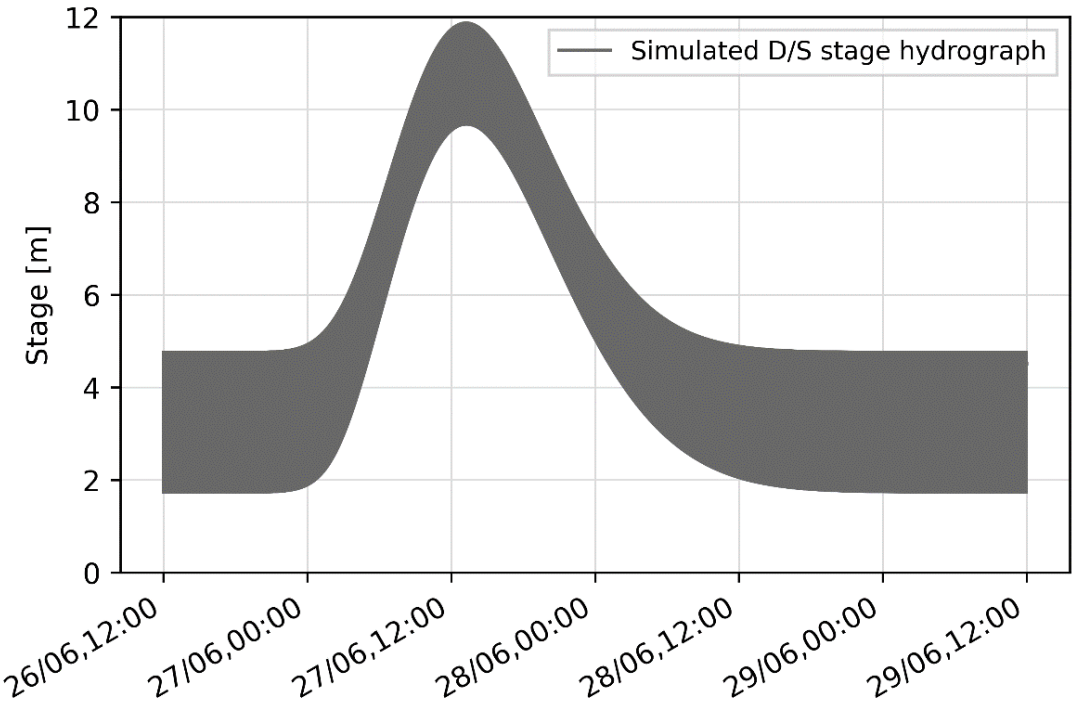

Figure 4.15: Plausible flood depths at the downstream boundary

4.3.4 Example 3 – Sensitivity and uncertainty analysis

Different river flow models represent the modelled system from a variety of perspectives and, inevitably, are imprecise representations of reality (Loucks & van Beek, 2017). Regardless of the model chosen, the primary source of error in any river modelling is the uncertainty associated with determining model parameters (e.g., Manning's n, channel geometry approximation) due to a mismatch between model complexity and available data (Devak & Dhanya, 2017; dos Reis et al., 2020).

Sensitivity analysis techniques aid in identifying parameters that have a significant effect on the model outputs and thus on the model response, while uncertainty analysis techniques aid in quantifying the output variability caused by input variability (Loucks & van Beek, 2017). Various methods are available to perform sensitivity and uncertainty analysis of river flow modelling processes. MC simulation is a widely used method for the same. Here, an additional example is not shown, rather results from Example 1 are interpreted to explain sensitivity and uncertainty analysis as the approach is similar.

Let us suppose that we want to see the impact of uncertainties in initial flow and Manning's n on model output (output stage evaluated with a modified KGE performance measure). From

Figures 4.10 and 4.13, we can infer that model output (or output stage) is not sensitive to initial flow as there is no visible pattern between sampled initial flows and the output stage in these plots. However, Figures 4.9 and 4.12 show that model output is sensitive to Manning's n as there is a clear visible pattern between KGE and Manning's n samples.

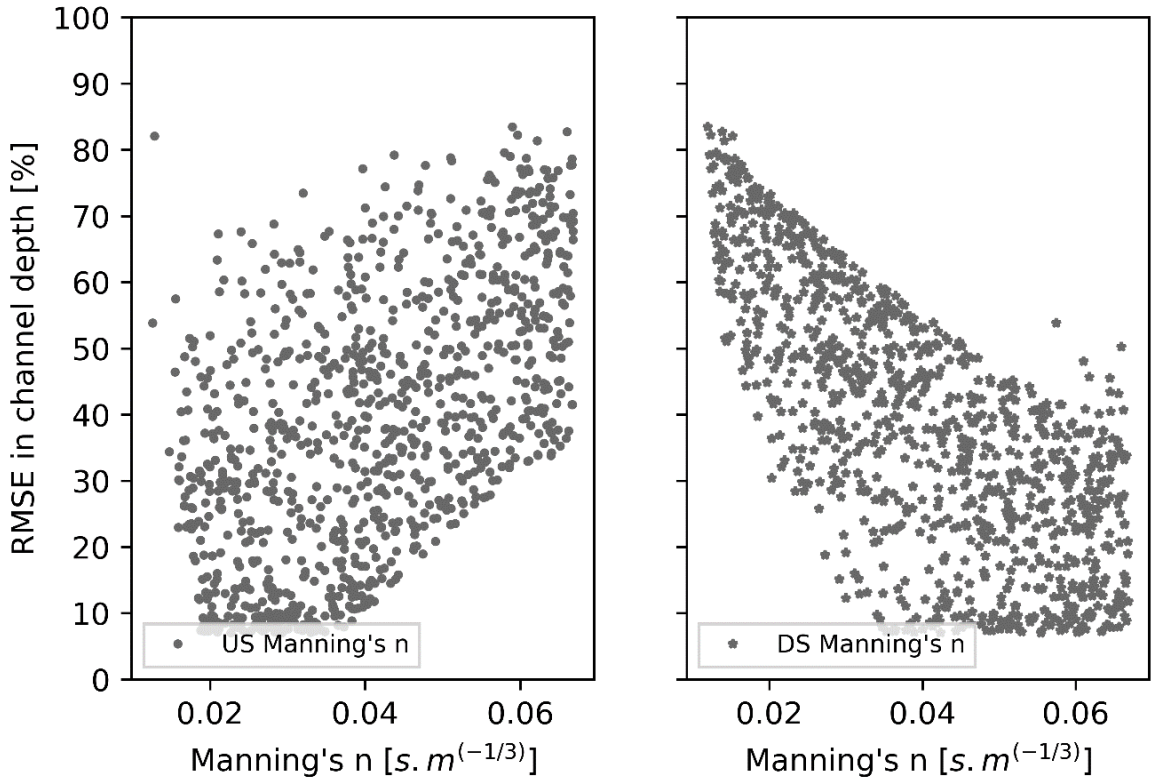

Figure 4.16: Change in root mean square error of river depth at downstream boundary with varying channel Manning's roughness coefficient. LHS) upstream to mid-stream and RHS) mid-stream to downstream.

In Figure 4.9 and LHS of 4.12, KGE increases with an increase of Manning's n value and then decreases after reaching an optimal point, which is similar to the result obtained by Pappenberger et al. (2005b). However, in the RHS of Figure 4.12, KGE increases with an increase in Manning's n value, showing the variability of Manning's n along the channel reach. Figure 4.16 shows the effect of channel Manning's roughness coefficient on the error in river depth at the downstream boundary. It can be seen that in the case of upstream-midstream river reach, the error in channel depth is increasing with the increase in Manning's roughness coefficient. However, in the case of the mid-stream to downstream river reach, the error in channel depth is decreasing with an increase in Manning's roughness coefficient. This result can be used to quantify the uncertainty in Manning's roughness on output channel depth in both the river reaches.

4.4 Common errors encountered

a)

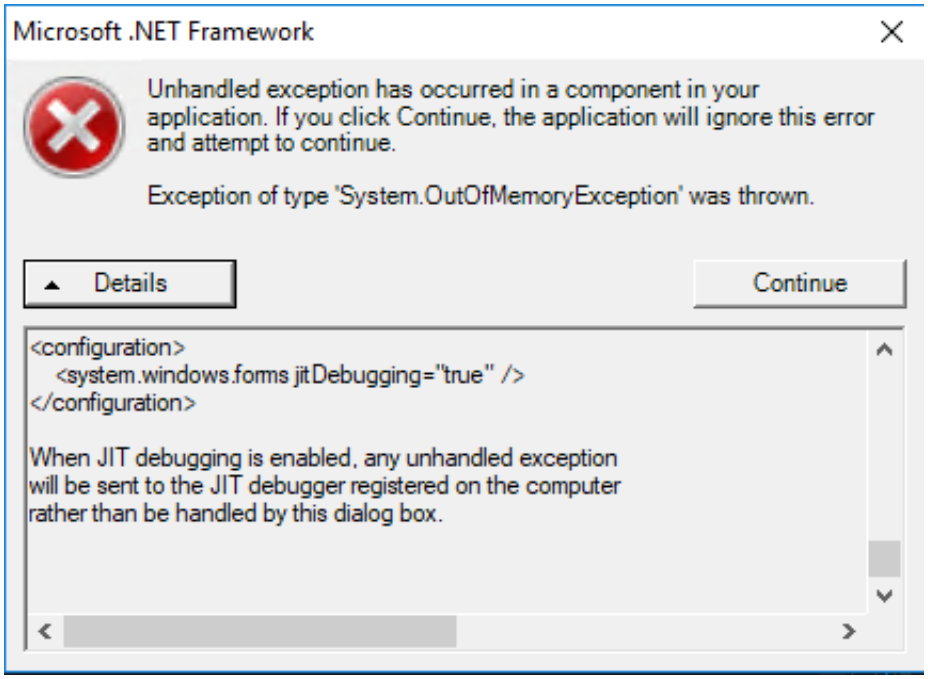

b)

```
number of stable runs= 708
===End of Backup Model=====
Traceback (most recent call last):

  File "<ipython-input-20-89111df594d9>", line 405, in <module>
    [TabWSE_MC[j,i], _, _, _, _, _, _] = hec.Output_NodeOutput(

  File "<COMObject RAS507.HECRASController>", line 3, in Output_NodeOutput

  File "C:\Users\ns4818\Anaconda3\lib\site-packages\win32com\client\dynamic.py", line 287, in _ApplyTypes_
    result = self._oleobj_.InvokeTypes(*(dispid, LCID, wFlags, retType, argTypes) + args)

com_error: (-2147024732, 'No more threads can be created in the system.', None, None)


In [21]:
```

Figure 4.17: Errors encountered while running Monte-Carlo simulations. a) System out of memory exception, and b) No more threads can be created in the system

Errors shown in Figure 4.17 (a) and (b) relate to excessive consumption of computational resources when HEC-RAS is run for a long duration during Monte-Carlo simulation (e.g., >10 days). Both errors can be overcome by deleting and initializing the dispatch in each loop as shown in Table 4.3. Furthermore, using .dss files to give upstream/downstream boundaries does not work with SI units. It is therefore necessary to use US customary units when working with .dss files.

Table 4.3: Script to overcome the errors shown in Figure 4.17

```
for loop:
hec = win32com.client.Dispatch ("RAS507.HECRASController")
'Body of code'
del hec
end of loop
```

4.5 Conclusions

This chapter describes Python scripts, along with examples, for implementing Monte Carlo simulations in HEC-RAS. Example 1 discusses the use of MC simulations to calibrate unsteady flow models. This example presents two cases of unsteady flow model calibration: 1) Manning's n is constant throughout the channel reach and 2) Manning's n varies in the reach. This example can be used to calibrate an ungauged river section and estimate river discharge using stage data alone. The approach demonstrated in Example 1 can also be used to calibrate steady flow models. The second example demonstrates how MC simulations can be used to analyse all plausible flood depth scenarios. Additionally, it demonstrates the handling of DSS files and their benefits, which were not included in previous studies. Example 2 can be extended to include error analysis to ascertain the effect of input parameter errors on model outputs. Finally, Example 3 demonstrates how to apply MC simulations to sensitivity and uncertainty analysis. Additionally, this chapter also includes a list of errors encountered during this study and the solutions adopted. It is worth noting that a complex model completed the MC simulations successfully in 37 days after the error was rectified.

MC simulations are especially advantageous when alternative approaches are difficult or impossible to implement, as they always work regardless of the model's complexity (Signoret & Leroy, 2021). With growing computational power and efficiency, this method is being increasingly used to solve difficult physical and mathematical problems. Using Python scripts to perform MC simulations in HEC-RAS opens new opportunities in river flow modelling, water management, river engineering, and flood risk management as both are open-source application programs and Python has a diverse range of functionality. The application of the Python script is not limited to the examples presented in this chapter. The scripts can be extended for additional purposes, such as sediment studies, probabilistic flood inundation mapping, optimization of hydraulic structures, etc.

5 Using a network of water level sensors for dynamic river discharge estimation

River discharge data is essential for river and water management strategies and for coping with water-related hazards such as floods. One of the most common methods for continuous automatic discharge measurement is based on water level observations, which are converted to discharge using a rating curve. However, obtaining and maintaining accurate rating curves is a major challenge, especially in rivers in which the relationship between water level and discharge is dynamic. This chapter addresses this issue by presenting a novel methodology for dynamic river discharge estimation using synchronous measurement of stage data from an array of sensors along a river reach. The proposed technique utilises only stage data from multiple sensors to calibrate unsteady flow parameters, in particular, Manning's roughness coefficient and initial flow, and estimate river discharge. The shallow water equations of river flow are solved in the full dynamic waveform for unsteady flow parameter calibration and dynamic discharge estimation. Here, I use the popular river flow analysis software HEC-RAS to obtain a unique solution to the shallow water equations. This methodology is then applied to several idealised rivers with various channel and flow conditions. The methodology was also tested on a kilometer-long stretch of the Wandle River in London, the United Kingdom. A sensitivity analysis was performed to evaluate the impact of measurement error in stage data on discharge estimation and the robustness of the developed methodology. The results indicate that the methodology can be applied to both prismatic and natural channels, as well as channels with the lateral flow, and can be used to develop rating curves at ungauged sites.

5.1 Introduction

The discharge of a river is the total volume of water flowing through a river channel at any given point. Various methods exist for the quantitative estimation of river discharge. As direct measurements of river discharge are impractical in most conditions, indirect methods are often used. One of the most accurate indirect methods is the velocity-area method, which involves multiplying the flow area of water in a river cross-section by the average velocity of water in that cross-section (Herschy, 2008). In this method, current meters are employed to determine the average velocity of water in a cross-section. Advanced equipment such as Acoustic Doppler Current Profilers (ADCP) and Acoustic Doppler Velocimeters (ADV), which are based on measuring the Doppler shift of the backscattered acoustic signal reflected by the solid particles moving within the stream flow, are being increasingly used to obtain the velocity profile of water in a cross-section (Morlock, 1996; Mueller, 2003; Kim, 2012; Shope et al., 2013). Both current meters and ADCPs should be in contact with the water surface to measure velocity. Therefore, using these poses safety concerns for operators when flow depth can vary significantly. Additionally, the measurement is manual and time-consuming; therefore, it is carried out only a limited number of times in a year, mostly during low flow conditions (Bonacci, 1983; Hauet, Creutin & Belleudy, 2008). In recent years, image-based methods such as large-scale particle image velocimetry (LSPIV), particle tracking velocimetry (PTV) (Tauro, Petroselli & Grimaldi, 2018) and radar-based methods such as surface velocity radars (SVRs) (Romeiser et al., 2007; Welber et al., 2016) are used for non-contact measurement of river velocity. In the image-based method, tracer particles are introduced into the river, and, for sufficiently small particles, it is assumed that the flow dynamics are valid. The water with suspended particles is illuminated in the images. The movement of the illuminated particles, using either an Eulerian or Lagrangian approach, in the subsequent images is used to estimate the surface velocity of the water (Tauro, Piscopia & Grimaldi, 2017). Radar sensors emit radio waves that are reflected by floating debris and received by the sensor. This information is used to measure the surface velocity. Both image and radar methods estimate the surface velocity and require additional processing and assumptions to determine the average velocity. Also, using the right tracers, lighting conditions, and image processing procedures is important for image-based methods to give accurate quantitative information (Fujita, Muste & Kruger, 1998; Jodeau et al., 2008). These constraints limit the application of the above approaches to niche users.

Because of the aforementioned limitations and challenges, continuous river discharge measurement using the velocity method is practically infeasible. Therefore, empirically developed stage-discharge relations (or Rating curves) are used to measure discharge at most gauging stations around the world (Spada et al., 2017b). However, using rating curves is fraught with difficulties, including:

- rating curves are mostly suitable for steady flows and unsteady flows that show kinematic behaviour - usually corresponds to rivers with steep bed slopes (>10^{-3}) (Dottori, Martina & Todini, 2009)
- rating curves need to be updated regularly due to changes in hydraulic resistance and channel geometry (Bakry, Gates & Khattab, 1992; Burguete et al., 2007),
- hysteresis or loop in the rating curve can cause an error in discharge estimation during unsteady flow because for the same river stage, discharge in the rising limb of the hydrograph is higher than that in the falling limb (Chow, 2006; Spada et al., 2017b),
- extrapolation error when estimating for low or high flows – error in discharge can reach up to 200% (Kiang et al., 2018).

Furthermore, because of the hysteresis effect during unsteady flow, peak discharge occurs before the peak stage. Therefore, if a hydrologic model is calibrated using discharge derived from the steady flow rating curves, then the time of peak discharge in the model will be wrong. Past studies have found that the delay in the time to peak for rivers with very mild slope (Dottori, Martina & Todini, 2009)Dottori, Martina & Todini, 2009).

To partially overcome the limitations of steady flow rating curves and estimate the unsteady flow discharge, recent studies (Aricò, Nasello & Tucciarelli, 2009; Aricò et al., 2011; Spada et al., 2017a; Harlan et al., 2021) have developed discharge estimation methods based on hydraulic routing or modelling. The hydraulic routing methods are based on the measurement of stage data from two water level sensors located at the ends of a selected river reach and the application of unsteady flow hydraulic modelling (solves governing equations or shallow water equations (SWE) of river flow). Most studies (for example, Birkhead & James, 1998; Franchini, Lambert & di Giammarco, 1999; Moramarco & Singh, 2001) have developed simple models to link stage data at downstream locations with discharge and rating curve data at the upstream river reach location. Birkhead & James (1998) method uses the classical Muskingum routing method to relate upstream flow to concurrent downstream stage hydrograph. The

authors assumed a one-to-one relationship between stage and discharge at a river location during unsteady flow; therefore, Moramarco & Singh (2001) concluded that this method was insufficient for unsteady flow discharge measurement. Franchini, Lambert & di Giammarco (1999) proposed an alternative technique for synthesising the rating curve at an ungauged site. The method employs a different formulation of the variable parameter Muskingum-Cunge method with a particular parameterization scheme to account for the space-time dynamics of the flood wave. Moramarco et al. (2005) noted that the estimation of nine parameters makes this method cumbersome to employ. Both the Birkhead & James (1998) and Franchini, Lambert & di Giammarco (1999) methods are of limited utility because they were developed based on a one-to-one relationship between stage and discharge and involve the estimation of numerous parameters using limited observed data. Dottori, Martina & Todini (2009) uses two gauged sections to estimate both the water depth and the water level gradient and to compute the corresponding discharge based on the assumption of zero local inertia. To apply this method, the distance between the sections must be large enough to permit accurate estimation of the water level gradient but short enough to assume negligible lateral inflows. Because of this and the requirement for an assumed Manning's roughness coefficient, this method is difficult to apply in the field.

More recently, Perumal et al. (2007), Aricò, Nasello & Tucciarelli (2009), and Aricò et al. (2010) developed and applied their flow routing algorithms to calibrate unknown Manning's roughness coefficient of the riverbed and estimate unsteady flow river discharge. Perumal et al. (2007) employ the variable parameter Muskingum stage hydrograph (VPMS) (Perumal, 1994a, 1994b) method to solve SWE and route an upstream stage to downstream locations. The VPMS method solves the diffusive form of SWE; that is, it includes the water depth gradient terms in the momentum equation but adopts a Muskingum numerical scheme. This results in the lack of a downstream boundary condition, which prevents the application of this methodology in the case of subcritical flow. Aricò, Nasello & Tucciarelli (2009), like Perumal et al. (2007), solve the SWE in diffusive form. However, it uses stage data from three water level sensors to calibrate Manning's roughness coefficient and estimate river discharge in the case of subcritical flow. Besides these studies, the discharge estimation from Dense Arrays of Pressure Transducers (DAPT) (Harlan et al., 2021) and Continuous Slope Area (CSA) (Lee, Firoozfar & Muste, 2017; Muste, Bacotiu & Thomas, 2019) methods have also been recently developed. Both these methods estimate reach-averaged discharge like Durand et al. (2014). The DAPT method uses a Bayesian discharge algorithm (Hagemann, Gleason & Durand, 2017)

developed for the upcoming Surface Water Ocean Topography satellite (SWOT) to estimate discharge, whereas the CSA method uses a modified form of the traditional slope area (Smith, Cordova & Wiele, 2010) approach. Both the DAPT and the CSA methods solve SWE in restricted form and require discharge values to estimate Manning's roughness coefficient. In addition, the authors reported that the CSA method underestimates the peak discharge by 30–40% and concluded that further research is required before its application in the field.

All of the above-mentioned methods (a) solve SWE in conservative form, (b) are most suitable for prismatic channels with no lateral flow thus reducing the possibilities for operational applications, (c) require one flow value, and (d) assume Manning's roughness or calibrate it by using observed stage data from two or three gauging locations. Although stage data from two or three gauging locations are theoretically sufficient to calibrate Manning's roughness, in practice error margins are still high due to the sub-optimal positioning of gauging stations or sensors, and the coarse temporal resolution of existing measurement networks.

Therefore, this study hypothesises that a larger network of high-frequency water level sensors allows for (1) better calibration of hydraulic parameters and 2) estimating unsteady flow discharge dynamically.

I tested this hypothesis using a network of more than 3 water level sensors operating at a one-minute and five-minutes frequency. The stage data from this network is used to constrain the unsteady flow hydraulic model set up in HEC-RAS and to extract the rating curve from the model simulations. This configuration is then applied to both an idealised river simulation and a real-world case study on the Wandle River in South London. For both case studies, I implement a sensitivity analysis to determine the relative impact of the observations and the hydraulic model on unsteady flow parameter calibration and discharge estimation. For the Wandle River, the results are also compared to the operational rating curve obtained by the Environment Agency of England and Wales.

5.2 Methodology

5.2.1 Hydraulic modelling approach

Our discharge estimation approach is based on a hydraulic model simulation of the river reach of interest using shallow water equations, which is constrained using data from the array of water level sensors. This involves two steps. First, the hydraulic model parameters of unsteady river flow are calibrated, and then the calibrated model is used to estimate the unsteady flow discharge dynamically.

In contrast to previous research (Aricò, Nasello & Tucciarelli, 2009; Perumal et al., 2010; Sahoo et al., 2014; Barbetta, Moramarco & Perumal, 2017), I did not develop a numerical scheme to solve SWE but instead used the existing river flow analysis software HEC-RAS (Hydrologic Engineering Centre – River Analysis System) as an SWE solver. HEC-RAS (Brunner et al., 2016) is a widely used river flow modelling software that has the following advantages:

- it solves the SWE in full form
- it can be used to model both prismatic and natural channels,
- it provides functionality to incorporate river reach with lateral flow and
- users can access additional functionality such as steady flow discharge estimation, flood inundation modelling or others as required.

A hydraulic model of unsteady flow in the HEC-RAS has two main parameters that need to be calibrated: a) Manning's roughness coefficient and b) initial flow of the model. Here, I implement a Monte Carlo method (Fryer & Rubinstein, 1983; Babister et al., 2016) (refer to section 2.6 for further details). A Python script has been developed to implement the Monte Carlo method for calibrating hydraulic model parameters and controlling and automating HEC-RAS simulations (refer to chapter 4).

5.2.2 Sensor setup

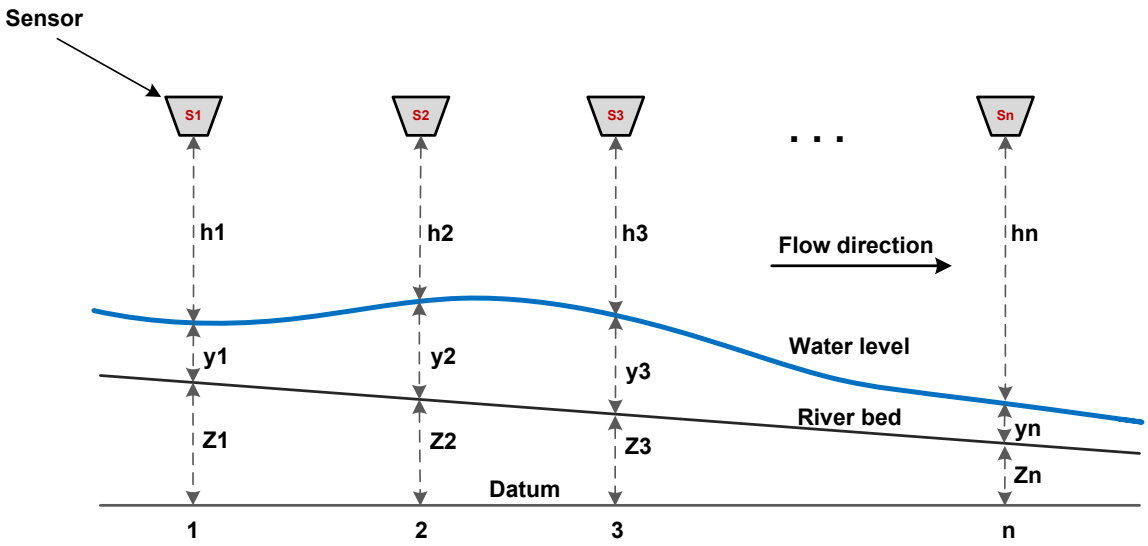

Figure 5.1: Schematic of a sensor network along a river reach

This method estimates the unsteady flow discharge at an ungauged location of a river using only river stage data from a network of sensors (refer to Figure 5.1). To estimate the unsteady flow discharge, the governing equations of river flow (or SWE) are solved in full form, i.e., including all the terms in the momentum equation 2.2. To solve the SWE using only stage data, channel geometry, Manning's roughness coefficient, initial condition (or discharge at t=0), and boundary conditions at the two ends (upstream and downstream) of a river reach are required. Therefore, first, an unsteady flow hydraulic model of a river reach (as seen in Figure 5.1) is set up in HEC-RAS. For setting up the model, the channel geometry of the river is required. In this study, channel geometry is either assumed to be prismatic or extracted from a high-resolution digital elevation model (DEM) of the river or a bathymetry survey of the channel. Stage hydrograph data is used as the upstream boundary condition, and normal depth (or average bed slope at the downstream boundary) is used as the downstream boundary condition.

Now unknown is the initial condition, Manning's roughness coefficient, and river discharge at all the nodes of the hydraulic model. Since there are too many unknowns for a unique solution to the SWE, a two-step procedure has been adopted to solve the SWE and estimate the river discharge. In the first step, the initial condition and Manning's coefficient of the channel are calibrated by employing the Monte Carlo method and using known river stage data from a network of sensors (such as Figure 5.1). Then, in the second step, the calibrated initial condition and Manning's roughness coefficient are used to estimate the river discharge dynamically.

5.2.3 Model calibration

The Monte Carlo method is used for the calibration of Manning's roughness and initial condition (or initial flow) (refer Figure 5.2). To implement the Monte Carlo method, at least one set of concurrent stage data should be available at the upstream (e.g., at location 1 in Figure 5.1) and the downstream (e.g., any location from 2 to n in Figure 5.1) of the ungauged river location. Here, it is assumed that the stage data is available from the sensor network. The observed upstream stage is routed with different sets of randomly sampled Manning's coefficient (upper and lower bounds of the sample set are based on Manning's coefficient table available for different channels and vegetation types (Chow, 2006)) and initial conditions to the downstream location. The routed stage at the downstream and other sensor locations is then compared with the observed stage at those locations by using the performance measures described in section 5.2.4.

The MC method requires a large number of simulations (for instance, 1000, 5000 or more) depending on the number of calibration parameters and statistical distribution of the parameters. However, HEC-RAS allows only a 'one-click-one-run option' to run a hydraulic model (Goodell, 2014). Therefore, in this study, a Python application was developed to control and automate HEC-RAS simulations. The developed Python application is discussed in detail with examples in chapter 4.

Furthermore, it should be noted that in almost all of the previous studies, for example, Perumal & Ranga Raju (2007); Perumal et al. (2007b), (2010); Dottori, Martina & Todini (2009); Sahoo et al. (2014); Barbetta, Moramarco & Perumal (2017), to the best of my knowledge, the initial flow is assumed and not calibrated. In this method, both initial flow and Manning's roughness coefficient are calibrated by using observed river stage data from more than three locations. Additionally, when required, the hydraulic model can be re-calibrated with stage data from a network of low-cost, non-contact sensors described and discussed in chapter 3.

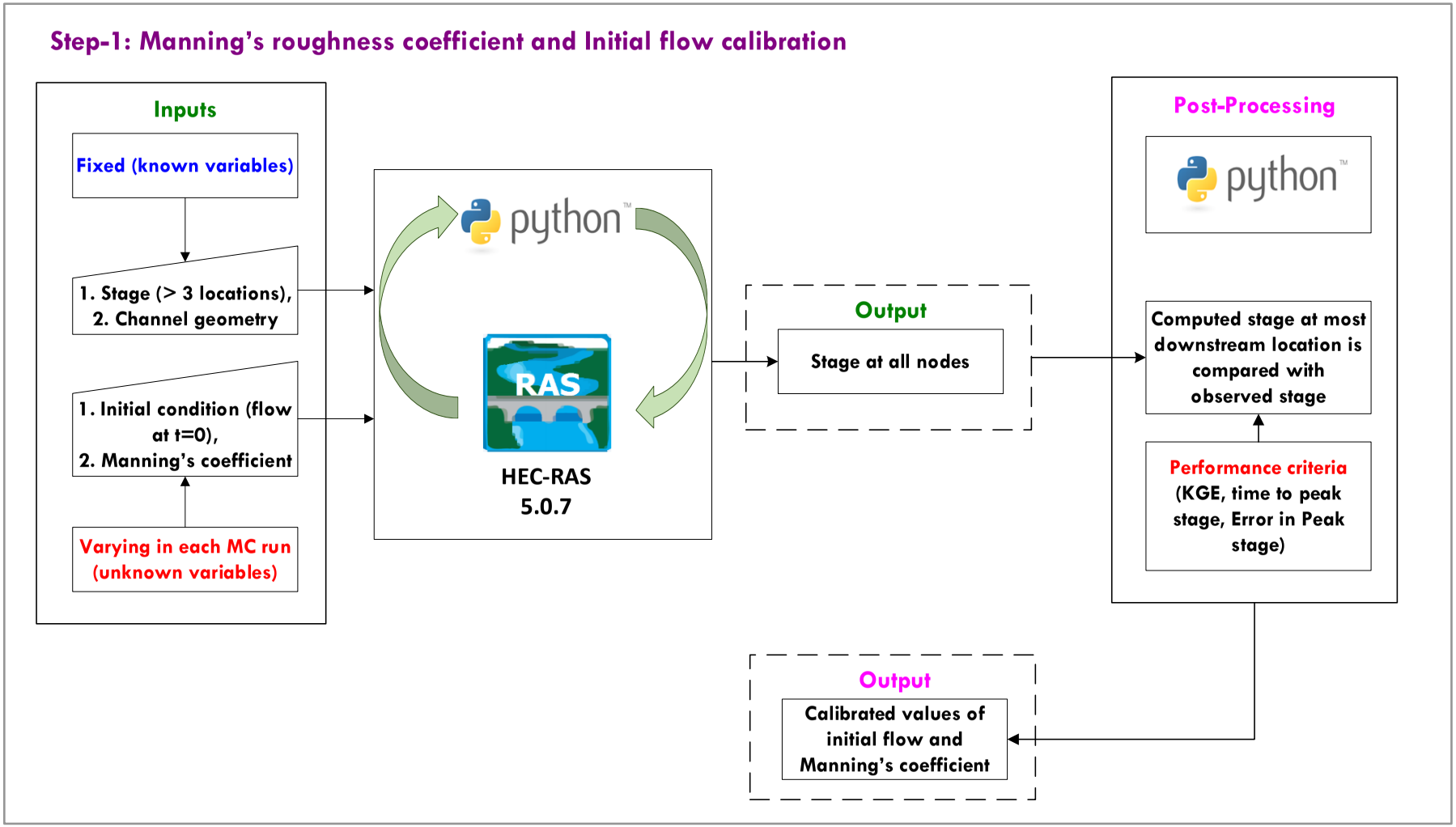

Figure 5.2: Flow chart for initial flow and Manning' s coefficient calibration

5.2.4 Model evaluation

The performance of the proposed approach was evaluated based on the following performance criteria that assess the quality of the match between the observed and simulated stage and discharge hydrographs (Aricò, Nasello & Tucciarelli, 2009; Perumal et al., 2007a; WMO, 2011):

$$Modified\ Kling-Gupta\ Efficiency\ (KGE) = 1 - \sqrt{(r-1)^2 + (\beta-1)^2 + (\gamma-1)^2} \tag{5.1}$$

$$r\ (correlation\ coefficient) = \frac{cov\ (Z_i^s,\ Z_i^o)}{\sigma\ (Z_i^s) *\ \sigma\ (Z_i^o)}$$

$$\beta\ (Bias\ ratio) = \frac{\mu\ (Z_i^s)}{\mu\ (Z_i^o)}$$

$$\gamma\ (Variability\ ratio) = \frac{CV\ (Z_i^s)}{CV\ (Z_i^o)} = \left(\frac{\sigma\ (Z_i^s)}{\mu\ (Z_i^s)}\right) \Big/ \left(\frac{\sigma\ (Z_i^o)}{\mu\ (Z_i^o)}\right)$$

$$Error\ in\ Z_p\ [\%] = \frac{Z_{max}^s - Z_{max}^o}{Z_{max}^o} * 100 \tag{5.2}$$

$$Error\ in\ T_p\ [min] = t_{max}^s - t_{max}^o \tag{5.3}$$

$$Root\ mean\ square\ error: RMSE = \sqrt{\frac{\sum_{i=1}^{N}(Q_i^s - Q_i^o)^2}{N}} \tag{5.4}$$

where, Z^s is the simulated stage, Z^o is the observed stage, Z_{max} is peak stage, t_{max}^s and t_{max}^o is time (in minutes) at which the simulated and observed peak reaches the gauging station, μ, σ is mean and standard deviation, cov is covariance, and CV is coefficient of variation.

i is the time step in hydrographs, N is the total number of time steps, Q_i^o is observed discharge at the i^{th} time step and Q_i^s is simulated discharge at the i^{th} time step.

The modified KGE is used as a performance measure for parameter calibration because it provides an optimal solution that is simultaneously good for bias, variability, and correlation (Knoben, Freer & Woods, 2019).

Manning's roughness and initial flow which provide the most optimal performance are chosen as the calibrated parameters of the hydraulic model. It should be noted that Manning's roughness coefficient can be assumed as homogenous throughout the reach or heterogenous, depending on the river reach characteristics.

5.2.5 Dynamic discharge estimation

Once the hydraulic model is calibrated, it can be used to estimate river discharge dynamically, as shown in Figure 5.3, avoiding the need for rating curve development. The developed method is verified with different idealised river channels and field testing.

It should be noted that, in case of the presence of lateral flow in the river, additional sensors can be installed on this reach and lateral flow can be estimated in the same way as described above. Additionally, using HEC-RAS makes it easier to include the lateral flow in the main channel.

The unsteady flow discharge estimation developed in this study was not compared with other methods because 1) past methods solved SWE in restricted or conservative form, 2) most past methods did not calibrate initial flow, 3) they were used to estimate flow in a prismatic channel only, and 4) there was a lack of availability of a developed numerical scheme to solve SWE.

The focus of this chapter was to develop a method to estimate discharge by using only stage data. Therefore, in the test applications shown in this chapter, the locations and spacings between the sensors are kept random. A methodology for the optimisation of sensor networks is discussed in detail in chapter 6.

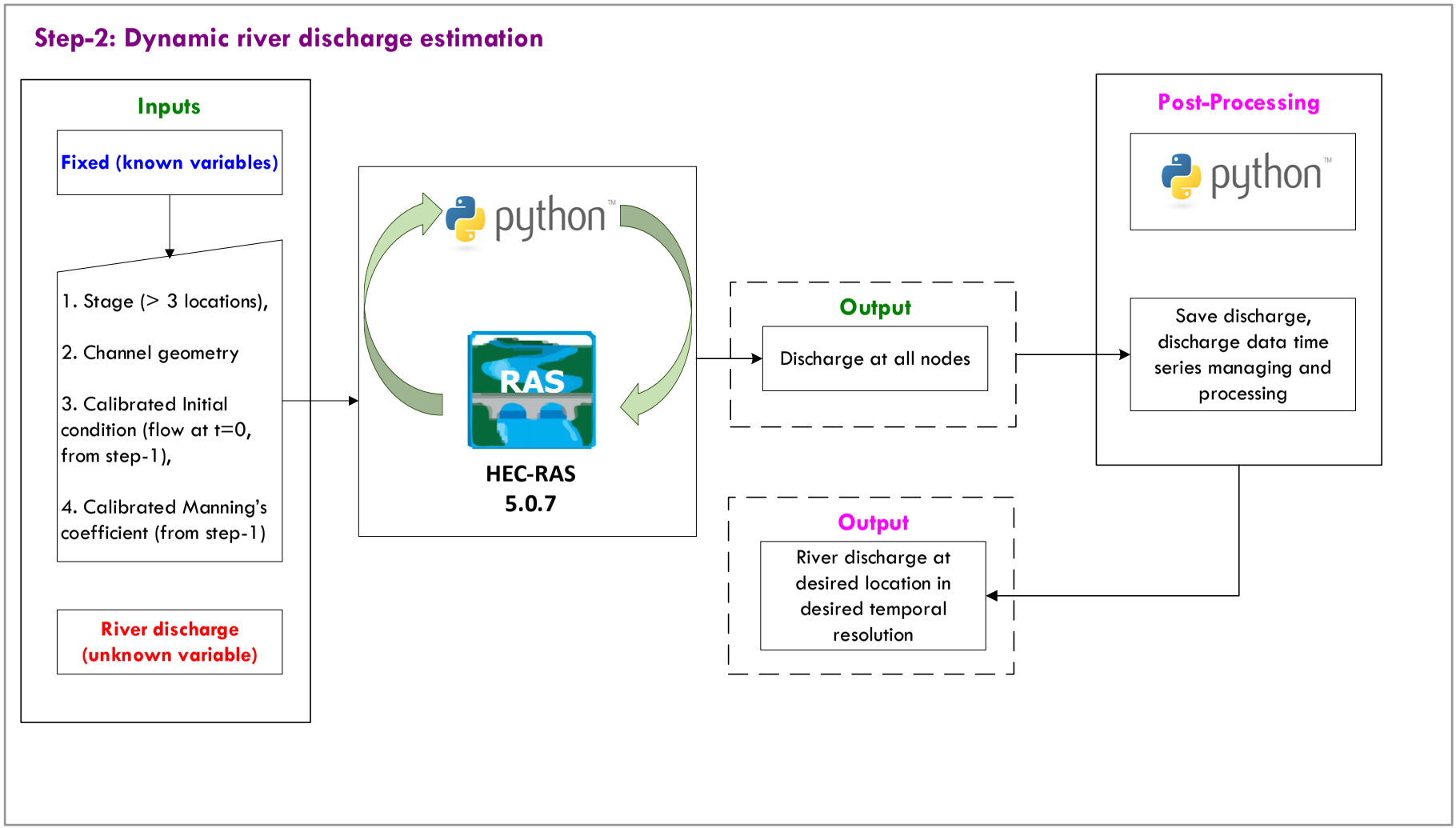

Figure 5.3: Flow chart for river discharge estimation.

5.3 Sensitivity analysis

In natural rivers, the water level data acquired by sensors is often affected by measurement error due to poor instrument accuracy, regional oscillation, wind, etc. Therefore, to determine the effects of the stage data error on the calibration of the model parameters and discharge estimation, a sensitivity analysis was performed. To determine the impact of the error, the following approach was used:

i. A randomly sampled measurement error was added to the upstream and downstream stage data. The measurement errors are assumed to be independent and normally distributed with a mean of μ and a standard deviation of σ respectively. Therefore,

$$Y_{US}{}' = Y_{US} + \varepsilon \sim N(\mu, \sigma) \text{ and } Y_{DS}{}' = Y_{DS} + \varepsilon \sim N(\mu, \sigma)$$

where, Y_{US} , Y_{DS} are observed stage at upstream and downstream locations and

$Y_{US}{}'$, $Y_{DS}{}'$ are upstream and downstream stages with errors.

ii. An unsteady flow hydraulic model with the new stage data, i.e., $Y_{US}{}'$ as an upstream boundary condition was set up in HEC-RAS

iii. This hydraulic model was then calibrated by employing the Monte Carlo method discussed in section 5.2.3. The only difference is that the routed/simulated stage at downstream was compared with the new downstream stage, i.e., $Y_{DS}{}'$ by using performance measures discussed in section 5.2.4. A similar analysis was performed for errors with different means and standard deviations

iv. Once, the model was calibrated, unsteady flow river discharge was estimated at the downstream boundary of the hydraulic model river reach

The method was tested on Case 3 of the idealised river channel. The root mean square error (RMSE) for computed and observed discharge was calculated and the results were analysed.

5.4 Application

5.4.1 Idealised rivers

The developed methodology was tested by calibrating idealised rivers having different channel and flow characteristics as outlined in Table 5.1. Various types of bed slopes and flow values have been employed to represent different flow conditions in the natural channel. The bed slopes values used for idealised rivers range from 10^{-3} (steep-slope) to 2.5×10^{-5} (very mild slope), including the intermediate values of 5×10^{-4}, 2×10^{-4}, $10^{-4,}$ and 5×10^{-5}.

Table 5.1: Channel and flow types for different cases of idealised rivers (Dottori, Martina & Todini, 2009)

	Cross section geometry (w = width; d = depth)	**Bed slope (S_0)**	**Time to peak (T_p)**	**Peak discharge [Q_p]**
Case 1	Rectangular (w = 50 m, d = 10 m)	10^{-4}	24 h	900
Case 2	Rectangular (w = 50 m, d = 10 m)	10^{-3}	24 h	900
Case 3	Rectangular (w = 50 m, d = 10 m)	10^{-4}	72 h	900
Case 4	Rectangular (w = 50 m, d = 10 m)	2×10^{-4}	24 h	900
Case 5	Rectangular (w = 50 m, d = 10 m)	2×10^{-4}	72 h	900
Case 6	Rectangular (w = 50 m, d = 10 m)	5×10^{-4}	24 h	900
Case 7	Rectangular (w = 400 m, d = 40 m)	5×10^{-5}	168 h	10000
Case 8	Rectangular (w = 400 m, d = 40 m)	2.5×10^{-5}	168 h	10000
Case 9	Variable (channel changes from rectangular to trapezoidal)	10^{-4}	24 h	900

Idealised rivers are simple prismatic models with a channel length of 10 km and various widths as described in Table 5.1. While setting up the hydraulic model in the HEC-RAS, depending upon the width of the rivers, the depths of the rivers are assumed to be 10 and 40 m. The river reach is assumed to have a constant bed slope (S_0). A stage hydrograph was used as an upstream boundary in all the test simulations. The stage hydrographs, as would be obtained from a sensors network, were simulated by running a reference hydraulic model with a known

discharge hydrograph and other model parameters such as initial flow and Manning's roughness coefficient in HEC-RAS. The stage and discharge hydrographs obtained at different locations of the reference model were considered as 'True or Observed hydrographs'.

The following relationship was used to obtain the discharge hydrograph for the reference model (Dottori, Martina & Todini, 2009):

$$Q\ (t) = \ Q_b + (Q_p - \ Q_b)\left[\frac{t}{T_p} exp\left(1 - \frac{t}{T_p}\right)\right]^{\gamma} \tag{5.5}$$

where, Q_b = base flow, Q_p = peak flow, T_p = time to peak, t = time instances and γ = coefficient = 16. For all idealised rivers, Q_b was set to 100 m^3/s, and t was set to 5 minutes. For reference model n was assumed as 0.035 and base flow was assumed as 100 m^3/s. For idealised rivers, the initial flow and base flow are the same as the model was assumed to be dry.

For simulating various stage hydrographs, three types of waves are used: a fast wave with a rising time of 24 hr and a peak discharge of 900 m^3/s, a medium wave with a rising time of 72 hr and a peak discharge of 900 m^3/s and a slow wave with a rising time of 168 hr and a peak discharge of 10,000 m^3/s. They were selected in accordance with previous studies (Lamberti & Pilati, 1990; Dottori, Martina & Todini, 2009). Additionally, the selected parameters conform to the real river; for example, the river Karnali at Chisapani, Nepal, has a width of about 250 m, a depth of about 10 m, and its peak discharge ranges between 5000 and 12000 m^3/s (Aryal et al., 2020).

For all cases of idealised rivers, the stage hydrograph was used as an upstream boundary condition in the hydraulic model. Normal depth, a Manning's equation approximation which needs an initial guess of the friction slope (average riverbed slope applied), was used as the downstream boundary condition. The simulation time was set at 60 seconds following Courant's condition to satisfy the stability and accuracy of the model (Brunner, 2016b).

5.4.2 Field case study

The developed method was tested on a 1012 m long reach of the river Wandle in Wimbledon, London, UK. This river reach was selected due to the presence of existing Environment Agency hydrometric stations (Environment Agency, 2021) at both ends of the reach, as shown in Figure

5.4. Additionally, although HEC-RAS can model hydraulic structures such as bridges and weirs, this river reach was relatively straight, and the bridges present were not considered in the model as they did not constrict the flow. However, under higher flow conditions, they would need to be included in the modelling. Four bespoke, low-cost sensors, named as 204, 205, 206 and 207 (refer to Figure 5.4), were installed along the river reach to measure the water level at one-minute intervals. These sensor locations were chosen as they were accessible for sensor installation. However, I intended to install more sensors towards the downstream end of the reach (reasoning for this is discussed in detail in chapter 6).

The channel geometry and riverbed slope for setting up an unsteady flow hydraulic model were obtained by conducting a bathymetry survey of the river. The average bed slope of the river reach was obtained as 0.00398 and the bed slope at the downstream boundary, to use it as a normal depth boundary condition, was obtained as 0.0015. The upstream and downstream cross-sections of the river reach are shown in Figure 5.6.

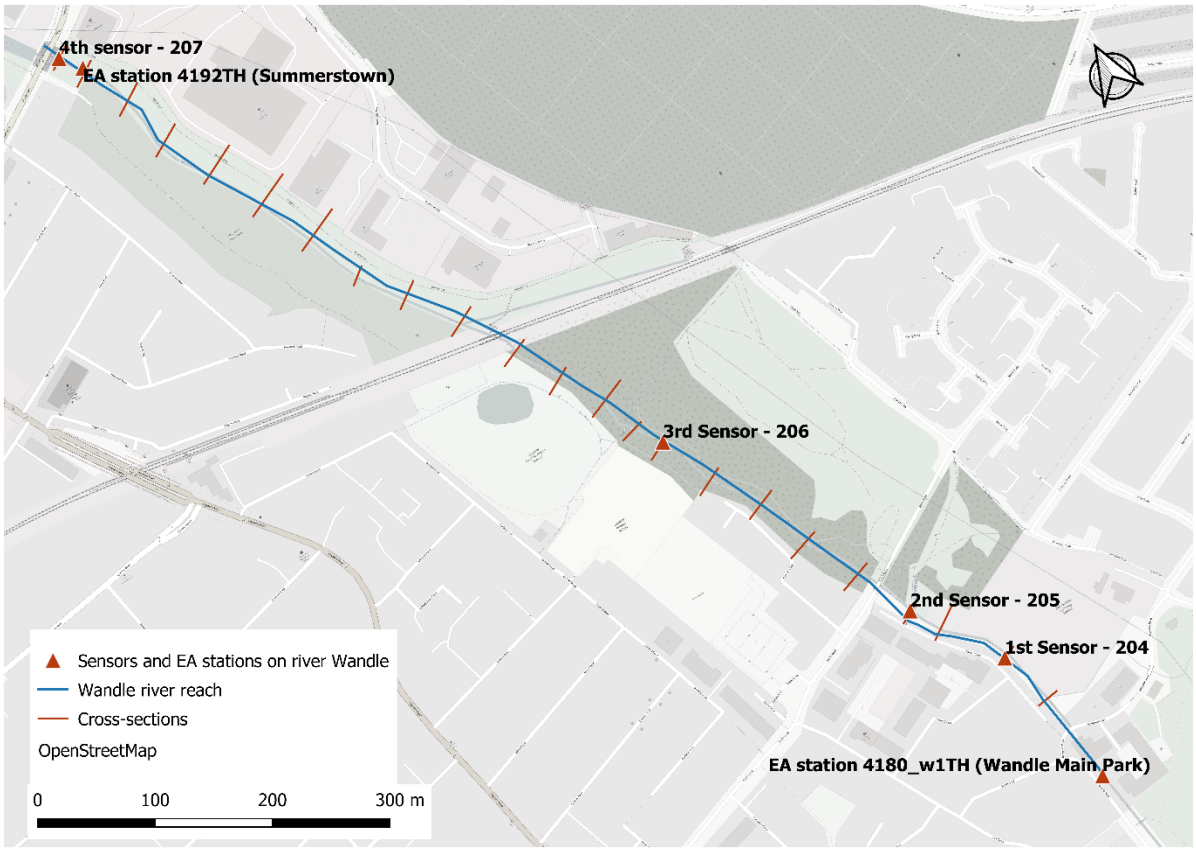

Figure 5.4: River Wandle reach selected for field testing of the method

The water level data obtained from the sensor is the distance between the water surface and the sensor receiver/emitter surface (i.e., h1 as shown in Figure 5.1). This water level data was converted to the stage (Z1 + y1) by referencing river depths (y1 as shown in Figure 5.1) to an ordnance survey (OS) datum (Ordnance Survey, 2021). In this study, the datum of the nearest OS was transferred to the sensor and channel cross-section locations by conducting a benchmark transfer survey. The detail of river Wandle model is provided in Table 5.2 and details of observed data is provided in Table 5.3. The locations of sensors and EA stations with their identifiers and stage datum are listed in Table 5.4.

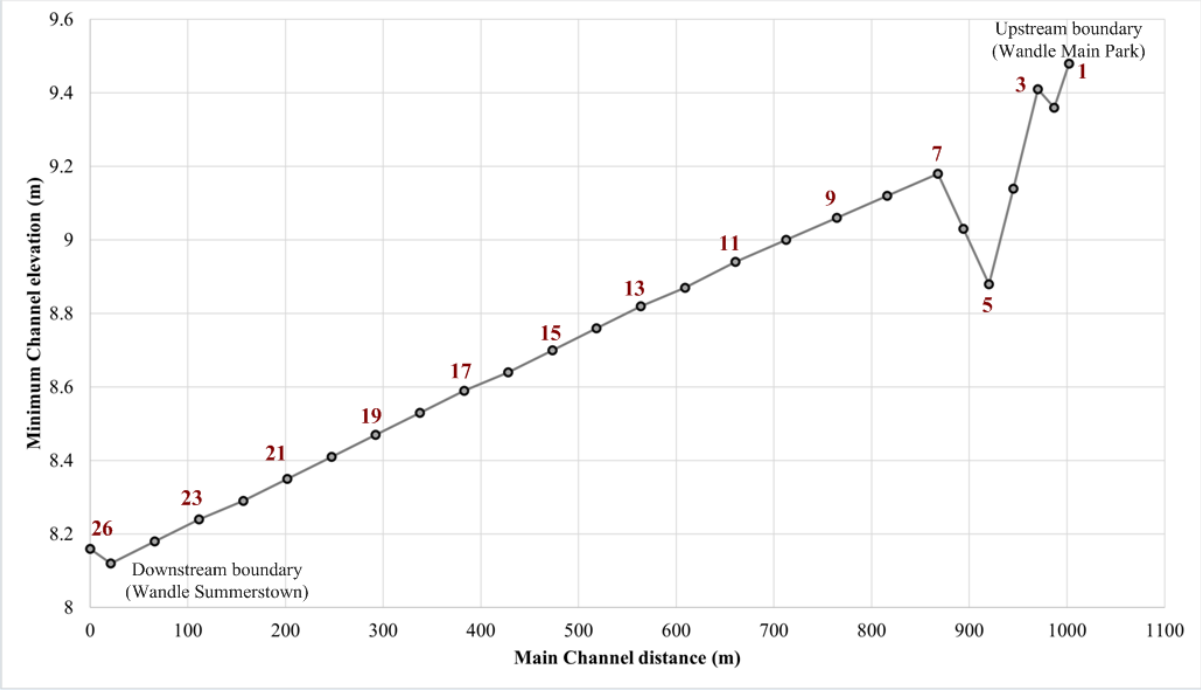

Figure 5.5: Profile plot of river Wandle model. Black circle represents cross-section locations

Table 5.2: Detail of River Wandle unsteady flow model inputs

Model inputs	Descriptions
River reach length	1012 m
River Wandle Geometry (cross-sections and riverbed slope)	Obtained from Bathymetry survey (discussed in Section 5.2) and 1m resolution lidar digital elevation model (Environment Agency, 2021b)
Number of cross-sections	26, including upstream and downstream boundaries

Model inputs	Descriptions
Upstream boundary	Stage hydrograph from sensor 204 (refer to Figure 5.5)
Downstream boundary	Normal depth, average bed slope at the downstream boundary obtained from Bathymetry survey, 0.0015
Manning's roughness coefficient $\left(\mathbf{s.m^{-1/3}}\right)$	Randomly selected from a uniform distribution n$\sim U[0.02, 0.08]$. Above values for n were chosen because river Wandle was straight, but with more stones and weeds. It also has deep pools as can be seen from Figure 5.5 (Chow, 2006)
Initial flow (m^3/s)	Randomly selected from a uniform distribution $Q_i \sim U[1.42, 2.27]$
Simulation time (seconds)	30, as per Courant's stability criteria (Brunner, 2016a)

Table 5.3: Observed data available at upstream and downstream boundaries of river Wandle unsteady flow model

Observed data	Descriptions
Rating curve at the upstream boundary	The rating curve for WPM station was obtained from the Environment Agency
Observed stage at the downstream boundary	Stage hydrograph from Summerstown station (Environment Agency, 2021c)
Observed discharge at the downstream boundary	It was assumed that discharge at upstream (i.e., WPM) is equal to the discharge at downstream
True/ observed initial flow (m^3/s)	1.75 from the rating curve at WPM station

Table 5.4: Summary of EA Gauging stations and sensor installations. mASD (meters above stage datum), is the elevation of the river zero flow point above the UK Ordnance Datum.

Station name (ID)	mASD (mAOD)	Coordinates	
		Latitude (°)	Longitude (°)
Wandle Park Main Channel* (ID: 4180_w1TH)	10.16	51.419659	-0.18127
Upstream sensor (US) – 1 (ID: 204)	9.383	51.4208	-0.18161
Upstream sensor (US) – 2 (ID: 205)	9.193	51.42145	-0.18234
Midstream sensor (MS) – 3 (ID: 206)	8.874	51.42364	-0.18361
Downstream sensor (DS) – 4 (ID: 207)	8.182	51.42841	-0.18768
Summerstown** (ID: 4192TH)	8.0	51.428571	-0.187677

* https://environment.data.gov.uk/flood-monitoring/id/stations/4180_w1TH.html
**https://environment.data.gov.uk/flood-monitoring/id/stations/4192TH.html

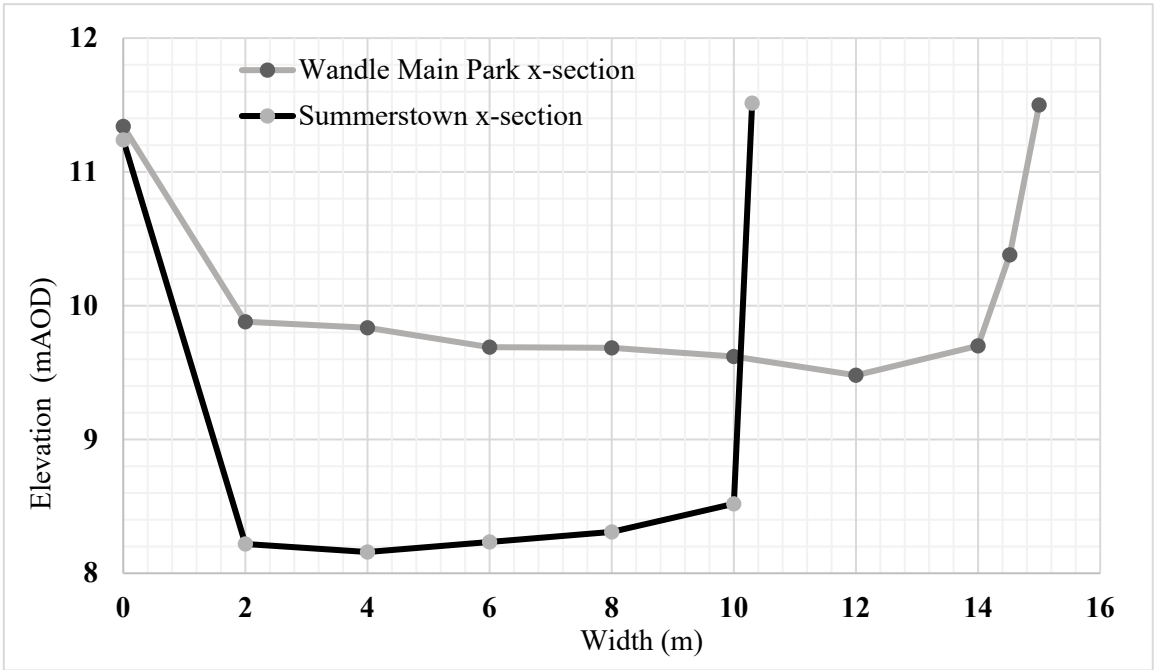

Figure 5.6: Upstream and downstream river Wandle cross-section used for hydraulic modelling. Cross-sections obtained from bathymetry survey

Photos of the bathymetry survey, datum transfer, and sensor installations are shown in Figure 5.7.

Figure 5.7: Field testing on river Wandle, London, UK. (a) Benchmark transfer using a level (b) Bathymetry survey for determining river profile and cross-sections (c) sensor installed at Wandle Main Park (upstream boundary) and (d) sensor installed at Wandle Summerstown (downstream boundary)

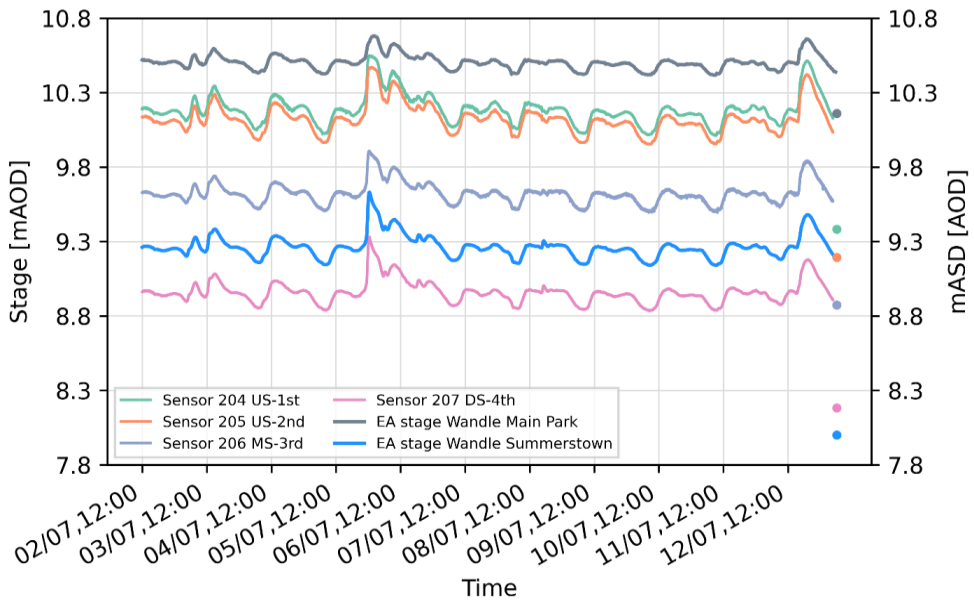

Figure 5.8: River Wandle stage (measured at one-minute frequency) from the four sensors installed on the river reach and the Environment Agency (named EA in the legend). The dots indicate the elevation of the zero-flow point above the Ordnance Datum (mASD).

An unsteady flow hydraulic model was set up on this river reach. It is assumed that the river reach has a homogenous Manning's roughness coefficient. The Manning's coefficient and initial flow of the river reach were calibrated by employing the Monte Carlo method and using stage data from the sensors (as shown in Figure 5.8). Two cases of calibration were carried out; 1) with two sensors (sensor at 204 and 207) and 2) with three sensors (sensors at 204, 206 and 207)

Stage hydrograph data for a flood event of July 4-8, 2021, was used to calibrate the model and also compare the observed and estimated discharge at the downstream location (i.e., sensor 207). Among the two EA stations, only the Wandle Park Main Channel (WPM) station has a rating curve (Environment Agency, 2021a; National River Flow Archive, 2021). Therefore, since the reach was small and there was no lateral inflow or outflow from the reach, it was assumed that the discharge at the downstream, that is at the sensor 207 location, was the same as the discharge at the upstream, that is at WPM.

5.5 Results and discussions

The developed methodology was tested on a set of idealised rivers and one real river (the river Wandle in London). Idealised rivers are rivers with a prismatic channel geometry and a constant bed slope. It is assumed that all the idealised rivers have a known Manning's roughness coefficient of 0.035 $\mathrm{s.m^{-1/3}}$ and an initial flow of 100 $\mathrm{m^3/s}$. The river reach considered for modelling is assumed to be straight, without any hydraulic structures such as bridges, and has a constant Manning's n throughout the reach. The stage/flow hydrograph used as an upstream boundary condition for calibrating these rivers is simulated using equation 4.5. Normal depth is used as the downstream boundary condition.

River Wandle is a natural river; however, it is in the city of London and has bridges, weirs, and an embankment wall throughout its reach. A straight reach without considering hydraulic structure is considered suitable for applying the developed discharge estimation method. The stage hydrograph obtained from the sensor is used as the upstream boundary condition, and the normal depth obtained from the bathymetry survey (or from DEM) is used as the downstream boundary condition. The range of Manning's n and initial flow required for running the Python script is selected from Manning's n for channels as provided in Chow (2006) and an estimate of river initial flow at the time of sensor installation, respectively. For the river Wandle, I used the float method to estimate the initial flow of the river.

Example 1, presented in Section 4.3.2, describes the modelling procedure, and demonstrates the application of the developed method in an idealised and real-world river case.

5.5.1 Idealised rivers

Table 5.5 presents the model calibration results with performance measures for all the idealised rivers. It can be seen that the KGE for all the idealised rivers, despite of varied morphology and flow condition, is 99.99%, which indicates that it is possible to simulate the stage hydrograph at the downstream location using the Monte Carlo method. Furthermore, except for case 5, the error in calibration of Manning's roughness coefficient is below 5 %. The increased error in Manning's roughness coefficient in case 5 may be due insufficient parameter sampling during the Monte Carlo simulation as other rivers of larger size and milder slopes are performing as expected. Additionally, the error in the peak stage and the error in the estimation of initial flow calibration are also below 10 %. Except for Case 5, the error in the time to peak

stage is zero. This means that the time of arrival of the peak stage at the downstream location in the simulated stage hydrograph is the same as that of the reference model. Furthermore, the Froude number, shown in Table 5.6, for calibrated parameters for different models shows that the modelled flow is subcritical at the downstream of the models. This is expected as Normal depth is used as the downstream boundary in all the model simulation. It can also be seen that the Froude number for steep river is higher than that of milder rivers. This is because steep rivers such as case 2 has higher average velocity at the downstream boundary cross-section. These results are consistent with past studies as the previously developed methods have performed well in prismatic channels.

However, past studies' assumptions and lack of availability of developed numerical schemes to solve SWE make them difficult to use. For example, to develop a rating curve at an ungauged location, Perumal et al. (2007a) assume that there is a one-to-one relationship between the estimated stage at an ungauged site and the steady discharge that occurs downstream of that location. Here, the location of the steady discharge has not been quantified.

Table 5.5: Summary of performance criteria and results of parameter calibration from idealised rivers

Cases	KGE [%]	Manning's n [s/m$^{(1/3)}$]	Estimated Initial flow (Q_i) [m^3/s]	Error in Time to peak (T_p) [min]	Error in peak stage (Z_p) [%]	Error in estimation of Initial flow (ε_{Q_i}) [%]	Error in estimation of n (ε_n) [%]
Case 1	99.99	0.0359	103.88	0	-0.42	3.88	2.57
Case 2	99.99	0.0357	102.53	0	0	2.53	2.00
Case 3	99.99	0.0358	113.58	0	0	13.58	2.29
Case 4	99.99	0.0357	115	0	0	15	2.00
Case 5	99.99	0.0376	94.13	5	-5.19	-5.87	7.43
Case 6	99.99	0.0358	96.42	0	0	-3.58	2.29
Case 7	99.99	0.0356	102.73	0	0.053	2.73	1.71
Case 8	99.99	0.0362	99.85	0	-1.23	-0.15	3.43
Case 9	99.99	0.0358	99.09	0	-0.42	-0.91	2.29

Table 5.6: Summary of hydraulic details for calibrated Manning's n and initial flow at the downstream boundary of the model

For calibrated Manning's n and initial flow at Downstream boundary								
Cases	**Hydraulic depth (Y [m])**		**Discharge (Q [m^3/s])**		**Average Velocity (V [m/s])**		**Froude No. (Fr)**	
	Y_min	**Y_max**	**Q_min**	**Q_max**	**V_min**	**V_max**	**Fr_min**	**Fr_max**
Case 1	2.67	10.99	99.60	880.88	0.75	1.60	0.15	0.15
Case 2	1.31	5.17	100.01	899.29	1.53	3.48	0.43	0.49
Case 3	2.67	11.11	100.01	898.33	0.75	1.62	0.15	0.15
Case 4	2.15	8.72	100.01	892.28	0.93	2.05	0.20	0.22
Case 5	2.15	8.77	100.44	903.02	0.93	2.06	0.20	0.22
Case 6	1.59	6.47	96.43	897.49	1.22	2.78	0.31	0.35
Case 7	0.92	14.77	102.73	9997.08	0.28	1.69	0.10	0.14
Case 8	1.13	18.31	99.85	9998.06	0.22	1.37	0.07	0.10
Case 9	2.82	8.19	99.09	881.16	0.81	1.54	0.15	0.17

In another study, Aricò, Nasello & Tucciarelli (2009) developed a numerical scheme to solve SWE in diffusive form and needed stage data from three locations to calibrate a hydraulic model and estimate discharge during sub-critical flow conditions. However, the method developed in this study does not make these assumptions, and the results show that stage data from two locations is enough to calibrate model parameters and estimate discharge with a high degree of accuracy in prismatic channels or idealised rivers with no lateral flow.

Figure 5.9 shows the results of Manning's roughness and initial flow calibration, true and observed stage and discharge hydrographs, and a simulated rating curve corresponding to the calibrated parameters. From Figure 5.9b, we can infer that the simulated stage is not sensitive to initial flow as there is no visible pattern between sampled initial flows and the simulated stage (or KGE). Furthermore, for range of initial flow value sampled, most of the KGE value is between 80 and 100 percent. However, Figure 5.9a shows that the simulated stage is significantly sensitive to Manning's n as there is a clear visible pattern between KGE and Manning's n samples. Although not shown here, similar results were obtained in all cases of idealised rivers. Figures 5.9c and 5.9d show the True upstream and downstream hydrographs

and simulated hydrographs corresponding to the maximum KGE. The calibrated hydrographs at the downstream are seen to be a close match to the true hydrographs. Figure 5.9e shows all the simulated rating curves and the rating curve corresponding to the maximum KGE. This shows that the developed method can be used to estimate unsteady flow discharge or develop a rating curve, similar to traditional rating curve, at an ungauged or desired location of a river reach.

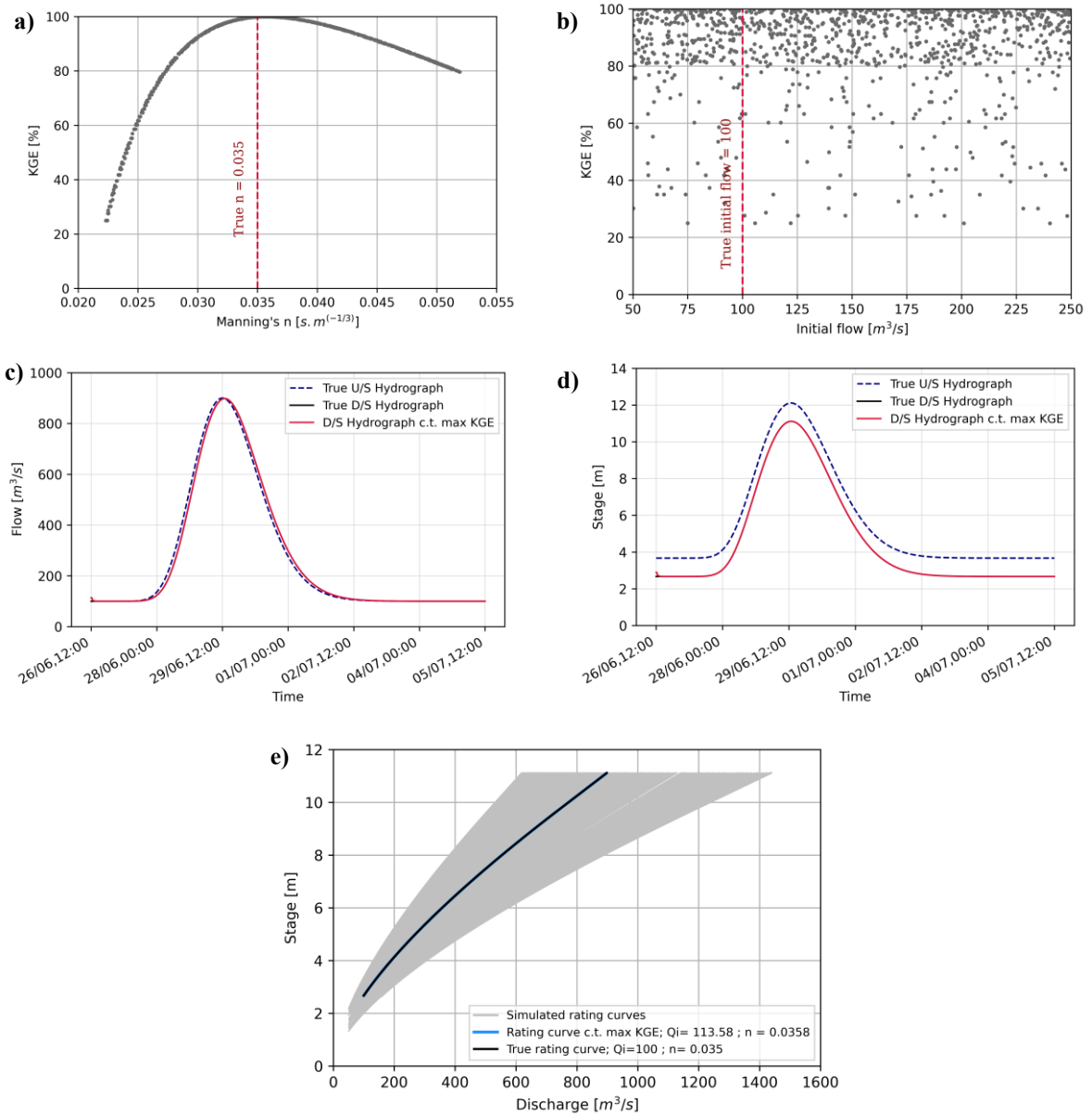

Figure 5.9: Calibration and discharge estimation for idealised river described in Case 3. (a) Modified KGE for different Manning's roughness coefficient, (b) Modified KGE for different Initial flows, (c)True and calibrated flow hydrographs, (d) True and calibrated stage hydrographs and (e) Simulated and estimated rating curves at the downstream location

5.5.2 Field case study

The results of the river Wandle hydraulic model parameter calibration and performance measures are presented in Table 5.7.

Table 5.7: Performance criteria and results of parameter calibration for river Wandle

Natural channel	KGE [%]	Manning's n [s/m$^{(1/3)}$]	Estimated Initial flow (Q_i) [m^3/s]	Error in Time to peak (T_p) [min]	Error in peak stage (Z_p) [%]	Error in estimation of Initial flow (ε_{Q_i}) [%]	No. of sensor data used for calibration and its location
Wandle	96.63	0.05172	1.673	0	2.84	-4.4	3 sensors at 204, 206 and 207
Wandle	91.99	0.0467	1.729	0	13.64	-1.15	2 sensors at 204 and 207

The sensors installed on the river Wandle were measuring the water level at 1-minute frequency (see Figure 5.8). Therefore, three sensors, sensors 205, 206, and 207, were able to capture the time lag between the peak stages. It was found that, unlike for idealised test cases where the quality of the match between the observed and simulated stage and discharge hydrographs was assessed by using KGE alone, combined criteria of error in time to peak (T_p) and KGE improved the match between observed and simulated stages, thereby improving unsteady flow parameter calibration and discharge estimation. In the combined criteria, KGE was only calculated for simulations where the error in the time to peak at different sensor locations (sensors 205, 206, and 207) was zero. Then, among these simulations, unsteady flow parameters corresponding to the maximum KGE were chosen as calibrated parameters and were used for dynamic river discharge estimation. It should be noted that unlike idealised river cases where KGE is 99.99 percent, the maximum KGE for the river Wandle is only 96 percent. This is expected, as we can never expect a perfect match between simulated and observed stages in natural river conditions where flow is affected by measurement error, eddies in flow, and other uncertainty.

Compared to two sensors, three sensors improved the calibration of Wandle model as the KGE for three sensors combination is higher (refer to Table 5.7). Furthermore, the river Wandle reach considered in this study is straight, with stones, tall weeds, and deep pools and therefore, the calibrated value of Manning's n is expected to be between 0.048 and 0.06 (Chow, 2006). However, with two sensors data, the calibrated value of Manning's n is underestimated thus resulting in overestimation of discharge at the Summerstown (see Figure 5.10c). I hypothesise that the sensor at location 206 can capture the celerity of the wave accurately aiding in good match between simulated and observed stage at downstream boundary (i.e., at sensor location 207). Further analysis on the value of additional sensors on parameter calibration and discharge estimation is discussed in detail in chapter 6.

From Figure 5.10b, we can see that, similar to idealised rivers, for natural channels too, simulated stages are not sensitive to initial flows.

After the Wandle model was calibrated, the discharge obtained by the developed method was compared to the observed discharge at Wandle Summerstown station. The observed stage at Summerstown and the rating curve at WPM were used to obtain the observed discharge at Summerstown station. Figure 5.10c shows all of the simulated rating curves as well as the rating curve corresponding to the calibrated parameters. It can be observed that this method is able to reproduce the traditional rating curve. However, it should be noted that this method uses non-contact sensors to measure river stage. This means that it would be able to monitor flood stage and precisely estimate flood discharge, something that is typically accomplished by extrapolation when a conventional rating curve is employed.

It should be noted that the methodology is not automated at the moment, meaning that the calibrated model needs to be run manually to obtain the discharge data in real time.

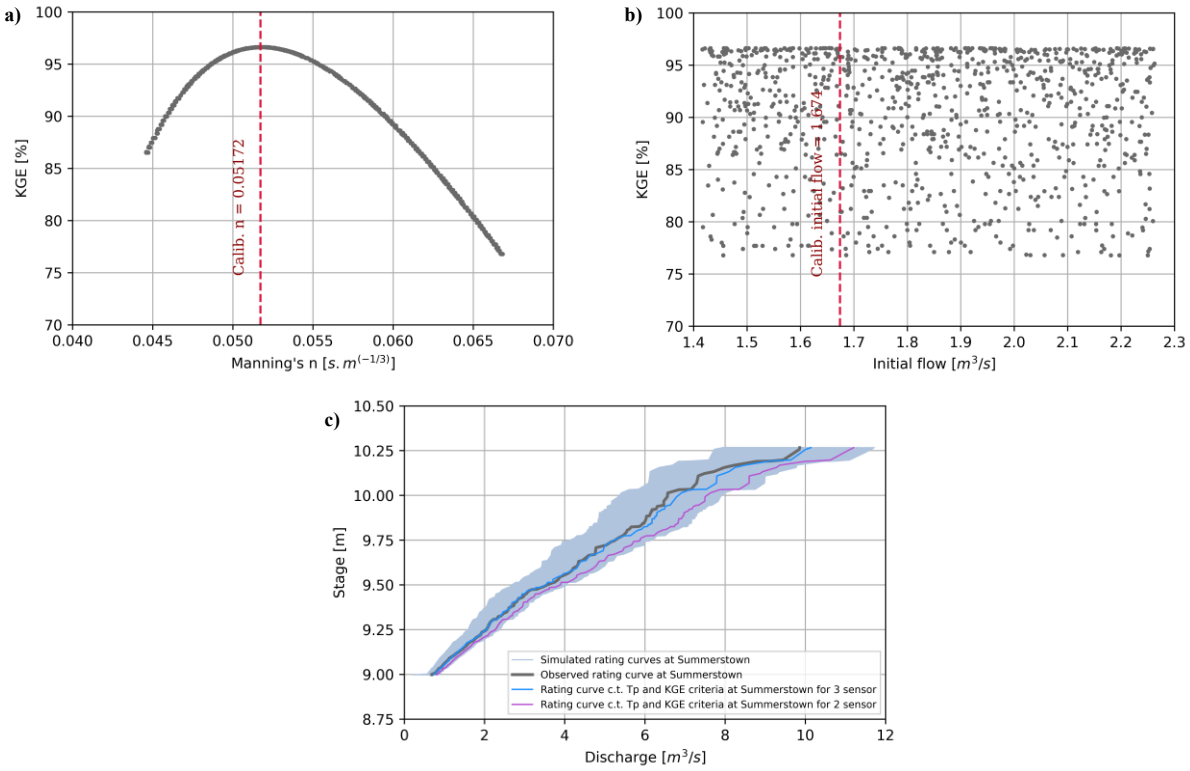

Figure 5.10: Calibration and discharge estimation for river Wandle. (a) Modified KGE for different Manning's roughness coefficient, (b) Modified KGE for different Initial flows, (c) Simulated and estimated rating curves at downstream location (Summerstown)

5.5.3 Sensitivity analysis

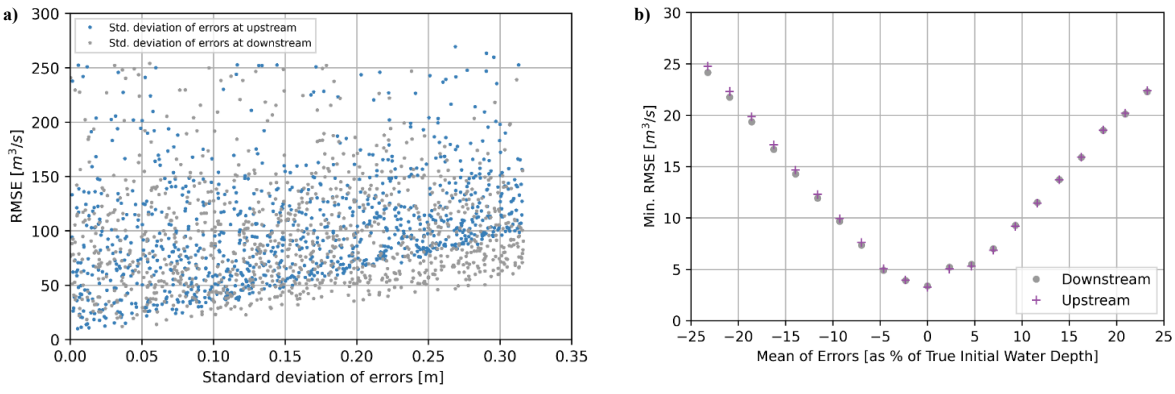

Figure 5.11: Effect of error in stage data on discharge estimation. (a) effect of error standard deviation on discharge and (b) effect of error mean on discharge estimation

Figure 5.11a depicts the relationship between the standard deviation of errors in the upstream and downstream stages and the error in discharge estimation at the downstream location of a hydraulic model (Case 3). This graph illustrates that as the standard deviation of errors increases, the error in discharge estimation also increases.

To test the robustness of the developed method, errors were generated with both positive and negative error means and added at random to both the upstream and downstream stages. The model was then calibrated for each error mean using the minimum RMSE criterion. Figure 5.11b depicts the relationship between different error means (expressed as a percentage of the true initial river depth) and minimum RMSE. Here, it is observed that the mean of errors is directly proportional to the minimum RMSE. However, the minimum RMSE is not zero when the mean error is zero. This could be due to the inherent randomness of the HEC-RAS model or a lower number of Monte Carlo simulations, resulting in insufficient parameter space coverage.

Figures 5.12 and 5.13 depict the calibrated values of Manning's n and simulated rating curves for various error mean values. From these figures, it can be observed that when the mean error is negative, the calibrated Manning's roughness coefficient is underestimated, thus resulting in an overestimation of discharge at the downstream location and vice-versa.

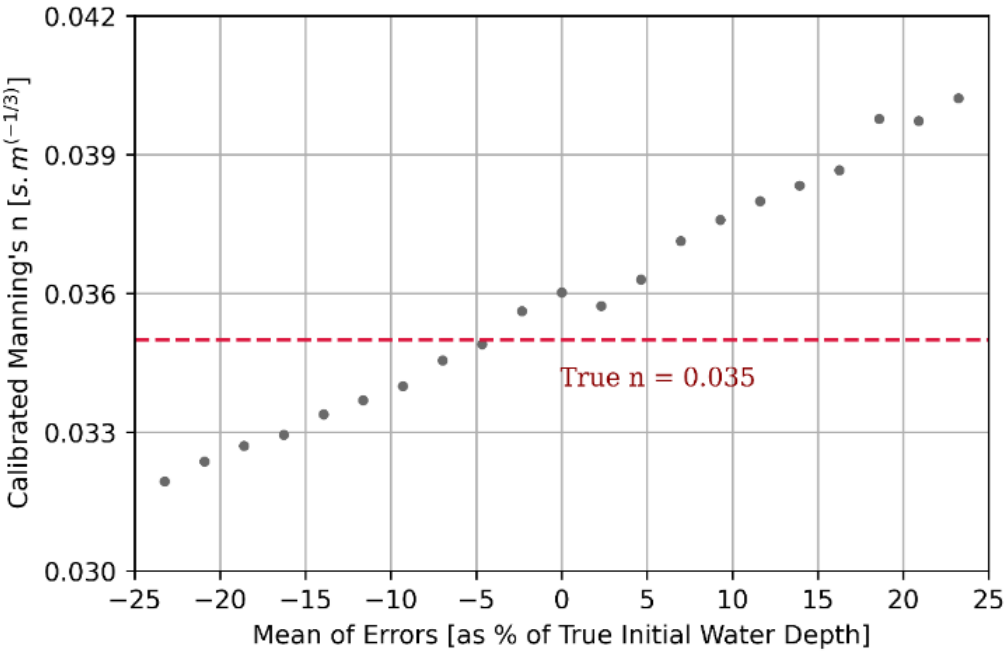

Figure 5.12: Calibrated Manning's roughness for the different mean of errors

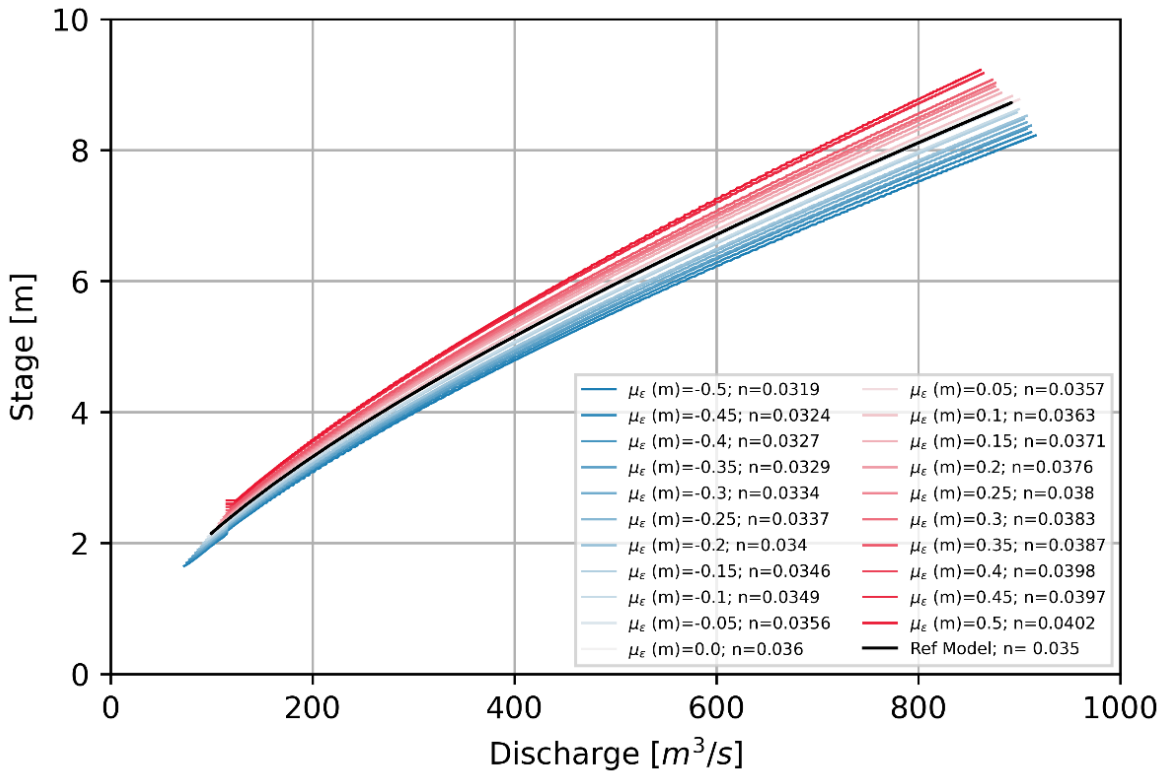

Figure 5.13: Simulated rating curves for the different mean of errors

It is interesting to note that, for a mean of error varying between -25 and 25 %, the error in the calibration of Manning's roughness coefficient is between -8.5 % and 14 %. This indicates that the developed model is robust. This is due to the use of the MC method where the most probable events occur first (i.e., it is self-approximating, refer to 2.6.1.1).

5.6 Conclusions

This chapter proposes a methodology for dynamically estimating unsteady flow discharge at a river location using stage data from a network of sensors. The method is applicable in prismatic and natural channels and does not require any measured discharge value. As HEC-RAS is used to model the rivers, the methodology would also work with lateral flows. However, this has not been tested in this study. The method was evaluated on several simulated rivers and a natural river. Two sensors are sufficient for hydraulic model parameter calibration and discharge estimation based on river simulations. However, field testing reveals that using more than two sensors improves unsteady river flow model calibration and discharge estimation. The sensitivity analysis suggests that the methodology is robust and can provide accurate estimate of river flow parameters and river discharge. The primary benefit of the method is that it allows simultaneous estimation of unknown river flow parameters and discharge. However, this method must be tested on additional natural rivers to determine its practical utility.

6 Optimising a water level sensor network for river discharge estimation

Theoretically, river stage data from two sensors is sufficient to calibrate an unsteady flow hydraulic model and estimate river discharge at an ungauged location. To calibrate the unsteady flow parameters and estimate river discharge, the governing equations of river flow (i.e., SWE) are solved. However, in the previous chapter, I found that utilising stage data from more than two sensors improves parameter calibration and discharge estimation. In the case of more than two sensors, the configuration of the sensors network, including 1) the location of the sensors, 2) the number of sensors, and 3) the distance between the sensors, has not previously been investigated. Therefore, this chapter proposes two approaches for utilising stage data from a network of sensors and optimising the sensor network. In one approach, stage data is used as internal boundary conditions of a hydraulic model, while in another, they are used to calibrate model parameters (i.e., used in post-processing of the model simulations). In both approaches, the Monte Carlo method is utilised to evaluate the value of additional sensors in unsteady flow calibration, discharge estimation, and optimal sensors network configuration. Both approaches have been evaluated on idealised river channels and a natural river channel (River Wandle, London). In both instances, the calibration parameters of an unsteady flow hydraulic model and discharge hydrograph obtained at a location with more than two sensors are compared to those obtained with only two sensors in order to determine the value of the additional sensors. Various sensors configurations are subjected to identical analyses in order to identify the optimal sensors network.

6.1 Introduction

In chapter 5, a method is presented for calibrating the input parameters of an unsteady flow river model and estimating discharge using stage data from a network of sensors. The method was evaluated using idealised and natural river channels. In the case of prismatic channels or idealised rivers, I found that two sensors are adequate to estimate unsteady flow discharge, while in the case of natural rivers, depending on the length of the modelled reach and channel geometry, three or more sensors are required to achieve best predictive performance. The configuration of the sensor network, such as the location of the sensors and the spacing between them, was not explored in chapter 5. Neither has prior research, including Dottori et al. (2009), Harlan et al. (2021), and Perumal et al. (2007), investigated the optimal sensor configuration. Therefore, according to my knowledge, this is the first study addressing the following questions:

A. Although two sensors are sufficient from a theoretical standpoint (for a straight river reach with linear water slope under steady state subcritical conditions), would additional sensors improve parameter calibration and discharge estimation in the case of idealised rivers? If so, what should be the optimal configuration of the additional sensors?

B. In the case of three or more sensors, what is the optimal sensor configuration for improving discharge estimation in natural rivers?

The configuration parameters under consideration in this study are 1) the location of the sensors, 2) the number of sensors (excluding the upstream and downstream boundaries), and 3) the spacing between the sensors.

Various metaheuristic optimisation algorithms such as differential evolution, particle swarm optimization, and genetic programming were reviewed to implement them for configuring optimal sensor networks. However, metaheuristic algorithms are computation intensive. Therefore, because of available computation capacity and previous usage of the Monte Carlo (MC) method in chapters 4 and 5, I employed the MC method to find the optimal sensor configuration parameters.

6.2 Methodology

The MC method is used to assess the value of the additional sensors in unsteady flow calibration, discharge estimation, and to configure the optimal sensor network. To implement the MC method, first an unsteady flow hydraulic model of a river reach (see Figure 6.1) is set up in the HEC-RAS. Then, in the second step, the discharge estimation method discussed in chapter 5 is employed to calibrate the unsteady flow parameters and estimate the river discharge. Here, however, two or more than two additional sensors are used in the first or in the second step of this methodology. The additional sensors are utilized:

i. as additional hydraulic model boundary conditions

Here, a different number of additional sensors, i.e., apart from the upstream boundary condition, such as 2,3, 4, 5, 6, and 7 are used as internal boundary conditions when setting up the unsteady flow hydraulic model in the HEC-RAS. HEC-RAS has a built-in functionality to assimilate stage observations at free cross sections along the simulated reach. It does so by forcing the simulated water level to coincide with the observed water level value. Then, the MC method is implemented to calibrate the unsteady flow parameters of the hydraulic model and estimate the river discharge at a given location.

ii. in hydraulic model calibration

In this case, additional sensors are used to evaluate the hydraulic model simulations (refer to 5.2.4) obtained from the MC method implementation. During the MC method implementation, randomly sampled errors, for example, uniformly sampled errors between ± 15 cm, are added to the upstream boundary condition (i.e., stage hydrograph). Then, a different number of additional sensors, for instance, two or more than two sensors, are used to calibrate the error in upstream boundary condition and the unsteady flow parameters. The objective is to find an MC simulation in which the error in the upstream boundary condition calibration is as close to zero as possible and the error in the unsteady flow parameter calibration is minimum.

In both cases, the calibration parameters and discharge hydrograph obtained at the downstream location by utilising more than two sensors are compared to those obtained by utilising only two sensors to determine the value of the additional sensors. Identical analyses are conducted on various sensor configurations to identify the optimal sensors network.

6.2.1 Optimisation strategy

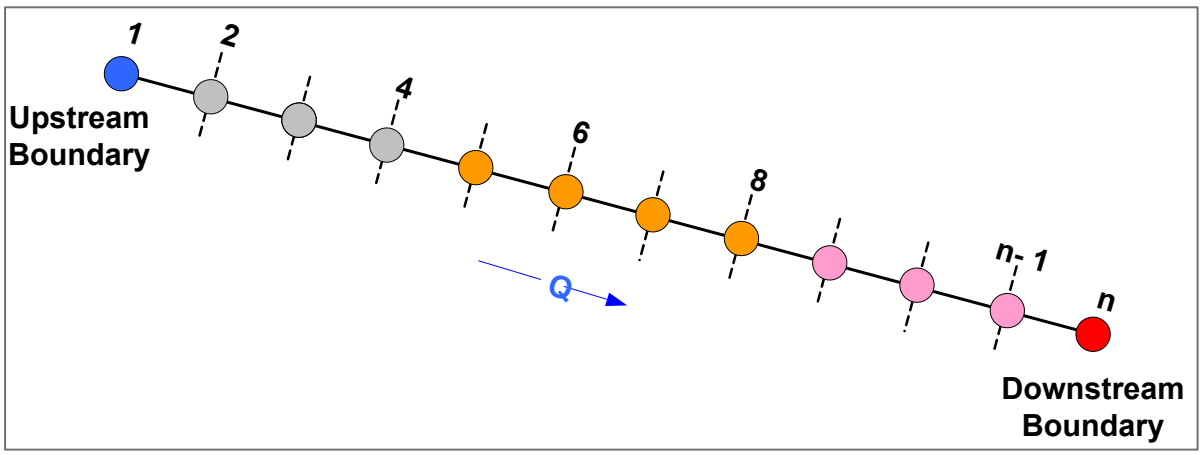

Figure 6.1: A schematic representation of an array of sensors positioned along a river reach.

The discharge estimation methodology developed in chapter 5 uses stage data from two or more than two sensors to solve the governing equations of river flow in full form to calibrate the unsteady flow parameters, Manning's roughness coefficient, and initial flow, and estimate river discharge at a location. To use the discharge estimation method discussed in chapter 5, we would require stage data from at least two sensors, one at the upstream boundary (as shown in Figure 6.1) and the other at any location, free of backwater effects, downstream of the upstream boundary i.e., at any location between "2" and "n" " (as shown in Figure 6.1). However, in the case of only two sensors, the second sensor is usually located at the downstream boundary i.e., at location 'n'. In this study, the additional sensors are assumed to be at any location between "2" and "n" (as shown in Figure 6.1) and the optimal sensor network configuration analysis is carried out for these additional sensors.

As discussed above, this study considers two approaches to assimilate the data from the additional sensors. In both approaches, the design of an optimal sensor configuration is carried out in three sequential steps:

i. Optimal sensor location

The optimal sensor location is determined by investigating if the additional sensors should be placed closer to the upstream boundary (represented by grey in Figure 6.1) or mid-stream (represented by orange in Figure 6.1) or downstream boundary (represented by pink in Figure 6.1), of the river reach.

ii. The number of sensors

After the location of the sensors has been determined, additional analysis is carried out to determine the optimal number of additional sensors, for instance 2, 3 or more, for parameter calibration and discharge estimation.

iii. Spacing between the sensors

Once the location and number of sensors have been determined, an optimization algorithm is used to determine the distance between sensors. The objective of both approaches is to minimize the error in the parameter calibration and unsteady flow discharge estimation. Here, modified KGE, error in time to peak stage and average absolute relative error (AARE), are used as performance measure to minimize the error in the parameter calibration.

6.2.1.1 Performance measures

The performance of MC simulations that assess the quality of the match between the observed and simulated stage and discharge hydrographs was evaluated based on the following performance criteria (Aricò, Nasello & Tucciarelli, 2009; Perumal et al., 2007a; WMO, 2011):

$$Modified\ Kling-Gupta\ Efficiency\ (KGE) = 1 - \sqrt{(r-1)^2 + (\beta-1)^2 + (\gamma-1)^2} \tag{6.1}$$

$$r\ (correlation\ coefficient) = \frac{cov\ (Z_i^s,\ Z_i^o)}{\sigma\ (Z_i^s) * \sigma\ (Z_i^o)}$$

$$\beta\ (Bias\ ratio) = \frac{\mu\ (Z_i^s)}{\mu\ (Z_i^o)}$$

$$\gamma\ (Variability\ ratio) = \frac{CV\ (Z_i^s)}{CV\ (Z_i^o)} = \left(\frac{\sigma\ (Z_i^s)}{\mu\ (Z_i^s)}\right) \Big/ \left(\frac{\sigma\ (Z_i^o)}{\mu\ (Z_i^o)}\right)$$

$$Error\ in\ T_p\ [min] = t_{max}^s - t_{max}^o \tag{6.2}$$

$$Error\ in\ Q_p\ [\%] = \frac{Q^s_{max} - Q^o_{max}}{Q^o_{max}} * 100 \tag{6.3}$$

$$Average\ absolute\ relative\ error\text{: } AARE\ [\%] = \left(\sum_{i=1}^{N} \left|\frac{Q^s_i - Q^o_i}{Q^o_i}\right| \Big/ N\right) \times 100 \tag{6.4}$$

where, Z^s is the simulated stage, Z^o is the observed stage, Z_{max} is peak stage, t^s_{max} and t^o_{max} is time (in minutes) at which the simulated and observed peak reaches the gauging station, μ, σ is mean and standard deviation, cov is covariance, and CV is coefficient of variation.

i is the time step in hydrographs, N is the total number of time steps, Q^o_i is observed discharge at the i^{th} time step and Q^s_i is simulated discharge at the i^{th} time step. Q^o_{max} and Q^s_{max} are the maximum observed and simulated discharges respectively.

Other similarity measures than AARE exist, such as Discrete Fréchet distance (Jekel, 2021) and Hausdorff distance (SciPy, 2021), which compare similarity between two curves, and can be applied to rating curves. These were tested but found to be too computationally demanding and therefore not incorporated in the performance evaluation.

6.3 Numerical experiments

6.3.1 Approach I: additional sensor as hydraulic model boundary conditions

In this experiment, additional sensors are used as internal boundary conditions into the unsteady flow hydraulic model in the HEC-RAS. Then, the discharge estimation methodology developed in chapter 5, which uses stage data from two or more than two sensors to solve the governing equations of river flow in full form to calibrate the unsteady flow parameters, Manning's coefficient, and initial flow, and estimate river discharge at a location, is utilised to calibrate river flow parameters and estimate discharge.

HEC-RAS allows the user to input a known stage hydrograph at an "open" cross-section (one not associated with a hydraulic structure) as an internal boundary condition (Brunner, 2016). For instance, in Figure 6.1, any cross-section location between "2" and "n-1" can be considered an open cross-section. During the execution of the hydraulic model, the HEC-RAS algorithm

forces the simulated stage to match the known stage by optimizing the routed unsteady flow simulations. Therefore, in this approach, different combinations of additional sensors, for instance 2, 3, 4, 5, 6, and 7, were placed as internal boundary conditions at different locations in river reach, and the developed discharge estimation method was utilised to calibrate the river flow parameters and estimate discharge. The error in calibration of river flow parameters and discharge at the downstream location with different sensor combinations was compared to evaluate the value of additional sensors.

6.3.1.1 Application

This approach was evaluated on different idealised rivers, i.e., cases 1, 2, 3, 4 and 6. The cases are shown in Table 6.1 below and discussed in detail in chapter 4.

Table 6.1: Idealised river cases used to test approach I

Cases	Cross section geometry (w = width; d = depth)	Bed slope (S_o)	Time to peak (T_p)	Peak discharge (m^3/s)
Case 1	Rectangular (w = 50 m, d = 10 m)	10^{-4}	24 h	900
Case 2	Rectangular (w = 50 m, d = 10 m)	10^{-3}	24 h	900
Case 3	Rectangular (w = 50 m, d = 10 m)	10^{-4}	72 h	900
Case 4	Rectangular (w = 50 m, d = 10 m)	2×10^{-4}	24 h	900
Case 6	Rectangular (w = 50 m, d = 10 m)	5×10^{-4}	24 h	900

All idealised river channels are assumed to have a length of 10 km and width of 50 m. The rivers are assumed to have a constant bed slope (S_o) as mentioned in the Table 6.1 and have uniformly spaced cross-sections at every 100 m. A stage hydrograph was used as an upstream boundary and normal depth, a Manning's equation approximation which needs an initial guess of the friction slope (average riverbed slope applied), was used as the downstream boundary condition in all cases. The simulation time was set in accordance with Courant's condition (refer to 2.4.3.2) to satisfy the stability and accuracy of the model (Brunner, 2016b).

This approach was not tested on natural rivers (explanation provided in 6.4.1).

The approach I implemented was as follows:

1. An unsteady flow hydraulic model of a river reach, as described in the discharge estimation method (see 5.2.2), is set up in HEC-RAS

2. Then, locations for internal boundary conditions are selected. Apart from the two sensors at the upstream and downstream boundaries, it was assumed that seven additional sensors placed at different open cross-sections would be adequate to evaluate the value of stage data from these seven additional sensors. However, in idealised river cases discussed above, there are 99 "open" cross-section locations at 100-metre spacing. Testing all combinations of seven sensors at these open cross-sections, i.e., ${}^{99}C_1 + {}^{99}C_2 +... + {}^{99}C_7$, would be impossible as the Monte Carlo approach used in the discharge estimation method takes, on an average, 24–50 hours to run a single combination. Therefore, instead of looking at all the possible combinations of the seven sensors and the open cross-sections, the internal boundary conditions were considered only at selected open cross-sections in three different regions as discussed above (refer to 6.2.1). Furthermore, when using two or more sensors as internal boundary conditions, adjacent sensor positions were avoided to account for any measurement error. In the field, local oscillations of the water surface can cause two adjacent measurements to be identical therefore the measurements would not capture the water surface profile.

3. The stage hydrographs, as would be obtained from a sensor network, were simulated by running a reference hydraulic model with a known discharge hydrograph and other model parameters such as initial flow (100 m^3/s) and Manning's roughness coefficient (0.035 s $m^{-(1/3)}$) in HEC-RAS. The stage and discharge hydrographs obtained at different locations of the reference model are considered true or observed hydrographs.

4. The stage hydrograph data obtained from the reference model are used as upstream boundary and known internal boundary (locations of additional sensors) of the hydraulic model.

5. During each Monte Carlo (MC) simulation of the model calibration (see 5.2.3) step of the discharge estimation method (chapter 5), a randomly sampled uniformly distributed error, for instance, $\varepsilon \sim U[-0.1, 0.1]$ m, is added to the stage hydrograph data of the

upstream boundary of a hydraulic model. This error is added because, during field experimentation with the lidar sensor, we encountered an error in measurement between 5 and 30 cm.

6. Then a fixed number of MC simulations is run

7. The performance of each MC simulations was evaluated as follows:

   i. Error in time to peak stage i.e., T_p is calculated by using equation 6.2
   ii. Common MC runs for which error in T_p is equal to a chosen value (for instance ± 5 minutes) or minimum value in the MC simulations at additional sensor locations are selected. This can be changed as per user needs
   iii. For the common runs obtained in step ii, modified KGE (using equation 6.1) is computed at downstream boundary
   iv. Parameters corresponding to the max KGE is selected as calibration parameters
   v. Error in maximum discharge of observed and that obtained from a calibrated model is computed by using equation 6.3

8. Once the river flow parameters have been calibrated, discharge at the downstream boundary of the river reach is computed. The peak value of computed or simulated discharge is compared with the peak value of observed or true discharge, derived from the reference model, to obtain the error in peak discharge using equation 6.3

6.3.2 Approach II: additional sensors in hydraulic model calibration

In this approach, stage data from additional sensors are utilised to evaluate the hydraulic model simulations (refer to 5.2.4) obtained from each MC run. That is using additional sensors stage data during post-processing of the MC simulations to find the unsteady flow calibration parameters.

The proposed approach is implemented as follows:

1. An unsteady flow hydraulic model of a river reach, as described in the discharge estimation method (see 5.2.2), is set up in HEC-RAS

2. During each Monte Carlo (MC) simulation of the model calibration (see 5.2.3) step of the discharge estimation method (chapter 5), a randomly sampled uniformly distributed

error, for instance, $\varepsilon \sim U[-0.2, 0.2]\ m$, is added to the stage hydrograph data of the upstream boundary of a hydraulic model. This error is added because, during field experimentation with the lidar sensor, we encountered an error in measurement between 5 and 30 cm.

3. Location of additional sensors, more than one, placed at different cross-sections, any location between "2" and "n" (refer to Figure 6.1), is pre-selected for post-processing.

4. The stage data of these additional sensors is obtained from a reference model, the same as that would be obtained from a sensor network, and is considered as true or observed stage

5. A randomly sampled uniformly distributed error, for instance, $\varepsilon \sim U[-0.15, 0.15]\ m$, is added to the true stage hydrograph of all the additional sensors

6. After the Monte Carlo simulations have been completed, the optimal Manning's roughness coefficient, initial flow and error in the upstream stage hydrograph are calibrated by comparing the simulated stage at additional sensor locations with the stage data obtained from step 5 (i.e., true stage with some error) at that location. The performance of each MC run is evaluated as follows:

   i. Error in time to peak stage i.e., T_p is calculated by using equation 6.2

   ii. Common MC runs for which error in T_p is equal to ± 2 minutes at additional sensor locations are selected. This can be changed as per user needs

   iii. For the common runs obtained in step ii, modified KGE (using equation 6.1) is computed at all the additional sensor locations

   iv. Then, the sum of $(1 - KGE)^2$, as shown in equation 6.5, at all additional sensor locations and for all the common runs obtained in step ii is minimized

$$\sum_{i=additional\ sensor\ locations}^{j=common\ runs\ c.t.\ T_{p\ criteria}} (1 - KGE_i)_j^2 \tag{6.5}$$

v. The parameters corresponding to the minimum value of $\sum(1 - KGE)^2$ is considered as calibrated parameters

vi. Once the river flow parameters have been calibrated, discharge at the downstream boundary of the river reach is computed. This computed or simulated discharge is compared with the observed or true discharge, derived from the reference model, to obtain the average absolute relative error in discharge hydrograph using equation 6.4

7. For one combination of additional sensor positions, which is pre-selected in step 3, steps 5 and 6 are repeated multiple times, such as 5000 times. The objective, for the pre-selected location of additional sensors, is to find the maximum frequency when additional sensor data can minimize the error in the upstream stage (or in other words, calibrate the upstream stage error approximately to zero) and discharge estimation (i.e., AARE within acceptable limit such as 5-10 %).

8. Steps 3 to 7 are repeated for different combinations of locations and numbers of sensors. The locations and number of sensors for which the frequency of calibrated upstream error and AARE within the acceptable limit is highest are chosen as the optimal positions and number of sensors

9. Once the locations and number of sensors have been determined, the spacing between the sensors is optimised by repeating steps 4 to 7 for different combinations of sensor positions within the optimal locations. For example, say cross-sections 8 to 15 (refer to Figure 6.1) are optimal sensor locations (i.e., 8 locations on the river reach) and the optimal number of sensors is three. Then, steps 4 to 7 are repeated for all combinations of three sensors at these eight locations; that is, ${}^{8}C_{3}$ or fifty-six combinations to determine the optimal spacing between the sensors.

6.3.2.1 Application

Approach II was tested on idealised river cases discussed in Table 6.1 and river Wandle in London. The case study of river Wandle is discussed below.

6.3.3 A case study of the river Wandle

The above optimisation approach (i.e., Approach II) is demonstrated with a case study of the river Wandle. It should be noted that this analysis is done before installing any sensors in the field so that the results can inform on optimal locations for sensor installation. In this example, Environment Agency's stage data of river Wandle Main Park station and Wandle on Summerstown is used to build the hydraulic model.

An unsteady flow hydraulic model of a river reach of Wandle was set up in HEC-RAS. The model inputs and observed data are described in Table 6.2 and Table 6.3 respectively.

Table 6.2: River Wandle unsteady flow model inputs

Model inputs	**Descriptions**
River reach length	1086 m (between Wandle Park Main Channel (WPM) and Summerstown EA stations - refer to Figure 5.4
River Wandle Geometry (cross-sections and riverbed slope)	Obtained from Bathymetry survey (discussed in Section 5.4.2) and 1m resolution lidar digital elevation model (Environment Agency, 2021b)
Number of cross-sections	26, including upstream and downstream boundaries
Upstream boundary	Stage hydrograph from WPM station (Environment Agency, 2021d)
Downstream boundary	Normal depth, average bed slope at the downstream boundary obtained from Bathymetry survey, 0.0015
Manning's roughness coefficient $\left(\mathbf{s.m^{-1/3}}\right)$	Randomly selected from a uniform distribution n$\sim U[0.02, 0.08]$ (Chow, 2006)
Initial flow (m^3/s)	Randomly selected from a uniform distribution $Q_i \sim U[1.42, 2.27]$
Simulation time (seconds)	30, as per Courant's stability criteria (Brunner, 2016a)

The above unsteady flow hydraulic model of the river Wandle was run for 1000 Monte Carlo simulations following model calibration (i.e., 5.2.3) of the discharge estimation method. However, in addition, during each Monte Carlo run, a randomly sampled error from a uniform distribution, i.e., $\varepsilon \sim U[-0.15, 0.15]\, m$, was added to the upstream stage hydrograph (as described in step 2 of this optimisation approach). It should be noted that the same error was added to all the stages of the hydrograph. A few combinations of three and two additional sensors placed at different locations, ranging from 2 to 26 cross-sections, along the river reach were determined. These locations were chosen to investigate if the additional sensors should be placed closer to the upstream boundary, mid-stream, or downstream boundary of the river reach. The stage data, as would be obtained from a sensor network, of these additional sensors was obtained by running the same river Wandle model with the observed data described in Table 6.3.

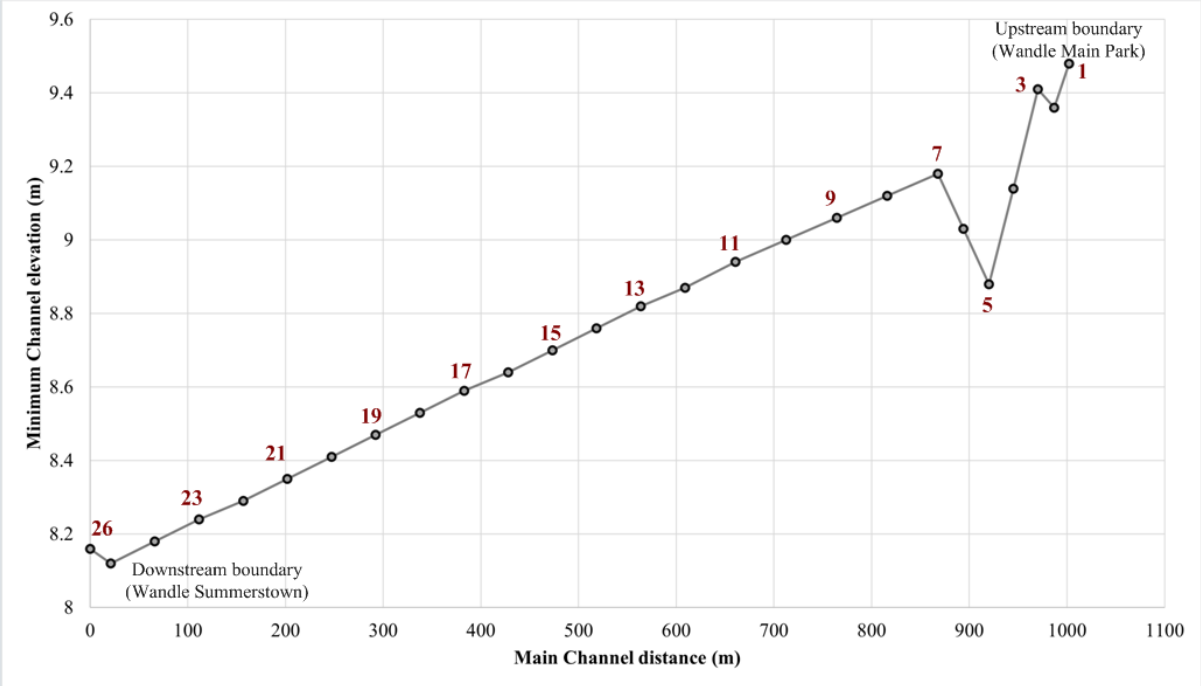

Figure 6.2: Longitudinal profile plot of river Wandle model. Black circle represents cross-section locations or locations for the additional sensors

Table 6.3: Observed data available at upstream and downstream boundaries of river Wandle unsteady flow model

Observed data	Descriptions
Rating curve at the upstream boundary	The rating curve for WPM station was obtained from the Environment Agency
Observed stage at the downstream boundary	Stage hydrograph from Summerstown station (Environment Agency, 2021c)
Observed discharge at the downstream boundary	It was assumed that discharge at upstream (i.e., WPM) is equal to the discharge at downstream
True/ observed initial flow (m^3/s)	1.75 from the rating curve at WPM station
True/ observed Manning's roughness coefficient (m^3/s)	0.05172, according to calibrated values derived from field testing of the discharge estimation method (refer to Table 5.2 of chapter 5)

After the locations and numbers of additional sensors were determined, steps 5 to 9 of the optimisation Approach II were followed. For finding the optimal spacing between the sensors, the following limits for upstream error calibration and AARE were applied:

a. Upstream error calibrated within ± 0.005 m [referred to as "US error criterion"]

b. AARE at downstream boundary is < 10 % [referred to as "AARE criterion"]

c. US error and AARE criteria combined – MC run that fulfils both a and b error criteria

The bespoke sensor can capture the time lag between the maximum peak stage as well as smaller peak stages. Therefore, the error in the time peak stage i.e., T_p (computed in step 6) was modified to include all peak stages above a certain threshold, as depicted by the black line in Figure 6.3. This threshold was chosen because below this threshold, there are no prominent peaks in the stage hydrograph seen in Figure 6.3. To estimate the modified error in time to the peak stage, the "find peak" function of Scipy, which finds all peaks (or local maxima) by simple comparison of neighbouring values based on peaks properties such as peak height, peak width, distance between two peaks, all the peaks above a threshold etc., was applied (Scipy, 2021). It

was found that modifying the error in time to the peak stage improved the calibration of flow parameters and discharge estimation.

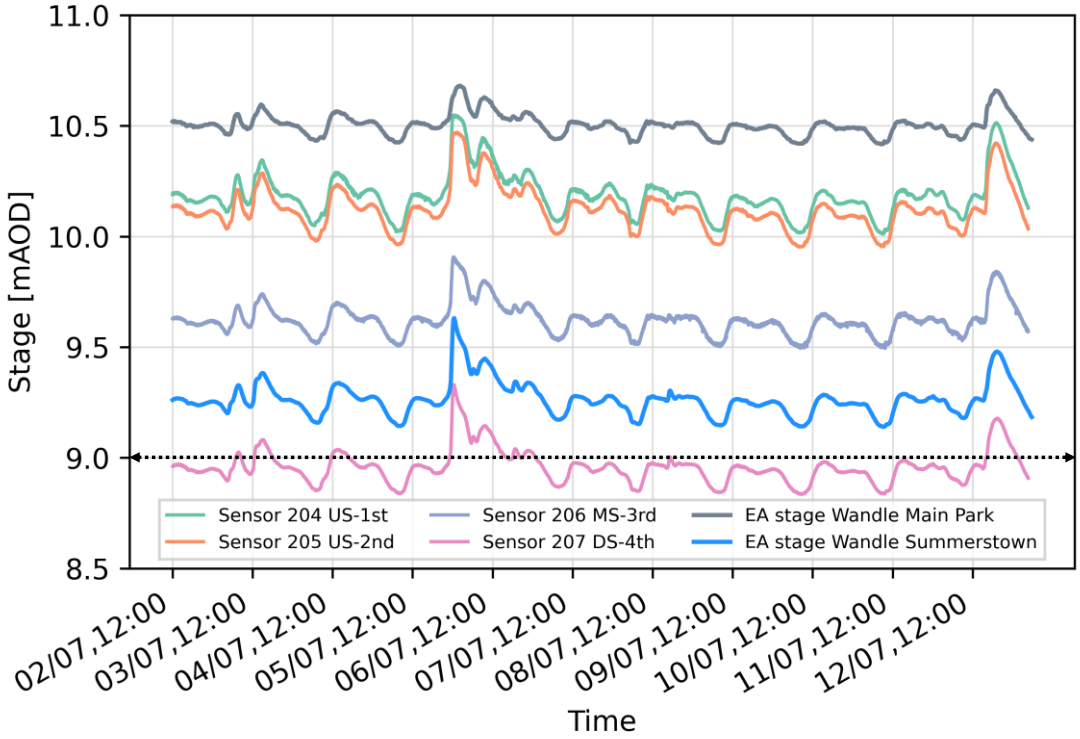

Figure 6.3: River Wandle stage (measured at a 1-min frequency) from the four sensors installed on the river reach, and the Environment Agency (EA) stage (measured at 15-min frequency). The Dotted black line demarks all the peak stages above the 9.0 m threshold for sensor 207.

6.4 Results and discussions

6.4.1 Approach I: additional sensor as hydraulic model boundary conditions

Various combinations of seven additional sensors placed closer to the upstream boundary, mid-stream, and closer to the downstream boundary of the river reach, as shown in Table 6.4 and Appendix A, were evaluated to determine the value of these additional sensors in discharge estimation and to determine the optimal position of these sensors. For each sensor combination, 1000 Monte Carlo simulations were run and evaluated to obtain the calibrated parameters. The calibrated parameters obtained from various sensor combinations were compared to the observed or true parameters. The error in parameter calibration of a model with two sensors was compared to that of various combinations of seven sensors to determine if additional sensors improved unsteady flow parameter calibration and, consequently, discharge estimates.

In addition, the observed peak discharge was compared with the peak discharge from various combinations of seven sensors to determine if the estimation of peak discharge had improved.

Table 6.4 summarises the performance evaluation of Case 1 of idealised rivers with different sensor combinations. The results from other idealised river cases are summarised in Appendix A. Table 6.4 shows that adding 3 sensors at "2", "4", and "6" locations improves, compared to the case of only 2 sensors, even though the KGE for 2 sensors is 99 %, the unsteady flow parameters calibration. However, the time to peak stage (T_p) is overestimated by 25 minutes, which is significant in the case of flood peaks. The error in time to peak stage is the same for various combinations of seven sensors when placed closer to the upstream boundary (i.e., between locations "2" and "14"). However, when various combinations of seven sensors are placed in mid-stream (i.e., between locations "50" and "62") and closer to the downstream boundary (i.e., between locations "80" and "92"), the error in time to peak stage is reduced to zero or five minutes. Furthermore, for mid-stream and closer to downstream locations, mixed results are observed in parameter calibration. For most combinations of sensors at mid-stream, for which the error in time to peak stage is zero, there is a significant error in initial flow calibration. The results of this idealised river case show that having two more sensors at locations "80" and "82," for a total of four sensors in a sensor network, improves the calibration of the unsteady flow parameters and the estimation of the discharge.

The analysis of various idealised river cases suggests that having more than two sensors closer to the downstream boundary improves the calibration of unsteady flow parameters and the estimation of discharge. However, while it can be inferred that more sensors should be placed closer to the downstream boundary in general, the idealised river case analysis did not clearly demonstrate this.

Furthermore, in most idealised river cases, one or two additional sensors are sufficient to improve parameter calibration and discharge estimation. Further analysis revealed that due to the way HEC-RAS uses stage data as internal boundary conditions, having more than two additional sensors in the case of idealised rivers is not advantageous. Therefore, the Approach I was not applied in natural river channels. Additionally, it should be noted that the hydraulic properties of the model, such as average velocity at the downstream boundary and Froude number, did not change with number of additional sensors as the intermediate boundaries.

The HEC-RAS program forces the simulated/routed stage at the internal boundary (or open) cross-section to match the observed or actual stage at that location. When forcing the observed stage, HEC-RAS also updates the simulated stages at all locations upstream of the open cross-sections to account for the difference between the simulated and observed stage at the open cross-sections. Therefore, if three additional sensors are located along the river reach, the true stage at the furthest downstream location will be forced to the simulated stage data at the other two additional sensor locations. Therefore, in a sense, the true stage data from two upstream additional sensors will not be utilized in improving model calibration. This was validated by running multiple simulations of idealised river models in which a known error was introduced to the true stages of the additional sensors. It was observed (results not shown) that the error in the true stage of the furthest downstream internal boundary propagates to all the cross-sections, affecting model calibration and discharge estimation. Therefore, the value of additional sensors in post-processing (or model calibration) of the simulated stages was evaluated, and the findings are presented in section 6.4.2.

6.4.2 Approach II: additional sensors in hydraulic model calibration

Because the selected river Wandle's reach is short, approximately 1.1 km, various combinations of only three and two additional sensors were evaluated to determine the value of additional sensors in parameter calibration and discharge estimation. Only selected results are shown here.

The histogram of calibrated upstream error for various combinations of three and two sensor locations is depicted in Figure 6.4. In the case of three additional sensors, the first is placed near the upstream boundary (i.e., at location 8), the second is placed in mid-stream (i.e., at location 16), and the third is placed near the downstream boundary (i.e., at location 25) – refer to Figure 6.2. In the case of two additional sensor combinations, one sensor is placed in mid-stream and the other closer to the downstream boundary (as depicted in the middle plot of Figure 6.4), whereas in the second combination, both additional sensors are placed closer to the downstream boundary (as shown in the right plot of Figure 6.4). Based on this analysis, it is evident that three additional sensors are advantageous to two additional sensors for calibrating the upstream stage error. Moreover, in the case of three additional sensors, a larger number of simulations calibrate upstream stage error to zero, indicating that the probability of compensating bias or error in the upstream stage increases as the number of sensors increases.

Table 6.4: Summary of performance criteria and results of parameter calibration when additional sensors are used as the internal boundary condition

Case	KGE [%]	Manning's n [s/m$^{(1/3)}$]	Estimated Initial flow (Q_i) [m^3/s]	Error in Time to peak (T_p) [min]	Error in peak flow (Q_p) [%]	Error in estimation of Initial flow (ε_{Q_i}) [%]	Error in estimation of n (ε_n) [%]	Intermediate Boundary locations	Remarks
Case 1	99.99	0.0359	103.88	0	-0.42	3.88	2.57	None	Model results when only two sensors data were used
	99.54	0.03524	97.36	25	-0.061	-2.64	0.69	2	**Sensors at upstream location**
	99.53	0.0354	98.98	25	-0.5	-1.02	1.14	2,4	
	99.5	0.0352	100.92	25	-0.1	0.92	0.57	2,4,6	
	99.46	0.0353	99.99	25	-0.024	-0.01	0.86	2,4,6,8	
	99.46	0.0354	102.19	25	-0.52	2.19	1.14	2,4,6,8,10	
	99.47	0.0355	106.12	25	-0.4	6.12	1.43	2,4,6,8,10,12	
	99.48	0.0355	107.95	25	-0.82	7.95	1.43	2,4,6,8,10,12,14	
	99.99	0.0358	85.43	0	0	-14.57	2.29	50	**Sensors at midstream location**
	99.99	0.0358	89.32	0	0.02	-10.68	2.29	50,52	
	99.99	0.0359	112.62	0	-0.39	12.62	2.57	50,52,54	
	99.99	0.0357	102.68	-5	0.04	2.68	2.00	50,52,54,56	
	99.98	0.0361	104.1	-5	-0.8	4.1	3.14	50,52,54,56,58	
	99.99	0.0357	103.05	-5	0.08	3.05	2.00	50,52,54,56,58,60	
	99.99	0.0358	109.22	-5	0.09	9.22	2.29	50,52,54,56,58,60,62	
	99.99	0.0356	90.31	0	0.43	-9.69	1.71	80	**Sensors at downstream location**
	99.99	0.0355	97.73	0	0.43	-2.27	1.43	80,82	
	99.99	0.0358	89.49	0	0.02	-10.51	2.29	80,82,84	
	99.98	0.0358	125.53	-5	-0.4	25.53	2.29	80,82,84,86	
	99.99	0.0358	109.86	-5	0.02	9.86	2.29	80,82,84,86,88	
	99.99	0.0358	89.12	-5	0.02	-10.88	2.29	80,82,84,86,88,90	
	99.97	0.0361	112.63	-5	0.81	12.63	3.14	80,82,84,86,88,90,92	

Table 6.5: Summary of hydraulic details for calibrated Manning's n and initial flow at the downstream boundary of the model for different combinations of sensors for Case 1

Hydraulic depth (Y [m])		Discharge (Q [m^3/s])		Average Velocity (V [m/s])		Froude No. (Fr)		Additional sensor location
Y_min	**Y_max**	**Q_min**	**Q_max**	**V_min**	**V_max**	**Fr_ min**	**Fr_ max**	
2.6	10.89	97.37	884.03	0.75	1.62	0.15	0.16	**2**
2.64	10.89	99	880.2	0.75	1.62	0.15	0.16	**2,4**
2.66	10.89	100.93	884.09	0.76	1.62	0.15	0.16	**2,4,6**
2.58	10.89	96	884.35	0.74	1.62	0.15	0.16	**2,4,6,8**
2.67	10.89	100.78	879.93	0.76	1.62	0.15	0.16	**2,4,6,8,10**
2.67	10.89	100.86	881.04	0.76	1.62	0.15	0.16	**2,4,6,8,10,12**
2.67	10.89	100.43	877.33	0.75	1.61	0.15	0.16	**2,4,6,8,10,12,14**
2.42	10.99	85.45	884.6	0.71	1.61	0.15	0.16	**50**
2.49	10.99	89.33	884.74	0.72	1.61	0.15	0.16	**50,52**
2.67	10.99	99.6	881.14	0.75	1.6	0.15	0.15	**50,52,54**
2.67	10.99	100	884.87	0.75	1.61	0.15	0.16	**50,52,54,56**
2.67	10.99	99.19	877.68	0.74	1.6	0.15	0.15	**50,52,54,56,58**
2.67	11	100.01	885.24	0.75	1.61	0.15	0.16	**50,52,54,56,58,60**
2.67	11	100.01	885.35	0.75	1.61	0.15	0.16	**50,52,54,56,58,60,62**
2.5	10.99	90.32	888.36	0.72	1.62	0.15	0.16	**80**
2.62	10.99	97.74	888.41	0.74	1.62	0.15	0.16	**80,82**
2.49	10.99	89.5	884.72	0.72	1.61	0.15	0.16	**80,82,84**
2.67	10.99	99.6	881.05	0.75	1.6	0.15	0.15	**80,82,84,86**
2.67	10.99	100.01	884.77	0.75	1.61	0.15	0.16	**80,82,84,86,88**
2.48	10.99	89.13	884.78	0.72	1.61	0.15	0.16	**80,82,84,86,88,90**
2.67	10.99	99.1	877.41	0.74	1.6	0.15	0.15	**80,82,84,86,88,90,92**

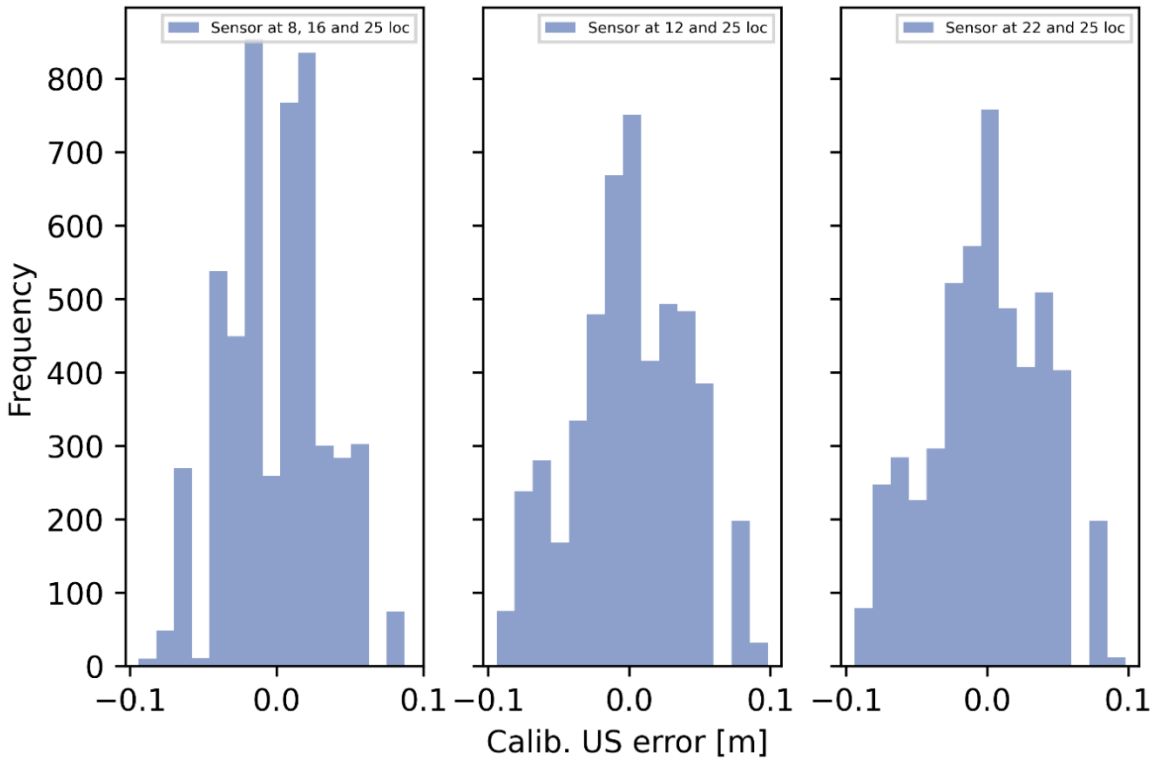

Figure 6.4: A histogram of calibrated upstream error values with various sensor combinations; left: three sensors at locations 8, 16, and 25, middle: two sensors at locations 12 and 25, and right: two sensors at locations 22 and 25. A larger number of runs centred around the zero (x-axis) indicates better performance of the model.

This result was confirmed by performing the same analysis three times with varying error conditions on the US stage and sensor locations. Findings suggest that placing additional sensors closer to the downstream boundary improves the result. This may be because there is a change in riverbed slope at cross-section location 25 (refer to Figure 6.2). Therefore, an additional sensor located closer to this location should be able to measure the abrupt change in water level at this location accurately. Additionally, I am comparing observed and modelled discharge at the downstream location. Therefore, placing additional sensors closer to the downstream boundary may reduce the uncertainty or inaccuracy in the simulated stage and flow hydrograph closer to the downstream site, resulting in improvement in results. This result may change for different channel and flow conditions.

The histogram of AARE values for various combinations of sensors, as shown in Figure 6.5, indicates that two additional sensors placed closer to the downstream boundary are adequate to improve the estimation of unsteady flow discharge. In addition, when three additional sensors

(illustrated in Figure 6.5) were positioned closer to the downstream boundary, it was observed that the discharge estimation improved, nevertheless, the improvement was marginal.

The optimisation analysis applied to the river Wandle suggests that placing two or three additional sensors closer to the downstream boundary improves the unsteady flow parameter calibration and discharge estimation.

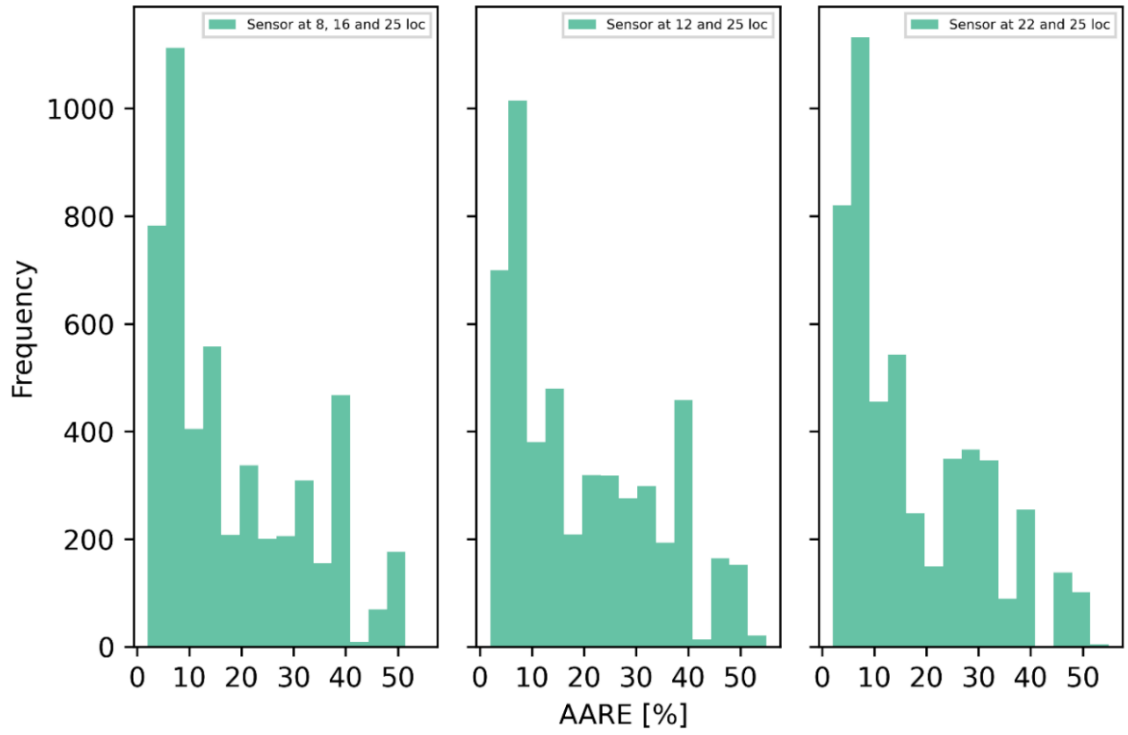

Figure 6.5: A histogram of AARE values with various sensor combinations; left: three sensors at locations 8, 16, and 25, middle: two sensors at locations 12 and 25, and right: two sensors at locations 22 and 25. A larger number of runs towards the zero (x-axis) indicates better performance of the model

To determine the optimal spacing between the additional sensors, all possible combinations of two and three sensors between locations 18 and 26 were evaluated. However, adjacent sensor combinations such as 18–19 and 18–19–20 were neglected to account for the variation of water surface slope and instrumental error. The average distance between two adjacent sensors is 45 metres.

Figure 6.6 depicts the evaluation of the performance of a sensor network for various combinations of two sensors. It can be observed that the US error criteria for various sensor combinations exhibit little variation. Therefore, sensor combinations are sorted according to AARE criteria (refer to Figure 6.7) for clarity.

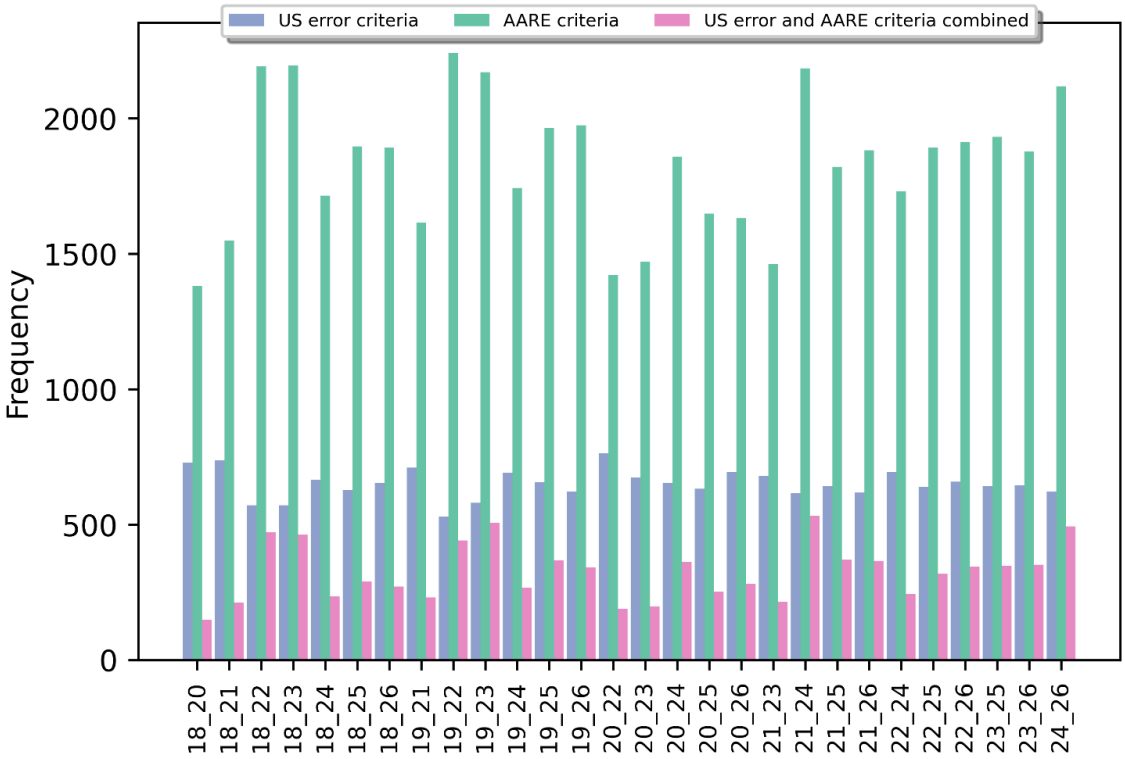

Figure 6.6: Performance evaluation of different combinations of two sensors. Y-axis shows, out of 5000 model evaluation, the number of times US error is calibrated within ± 0.0005 m, AARE is <10 % and common number of runs for which both US error and AARE criteria is met

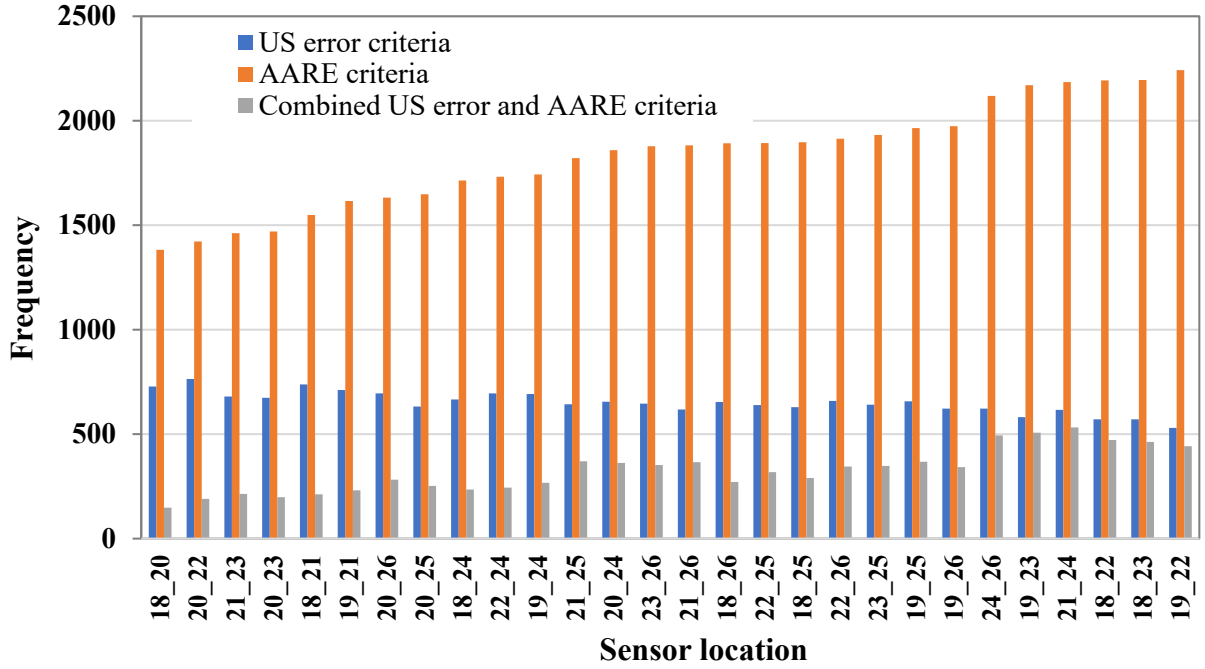

Figure 6.7: Same as Figure 6.6 but results are sorted according to increasing AARE criteria

For certain sensor combinations, such as 19-22, 18-23, 18-22, 21-24 and 19-23 there is a significant improvement in the discharge estimation, as it is more likely to achieve an AARE of less than ten percent (refer to Figure 6.7). We can observe that the optimal distance between sensors for these sensor combinations ranges between 145 and 225 m. It should be noted that in none of the aforementioned combinations is the additional sensor located at the downstream boundary, or location 26.

Although all five combinations provide optimal results, based on US error and AARE criteria combined, the optimal position for two additional sensors is determined to be between 21 and 24. In this instance, 135 m would be the optimal distance between sensors. It should be noted that this optimization would give a range of optimal solutions for additional sensor locations, and the decision to choose the additional sensor location would be up to the user and the accessibility of the location to install the sensor. For instance, if a user decides to keep spacing between the sensor constant, say 90 metres (or if this is the only feasible distance during field installation). Then, having additional sensors placed at location 24 and 26 would provide optimal results (refer to Figure 6.8). Similarly, if during field installation, only 135 metres spacing is feasible, then 19-22 sensor combinations would be an ideal choice for additional sensor (see Figure 6.9).

Because the average riverbed slope of Wandle is 0.00398 and the sensor used in this study has a resolution of 1 mm, it would be possible to measure the variation in the river's water surface slope even if sensors were placed at adjacent locations.

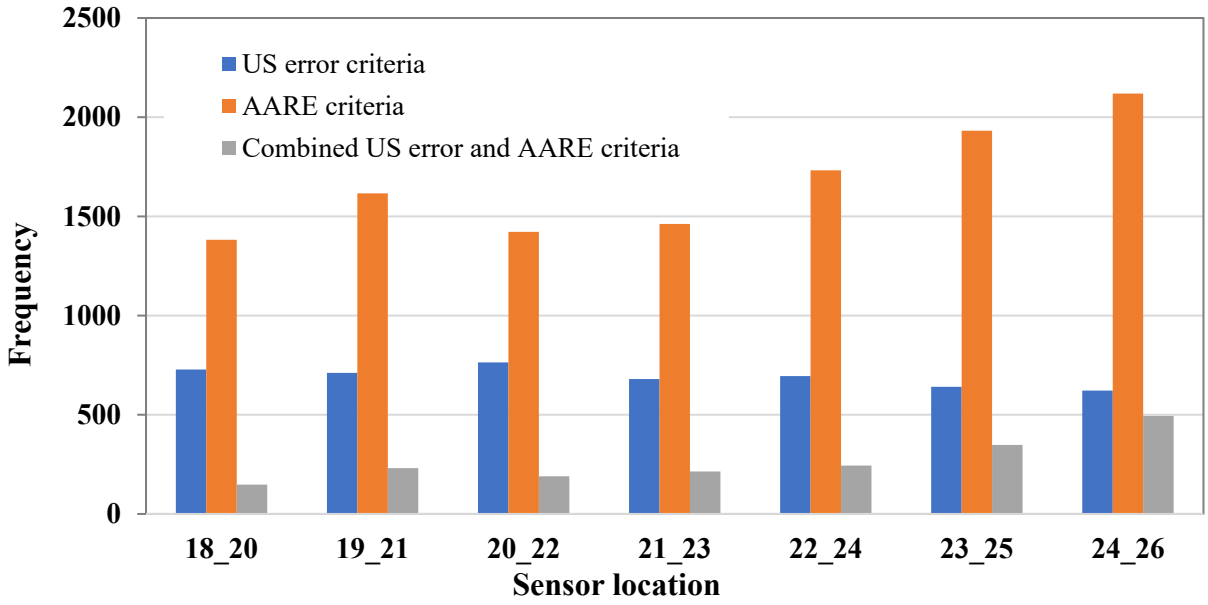

Figure 6.8: Performance evaluation of two sensor combination when the spacing between the sensors is kept constant at 90 metres

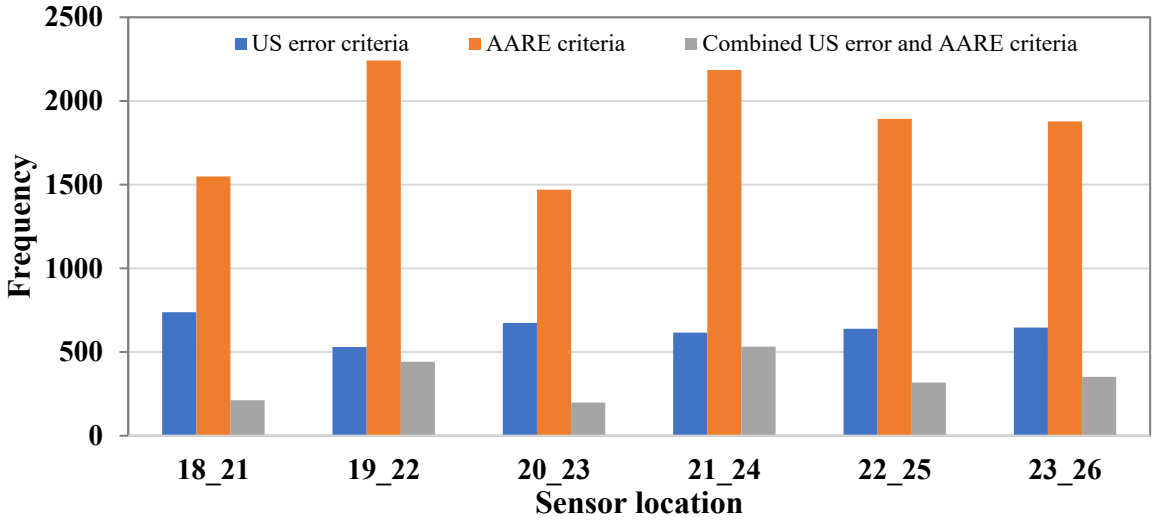

Figure 6.9: Performance evaluation of two sensor combination when the spacing between the sensors is kept constant at 135 metres

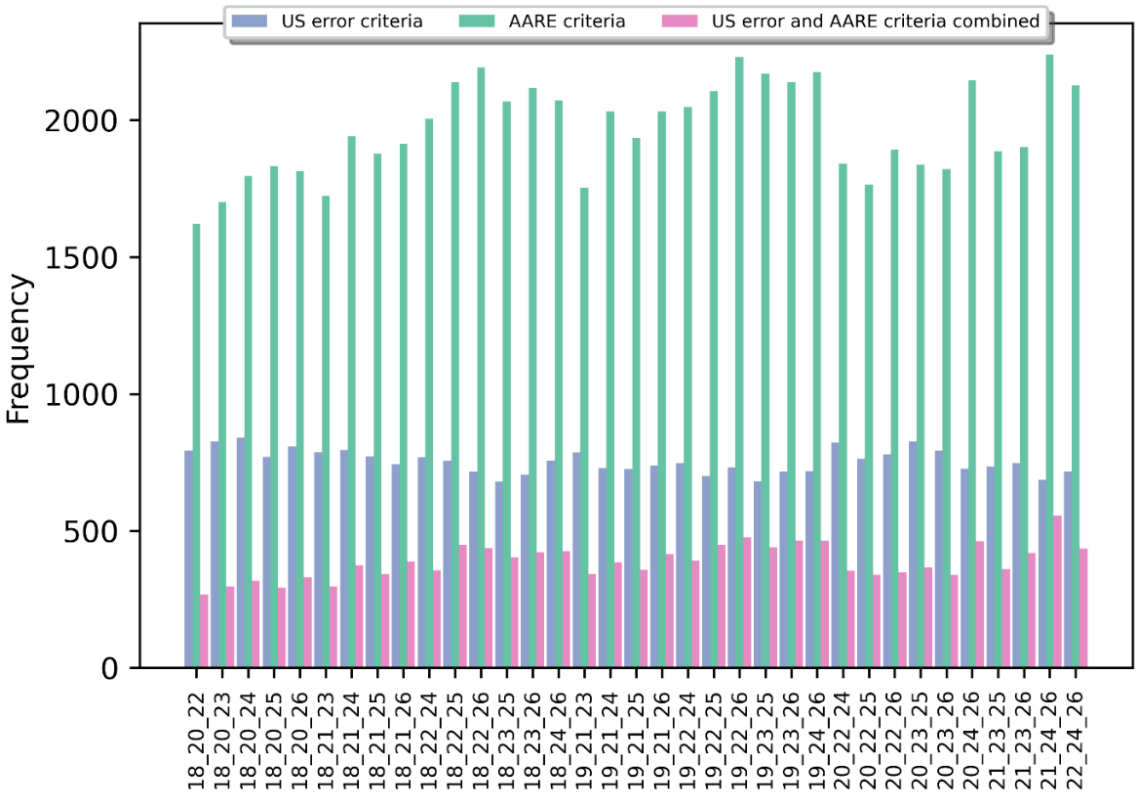

Figure 6.10: Performance evaluation of different combinations of three sensors. Y-axis shows, out of 5000 model evaluation, the number of times US error is calibrated within ± 0.0005 m, AARE is <10 % and common number of runs for which both US error and AARE criteria is met

Figure 6.10 illustrates the evaluation of the performance of a sensor network for various combinations of three sensors. Similar to two-sensor combinations, the variation in US error criteria for three-sensor combinations is minimal. Therefore, sensor combinations are sorted according to AARE criteria (refer to Figure 6.11) for clarity.

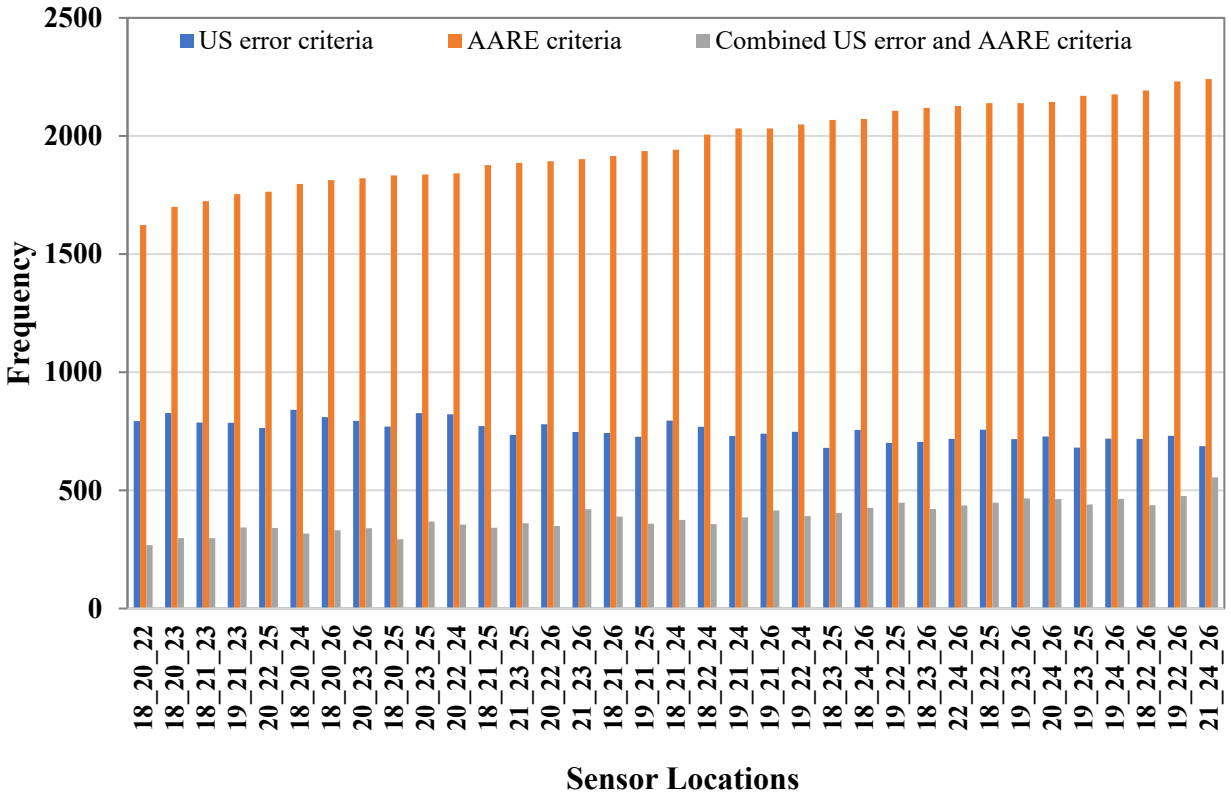

Figure 6.11: Same as Figure 6.10 but results are sorted according to increasing AARE criteria

For three distinct sensor combinations, namely 21-24-26, 19-22-26 and 18-22-26, there is a significant improvement in the discharge estimation, as it is more likely to achieve an AARE of less than 10%. Notably, the improvement in discharge estimation with three sensor combinations is greater than with two sensor combinations. Also, unlike two-sensor combinations, three-sensor combinations most of the time include an additional sensor at the downstream boundary (see RHS of the x-axis of Figure 6.11), or location 26. Based on US error and AARE criteria combined, the optimal location for three additional sensors is determined to be between 21, 24 and 26. Therefore, 135 and 90 metres is the optimal distance between these sensors.

In idealised river cases, similar results (not shown) were obtained. Compared to having no additional sensors, having two additional sensors (for a total of four) placed closer to the downstream boundary improved unsteady flow parameter calibration and discharge estimation.

6.5 Conclusions

This chapter test two approaches for optimising the location, number, and spacing of a sensor network. Both approaches demonstrate that the use of more than two sensors reduces the error in unsteady flow parameter calibration and discharge estimation. However, Approach I, which incorporates additional sensors as internal boundary conditions, is computationally demanding. In addition, the evaluation of a variety of idealised river scenarios revealed that the addition of more than two sensors did not provide a significant advantage.

Approach II includes stage data from the additional sensors in the post-processing of simulated stages or model calibration. This optimisation approach was evaluated using an unsteady flow model of the Wandle River. This approach provides evidence that compared to using two additional sensors, utilising three additional sensors placed closer to the downstream boundary improves parameter calibration and discharge estimation. However, calibration and discharge estimation improvement are marginal (approximately 3%). Nevertheless, the sensor network with three additional sensors (for a total of four sensors) is more reliable because the additional sensors can compensate for various errors in the upstream stage and reduce errors in discharge estimates at the downstream boundary. The Wandle case study demonstrated that this optimisation approach can be utilised to configure an optimal sensor network.

However, additional field testing and analysis are required to generalise the sensor optimisation algorithm for rivers with varying morphological characteristics. Also, in the case of low to moderate flows, AARE should be calculated by comparing the discharge from this method to the discharge obtained from more accurate methods, such as ADCP. Other parameters, such as measurement frequency, should also be incorporated into the optimization algorithm for studying floods.

7 Conclusions

River monitoring and discharge estimation are becoming ever more important practices to support the development of mitigation measures for weather and climate extremes. Past studies have concluded that the ideal river gauge of the future should directly monitor the variables that govern discharge (river stage), be able to do so continually, and not require devices to be placed in the water. This could significantly expand the measurement range, including high flows, make the results more accurate, and the procedure safer to implement. In line with this vision, the overall aim of this research was to explore the potential of self-built, low-cost, non-contact lidar sensors and sensor networks in monitoring river levels and develop a methodology to use stage data from such sensor networks to estimate unsteady flow river discharge dynamically at an ungauged location.

The lidar sensors employed in this study emit near-infrared light of wavelength 905nm and use the time-of-flight method to compute the distance between the sensor and the water surface. Various laboratory and field experiments were carried out to assess the sensor's performance as a function of measurement distance, surface roughness, air temperature, water turbidity, and measurement angle. The experiments concluded that the sensor could take measurements under all tested conditions, up to an incidence angle of ~ 40°. The accuracy of the sensor was found to be within a relative error of around 0.1%. A strong correlation between sensor temperature and accuracy was also observed. This could be due to suboptimal internal electronic compensation. Further, it was found that the precision of the sensor decreased with increasing measured distance and increased with the surface roughness of the water body. This means that sensors are better suited to monitor fast-flowing rivers.

After it was established that the sensors can efficiently monitor river levels, a methodology to use stage data from a network of sensors to estimate river discharge dynamically was developed. This methodology solves the governing equations of river flow, i.e., shallow water

equations, by utilising river geometry and synchronous measurement of stage data from the sensors network. Here, I use HEC-RAS as a numerical solver to obtain a unique solution for the shallow water equations. A Python script was developed to control and automate hydraulic simulations in the HEC-RAS. The developed discharge estimation methodology is employed in two steps. First, using stage data from sensors, it calibrates Manning's roughness coefficient and the initial condition of an unsteady flow river. Then, it uses the calibrated model to estimate the discharge dynamically. In this methodology, the Monte Carlo method is used to calibrate the parameters of the hydraulic model of rivers. This developed methodology was tested on several idealised rivers with various channel and flow conditions as well as on a kilometre-long stretch of the Wandle River in London, the United Kingdom. A sensitivity analysis was also performed to evaluate the impact of measurement error in stage data on discharge estimation and the robustness of the developed methodology. The results indicate that the methodology can be successfully applied to both prismatic and natural channels, as well as channels with lateral flows, does not require any discharge value, and can be used to develop rating curves at ungauged sites. The sensitivity analysis results show that for a mean of error varying between ± 25 %, the error in the calibration of Manning's roughness coefficient is between -8.5 % and 14 %. This indicates that the developed model is robust.

Although theoretically, stage data from two sensors are adequate to calibrate an unsteady flow hydraulic model and estimate river discharge at an ungauged location, it was found that utilising stage data from more than two sensors improves parameter calibration and discharge estimation. In the case of more than two sensors, the configuration of the sensor network, including 1) the location of the sensors, 2) the number of sensors, and 3) the distance between the sensors, has not previously been investigated. Therefore, two approaches for utilising stage data from a network of sensors and optimising the sensor network were explored. In the first approach, stage data is used as internal boundary conditions of a hydraulic model, while in the second, they are used to calibrate model parameters (i.e., used in post-processing of the model simulations). In both approaches, the Monte Carlo method is utilised to evaluate the value of additional sensors in unsteady flow calibration, discharge estimation, and optimal sensor network configuration. Both approaches were evaluated on idealised river channels and a natural river channel (River Wandle, London). In both instances, the calibration parameters of an unsteady flow hydraulic model and discharge hydrograph obtained at a location with more than two sensors were compared to those obtained with only two sensors to determine the value

of the additional sensors. Various sensor configurations were subjected to identical analyses to identify the optimal sensor network.

Both approaches demonstrated that the use of more than two sensors reduces the error in unsteady flow parameter calibration and discharge estimation. However, Approach I, which incorporates additional sensors as internal boundary conditions, is computationally demanding. In addition, the evaluation of a variety of idealised river scenarios revealed that the addition of more than two sensors did not provide a significant advantage. The results of Approach II, which includes stage data from the additional sensors in the post-processing of simulated stages, show that compared to using two additional sensors, utilising three additional sensors placed closer to the downstream boundary improves parameter calibration and discharge estimation. However, calibration and discharge estimation improvements are marginal (approximately 3%). Nevertheless, the sensor network with three additional sensors (for a total of four sensors) is more reliable because the additional sensors can compensate for various errors in the upstream stage and reduce errors in discharge estimates at the downstream boundary. The Wandle case study demonstrated that this optimisation approach can be utilised to configure an optimal sensor network.

The Python script developed for the discharge estimation methodology has been extended for 1) calibrating hydraulic models under homogenous and heterogenous Manning's roughness coefficient assumptions, 2) performing uncertainty and sensitivity analyses of unsteady flow parameters, and 3) conducting probabilistic flood inundation analyses in HEC-RAS. The developed scripts were tested on both an idealised river case and a real river, the river Brent in London.

7.1 Contribution to Science

This thesis made the following contributions:

- Demonstrated the use of low-cost sensors, developed as part of this thesis, for cost-effective and flexible method for river level measurement at high frequency.
- Developed a novel dynamic discharge estimation method to estimate river discharge using only stage data from network of sensors
- Developed and demonstrated a Python application to 1) calibrate hydraulic models under homogenous and heterogenous channel roughness assumptions, 2) perform

uncertainty and sensitivity analysis of unsteady flow parameters, and 3) perform probabilistic flood inundation analysis in HEC-RAS.

7.2 Limitations

Following are the limitations of this study:

- I could not compare lidar sensor with other sensors. Therefore, it would be useful to determine whether our findings could be generalised to sensors other than the one we used (e.g., lasers of different wavelengths, power, and pulse width).
- The developed discharge estimation method was only tested on medium and large idealised rivers. Therefore, the methodology can be tested for a few small rivers
- The developed dynamic discharge estimation method was tested in only one natural river, i.e., river Wandle, therefore, it should be tested in different rivers in the field
- River Wandle is an urban river with in-stream flow control measures such as spillways and sluice gate. Therefore, the flow in the river is mostly laminar. Thus, the discharge estimation methodology needs to be tested in turbulent river flow conditions.
- The discharge estimation methodology was not tested for river channel with lateral flows and hydraulic structures

7.3 Further work

This study tested the potential of a specific lidar sensor in monitoring river levels. However, it would be useful to determine whether the findings of this study could be generalised to sensors other than the ones used (e.g., lasers of different wavelengths, power, and pulse width) in this study. The wireless prototype sensors employed in this thesis use the Zigbee wireless data transmission protocol. Zigbee is a proprietary low-power, close-proximity (25–100 m) wireless network (Shah, 2018b). More recently, the LoRa (long range) standard has been developed specifically for IoT (Internet of Things) applications (Shah, 2018a). LoRa has a higher range (2–8 km) than Zigbee but a lower data transmission rate. Although ad-hoc experimental results can be found in the grey literature (The Things Network, 2017), no comprehensive tests have been published on the performance of Zigbee and LoRa in environmental settings typical for hydrometry (e.g., dense vegetation, riverbanks, complex topography). Therefore, further work can be carried out to test the performance of both transmission technologies under various

environmental conditions such as open grassland and forest of varying densities to choose a suitable technology for the sensor.

Only limited field testing of the discharge estimation methodology could be carried out in this study. Therefore, additional field testing and analysis can be carried out to generalise the discharge estimation and sensor optimisation algorithms for rivers with varying morphological characteristics. Furthermore, where available, discharge data from a rating curve was used to compare the discharge obtained from the developed methodology. Therefore, in the future, discharge obtained from more accurate methods, such as ADCP, should be used. In chapter five, the Monte Carlo method was employed to configure an optimal sensor network. As a next step, the optimisation algorithm proposed in this study can be made better by comparing it to metaheuristic algorithms like genetic programming. For example, measurement frequency could be added as one of the optimisation parameters.

River discharge data is used for a variety of scientific purposes, but one of the most important is constraining catchment-scale rainfall-runoff models, which are essential catchment management tools. Calibrating these models and reducing their predictive uncertainties is still a significant scientific challenge (Pappenberger & Beven, 2006; Beven & Westerberg, 2011), and the contribution of errors from discharge estimations has received considerable attention (e.g., Ocio et al., 2017 and references therein). In addition, recent research has demonstrated that "less-than-ideal" data, such as water level measurements and discharge measurements of lower accuracy or shorter duration, can be informative for calibrating models (Seibert & Beven, 2009; van Meerveld, Vis & Seibert, 2017). This is attributable to the decrease in information capacity with increasing time series length and the importance of time series attributes such as timing and the slope of the recession curve for calibration, which is frequently well captured in water level data. Therefore, it is necessary to investigate how data from a sensor network like the one proposed in this study can be utilised to constrain rainfall-runoff models.

References

Akan, A.O. (2006) Fundamentals of open-channel flow. In: *Open Channel Hydraulics*. Elsevier. pp. 1–23. doi:10.1016/B978-075066857-6/50002-3.

Alabyan, A.M., Krylenko, I.N., Potryasaev, S.A., Sokolov, B. v., Yusupov, R.M. & Zelentsov, V.A. (2016) Development of intelligent information systems for operational river-flood forecasting. *Herald of the Russian Academy of Sciences*. 86 (1). doi:10.1134/S1019331616010056.

Alhashimi, A., Varagnolo, D. & Gustafsson, T. (2015) Joint temperature-lasing mode compensation for time-of-flight LiDAR sensors. *Sensors (Switzerland)*. 15 (12). doi:10.3390/s151229854.

Alimenti, F., Bonafoni, S., Gallo, E., Palazzi, V., Vincenti Gatti, R., Mezzanotte, P., Roselli, L., Zito, D., Barbetta, S., Corradini, C., Termini, D. & Moramarco, T. (2020) Noncontact measurement of river surface velocity and discharge estimation with a low-cost doppler radar sensor. *IEEE Transactions on Geoscience and Remote Sensing*. 58 (7), 5195–5207. doi:10.1109/TGRS.2020.2974185.

Allouis, T., Bailly, J.-S. & Feurer, D. (2012) Assessing water surface effects on LiDAR bathymetry measurements in very shallow rivers: a theoretical study. In: *ESA 2nd Space for Hydrology Workshop*. 2012 p.

Andreadis, K.M., Brinkerhoff, C.B. & Gleason, C.J. (2020) Constraining the Assimilation of SWOT Observations With Hydraulic Geometry Relations. *Water Resources Research*. 56 (5). doi:10.1029/2019WR026611.

Anon (2016) *Monte Carlo method*. 2016. https://en.wikipedia.org/wiki/Monte_Carlo_method [Accessed: 24 January 2022].

Anon (2021) *QGIS: A Free and Open Source Geographic Information System*. 2021. https://qgis.org/en/site/index.html [Accessed: 28 October 2021].

Aricò, C., Corato, G., Tucciarelli, T., Meftah, M. ben, Petrillo, A.F. & Mossa, M. (2010) Discharge estimation in open channels by means of water level hydrograph analysis. *Journal of Hydraulic Research*. 48 (5), 612–619. doi:10.1080/00221686.2010.507352.

Aricò, C., Nasello, C. & Tucciarelli, T. (2009) Using unsteady-state water level data to estimate channel roughness and discharge hydrograph. *Advances in Water Resources*. 32 (8), 1223–1240. doi:10.1016/j.advwatres.2009.05.001.

Aricò, C., Sinagra, M., Begnudelli, L. & Tucciarelli, T. (2011) MAST-2D diffusive model for flood prediction on domains with triangular Delaunay unstructured meshes. *Advances in Water Resources*. 34 (11). doi:10.1016/j.advwatres.2011.08.002.

Aronica, G., Hankin, B. & Beven, K. (1998) Uncertainty and equifinality in calibrating distributed roughness coefficients in a flood propagation model with limited data. *Advances in Water Resources*. 22 (4), 349–365. doi:10.1016/S0309-1708(98)00017-7.

Aryal, D., Wang, L., Adhikari, T.R., Zhou, J., Li, X., Shrestha, M., Wang, Y. & Chen, D. (2020) A model-based flood hazard mapping on the southern slope of Himalaya. *Water (Switzerland)*. 12 (2). doi:10.3390/w12020540.

Assumpção, T.H., Popescu, I., Jonoski, A. & Solomatine, D.P. (2018) Citizen observations contributing to flood modelling: Opportunities and challenges. *Hydrology and Earth System Sciences*. doi:10.5194/hess-22-1473-2018.

Atanassov, E. & Dimov, I.T. (2008) What Monte Carlo models can do and cannot do efficiently? *Applied Mathematical Modelling*. 32 (8). doi:10.1016/j.apm.2007.04.010.

Babister, M., Retallick, M., Loveridge, M., Testoni, I., Varga, C. & Craig, R. (2016a) A Monte Carlo framework for assessment of how mitigation options affect flood hydrograph characteristics. *Australian Journal of Water Resources*. 20 (1), 30–38. doi:10.1080/13241583.2016.1145851.

Babister, M., Retallick, M., Loveridge, M., Testoni, I., Varga, C. & Craig, R. (2016b) A Monte Carlo framework for assessment of how mitigation options affect flood hydrograph characteristics. *Australian Journal of Water Resources*. 20 (1), 30–38. doi:10.1080/13241583.2016.1145851.

Bakry, M.F., Gates, T.K. & Khattab, A.F. (1992) Field-Measured Hydraulic Resistance Characteristics in Vegetation-Infested Canals. *Journal of Irrigation and Drainage Engineering*. 118 (2). doi:10.1061/(asce)0733-9437(1992)118:2(256).

Balaji, B. & Kumar, S. (2018) Dam break analysis of kalyani dam using HEC-RAS. *International Journal of Civil Engineering and Technology*. 9 (5).

di Baldassarre, G. & Montanari, A. (2009) Uncertainty in river discharge observations: A quantitative analysis. *Hydrology and Earth System Sciences*. 13 (6). doi:10.5194/hess-13-913-2009.

Barbetta, S., Moramarco, T. & Perumal, M. (2017) A Muskingum-based methodology for river discharge estimation and rating curve development under significant lateral inflow conditions. *Journal of Hydrology*. 554, 216–232. doi:10.1016/j.jhydrol.2017.09.022.

Basyal, G., Gregory, J., Palmberg, B. & Tarbet, K. (2019) *Pydsstools*. https://github.com/gyanz/pydsstools.

Beven, K. & Binley, A. (1992) The future of distributed models: Model calibration and uncertainty prediction. *Hydrological Processes*. 6 (3), 279–298. doi:10.1002/hyp.3360060305.

Beven, K. & Westerberg, I. (2011) On red herrings and real herrings: disinformation and information in hydrological inference. *Hydrological Processes*. 25 (10), 1676–1680. doi:10.1002/hyp.7963.

Bharath, A., Shivapur, A. v., Hiremath, C.G. & Maddamsetty, R. (2021) Dam break analysis using HEC-RAS and HEC-GeoRAS: A case study of Hidkal dam, Karnataka state, India. *Environmental Challenges*. 5. doi:10.1016/j.envc.2021.100401.

Bhargava, D.S. & Mariam, D.W. (1991) Light penetration depth, turbidity and reflectance related relationship and models. *ISPRS Journal of Photogrammetry and Remote Sensing*. 46 (4). doi:10.1016/0924-2716(91)90055-Z.

Bhargava, D.S. & Mariam, D.W. (1990) Spectral reflectance relationships to turbidity generated by different clay materials. *Photogrammetric Engineering and Remote Sensing*. 56 (2), 225–229.

Bhusal, J., Ballesteros-Cánovas, J.A., Allen, S., Paul, J.D., Smith, P.J., Schiller, A., Dewulf, A., Supper, R., Neupane, B., Nayaval, J.L., Stoffel, M., Dhital, M.R., Dugar, S., Liu, W., Clark, J., Hannah, D.M., Cieslik, K. & Buytaert, W. (2017) Citizen science for hydrological risk reduction and resilience building. *Wiley Interdisciplinary Reviews: Water*. 5 (1), e1262. doi:10.1002/wat2.1262.

Birkhead, A.L. & James, C.S. (1998) Synthesis of rating curves from local stage and remote discharge monitoring using nonlinear muskingum routing. *Journal of Hydrology*. 205 (1–2). doi:10.1016/S0022-1694(97)00131-5.

Bjerklie, D.M., Birkett, C.M., Jones, J.W., Carabajal, C., Rover, J.A., Fulton, J.W. & Garambois, P.A. (2018) Satellite remote sensing estimation of river discharge: Application to the Yukon River Alaska. *Journal of Hydrology*. 561, 1000–1018. doi:10.1016/j.jhydrol.2018.04.005.

Bonacci, O. (1983) Several methods for discharge measurements of floods/Plusieures méthodes de mesure du débit des crues. *Hydrological Sciences Journal*. 28 (4). doi:10.1080/02626668309491992.

Boon, J.D. & Brubaker, J.M. (2008) Acoustic-microwave water level sensor comparisons in an estuarine environment. In: *OCEANS 2008*. 2008 p. doi:10.1109/OCEANS.2008.5151893.

Bozzi, S., Passoni, G., Bernardara, P., Goutal, N. & Arnaud, A. (2015) Roughness and Discharge Uncertainty in 1D Water Level Calculations. *Environmental Modeling & Assessment*. 20 (4), 343–353. doi:10.1007/s10666-014-9430-6.

British Oceanographic Data Centre (BODC) (n.d.) *Wave data series*. 2018. https://www.bodc.ac.uk/data/bodc_database/waves/ [Accessed: 16 January 2023].

Brunner, G.W. (2016a) *HEC-RAS Hydraulic Reference Manual*. (February) p.547.

Brunner, G.W. (2016b) *HEC-RAS River Analysis System User ' s Manual*. (February) p.962. https://www.hec.usace.army.mil/software/hec-ras/download.aspx.

Brunner, G.W., Warner, J.C., Wolfe, B.C., Piper, S.S. & Marston, L. (2016) *HEC-RAS Applications Guide*. (February) p.519.

Burguete, J., García-Navarro, P., Murillo, J. & García-Palacín, I. (2007) Analysis of the Friction Term in the One-Dimensional Shallow-Water Model. *Journal of Hydraulic Engineering*. 133 (9). doi:10.1061/(asce)0733-9429(2007)133:9(1048).

Buytaert, W., Zulkafli, Z., Grainger, S., Acosta, L., Alemie, T.C., et al. (2014) Citizen science in hydrology and water resources: Opportunities for knowledge generation, ecosystem service management, and sustainable development. *Frontiers in Earth Science*.2. doi:10.3389/feart.2014.00026.

Cervantes, M. (1972) Chapter 4 The Monte Carlo Method. In: *Mathematics in Science and Engineering*. pp. 181–208. doi:10.1016/S0076-5392(08)61352-1.

Chacon-Hurtado, J.C., Alfonso, L. & Solomatine, D.P. (2017) Rainfall and streamflow sensor network design: A review of applications, classification, and a proposed framework. *Hydrology and Earth System Sciences*. doi:10.5194/hess-21-3071-2017.

Chaparro, B.M., Thuillier, S., Menezes, L.F., Manach, P.Y. & Fernandes, J. v. (2008) Material parameters identification: Gradient-based, genetic and hybrid optimization algorithms. *Computational Materials Science*. 44 (2). doi:10.1016/j.commatsci.2008.03.028.

Cheng, L., Niu, J., Luo, C., Shu, L., Kong, L., Zhao, Z. & Gu, Y. (2018) Towards minimum-delay and energy-efficient flooding in low-duty-cycle wireless sensor networks. *Computer Networks*. 134. doi:10.1016/j.comnet.2018.01.012.

Chow, V. te (2006) *Open Channel Hydraulics*. Elsevier. doi:10.1016/B978-0-7506-6857-6.X5000-0.

Coddington, I., Swann, W.C., Nenadovic, L. & Newbury, N.R. (2009) Rapid and precise absolute distance measurements at long range. *Nature Photonics*. 3 (6). doi:10.1038/nphoton.2009.94.

Comina, C., Lasagna, M., de Luca, D.A. & Sambuelli, L. (2014) Geophysical methods to support correct water sampling locations for salt dilution gauging. *Hydrology and Earth System Sciences*. 18 (8). doi:10.5194/hess-18-3195-2014.

Costa, J.E., Cheng, R.T., Haeni, F.P., Melcher, N., Spicer, K.R., Hayes, E., Plant, W., Hayes, K., Teague, C. & Barrick, D. (2006) Use of radars to monitor stream discharge by noncontact methods. *Water Resources Research*. 42 (7), 1–14. doi:10.1029/2005WR004430.

Costa, J.E., Spicer, K.R., Cheng, R.T., Haeni, F.P., Melcher, N.B., Thurman, E.M., Plant, W.J. & Keller, W.C. (2000) Measuring stream discharge by non-contact methods: A proof-of-concept experiment. *Geophysical Research Letters*. 27 (4). doi:10.1029/1999GL006087.

Courant, R., Friedrichs, K. & Lewy, H. (1928) Über die partiellen Differenzengleichungen der mathematischen Physik. *Mathematische Annalen*. 100 (1), 32–74. doi:10.1007/BF01448839.

Crawford, C.G. (1991) Estimation of suspended-sediment rating curves and mean suspended-sediment loads. *Journal of Hydrology*. 129 (1–4). doi:10.1016/0022-1694(91)90057-O.

Devak, M. & Dhanya, C.T. (2017) Sensitivity analysis of hydrological models: review and way forward. *Journal of Water and Climate Change*. 8 (4), 557–575. doi:10.2166/wcc.2017.149.

Ding, Y. & Wang, S.S.Y. (2006) Optimal Control of Open-Channel Flow Using Adjoint Sensitivity Analysis. *Journal of Hydraulic Engineering*. 132 (11). doi:10.1061/(asce)0733-9429(2006)132:11(1215).

Dobriyal, P., Badola, R., Tuboi, C. & Hussain, S.A. (2017) A review of methods for monitoring streamflow for sustainable water resource management. *Applied Water Science*. 7 (6), 2617–2628. doi:10.1007/s13201-016-0488-y.

Dottori, F., Martina, M.L. v. & Todini, E. (2009) A dynamic rating curve approach to indirect discharge measurement. *Hydrology and Earth System Sciences*. 13 (6), 847–863. doi:10.5194/hess-13-847-2009.

Durand, M., Gleason, C.J., Garambois, P.A., Bjerklie, D., Smith, L.C., et al. (2016) An intercomparison of remote sensing river discharge estimation algorithms from measurements of river height, width, and slope. *Water Resources Research*. doi:10.1002/2015WR018434.

Durand, M., Neal, J., Rodríguez, E., Andreadis, K.M., Smith, L.C. & Yoon, Y. (2014) Estimating reach-averaged discharge for the River Severn from measurements of river water surface elevation and slope. *Journal of Hydrology*. 511, 92–104. doi:10.1016/j.jhydrol.2013.12.050.

Dysarz, T. (2018) Application of Python Scripting Techniques for Control and Automation of HEC-RAS Simulations. *Water*. 10 (10), 1382. doi:10.3390/w10101382.

Eltner, A., Sardemann, H. & Grundmann, J. (2019) Flow velocity and discharge measurement in rivers using terrestrial and UAV imagery. *Hydrology and Earth System Sciences Discussions*. (June), 1–29. doi:10.5194/hess-2019-289.

Environment Agency (2021a) *Environment Agency Real Time flood monitoring API*. 15 July 2021. https://environment.data.gov.uk/flood-monitoring/doc/reference#individual-measure [Accessed: 10 July 2021].

Environment Agency (2021b) *LIDAR composite DTM 2020 - 1m*. 13 September 2021. https://environment.data.gov.uk/dataset/668881ad-4f8f-42bd-b835-89acf0269496 [Accessed: 13 August 2021].

Environment Agency (2021c) *Summerstown*. 11 June 2021. https://environment.data.gov.uk/flood-monitoring/id/stations/4192TH.html [Accessed: 31 August 2022].

Environment Agency (2021d) *Wandle Park Main Channel*. 11 June 2021. https://environment.data.gov.uk/flood-monitoring/id/stations/4180_w1TH.html [Accessed: 31 August 2022].

Environment Agency (UK) (2018) *National River Flow Archive*. 2018. https://nrfa.ceh.ac.uk/gauging-station-information [Accessed: 8 January 2018].

Fekete, B.M. & Vörösmarty, C.J. (2007) The current status of global river discharge monitoring and potential new technologies complementing traditional discharge measurements. *International Association of Hydrological Sciences*. (November 2002), 20–22.

Fenton, J.D. & Keller, R.J. (2001) The Calculation of Streamflow from Measurements of Stage. *Technical Report 01/6*. (September), 84. http://www.catchment.crc.org.au/pdfs/technical200106.pdf.

Fernandez-Diaz, J.C., Glennie, C.L., Carter, W.E., Shrestha, R.L., Sartori, M.P., Singhania, A., Legleiter, C.J. & Overstreet, B.T. (2014) Early results of simultaneous terrain and shallow water bathymetry mapping using a single-wavelength airborne LiDAR sensor. *IEEE Journal of Selected Topics in Applied Earth Observations and Remote Sensing*. 7 (2). doi:10.1109/JSTARS.2013.2265255.

Franchini, M., Lambert, P. & di Giammarco, P. (1999) Rating curve estimation using local stages, upstream discharge data and a simplified hydraulic model. *Hydrology and Earth System Sciences*. 3 (4). doi:10.5194/hess-3-541-1999.

Fread, D.L. (1974) *Numerical properties of implicit four-point finite difference equations of unsteady flow*. https://repository.library.noaa.gov/view/noaa/13510.

Fread, D.L. & Smith, G.F. (1978) CALIBRATION TECHNIQUE FOR 1-D UNSTEADY FLOW MODELS. *ASCE J Hydraul Div*. 104 (7). doi:10.1061/jyceaj.0005026.

Freer, J., Beven, K. & Ambroise, B. (1996) Bayesian estimation of uncertainty in runoff prediction and the value of data: An application of the GLUE approach. *Water Resources Research*.32 (7). doi:10.1029/95WR03723.

Fryer, M.J. & Rubinstein, R.Y. (1983) Simulation and the Monte Carlo Method. *Journal of the Royal Statistical Society. Series A (General)*. 146 (1), 95. doi:10.2307/2981504.

Fujita, I., Muste, M. & Kruger, A. (1998) Large-scale particle image velocimetry for flow analysis in hydraulic engineering applications. *Journal of Hydraulic Research*. 36 (3). doi:10.1080/00221689809498626.

Garambois, P.A. & Monnier, J. (2015) Inference of effective river properties from remotely sensed observations of water surface. *Advances in Water Resources*. 79. doi:10.1016/j.advwatres.2015.02.007.

Garmin (2016) *Operation manual and technical specifications*.

Gerlak, A.K., Lautze, J. & Giordano, M. (2011) Water resources data and information exchange in transboundary water treaties. *International Environmental Agreements: Politics, Law and Economics*. 11 (2). doi:10.1007/s10784-010-9144-4.

Gleason, C.J., Garambois, P.A. & Durand, M.T. (2018) Tracking river flows from space. *Eos*. 99 (1). doi:10.1029/2017eo078085.

Goodell, C. (2014) *Breaking the HEC-RAS code-A user's guide to automating HEC-RAS*. First. California, h2ls. www.therassolution.com.

Gordon, N.D., McMahon, T.A., Finlayson, B.L., Gippel, C.J. & Nathan, R.J. (2004) *Stream hydrology: An introduction for ecologists, Second Edition, Ecological Engineering.*

Gubbi, J., Buyya, R., Marusic, S. & Palaniswami, M. (2013) Internet of Things (IoT): A vision, architectural elements, and future directions. *Future Generation Computer Systems*. 29 (7), 1645–1660. doi:10.1016/j.future.2013.01.010.

Guenther, G.C. (1986) Wind And Nadir Angle Effects On Airborne Lidar Water 'Surface' Returns. In: *Ocean Optics VIII*. 1986 p. doi:10.1117/12.964243.

Gutierrez, J., Villa-Medina, J.F., Nieto-Garibay, A. & Porta-Gandara, M.A. (2014) Automated irrigation system using a wireless sensor network and GPRS module. *IEEE Transactions on Instrumentation and Measurement*. 63 (1). doi:10.1109/TIM.2013.2276487.

Hagemann, M.W., Gleason, C.J. & Durand, M.T. (2017) BAM: Bayesian AMHG-Manning Inference of Discharge Using Remotely Sensed Stream Width, Slope, and Height. *Water Resources Research*. 53 (11). doi:10.1002/2017WR021626.

Hannah, D.M., Demuth, S., van Lanen, H.A.J., Looser, U., Prudhomme, C., Rees, G., Stahl, K. & Tallaksen, L.M. (2011) Large-scale river flow archives: Importance, current status and future needs. *Hydrological Processes*. doi:10.1002/hyp.7794.

Harlan, M.E., Gleason, C.J., Altenau, E.H., Butman, D., Carter, T., et al. (2021) Discharge Estimation From Dense Arrays of Pressure Transducers. *Water Resources Research*. 57 (3). doi:10.1029/2020WR028714.

Hart, J.K. & Martinez, K. (2006) Environmental Sensor Networks: A revolution in the earth system science? *Earth-Science Reviews*. 78 (3–4), 177–191. doi:10.1016/j.earscirev.2006.05.001.

Hauet, A., Creutin, J.D. & Belleudy, P. (2008) Sensitivity study of large-scale particle image velocimetry measurement of river discharge using numerical simulation. *Journal of Hydrology*. doi:10.1016/j.jhydrol.2007.10.062.

Herschy, R.W. (2008) *Streamflow Measurement*. CRC Press.

Hoang, T., Rahman, A., Weinmann, P.E., Laurenson, E. & Nathan, R. (1999) Joint probability description of design rainfalls. In: *Water 99 Joint Congress, Brisbane, Australia, Institution of Engineers*. 1999 p.

Höfle, B., Vetter, M., Pfeifer, N., Mandlburger, G. & Stötter, J. (2009) Water surface mapping from airborne laser scanning using signal intensity and elevation data. *Earth Surface Processes and Landforms*. 34 (12). doi:10.1002/esp.1853.

Huang, Y. & Qin, X. (2014) Uncertainty analysis for flood inundation modelling with a random floodplain roughness field. *Environmental Systems Research*. 3 (1), 9. doi:10.1186/2193-2697-3-9.

Hund, S. v., Johnson, M.S. & Keddie, T. (2016) Developing a Hydrologic Monitoring Network in Data-Scarce Regions Using Open-Source Arduino Dataloggers. *Agricultural & Environmental Letters*. 1 (1). doi:10.2134/ael2016.02.0011.

Husain, A. (2017) Flood Modelling by using HEC-RAS. *International Journal of Engineering Trends and Technology*. 50 (1), 1–7. doi:10.14445/22315381/ijett-v50p201.

Jekel, C. (2021) *Discrete Frechet distance*. 20 August 2021. https://pypi.org/project/similaritymeasures/ [Accessed: 31 August 2022].

Jensen, O.B., Andersen, P.E., Sumpf, B., Hasler, K.-H., Erbert, G. & Petersen, P.M. (2009) 15 W green light generation by single-pass second harmonic generation of a single-frequency tapered diode laser. *Optics Express*. 17 (8). doi:10.1364/oe.17.006532.

Jodeau, M., Hauet, A., Paquier, A., le Coz, J. & Dramais, G. (2008) Application and evaluation of LS-PIV technique for the monitoring of river surface velocities in high flow conditions. *Flow Measurement and Instrumentation*. 19 (2). doi:10.1016/j.flowmeasinst.2007.11.004.

Joshi, N., Lamichhane, G.R., Rahaman, M.M., Kalra, A. & Ahmad, S. (2019) Application of HEC-RAS to study the sediment transport characteristics of Maumee River in Ohio. In: *World Environmental and Water Resources Congress 2019: Hydraulics, Waterways, and Water Distribution Systems Analysis - Selected Papers from the World Environmental and Water Resources Congress 2019*. 2019 p. doi:10.1061/9780784482353.024.

Jung, Y. & Merwade, V. (2012) Uncertainty Quantification in Flood Inundation Mapping Using Generalized Likelihood Uncertainty Estimate and Sensitivity Analysis. *Journal of Hydrologic Engineering*. 17 (4), 507–520. doi:10.1061/(ASCE)HE.1943-5584.0000476.

Kiang, J.E., Gazoorian, C., McMillan, H., Coxon, G., le Coz, J., Westerberg, I.K., Belleville, A., Sevrez, D., Sikorska, A.E., Petersen-Øverleir, A., Reitan, T., Freer, J., Renard, B., Mansanarez, V. & Mason, R. (2018) A Comparison of Methods for Streamflow Uncertainty Estimation. *Water Resources Research*. 54 (10). doi:10.1029/2018WR022708.

Kikuta, H., Iwata, K. & Nagata, R. (1986) Distance measurement by the wavelength shift of laser diode light. *Applied Optics*. 25 (17). doi:10.1364/ao.25.002976.

Kilpelä, A., Pennala, R. & Kostamovaara, J. (2001) Precise pulsed time-of-flight laser range finder for industrial distance measurements. *Review of Scientific Instruments*. 72 (4). doi:10.1063/1.1355268.

Kim, D. (2012) Assessment of longitudinal dispersion coefficients using Acoustic Doppler Current Profilers in large river. *Journal of Hydro-Environment Research*. 6 (1). doi:10.1016/j.jher.2011.06.001.

Kleinschmidt (2019) *HEC-RAS Help*. 2019. https://www.kleinschmidtgroup.com/the-ras-solution-forum/forum/hec-ras-help/ [Accessed: 10 October 2019].

Knoben, W.J.M., Freer, J.E. & Woods, R.A. (2019) Technical note: Inherent benchmark or not? Comparing Nash–Sutcliffe and Kling–Gupta efficiency scores. *Hydrology and Earth System Sciences*. 23 (10), 4323–4331. doi:10.5194/hess-23-4323-2019.

Lacasta, A., Morales-Hernández, M., Burguete, J., Brufau, P. & García-Navarro, P. (2017) Calibration of the 1D shallow water equations: A comparison of Monte Carlo and gradient-based optimization methods. *Journal of Hydroinformatics*. 19 (2). doi:10.2166/hydro.2017.021.

Lai, C. (1986) NUMERICAL MODELING OF UNSTEADY OPEN-CHANNEL FLOW. *Advances in Hydroscience*. 14. doi:10.1016/b978-0-12-021814-1.50008-2.

Lamberti, P. & Pilati, S. (1990) Quasi-kinematic flood wave propagation. *Meccanica*. 25 (2). doi:10.1007/BF01566211.

Lawson, T.B. (1995) *Fundamentals of Aquacultural Engineering*. doi:10.1007/978-1-4615-7047-9.

Lednev, V.N., Pershin, S.M., Yulmetov, R.N. & Bunkin, A.F. (2013) Remote sensing of ice and snow by compact Raman LIDAR. In: *Proceedings of the International Conference on Port and Ocean Engineering under Arctic Conditions, POAC*. 2013 p.

Lee, J., Kim, Y.J., Lee, K., Lee, S. & Kim, S.W. (2010) Time-of-flight measurement with femtosecond light pulses. *Nature Photonics*. 4 (10). doi:10.1038/nphoton.2010.175.

Lee, K., Firoozfar, A.R. & Muste, M. (2017) Technical Note: Monitoring of unsteady open channel flows using the continuous slope-area method. *Hydrology and Earth System Sciences*. 21 (3), 1863–1874. doi:10.5194/hess-21-1863-2017.

Lee, K.T., Ho, Y.-H. & Chyan, Y.-J. (2006) Bridge Blockage and Overbank Flow Simulations Using HEC–RAS in the Keelung River during the 2001 Nari Typhoon. *Journal of Hydraulic Engineering*. 132 (3). doi:10.1061/(asce)0733-9429(2006)132:3(319).

Leon, A.S. & Goodell, C. (2016a) Controlling HEC-RAS using MATLAB. *Environmental Modelling & Software*. 84, 339–348. doi:10.1016/j.envsoft.2016.06.026.

Leon, A.S. & Goodell, C. (2016b) Controlling HEC-RAS using MATLAB. *Environmental Modelling & Software*. 84, 339–348. doi:10.1016/j.envsoft.2016.06.026.

Li, Y., Geng, Y. & Mao, L. (2020) Calibration method for Manning's roughness coefficient for a river flume model. *Water Science and Technology: Water Supply*. 20 (8), 3597–3603. doi:10.2166/ws.2020.235.

Liggett, J.A. & Cunge, J.A. (1975) *Numerical methods for the solution of the unsteady flow equations*. In: K. Mahmood & V. Yevjevich (eds.). Littleton, Water Resources Publications. p.

Liu, D. (2009) *Uncertainty quantification with shallow water equations*. Braunschweig, Technical University of Braunschweig. doi:https://doi.org/10.24355/dbbs.084-201001211026-0.

Liu, X., Peterson, J. & Zhang, Z. (2005) High-resolution DEM generated from LiDAR data for water resource management. In: *MODSIM05 - International Congress on Modelling and Simulation: Advances and Applications for Management and Decision Making, Proceedings*. 2005 p.

Loucks, D.P. & van Beek, E. (2017) *Water resource systems planning and management: An introduction to methods, models, and applications*. doi:10.1007/978-3-319-44234-1.

Mao, F., Clark, J., Buytaert, W., Krause, S. & Hannah, D.M. (2018) Water sensor network applications: Time to move beyond the technical? *Hydrological Processes*.32 (16). doi:10.1002/hyp.13179.

van Meerveld, H.J.I., Vis, M.J.P. & Seibert, J. (2017) Information content of stream level class data for hydrological model calibration. *Hydrology and Earth System Sciences*. 21 (9), 4895–4905. doi:10.5194/hess-21-4895-2017.

Milan, D.J., Heritage, G.L., Large, A.R.G. & Entwistle, N.S. (2010) Mapping hydraulic biotopes using terrestrial laser scan data of water surface properties. *Earth Surface Processes and Landforms*. 35 (8). doi:10.1002/esp.1948.

Montesano, F.F., van Iersel, M.W., Boari, F., Cantore, V., D'Amato, G. & Parente, A. (2018) Sensor-based irrigation management of soilless basil using a new smart irrigation system: Effects of set-point on plant physiological responses and crop performance. *Agricultural Water Management*. 203. doi:10.1016/j.agwat.2018.02.019.

Moore, M.F., Vasconcelos, J.G., Zech, W.C. & Soares, E.P. (2016) A procedure for resolving thermal artifacts in pressure transducers. *Flow Measurement and Instrumentation*. 52. doi:10.1016/j.flowmeasinst.2016.10.010.

Moramarco, T., Barbetta, S., Melone, F. & Singh, V.P. (2005) Relating Local Stage and Remote Discharge with Significant Lateral Inflow. *Journal of Hydrologic Engineering*. 10 (1). doi:10.1061/(asce)1084-0699(2005)10:1(58).

Moramarco, T. & Singh, V.P. (2001) Simple Method for Relating Local Stage and Remote Discharge. *Journal of Hydrologic Engineering*. 6 (1). doi:10.1061/(asce)1084-0699(2001)6:1(78).

Morlock, S.E. (1996) Evaluation of Acoustic Doppler Current Profiler Measurements of River Discharge. *Water-Resources Investigations Report 95-4218*.

Mueller, D.S. (2003) Field evaluation of boat-mounted acoustic Doppler instruments used to measure streamflow. In: *Proceedings of the IEEE Working Conference on Current Measurement*. 2003 p. doi:10.1109/ccm.2003.1194278.

Mueller, D.S. & Wagner, C.R. (2009) Measuring discharge with acoustic Doppler current profilers from a moving boat. *U. S. Geological Survey Techniques and Methods*. (December).

Muste, M., Bacotiu, C. & Thomas, D. (2019) Evaluation of the slope-area method for continuous streamflow monitoring. In: *38th IAHR World Congress - 'Water: Connecting the World'*. 1 September 2019 pp. 121–130. doi:10.3850/38WC092019-1860.

Nasirudin, M.A., Za'bah, U.N. & Sidek, O. (2011) Fresh water real-time monitoring system based on wireless sensor network and GSM. In: *2011 IEEE Conference on Open Systems, ICOS 2011*. 2011 p. doi:10.1109/ICOS.2011.6079290.

National River Flow Archive (2021) *Wandle at Wandle Park*. 4 June 2021. https://nrfa.ceh.ac.uk/data/station/info/39085 [Accessed: 22 August 2022].

von Neumann, J. (1951) Various techniques used in connection with random digits. *Nat. Bureau Standards*. 12, 36–38.

Nihei, Y. & Kimizu, A. (2008) A new monitoring system for river discharge with horizontal acoustic Doppler current profiler measurements and river flow simulation. *Water Resources Research*. 44 (4). doi:10.1029/2008WR006970.

NRFA (2022) *UK River and flow regimes*. 2022. https://nrfa.ceh.ac.uk/uk-river-flow-regimes [Accessed: 15 January 2023].

Oberg, K. & Mueller, D.S. (2007) Validation of Streamflow Measurements Made with Acoustic Doppler Current Profilers. *Journal of Hydraulic Engineering*. 133 (12). doi:10.1061/(asce)0733-9429(2007)133:12(1421).

Ocio, D., le Vine, N., Westerberg, I., Pappenberger, F. & Buytaert, W. (2017) The role of rating curve uncertainty in real-time flood forecasting. *Water Resources Research*. 53 (5). doi:10.1002/2016WR020225.

O'Connor, P.D.T. & Kleyner, A. (2011) *Practical Reliability Engineering*. Chichester, UK, John Wiley & Sons, Ltd. doi:10.1002/9781119961260.

Ordnance Survey (2021) *Datum height Differences*. 2 June 2021. https://www.ordnancesurvey.co.uk/gps/legacy-control-information/liverpool-to-newlyn.

OTT HydroMet (2018) *Surface Water-Level Sensor Selection Guide*. 2018. https://www.ott.com/download/surface-water-level-sensor-guide/ [Accessed: 4 October 2021].

Oubanas, H., Gejadze, I., Malaterre, P.O. & Mercier, F. (2018) River discharge estimation from synthetic SWOT-type observations using variational data assimilation and the full Saint-Venant hydraulic model. *Journal of Hydrology*. 559 (2018), 638–647. doi:10.1016/j.jhydrol.2018.02.004.

Ozcan, A.H. & Unsalan, C. (2017) LiDAR data filtering and DTM generation using empirical mode decomposition. *IEEE Journal of Selected Topics in Applied Earth Observations and Remote Sensing*. 10 (1). doi:10.1109/JSTARS.2016.2543464.

Pan, F. (2013) Remote sensing of river stage and discharge. *SPIE Newsroom*. (December 2012), 2–5. doi:10.1117/2.1201212.004611.

Pan, F., Wang, C. & Xi, X. (2016) Constructing river stage-discharge rating curves using remotely sensed river cross-sectional inundation areas and river bathymetry. *Journal of Hydrology*. 540. doi:10.1016/j.jhydrol.2016.06.024.

Pappenberger, F., Beven, K., Horritt, M. & Blazkova, S. (2005a) Uncertainty in the calibration of effective roughness parameters in HEC-RAS using inundation and downstream level observations. *Journal of Hydrology*. 302 (1–4), 46–69. doi:10.1016/j.jhydrol.2004.06.036.

Pappenberger, F., Beven, K., Horritt, M. & Blazkova, S. (2005b) Uncertainty in the calibration of effective roughness parameters in HEC-RAS using inundation and downstream level observations. *Journal of Hydrology*. 302 (1–4), 46–69. doi:10.1016/j.jhydrol.2004.06.036.

Pappenberger, F. & Beven, K.J. (2006) Ignorance is bliss: Or seven reasons not to use uncertainty analysis. *Water Resources Research*. 42 (5), 1–8. doi:10.1029/2005WR004820.

Pappenberger, F., Matgen, P., Beven, K.J., Henry, J.-B., Pfister, L. & Fraipont, P. de (2004) The influence of rating curve uncertainty on flood inundation predictions. *Uncertainty Symposium*.

Parhi, P.K., Sankhua, R.N. & Roy, G.P. (2012) Calibration of Channel Roughness for Mahanadi River, (India) Using HEC-RAS Model. *Journal of Water Resource and Protection*. 04 (10), 847–850. doi:10.4236/jwarp.2012.410098.

Pasiok, R. & Dębek, Ł. (2015) *RiverGIS*. 2015. http://rivergis.com/about.html [Accessed: 28 October 2021].

Paul, J.D., Buytaert, W., Paul, J.D. & Buytaert, W. (2018) Sensor networks in rivers: current state and future 1 opportunities. *WATER RESOURCES RESEARCH*. doi:10.1029/.

Paul, J.D., Buytaert, W. & Sah, N. (2020) A Technical Evaluation of Lidar-Based Measurement of River Water Levels. *Water Resources Research*. 56 (4). doi:10.1029/2019WR026810.

Paul, J.D., Cieslik, K., Sah, N., Shakya, P., Parajuli, B.P., Paudel, S., Dewulf, A. & Buytaert, W. (2020) Applying Citizen Science for Sustainable Development: Rainfall Monitoring in Western Nepal. *Frontiers in Water*. 2. doi:10.3389/frwa.2020.581375.

Perumal, M. (1994a) Hydrodynamic derivation of a variable parameter muskingum method: 1. Theory and solution procedure. *Hydrological Sciences Journal*. 39 (5), 431–442. doi:10.1080/02626669409492766.

Perumal, M. (1994b) Hydrodynamic derivation of a variable parameter muskingum method: 2. Verification. *Hydrological Sciences Journal*. 39 (5), 443–458. doi:10.1080/02626669409492767.

Perumal, M., Moramarco, T., Sahoo, B. & Barbetta, S. (2007a) A methodology for discharge estimation and rating curve development at ungauged river sites. *Water Resources Research*. 43 (2). doi:10.1029/2005WR004609.

Perumal, M., Moramarco, T., Sahoo, B. & Barbetta, S. (2007b) A methodology for discharge estimation and rating curve development at ungauged river sites. *Water Resources Research*. 43 (2). doi:10.1029/2005WR004609.

Perumal, M., Moramarco, T., Sahoo, B. & Barbetta, S. (2010) On the practical applicability of the VPMS routing method for rating curve development at ungauged river sites. *Water Resources Research*. 46 (3), 1–9. doi:10.1029/2009WR008103.

Perumal, M. & Ranga Raju, K.G. (2007) Variable Parameter Muskingum Routing Considering Downstream Effects. *Journal of Hydraulic Engineering*. 133 (11). doi:10.1061/(asce)0733-9429(2007)133:11(1249).

Pfeffer, M.J. & Wagenet, L.P. (2012) Volunteer Environmental Monitoring, Knowledge Creation and Citizen-Scientist Interaction. In: *The SAGE Handbook of Environment and Society*. p. doi:10.4135/9781848607873.n16.

Pfeifer, N., Höfle, B., Briese, C., Rutzinger, M. & Haring, A. (2008) Analysis Of The Backscattered Energy In Terrestrial Laser Scanning Data. In: *The International Archives of the Photogrammetry, Remote Sensing and Spatial Information Science*. 2008 p.

Piasecki, M. & Sanders, B.F. (2002) Optimization of Multiple Freshwater Diversions in Well-Mixed Estuaries. *Journal of Water Resources Planning and Management*. 128 (1). doi:10.1061/(asce)0733-9496(2002)128:1(74).

Process Sensing Technologies (2017) *Seven main types of level sensing methods - how do they differ?* 27 July 2017. https://sstsensing.com/7-main-types-of-level-sensors/ [Accessed: 4 October 2021].

Prudhomme, C., Hannaford, J., Harrigan, S., Boorman, D., Knight, J., et al. (2017) Hydrological Outlook UK: an operational streamflow and groundwater level forecasting system at monthly to seasonal time scales. *Hydrological Sciences Journal*. 62 (16), 2753–2768. doi:10.1080/02626667.2017.1395032.

Rahman, A., Weinmann, P.E., Hoang, T.M.T. & Laurenson, E.M. (2002) Monte Carlo simulation of flood frequency curves from rainfall. *Journal of Hydrology*. 256 (3–4). doi:10.1016/S0022-1694(01)00533-9.

dos Reis, G. da C., Pereira, T.S.R., Faria, G.S. & Formiga, K.T.M. (2020) Analysis of the uncertainty in estimates of manning's roughness coefficient and bed slope using glue and dream. *Water (Switzerland)*. 12 (11), 1–15. doi:10.3390/w12113270.

Romeiser, R., Runge, H., Suchandt, S., Sprenger, J., Weilbeer, H., Sohrmann, A. & Stammer, D. (2007) Current measurements in rivers by spaceborne along-track InSAR. In: *IEEE Transactions on Geoscience and Remote Sensing*. 2007 p. doi:10.1109/TGRS.2007.904837.

Sahoo, B., Perumal, M., Moramarco, T. & Barbetta, S. (2014) Rating curve development at ungauged river sites using variable parameter Muskingum discharge routing method. *Water Resources Management*. 28 (11), 3783–3800. doi:10.1007/s11269-014-0709-9.

Sanders, B.F. & Katopodes, N.D. (2000) Adjoint Sensitivity Analysis for Shallow-Water Wave Control. *Journal of Engineering Mechanics*. 126 (9). doi:10.1061/(asce)0733-9399(2000)126:9(909).

Scipy (2021) *Find peaks*. 12 September 2021. https://docs.scipy.org/doc/scipy/reference/generated/scipy.signal.find_peaks.html [Accessed: 1 September 2022].

SciPy (2021) *Hausdorff distance*. 20 August 2021. https://docs.scipy.org/doc/scipy/reference/generated/scipy.spatial.distance.directed_hausdorff.html [Accessed: 31 August 2022].

Seibert, J. & Beven, K.J. (2009) Gauging the ungauged basin: how many discharge measurements are needed? *Hydrology and Earth System Sciences*. 13 (6), 883–892. doi:10.5194/hess-13-883-2009.

Shah, H. (2018a) *IoT communication protocols-Their application, limitations, usage and speed 2018*. 2018. https://www.simform.com/internet-of-things-coomunication-protocols-applications-limitations-use/ [Accessed: 17 March 2019].

Shah, H. (2018b) *LoRaWAN vs Zigbee: Part1-How to compare and select*. 2018. https://www.simform.com/lorawan-vs-zigbee-comparison-part-1/ [Accessed: 17 March 2019].

Shahrim, M.F. & Ros, F.C. (2020) Dam Break Analysis of Temenggor Dam Using HEC-RAS. In: *IOP Conference Series: Earth and Environmental Science*. 2020 p. doi:10.1088/1755-1315/479/1/012041.

Shiklomanov, A.I., Lammers, R.B. & Vörösmarty, C.J. (2002) Widespread decline in hydrological monitoring threatens Pan-Arctic research. *Eos*. 83 (2). doi:10.1029/2002EO000007.

Shope, C.L., Bartsch, S., Kim, K., Kim, B., Tenhunen, J., Peiffer, S., Park, J.H., Ok, Y.S., Fleckenstein, J. & Koellner, T. (2013) A weighted, multi-method approach for accurate basin-wide streamflow estimation in an ungauged watershed. *Journal of Hydrology*. 494. doi:10.1016/j.jhydrol.2013.04.035.

Shrestha, B., Cochrane, T.A., Caruso, B.S., Arias, M.E. & Piman, T. (2016) Uncertainty in flow and sediment projections due to future climate scenarios for the 3S Rivers in the Mekong Basin. *Journal of Hydrology*. 540, 1088–1104. doi:10.1016/j.jhydrol.2016.07.019.

Signoret, J.-P. & Leroy, A. (2021) *Reliability Assessment of Safety and Production Systems*. Springer Series in Reliability Engineering. Cham, Springer International Publishing. doi:10.1007/978-3-030-64708-7.

Simon, R.N., Tormos, T. & Danis, P.-A. (2015) Very high spatial resolution optical and radar imagery in tracking water level fluctuations of a small inland reservoir. *International Journal of Applied Earth Observation and Geoinformation*. 38. doi:10.1016/j.jag.2014.12.007.

Sisinggih, D., Wahyuni, S., Nugroho, R., Hidayat, F. & Idi Rahman, K. (2020) Sediment transport functions in HEC-RAS 4.0 and their evaluation using data from sediment flushing of Wlingi reservoir - Indonesia. In: *IOP Conference Series: Earth and Environmental Science*. 2020 p. doi:10.1088/1755-1315/437/1/012014.

Smart, G.M., Bind, J. & Duncan, M.J. (2009) River bathymetry from conventional LiDAR using water surface returns. In: *18th World IMACS Congress and MODSIM 2009 - International Congress on Modelling and Simulation: Interfacing Modelling and Simulation with Mathematical and Computational Sciences, Proceedings*. 2009 p.

Smith, C.F., Cordova, J.T. & Wiele, S.M. (2010) *The continuous slope-area method for computing event hydrographs*.

Smith, L.C. & Pavelsky, T.M. (2008) Estimation of river discharge, propagation speed, and hydraulic geometry from space: Lena River, Siberia. *Water Resources Research*. doi:10.1029/2007WR006133.

Sönmez, O. & Doğan, E. (2016) Determination of flood inundation area in Cedar River using calibrated and validated 1D and 1D/2D model. In: *SAÜ Fen Bil Der 20. Cilt*. 2016 p.

Soulis, K.X. & Elmaloglou, S. (2018) Optimum soil water content sensors placement for surface drip irrigation scheduling in layered soils. *Computers and Electronics in Agriculture*. 152. doi:10.1016/j.compag.2018.06.052.

Spada, E., Sinagra, M., Tucciarelli, T., Barbetta, S., Moramarco, T. & Corato, G. (2017a) Assessment of river flow with significant lateral inflow through reverse routing modeling. *Hydrological Processes*. 31 (7). doi:10.1002/hyp.11125.

Spada, E., Sinagra, M., Tucciarelli, T. & Biondi, D. (2017b) Unsteady state water level analysis for discharge hydrograph estimation in rivers with torrential regime: The case study of the February 2016 flood event in the Crati River, South Italy. *Water (Switzerland)*. doi:10.3390/w9040288.

Stevens water monitoring systems Inc. (2017) *Water level sensors overview*. 2017. https://stevenswater.com/news-and-articles/water-level-sensors-overview/ [Accessed: 5 October 2021].

Strelkoff, T.S. (1969) One-Dimensional Equations of Open-Channel Flow. *Journal of the Hydraulics Division*. 95 (3). doi:10.1061/jyceaj.0002105.

Tamari, S. & Guerrero-Meza, V. (2016) Flash flood monitoring with an inclined Lidar installed at a river bank: Proof of concept. *Remote Sensing*. 8 (10). doi:10.3390/rs8100834.

Tang, G., Long, D., Hong, Y., Gao, J. & Wan, W. (2018) Documentation of multifactorial relationships between precipitation and topography of the Tibetan Plateau using spaceborne precipitation radars. *Remote Sensing of Environment*. 208. doi:10.1016/j.rse.2018.02.007.

Tauro, F., Petroselli, A. & Grimaldi, S. (2018) Optical sensing for stream flow observations: A review. *Journal of Agricultural Engineering*.49 (4). doi:10.4081/jae.2018.836.

Tauro, F., Piscopia, R. & Grimaldi, S. (2017) Streamflow Observations From Cameras: Large-Scale Particle Image Velocimetry or Particle Tracking Velocimetry? *Water Resources Research*. 53 (12). doi:10.1002/2017WR020848.

The Things Network (2017) *Ground breaking world record! LoRaWAN packet received at 702 km distance*. 2017. https://www.thethingsnetwork.org/article/ground-breaking-world-record-lorawan-packet-received-at-702-km-436-miles-distance [Accessed: 17 March 2019].

Timbadiya, P. v., Patel, P.L. & Porey, P.D. (2011) Calibration of HEC-RAS Model on Prediction of Flood for Lower Tapi River, India. *Journal of Water Resource and Protection*. 03 (11), 805–811. doi:10.4236/jwarp.2011.311090.

USACE (2009) HEC-DSSVue Data Storage System Visual Utility Engine User ' s Manual. *U.S. Army Corps of Engineers*. (July).

Vansteenkiste, T., Tavakoli, M., Ntegeka, V., de Smedt, F., Batelaan, O., Pereira, F. & Willems, P. (2014) Intercomparison of hydrological model structures and calibration approaches in climate scenario impact projections. *Journal of Hydrology*. 519 (PA), 743–755. doi:10.1016/j.jhydrol.2014.07.062.

Venant, S. de (1871) Théorie de mouvement non-permanant des eaux avec application aux crues des rivières et à l'introduction des marées dans leur lit. *Comptes Rendus des Séances de Académie des Sciences*. 73, 148–154.

Villarini, G. & Strong, A. (2014) Roles of climate and agricultural practices in discharge changes in an agricultural watershed in Iowa. *Agriculture, Ecosystems and Environment*. 188. doi:10.1016/j.agee.2014.02.036.

Vojtek, M., Petroselli, A., Vojteková, J. & Asgharinia, S. (2019) Flood inundation mapping in small and ungauged basins: sensitivity analysis using the EBA4SUB and HEC-RAS modeling approach. *Hydrology Research*. 50 (4), 1002–1019. doi:10.2166/nh.2019.163.

Vrugt, J.A. & ter Braak, C.J.F. (2011) DREAM (D): An adaptive Markov Chain Monte Carlo simulation algorithm to solve discrete, noncontinuous, and combinatorial posterior parameter estimation problems. *Hydrology and Earth System Sciences*. 15 (12), 3701–3713. doi:10.5194/hess-15-3701-2011.

Wai-Lok Lai, W., Dérobert, X. & Annan, P. (2018) A review of Ground Penetrating Radar application in civil engineering: A 30-year journey from Locating and Testing to Imaging and Diagnosis. *NDT and E International*. 96. doi:10.1016/j.ndteint.2017.04.002.

Wara, C., Thomas, M., Mwakurya, S. & Katuva, J. (2019) Development of River Rating Curves for Simple to Complex Hydraulic Structure Based on Calibrated HEC-RAS Hydraulic Model, in Kwale, Coastal Kenya. *Journal of Water Resource and Protection*. 11 (04), 468–490. doi:10.4236/jwarp.2019.114028.

Wasantha Lal, A.M. (1995) Calibration of Riverbed Roughness. *Journal of Hydraulic Engineering*. 121 (9). doi:10.1061/(asce)0733-9429(1995)121:9(664).

Water and Energy Commission Secretariat (WECS) (2011) *Water Resources of Nepal in the Context of Climate Change*.

Weinmann, P.E., Rahman, A., Hoang, T.M.T., Laurenson, E.M. & Nathan, R.J. (2002) Monte Carlo Simulation of Flood Frequency Curves from Rainfall – The Way Ahead. *Australasian Journal of Water Resources*. 6 (1). doi:10.1080/13241583.2002.11465212.

Welber, M., le Coz, J., Laronne, J.B., Zolezzi, G., Zamler, D., Dramais, G., Hauet, A. & Salvaro, M. (2016) Field assessment of noncontact stream gauging using portable surface velocity radars (SVR). *Water Resources Research*. 52 (2). doi:10.1002/2015WR017906.

WMO (2011) *Manual on flood forecasting and warning*.

Wolfs, V. & Willems, P. (2014) Development of discharge-stage curves affected by hysteresis using time varying models, model trees and neural networks. *Environmental Modelling and Software*. 55, 107–119. doi:10.1016/j.envsoft.2014.01.021.

Wydeven, T. (1977) Plasma polymerized coating for polycarbonate: single layer, abrasion resistant, and antireflection. *Applied Optics*. 16 (3). doi:10.1364/ao.16.000717.

Xiong, Y. (2011) A Dam Break Analysis Using HEC-RAS. *Journal of Water Resource and Protection*. 03 (06). doi:10.4236/jwarp.2011.36047.

Yang, T.H., Ho, J.Y., Hwang, G. do & Lin, G.F. (2014) An indirect approach for discharge estimation: A combination among micro-genetic algorithm, hydraulic model, and in situ measurement. *Flow Measurement and Instrumentation*. doi:10.1016/j.flowmeasinst.2014.07.003.

Yen, B.C. (1973) OPEN-CHANNEL FLOW EQUATIONS REVISITED. *ASCE J Eng Mech Div*.

YSI Incorporated (2017) *Water level measurement*. 2017. https://www.ysi.com/parameters/level [Accessed: 5 October 2021].

Zhang, Z., Glaser, S.D., Bales, R.C., Conklin, M., Rice, R. & Marks, D.G. (2017) Technical report: The design and evaluation of a basin-scale wireless sensor network for mountain hydrology. *Water Resources Research*. 53 (5). doi:10.1002/2016WR019619.

Appendix A: Summary of performance criteria and results of parameter calibration when additional sensors are used as internal boundary conditions

Cases	KGE [%]	Manning's n [s/m$^{(1/3)}$]	Estimated Initial flow (Q_i) [m^3/s]	Error in Time to peak (T_p) [min]	Error in peak flow (Q_p) [%]	Error in estimation of Initial flow (ε_{Q_i}) [%]	Error in estimation of n (ε_n) [%]	Intermediate Boundary locations	Remarks
Case 2	99.99	0.0357	102.53	0	0	2.53	2.00	None	
	99.99	0.0358	81.33	0	0	-18.67	2.29	2	**Sensors at upstream location**
	99.99	0.0358	107.69	0	-0.41	7.69	2.29	2,4	
	99.99	0.0358	113.58	0	0	13.58	2.29	2,4,6	
	99.99	0.0359	99.55	0	-0.41	-0.45	2.57	2.,4,6,8	
	99.99	0.0358	88.82	0	0.01	-11.18	2.29	2.,4,6,8,10	
	99.99	0.0357	109.73	0	0.01	9.73	2.00	2,4,6,8,10,12	
	99.99	0.0357	107.87	0	0.01	7.87	2.00	2,4,6,8,10,12,14	
	99.99	0.0359	111.11	0	-0.42	11.11	2.57	50	**Sensors at midstream location**
	99.99	0.0357	86.32	0	0	-13.68	2.00	50,52	
	99.99	0.0356	93.51	0	0.422	-6.49	1.71	50,52,54	
	99.99	0.0357	86.65	0	0.004	-13.35	2.00	50,52,54,56	
	99.99	0.0358	84.092	0	-0.34	-15.908	2.29	50,52,54,56,58	
	99.99	0.0358	99.86	0	-0.41	-0.14	2.29	50,52,54,56,58,60	
	99.99	0.0357	116.03	0	0	16.03	2.00	50,52,54,56,58,60,62	
	99.99	0.0358	105.62	0	0	5.62	2.29	80	**Sensors at downstream location**
	99.99	0.0357	99.34	0	0	-0.66	2.00	80,82	
	99.99	0.0358	92.34	0	0	-7.66	2.29	80,82,84	
	99.99	0.0355	106.25	0	0.42	6.25	1.43	80,82,84,86	
	99.99	0.0359	109.13	0	-0.41	9.13	2.57	80,82,84,86,88	
	99.99	0.0357	107.78	0	0	7.78	2.00	80,82,84,86,88,90	
	99.99	0.0356	99.21	0	0.42	-0.79	1.71	80,82,84,86,88,90,92	

Cases	KGE [%]	Manning's n [s/m$^{(1/3)}$]	Estimated Initial flow (Q_i) [m^3/s]	Error in Time to peak (T_p) [min]	Error in peak flow (Q_p) [%]	Error in estimation of Initial flow (ε_{Q_i}) [%]	Error in estimation of n (ε_n) [%]	Intermediate Boundary locations	Remarks
Case 3	99.99	0.0358	113.58	0	-9.24	13.58	2.29	None	
	99.99	0.0357	107.31	0	-0.23	7.31	2.00	2	Sensors at upstream location
	99.99	0.0357	110.17	0	0.43	10.17	2.00	2,4	
	99.99	0.0358	106.95	0	-0.29	6.95	2.29	2,4,6	
	99.99	0.0357	99.13	0	0.01	-0.87	2.00	2.,4,6,8	
	99.99	0.0358	109.78	-5	0.02	9.78	2.29	2.,4,6,8,10	
	99.99	0.0357	92.74	0	-4.77	-7.26	2.00	2,4,6,8,10,12	
	99.99	0.0356	132.04	-5	0.44	32.04	1.71	2,4,6,8,10,12,14	
	99.99	0.0357	88.64	0	-0.18	-11.36	2.00	50	Sensors at midstream location
	99.99	0.0358	98.95	0	0	-1.05	2.29	50,52	
	99.99	0.0357	100.87	-5	0	0.87	2.00	50,52,54	
	99.99	0.0358	78.16	-5	0	-21.84	2.29	50,52,54,56	
	99.99	0.0356	109.44	-5	0.43	9.44	1.71	50,52,54,56,58	
	99.99	0.0357	85.69	-5	0.01	-14.31	2.00	50,52,54,56,58,60	
	99.99	0.0357	113.78	-5	0.01	13.78	2.00	50,52,54,56,58,60,62	
	99.99	0.0358	84.48	0	0	-15.52	2.29	80	Sensors at downstream location
	99.99	0.0358	90.4	0	0	-9.6	2.29	80,82	
	99.99	0.0357	95.11	-5	0	-4.89	2.00	80,82,84	
	99.99	0.0358	93.43	-5	-0.41	-6.57	2.29	80,82,84,86	
	99.99	0.0358	117.54	-5	0	17.54	2.29	80,82,84,86,88	
	99.99	0.0357	97.76	-5	0.003	-2.24	2.00	80,82,84,86,88,90	
	99.99	0.0357	100.11	-5	0.003	0.11	2.00	80,82,84,86,88,90,92	

Cases	KGE [%]	Manning's n [s/m$^{(1/3)}$]	Estimated Initial flow (Q_i) [m^3/s]	Error in Time to peak (T_p) [min]	Error in peak flow (Q_p) [%]	Error in estimation of Initial flow (ε_{Q_i}) [%]	Error in estimation of n (ε_n) [%]	Intermediate Boundary locations	Remarks
Case 4	99.99	0.0357	115	0	0	15	2.00	None	
	99.99	0.0356	96.76	0	0.44	-3.24	1.71	2	Sensors at upstream location
	99.99	0.0357	94.28	0	0.03	-5.72	2.00	2,4	
	99.99	0.0354	104.82	0	0.89	4.82	1.14	2,4,6	
	99.99	0.0356	106.08	0	0.48	6.08	1.71	2.,4,6,8	
	99.99	0.0359	94.24	0	-0.36	-5.76	2.57	2.,4,6,8,10	
	99.99	0.0358	93.04	0	0.08	-6.96	2.29	2,4,6,8,10,12	
	99.99	0.0357	90.57	0	0.08	-9.43	2.00	2,4,6,8,10,12,14	
	99.99	0.0357	94.63	0	-0.04	-5.37	2.00	50	Sensors at midstream location
	99.99	0.0359	105.61	0	-0.4	5.61	2.57	50,52	
	99.99	0.0358	111.6	0	0.03	11.6	2.29	50,52,54	
	99.99	0.0357	91.51	0	0.33	-8.49	2.00	50,52,54,56	
	99.99	0.0358	94.19	0	0.04	-5.81	2.29	50,52,54,56,58	
	99.99	0.0359	94.1	0	-0.37	-5.9	2.57	50,52,54,56,58,60	
	99.99	0.0356	105.47	-5	0.11	5.47	1.71	50,52,54,56,58,60,62	
	99.99	0.0358	98.65	0	0.005	-1.35	2.29	80	Sensors at downstream location
	99.99	0.0357	105.1	0	0.01	5.1	2.00	80,82	
	99.99	0.0358	95.94	0	-0.44	-4.06	2.29	80,82,84	
	99.99	0.0358	111.95	0	0.01	11.95	2.29	80,82,84,86	
	99.99	0.0358	93.25	0	-0.4	-6.75	2.29	80,82,84,86,88	
	99.98	0.0356	91.2	-5	0.43	-8.8	1.71	80,82,84,86,88,90	
	99.99	0.0357	89.1	-5	0.01	-10.9	2.00	80,82,84,86,88,90,92	

Cases	KGE [%]	Manning's n [s/m$^{(1/3)}$]	Estimated Initial flow (Q_i) [m^3/s]	Error in Time to peak (T_p) [min]	Error in peak flow (Q_p) [%]	Error in estimation of Initial flow (ε_{Q_i}) [%]	Error in estimation of n (ε_n) [%]	Intermediate Boundary locations	Remarks
Case 6	99.99	0.0358	96.42	0	0	-3.58	2.29	None	
	99.99	0.0357	104.41	0	0.01	4.41	2.0	2	Sensors at upstream location
	99.99	0.0359	96.37	0	-0.41	-3.63	2.6	2,4	
	99.99	0.0359	83.88	0	-0.4	-16.12	2.6	2,4,6	
	99.99	0.0358	94.86	0	-0.37	-5.14	2.3	2.,4,6,8	
	99.99	0.0359	95.47	0	-0.4	-4.53	2.6	2.,4,6,8,10	
	99.99	0.0357	102.11	-5	0.024	2.11	2.0	2,4,6,8,10,12	
	99.99	0.0355	93.93	-5	0.45	-6.07	1.4	2,4,6,8,10,12,14	
	99.99	0.0358	97.09	0	-0.41	-2.91	2.3	50	Sensors at midstream location
	99.99	0.0357	95.95	0	0.425	-4.05	2.0	50,52	
	99.99	0.0358	108.55	0	-0.4	8.55	2.3	50,52,54	
	99.99	0.0357	85.24	0	0.01	-14.76	2.0	50,52,54,56	
	99.99	0.0357	102.77	0	0.01	2.77	2.0	50,52,54,56,58	
	99.98	0.0361	104.89	0	-0.81	4.89	3.1	50,52,54,56,58,60	
	99.99	0.0358	98.88	-5	-0.34	-1.12	2.3	50,52,54,56,58,60,62	
	99.99	0.0358	103.27	0	0	3.27	2.3	80	Sensors at downstream location
	99.99	0.0357	87.11	0	0.003	-12.89	2.0	80,82	
	99.99	0.0356	117.54	0	0.42	17.54	1.7	80,82,84	
	99.99	0.0358	104.94	0	0	4.94	2.3	80,82,84,86	
	99.99	0.0357	95.8	0	0	-4.2	2.0	80,82,84,86,88	
	99.99	0.0358	99.16	0	-0.41	-0.84	2.3	80,82,84,86,88,90	
	99.99	0.0358	84.36	-5	0	-15.64	2.3	80,82,84,86,88,90,92	